ORBITAL PERTURBATIONS FOR SPACE SITUATIONAL AWARENESS

A Dissertation

Submitted to the Faculty

of

Purdue University

by

Smriti Nandan Paul

In Partial Fulfillment of the

Requirements for the Degree

of

Doctor of Philosophy

August 2020

Purdue University

West Lafayette, Indiana

THE PURDUE UNIVERSITY GRADUATE SCHOOL STATEMENT OF DISSERTATION APPROVAL

Dr. Carolin Frueh, Chair

School of Aeronautics and Astronautics

Dr. Kathleen Howell

School of Aeronautics and Astronautics

Dr. James M. Longuski

School of Aeronautics and Astronautics

Dr. Inseok Hwang

School of Aeronautics and Astronautics

Approved by:

Dr. Gregory Blaisdell

Associate Head of Gambaro Graduate Program of Aeronautics and Astronautics

To all the great mentors in my life

ACKNOWLEDGMENTS

I would like to thank my advisor, Dr. Carolin Frueh, for mentoring and guiding me over the years. Since the time I joined Purdue University, I have grown a lot both as a researcher and as a teacher, and I owe it to the persistent guidance from Dr. Frueh. I would like to thank my PhD committee members for their insightful comments. My parents, sister, and other family members have always been supportive of my academic ambitions, and I am grateful for that. I would also like to thank my first roommates, Roshan and Sri Anish, for brainstorming on various research ideas and for their constructive criticism. Last but not the least, I would like to thank my office-mates for their camaraderie and tolerating my poor jokes, both of which made the graduate life much more enjoyable.

TABLE OF CONTENTS

LIST OF TABLES

LIST OF FIGURES

ABSTRACT

Paul, Smriti Nandan PhD, Purdue University, August 2020. Orbital Perturbations for Space Situational Awareness. Major Professor: Carolin Frueh.

Because of the increasing population of space objects, there is an increasing necessity to monitor and predict the status of the near-Earth space environment, especially of critical regions like geosynchronous Earth orbit (GEO) and low Earth orbit (LEO) regions, for a sustainable future. Space Situational Awareness (SSA), however, is a challenging task because of the requirement for dynamically insightful fast orbit propagation models, presence of dynamical uncertainties, and limitations in sensor resources. Since initial parameters are often not known exactly and since many SSA applications require long-term orbit propagation, long-term effects of the initial uncertainties on orbital evolution are examined in this work. To get a long-term perspective in a fast and efficient manner, this work uses analytical propagation techniques. Existing analytical theories for orbital perturbations are investigated, and modifications are made to them to improve accuracy. While conservative perturbation forces are often studied, of particular interest here is the orbital perturbation due to non-conservative forces. Using the previous findings and the developments in this thesis, two SSA applications are investigated in this work. In the first SSA application, a sensor tasking algorithm is designed for the detection of new classes of GEO space objects. In the second application, the categorization of near-GEO objects is carried out by combining knowledge of orbit dynamics with machine learning techniques.

1 INTRODUCTION

The last two decades have seen phenomenal growth in the object population in the near-Earth space environment due to an increase in the number of launch providers, ambitious satellite constellation programs, and undesirable experiments featuring anti-satellite weapons. The growth in object population increases the risk of collision among space objects threatening the sustainability of this precious space. Thus, there is a necessity for better Space Situational Awareness (SSA), which is defined by the Space Foundation as[1] *"the ability to view, understand and predict the physical location of natural and man-made objects in orbit around the Earth, with the objective of avoiding collisions."*

Orbit propagation is often an essential part of SSA applications like the prediction of object populations, collision avoidance maneuvers, object detection, object tracking, and catalog maintenance. The selection of the orbit propagation technique for any SSA task depends on the user requirement for accuracy and computational time. Accurate orbital trajectories of space objects can be obtained using numerical techniques. However, numerical techniques are computationally expensive, thereby making them unsuitable when the propagation period is large. Numerical techniques also provide no general insight other than the specific orbit being propagated. Computational complexity involving numerical techniques can be overcome by propagating orbits using analytical perturbation techniques, which not only facilitate fast orbit propagation but also permit meaningful theoretical insight into the structure of the orbital perturbations. Popular analytical techniques include (1) using analytical expressions obtained from integration of Lagrange's planetary equations (for conservative perturbation forces) so that short-period variations do not appear in the final solution (2) using analytical expressions obtained via integration of Gauss's variational equations (for both non-conservative and conservative perturbation forces) (3) using averaging techniques involving Hamiltonian formulation (for conservative perturbation forces).

[1] `https://www.spaceacademy.net.au/intell/ssa.htm`. Last accessed: May 02, 2020.

Apart from pure numerical or pure analytical techniques, a compromise between the accuracy of numerical techniques and the computational simplicity of analytical techniques can be achieved through the use of semi-analytical techniques.

One can select from an array of different sets of orbital elements while developing analytical orbital perturbation expressions or while numerically integrating an orbit. Keplerian elements are the most popular ones, and they are used in this research work because of easy geometric interpretation and elegant perturbation expressions. However, analytical theories based on classical Keplerian elements are often prone to singularities from small eccentricity, small inclination, or other singular factors depending on the formulation of the analytical theory. Equinoctial elements, whose direct geometric interpretation is relatively difficult, have the advantage that they are free from singularities. Some authors prefer to use Lagrangian and Hamiltonian dynamics and hence use canonical variables like Delaunay elements (canonical counterpart to Keplerian elements) and Poincaré elements (canonical counterpart to equinoctial elements). Analytical formulas based on Delaunay elements suffer from singularities because of small eccentricity and small inclination, whereas the ones based on Poincaré elements do not suffer from these singularities.

Significant literature exists in the development of analytical orbital perturbation theory. Kozai [1] presents one of the earliest theories for analytical orbit propagation. Kozai uses averaging techniques on Lagrange's planetary equations (LPE) in order to obtain second-order secular and first-order periodic variations in Kepler's elements. Kozai's work deals with the zonal harmonics J_2, J_3, J_4 of Earth's gravitational potential, and ignores the effect of atmospheric drag. In the same year as work by Kozai, Brouwer [2] presents an analytical theory for perturbation due to zonal harmonics J_2, J_3, J_4, J_5. Brouwer's theory [2], which is based on the method of Von Zeipel, is developed through two successive canonical transformations of Hamiltonian mechanics using Delaunay variables; it becomes the basis for several later works. Kozai [3] extends Brouwer's theory to derive second-order periodic perturbations and third-order

secular perturbations in the presence of J_2 through J_8 zonal harmonic perturbations. Since Brouwer's theory is singular for small eccentricities and inclinations, Lyddane [4] proposes a modification to Brouwer's theory by using Poincare variables instead of the Delaunay variables. Brouwer and Hori [5] provide an analytical solution using Delaunay variables to the combined effects of atmospheric drag and J_2, J_3, J_4, J_5 zonal harmonics of Earth's gravitational potential. The authors use an exponential model for the Earth's atmosphere with the assumption that there is no atmospheric rotation. Their work demonstrates the usefulness of canonical transformations even when non-conservative perturbation forces are considered in a system. Aksnes [6] provides second-order perturbation theory corresponding to J_2, J_3, J_4 zonal perturbations using a rotating ellipse as an intermediate orbit. His theory is based on Lie-Hori method [7] and uses Hill variables. Although his theory has a singularity in the form of critical inclination, it is valid for any eccentricity. Deprit and Rom [8] use Deprit-Lie method [9] and give third-order short and long period perturbations and fourth-order secular perturbations due to J_2 zonal harmonic. The authors use Delaunay variables and make expansions in the power series of eccentricity in order to avoid zero eccentricity singularity. Their theory, however, is limited to near-circular orbits. Cook [10] derives analytical expressions for long-period variations in Keplerian elements due to tesseral harmonics up to the fourth degree, for orbits of any eccentricity and inclination. Kaula [11], with the help of so-called 'inclination functions' and 'eccentricity functions', derives first-order perturbation expressions for any zonal or tesseral term of the Earth's gravitational potential. Wnuk [12] uses a modification of Kaula's expressions [11] to give a first-order perturbation theory due to the Earth's tesseral harmonics up to an arbitrary degree and order. He bases his theory on Hori's Lie series [7]. The perturbations are given in non-singular orbital elements, which are functions of eccentricity and Delaunay variables. Wnuk [13], following his previous work [12], further gives perturbations in the Keplerian orbital elements due to tesseral harmonics of Earth's gravitational potential. Lane [14] uses

LPE to provide a first-order analytical solution to the perturbations in Keplerian elements due to tesseral harmonic resonance. The author manipulates LPE to resemble the equation of motion of a simple pendulum to derive the expressions. Based on the integration of GVE, Cook [15] provides a first-order analytical theory for secular and long-periodic orbital changes due to luni-solar perturbations. Roy [16] derives analytical first-order secular and periodic changes due to Luni-solar perturbation forces for a near-Earth artificial satellite. The author bases his theory on Brown's lunar theory [17] and uses Keplerian orbital elements for his analysis. Giacaglia [18] has calculated short-period, long-period, and secular perturbation terms due to the Moon. His expressions use ecliptic elements for the Moon and equatorial elements for the satellite. The earlier mentioned work by Cook [15] also derives perturbation expressions for Keplerian elements due to direct solar radiation pressure. His expressions are obtained through the analytical integration of GVE. The author assumes a cylindrical model for Earth's shadow and expresses the perturbations in terms of shadow entry and exit true anomalies. Kozai [19] derives expressions similar to that of Cook [15] using GVE but in terms of shadow entry and exit eccentric anomalies. While Kozai [19] does not assume any specific form for the solar radiation pressure and leaves few integrals unevaluated, Aksnes [20] assumes a cannonball model for the direct solar radiation pressure and uses Kozai's formulas to give short periodic and long periodic perturbations. The author also corrects three misprints in Kozai's formula and gives modifications for handling small eccentricities and small inclinations. Peng and Gao [21] use Gauss's variational equations to develop analytical perturbation due to Lorentz force. The authors model the Earth's magnetic field as a dipole and assume that the dipole orientation does not change during one orbital period.

Schaub and Alfriend [22] has developed an analytical technique to establish J_2 invariant relative orbits for spacecraft formation flying. With the help of Brouwer's satellite theory [2], the authors use mean orbital elements to design J_2 invariant orbits. In their method, the authors establish two first-order conditions between the differences

in semi-major axis, eccentricity, and inclination angle in order to match the drift rates of two neighboring orbits. Mahajan, Vadali, and Alfriend [23] have developed an analytical solution for relative motion under the complete zonal perturbations. The authors provide an analytical solution for secular rates, second-order short-period, and first-order long-period generating functions in closed-form in eccentricity. Rosengren and Scheeres have carried out a number of work using semi-analytical techniques for orbit propagation. In Ref. [24], the authors develop a first-order averaged model in terms of Milankovitch elements in order to study the long-term dynamics of HAMR objects. The authors shed light on the behavior of Saros resonance and the systematic structure of the inclination-node phase space through their work. A similar investigation is also carried out by Rosengren and Scheeres in Refs. [25] and [26]. Wiesel [27] provides a solution for satellite relative motion about an oblate Earth by employing the Floquet theory and semi-analytical perturbation theory. In the proposed modeling, the author includes all zonal harmonics of the Earth's gravitational field producing a solution accuracy that is at least three orders of magnitude better than the traditional Clohessy-Wiltshire solution. Der [28] provides an analytical first-order Keplerian state transition matrix. The author makes a comparison of his analytical state transition matrix with other forms of state transition matrices in local-vertical coordinate system. Pollock, Gangestad, and Longuski [29] present an analytical solution for the relative motion of a charged spacecraft under Lorentz force perturbations. The authors linearize their dynamical models for obtaining approximate solutions.

Some of the existing analytical theories due to Earth zonal and tesseral gravitational attractions, Sun and Moon gravitational forces, solar radiation pressure, and Lorentz force are investigated in this thesis for a better understanding of the assumptions and derivations and improved upon whenever required. In this thesis, Brouwer's theory [2] is used for modeling zonal perturbations, and Lane's analytical theory [14] is used for modeling the effect of tesseral resonance. Cook's first order theory for third body perturbations [15] lacks adequate accuracy, so a second-order theory is proposed in

this thesis. Cook's analytical theory for solar radiation pressure perturbations [15] diverges with time, so a modified update scheme that improves the accuracy by one order of magnitude is proposed in this thesis. The analytical formulation for Lorentz perturbations by Peng and Gao [21] is applicable only for low Earth orbit, so a set of modified analytical formulas applicable for all near-Earth altitudes is derived in this thesis.

Through the use of analytical orbital theories, the goal of this research work is to investigate the propagation of initial uncertainties in orbital and dynamics parameters with its applicability pertaining to SSA. Initial uncertainties in these parameters arise from a plethora of sources including imperfect sensor measurements, inadequate knowledge about object shape, attitude, material, nature of the interaction between object and environment, and various types of sensor limitations. In this work, the initial uncertainty is addressed by assuming a probability distribution for the initial state and for the uncertain design parameters. Two strategies are followed for capturing and propagating the initial uncertainties. The first approach is the Monte Carlo approach, where a large number of particles are sampled from initial distribution, and these are propagated via analytical techniques. In the second approach, only a few carefully selected particles are used; these so-called sigma points are obtained through the technique of unscented transform (UT) [30]. These sigma points are then propagated via analytical formulas. The results from the UT based method are then compared to the Monte Carlo method in order to study or validate the accuracy of this technique. Although the use of analytical techniques makes the propagation much faster compared to numerical or semi-analytical techniques, the Monte Carlo approach still requires many samples when compared to the UT approach. On the other hand, the main disadvantage of the UT approach is that it captures only the first two moments of the distribution, so information on higher moments is lost. Finally, design of a sensor tasking algorithm for detection of object population is carried out. While both variational equations and sensor tasking strategies have been han-

dled individually in the past, the novelty of this work is to combine these two concepts together.

Detection of new object classes is of particular interest in this research work. One such class of objects that this research work investigates is high area-to-mass ratio (HAMR) objects. HAMR objects, which have first been detected in the geosynchronous region by Schidknecht et al. [31, 32], are susceptible to large perturbations mainly from non-conservative forces. This makes their detection and tracking challenging and very few of them are currently cataloged in the space catalogs. These objects have AMR typically greater than 1 m^2/kg. The source of origin of HAMR objects is still debatable, but it is suspected that most of them originate from the delamination of multi-layer insulation (MLI) used for thermal insulation of spacecraft. As indicated, the investigation of the effect of non-conservative perturbation forces is important for the detection of new object classes. While many authors do consider the non-conservative solar radiation pressure in their orbital investigation, they tend to exclude Lorentz force perturbation from their analysis because of its relatively small magnitude compared to other perturbation forces. However, space objects are sometimes susceptible to getting highly charged especially during eclipses [33], during solar energetic particle events [34], and inside high charge plasma environment like the auroral ovals [35]. Under these high-charge scenarios, Lorentz force can be comparable to few other perturbative forces. Thus, the novelty and occasional occurrence of these high-charge events call for a special investigation of Lorentz force perturbations.

While analytical formulas only give insight into the dynamics of space objects, the last two decades have also seen an outpour of space data because of better and increased detection/tracking capabilities and increased number of space objects, and this calls for a combined dynamics-data approach to tackle SSA. The data approach has slowly but steadily gained traction in the SSA community because of increasing computational capabilities and reinforced confidence stemming from its acceptability

across other disciplines of science and technology. A concerted effort towards making data more accessible to the public via open source or public domain licensing to encourage a wider community-based SSA has also led to the increased popularity of a data-based approach. Machine learning or data-based approach can be used for a plethora of SSA applications, most notably for the detection of maneuvers and anomalous events in space objects.

Apart from sensor tasking for object detection, another SSA application that has been investigated upon in this research work is the categorization of near-geosynchronous space objects. The focus is upon the long-term evolutionary trend in the categorization of space objects. Object categorization allows for more methodical treatment of space objects for SSA purposes. Objects in a single cluster or group can have similar dynamical characteristics, and they may pose a similar level of threat to active space assets. Sometimes, an effort to cluster space objects into different groups can also lead to the discovery of objects with unique and novel properties. In this research work, orbital information on near-geosynchronous objects is first extracted from publicly available two-line element (TLE) data. Criteria based on dynamical knowledge is then used to categorize these objects into eight different groups. Thereafter, a supervised machine learning technique (Neural Network) is used to learn from this input orbital data and its categorization to estimate the categorization of any new orbital data.

1.1 Research Questions

This thesis tries to answer the following four broad research questions:

1. How can we improve upon existing analytical propagation theories so that there is no significant divergence or trend mismatch over decade-long propagation periods, especially for non-conservative perturbation forces?

2. Can initial uncertainties in dynamical parameters be captured and propagated in a computationally efficient manner for SSA relevant applications?

3. Can variational equations in presence of uncertainties be used for sensor tasking for detection of new classes of space objects?

4. How can we combine knowledge of dynamics with data based approach for space object categorization?

1.2 Outline of the Dissertation

Chapter 2 details the assumptions and derivations of analytical orbital perturbation theories. It introduces orbital perturbations due to higher harmonics of Earth's gravitational potential, analytical expressions corresponding to luni-solar perturbations along with higher-order improvements, and analytical perturbations corresponding to solar radiation pressure with divergence improvements. A discussion on numerical orbit propagation and a comparison between numerical and analytical orbit propagation results are also carried out.

Chapter 3 is dedicated to Lorentz force perturbations. A detailed discussion on numerical modeling of Lorentz force is first carried out. This is followed by the development of an analytical theory for Lorentz perturbations applicable to all near-Earth altitudes.

Chapter 4 discusses uncertainties in orbital and dynamical parameters. Simulations investigating the propagation of uncertainties using analytical techniques are presented, and a comparison between the unscented transformation technique and Monte Carlo technique for orbit uncertainty propagation is provided. Furthermore, justification is also provided for the use of Gaussian distribution over other distributions for initial uncertainty representation.

Chapter 5 introduces the topic of sensor tasking for the detection of GEO space objects. Sensor tasking is posed as an optimization problem following the formulation by Frueh et al. [36]. The sensor tasking formulation relies on a "hypothesis surface" constructed with the help of variational equations. A simulation is carried out for the detection of known GEO objects using the sensor tasking strategy. The analysis leads to the successful detection of a large number of GEO objects and serves as a confidence-building step. Thereafter, a simulation is carried out for the detection of unknown HAMR objects in the GEO region.

Chapter 6 presents a discussion on the dynamic characteristics of near-GEO space objects, orbital data processing, and the Neural Network learning algorithm. A schematic based on combined dynamics and machine learning for categorization of near-GEO space objects is presented. Based on the schematic, a simulation is carried out to investigate the evolution of trends in the categorization of space objects between the years 2001 and 2013.

Chapter 7 provides a summary of the work done and proposes future work.

2 MODELING ANALYTICAL PERTURBATIONS

It is important to analyze and discuss the assumptions and derivations of analytical orbital theories and compare them against accurate numerical models to understand the nuances in perturbation structures and assess if there is a need for new or improved analytical theories in order to meet a desired accuracy level. This chapter highlights the derivations for various analytical theories that form the basis for SSA applications discussed in later chapters. Contributions in this chapter constitute the development of a higher-order theory for third-body perturbations and modifications to the update scheme for solar radiation pressure perturbations.

2.1 Modeling Perturbations Due to Zonal and Tesseral Harmonics of Earth's Gravity

The gravitational effect of the departure of Earth from an ideal sphere can be modeled through latitude dependent zonal harmonic terms, latitude/longitude dependent tesseral harmonic terms, and longitude dependent sectorial harmonic terms [37]. This research only takes into consideration the first three zonal harmonics, J_2, J_3, J_4, with J_2 being the most dominant zonal harmonic term. The effect of tesseral and sectorial harmonics on orbital elements is mainly significant under resonance condition (described later). For the GEO objects simulated later in this work, only the effect of dominant $J_{[2,2]}$ tesseral harmonic term is considered.

2.1.1 Modeling Zonal Perturbations

For obtaining zonal perturbations, the well-known Brouwer's analytic formulas [2] are used in this thesis. To use Brouwer's analytical formulas, one needs to compute the so-called 'Brouwer mean elements,' which can be obtained from the osculating elements using Cain's iteration scheme [38]. Brouwer's theory has singularity near the critical inclination of 63.4^0, but that issue will not be addressed here, as this research

mostly deals with orbits of lower inclinations.

A comparison between Brouwer's orbit propagation and numerical orbit propagation is carried out next to demonstrate the accuracy of Brouwer's analytical theory. The numerical results are obtained via the direct integration of GVE using Dormand and Prince's Runge-Kutta (4,5) ODE solver [39] with relative tolerance of 10^{-12} and absolute tolerance of 10^{-12}. The rationale behind the selection of the numerical method is discussed later in section 2.4. For completion, the GVE are given as:

$$\frac{da}{dt} = \frac{2}{n\sqrt{1-e^2}}\Big[Se\sin f + T(1+e\cos f)\Big] \tag{1a}$$

$$\frac{de}{dt} = \frac{\sqrt{1-e^2}}{na}\Big[S\sin f + T(\cos f + \cos E)\Big] \tag{1b}$$

$$\frac{di}{dt} = \frac{r\cos(\omega+f)}{na^2\sqrt{1-e^2}}W \tag{1c}$$

$$\frac{d\Omega}{dt} = \frac{r\sin(\omega+f)}{na^2\sqrt{1-e^2}\sin i}W \tag{1d}$$

$$\frac{d\omega}{dt} = \frac{\sqrt{1-e^2}}{nae}\Big[-S\cos f + T\Big(1+\frac{r}{p}\Big)\sin f\Big] - \cos i\frac{d\Omega}{dt} \tag{1e}$$

$$\frac{dM}{dt} = n - \frac{1}{na}\Big[\frac{2r}{a} - \frac{1-e^2}{e}\cos f\Big]S - \frac{(1-e^2)}{nae}\Big[1+\frac{r}{a(1-e^2)}\Big]\sin fT \tag{1f}$$

where a, e, i, Ω, ω, M, f, E represent the Keplerian orbital parameters of semi-major axis, eccentricity, inclination, right ascension of ascending node (RAAN), argument of perigee (AoP), mean anomaly, true anomaly, and eccentric anomaly, respectively. The parameters n, r, p represent orbital mean motion, the radial distance of the object from Earth center, and orbital semilatus rectum, respectively. S is the component of perturbation acceleration in the radial direction, T is the component perpendicular to radial vector in the orbital plane and velocity-increasing direction, and W is the component perpendicular to the orbital plane and completes the right-handed orthogonal system. The expressions for S, T, and W, for the first three zonal harmonics,

are given as [40] [2]:

$$S = \frac{\mu_E}{r^2}\left[\frac{3}{2}J_2\left(\frac{R_E}{r}\right)^2(3f_nS_n^2-1) + 2J_3\left(\frac{R_E}{r}\right)^3\sin i \right. \\ \left. (5f_nS_n^3 - 3S_n) + \frac{5}{8}J_4\left(\frac{R_E}{r}\right)^4(35f_n^2S_n^4 - 30f_nS_n^2+3)\right] \tag{2}$$

$$T = -\frac{\mu_E}{r^2}\sin i\cos u\left[3J_2\left(\frac{R_E}{r}\right)^2\sin i\sin u + \frac{3}{2}J_3\left(\frac{R_E}{r}\right)^3 \right. \\ \left. (5f_nS_n^2-1) + \frac{5}{2}J_4\left(\frac{R_E}{r}\right)^4\sin i(7f_nS_n^3 - 3S_n)\right] \tag{3}$$

$$W = -\frac{\mu_E}{r^2}\cos i\left[3J_2\left(\frac{R_E}{r}\right)^2\sin i\sin u + \frac{3}{2}J_3\left(\frac{R_E}{r}\right)^3(5f_nS_n^2-1) \right. \\ \left. + \frac{5}{2}J_4\left(\frac{R_E}{r}\right)^4\sin i(7f_nS_n^3 - 3S_n)\right] \tag{4}$$

where $f_n = \sin^2 i$, $S_n = \sin u$, with $u = (\omega + f)$ being the argument of latitude. J_2, J_3, J_4 are the zonal harmonic coefficients. The parameters R_E and μ_E represent Earth equatorial radius and Earth standard gravitational parameter, respectively.

Fig. 2.1 shows a comparison between analytical and numerical results for an object perturbed by zonal harmonics with the corresponding simulation set-up given in Table 1. In Figs. 2.1(a), 2.1(c), 2.1(e), 2.1(g), 2.1(i), the

Table 1: Simulation parameters for comparison between numerical and analytical methods for zonal perturbation.

Parameter	Value
Initial Semi-major Axis	42164 km
Initial Eccentricity	.01
Initial Inclination	10^0
Initial AoP	$.1^0$
Initial RAAN	$.1^0$
Initial Epoch	2437582.5 JD
Propagation Period	15 years

[2] Merson [40] has a typo in his expression for S, which has been corrected here.

red curve corresponds to analytical simulation and the blue curve corresponds to numerical integration. Figs. 2.1(b), 2.1(d), 2.1(f), 2.1(h), 2.1(j) show the difference between analytical and numerical results. The semi-major axis differences, eccentricity differences, inclination differences, and AoP differences have no obvious secular trends. During this interval, the maximum semi-major axis difference is a mere 0.14 m approximately, the maximum eccentricity difference is 3.5×10^{-8} approximately, the maximum inclination difference is 7.5×10^{-7} degrees approximately, and the maximum AoP difference is 8.3×10^{-4} degrees approximately. The RAAN differences have a secular trend but the absolute value of maximum differences stands at a mere 1.3×10^{-5} degrees approximately. Since the analytical simulation is able to follow the expensive numerical simulation, it is decided not to pursue a further higher-order analytic theory for modeling zonal perturbations.

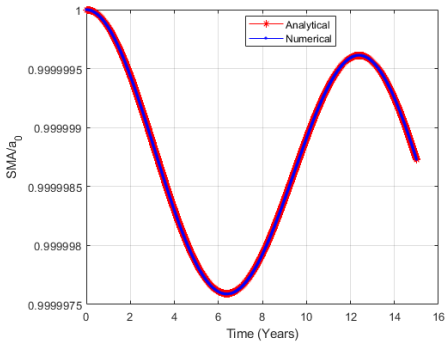

(a) Semi-Major Axis.

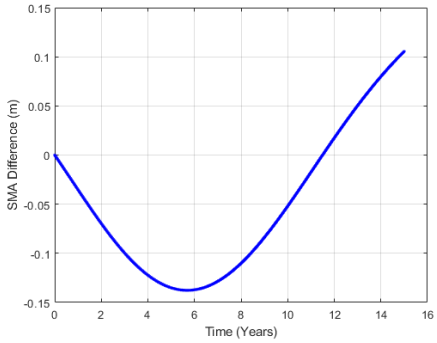

(b) Δ Semi-Major Axis.

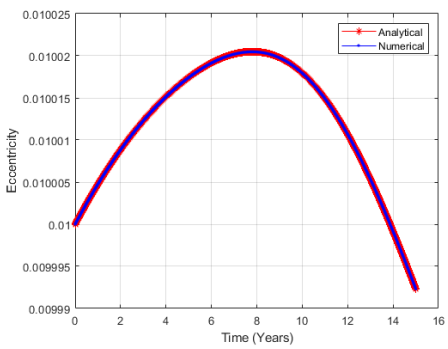

(c) Eccentricity.

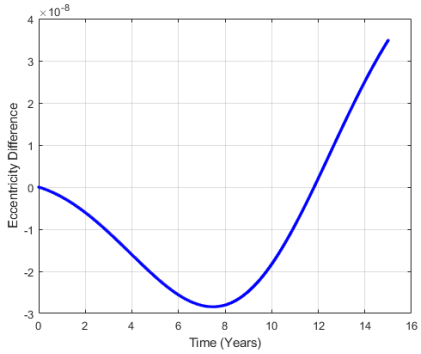

(d) Δ Eccentricity.

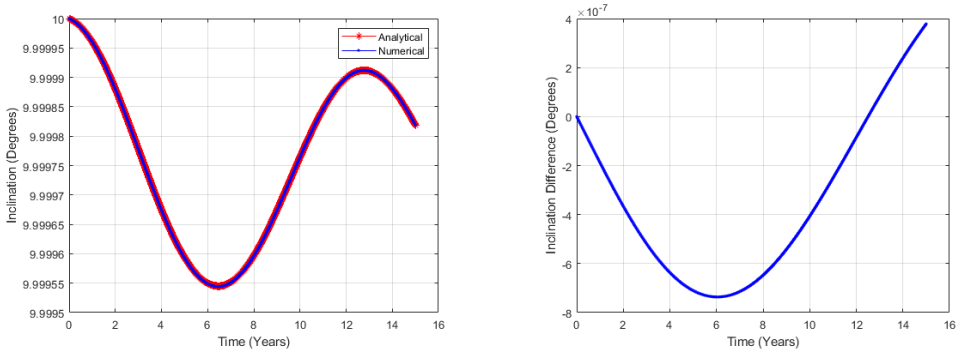

(e) Inclination.

(f) Δ Inclination.

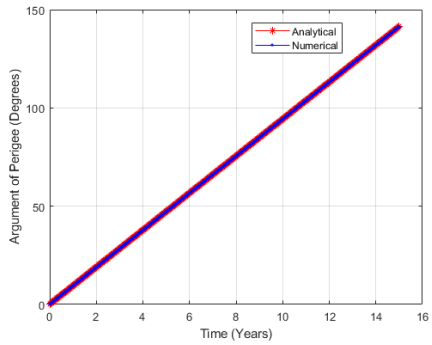

(g) AoP.

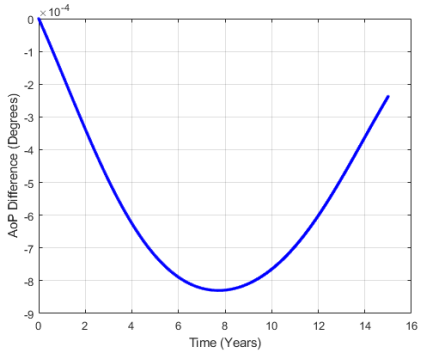

(h) Δ AoP.

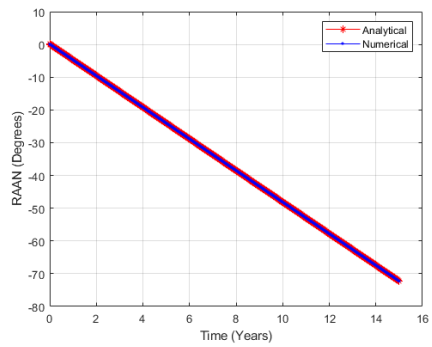

(i) RAAN.

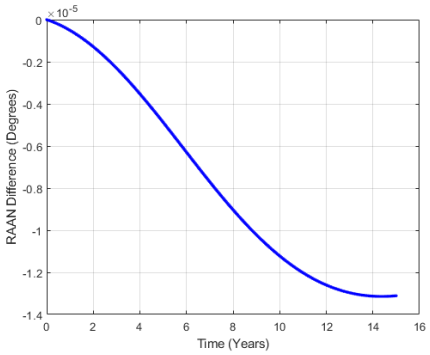

(j) Δ RAAN.

Figure 2.1: Analytical versus numerical simulation for perturbation due to Earth zonal harmonics.

2.1.2 Modeling Tesseral Perturbations

Near-GEO objects often have orbital periods close to Earth's rotation period, thereby satisfying the criterion for orbital resonance. Under this so-called '1:1 resonance condition', the tesseral harmonic term $J_{[2,2]}$ is a dominant contributor to orbital perturbations. Model-

ing analytical perturbations due to tesseral harmonics under resonance condition is rather a challenging task, and its derivation deserves special attention. This research work uses Lane's analytical theory [14] for tesseral perturbations.

Lane uses an analogy between Lagrange's planetary equations and simple pendulum equations of motion (EoM) to obtain his analytical expressions. Lane's theory is based on Kaula's expression [11] for geopotential disturbing function:

$$V = \sum_{l=2}^{\infty} \sum_{m=0}^{l} \sum_{p=0}^{l} \sum_{q=-\infty}^{q=\infty} V_{lmpq} \tag{5}$$

$$V_{lmpq} = \left(\frac{\mu_E}{a}\right)\left(\frac{R_E}{a}\right)^l F_{lmp}(i) G_{lpq}(e) J_{[l,m]} \begin{cases} \cos\psi_{lmpq} & l-m \ \ even \\ \sin\psi_{lmpq} & l-m \ \ odd \end{cases} \tag{6}$$

where μ_E, R_E, a represent Earth equatorial radius, Earth standard gravitational parameter, and semi-major axis, respectively. Inclination function $F_{lmp}(i)$ and eccentricity function $G_{lpq}(e)$ can be obtained from Kaula [11]. The parameter $J_{[l,m]} = \sqrt{C_{lm}^2 + S_{lm}^2}$, with C_{lm}, S_{lm} being unnormalized spherical harmonic coefficients of degree l and order m. The angular parameter ψ_{lmpq} is defined shortly. The indices l and m represent degree and order of the spherical harmonic respectively (i.e., $l = 2$ and $m = 2$ for $J_{[2,2]}$), index p can take integer values between 0 and l, and index q can take any integer value. Critical indices l, m, p, q which result in resonance satisfy $l - 2p + q = \frac{m}{s_0}$, where s_0 is the integer closest to object's mean motion in revolutions per day (for near-GEO, $s_0 = 1$). In this research, as an approximation, only the effect of dominant term corresponding to $l = 2, m = 2, p = 0, q = 0$ is considered.

Variation of the Semi-major Axis

The disturbing function for an even $(l-m)$, corresponding to the dominant critical indices, is given as:

$$R = V_{lmpq} = \left(\frac{\mu_E}{a}\right)\left(\frac{R_E}{a}\right)^l F_{lmp}(i) G_{lpq}(e) J_{[l,m]} \cos\psi_{lmpq} \tag{7}$$

The angular argument ψ_{lmpq} is given as:

$$\psi_{lmpq} = m(\lambda - \lambda_{lm}) - q\omega \tag{8}$$

where m and q are critical indices, $\lambda_{lm} = (1/m)\tan^{-1}(S_{lm}/C_{lm})$, and ω is argument of perigee. The stroboscopic mean node λ is given as:

$$\lambda = \frac{1}{s_0}(M + \omega) - (\theta - \Omega) \tag{9}$$

where s_0 is integer closest to object mean motion in revolutions per day, M is mean anomaly, ω is argument of perigee, θ is mean Greenwich sidereal time, and Ω is RAAN.

Lane used first order approximation of $\ddot{\omega} = \ddot{\Omega} = 0$ in Eqs. (8) and (9) to write the following double differential equation:

$$\ddot{\psi}_{lmpq} = m\ddot{\lambda} = \frac{m}{s_0}\ddot{M} = \frac{m}{s_0}\dot{n} \tag{10}$$

where $\dot{n}$ is time rate of change of mean motion. Eq. (10) can also be written as:

$$\ddot{\psi}_{lmpq} = \frac{m}{s_0}\frac{\partial n}{\partial a}\dot{a} \tag{11}$$

Using $n = \sqrt{\mu_E/a^3}$ in Eq. (11), one can write:

$$\ddot{\psi}_{lmpq} = \frac{m}{s_0}\sqrt{\mu_E}\left(-\frac{3}{2}\right)a^{-\frac{5}{2}}\dot{a} \tag{12}$$

The expression for $\dot{a}$ can be obtained from Lagrange's planetary equation for semi-major axis, which is given as:

$$\dot{a} = \frac{2}{na}\frac{\partial R}{\partial M} \tag{13}$$

Taking a partial derivative of the disturbing function given in Eq. (7) w.r.t mean anomaly M, where it is to be kept in mind that ψ_{lmpq} is related to mean anomaly via Eqs. (8) and (9), one obtains:

$$\dot{a} = -\frac{2m\mu_E}{ns_0a^2}\left(\frac{R_E}{a}\right)^l F_{lmp}(i)G_{lpq}(e)J_{[l,m]}\sin\psi_{lmpq} \tag{14}$$

Substituting expression for $\dot{a}$ from Eq. (14) into Eq. (12) and dropping the subscript $lmpq$ for convenience, one obtains:

$$\ddot{\psi} = P \sin \psi \tag{15}$$

where,

$$P = \frac{3m^2 \mu_E}{s_0^2 a^3} \left(\frac{R_E}{a} \right)^l F_{lmp}(i) G_{lpq}(e) J_{[l,m]} \tag{16}$$

If P is negative, Eq. (15) is similar in form to that of a simple pendulum equation, $\ddot{x} = -C \sin x$, where C is a positive constant. If P is positive, one can define a new variable $\tilde{\psi} = \psi + \pi$, which will transform Eq. (15) into $\ddot{\tilde{\psi}} = -P \sin \tilde{\psi}$, which again is similar to simple pendulum equation. Lane solves the simple pendulum equation and provides the following integration results (refer Lane [14]; derivation excluded from here for brevity):

$$\int_{t_0}^{t} \sin \psi dt = \begin{cases} \frac{2}{kQ} \left[cn(u_0, \frac{1}{k}) - cn(u, \frac{1}{k}) \right] & |k| > 1 \\ \frac{2}{kQ} \left[dn(u_0, k) - dn(u, k) \right] & |k| < 1 \end{cases} \tag{17}$$

$$\int_{t_0}^{t} \cos \psi dt = \begin{cases} \frac{2}{Q} \left[E(u, \frac{1}{k}) - E(u_0, \frac{1}{k}) \right] - \frac{1}{Q}[u - u_0] & |k| > 1 \\ \frac{2}{kQ} \left[E(u, k) - E(u_0, k) \right] - \left(\frac{k'^2 + 1}{kQ} \right)[u - u_0] & |k| < 1 \end{cases} \tag{18}$$

where t_0 is a reference time, t is a general time, and $Q = \sqrt{|P|}$. $sn(\cdot, \cdot)$, $cn(\cdot, \cdot)$, and $dn(\cdot, \cdot)$ are Jacobi elliptic functions. $E(\cdot, \cdot)$ represents incomplete elliptic integral of the second kind. The parameter k is given as:

$$k = \frac{1}{\sin \frac{\psi_m}{2}} \tag{19}$$

with,

$$\sin^2 \frac{\psi_m}{2} = \frac{\dot{\psi}_0^2 - 2Q^2 \cos \psi_0 + 2Q^2}{4Q^2} \tag{20}$$

where ψ_0 is the value of the parameter ψ at the reference time t_0. The sign of $\sin(\psi_m/2)$ in Eq. (20) is given by the sign of $\dot{\psi}_0$.

The parameter k'^2 in Eq. (18) can be obtained from k using $k'^2 = 1 - k^2$. The parameter u (with u_0 being the value of u at reference time t_0) in Eqs. (17) and (18) is given as:

$$u = \begin{cases} Q(t-t_0) + F\left(\frac{1}{k}, \sin^{-1}(k \sin\frac{\psi_0}{2})\right) & |k| > 1 \\ \\ \frac{Q}{k}(t-t_0) + F\left(k, \frac{\psi_0}{2}\right) & |k| < 1 \end{cases} \tag{21}$$

where $F(\cdot,\cdot)$ is the incomplete elliptic integral of the first kind.

Eq. (14) can now be integrated w.r.t time to obtain the expression for change in semi-major axis:

$$\Delta a = A \begin{cases} cn(u_0, \frac{1}{k}) - cn(u, \frac{1}{k}) & |k| > 1 \\ \\ dn(u_0, k) - dn(u, k) & |k| < 1 \end{cases} \tag{22}$$

where $A = 4as_0Q/(3nmk)$.

Variation of the Eccentricity

Lagrange's planetary equation for eccentricity is given as:

$$\frac{de}{dt} = \frac{1-e^2}{nea^2}\frac{\partial R}{\partial M} - \frac{\sqrt{1-e^2}}{nea^2}\frac{\partial R}{\partial \omega} \tag{23}$$

Taking partial derivatives of the disturbing function R given in Eq. (7) w.r.t mean anomaly M and argument of perigee ω, where it is to be kept in mind that ψ_{lmpq} is related to mean anomaly and argument of perigee via Eqs. (8) and (9), one obtains:

$$\begin{aligned} \frac{de}{dt} = & \frac{1-e^2}{nea^2}\frac{\mu_E}{a}\left(\frac{R_E}{a}\right)^l F_{lmp}(i) G_{lpq}(e) J_{[l,m]}\left(\frac{m}{s_0}\right)(-\sin\psi) \\ & - \frac{\sqrt{1-e^2}}{nea^2}\frac{\mu_E}{a}\left(\frac{R_E}{a}\right)^l F_{lmp}(i) G_{lpq}(e) J_{[l,m]}\left(\frac{m}{s_0} - q\right)(-\sin\psi) \end{aligned} \tag{24}$$

Integrating Eq. (24) w.r.t time and using the integration result from Eq. (17) yields:

$$\Delta e = \frac{\mu_E}{na^3}\left(\frac{R_E}{a}\right)^l |F_{lmp}(i)G_{lpq}(e)|J_{[l,m]}\left[\frac{m}{s_0}\left(\frac{1-e^2-\sqrt{1-e^2}}{e} + \frac{q\sqrt{1-e^2}}{e}\right)\right]\left(\frac{2}{kQ}\right)\begin{cases} cn(u_0,\frac{1}{k}) - cn(u,\frac{1}{k}) & |k|>1 \\ dn(u_0,k) - dn(u,k) & |k|<1 \end{cases} \tag{25}$$

Variation of the Inclination

Lagrange's planetary equation for inclination is given as:

$$\frac{di}{dt} = \frac{\cos i}{na^2\sqrt{1-e^2}\sin i}\frac{\partial R}{\partial \omega} - \frac{1}{na^2\sqrt{1-e^2}\sin i}\frac{\partial R}{\partial \Omega} \tag{26}$$

Taking partial derivatives of the disturbing function R given in Eq. (7) w.r.t argument of perigee ω and RAAN Ω, where it is to be kept in mind that ψ_{lmpq} is related to argument of perigee and RAAN via Eqs. (8) and (9), one obtains:

$$\begin{aligned}\frac{di}{dt} = &\frac{\cos i}{na^2\sqrt{1-e^2}\sin i}\frac{\mu_E}{a}\left(\frac{R_E}{a}\right)^l F_{lmp}(i)G_{lpq}(e)J_{[l,m]}\big(\frac{m}{s_0}-q\big)(-\sin\psi) \\ &- \frac{1}{na^2\sqrt{1-e^2}\sin i}\frac{\mu_E}{a}\left(\frac{R_E}{a}\right)^l F_{lmp}(i)G_{lpq}(e)J_{lm}m(-\sin\psi)\end{aligned} \tag{27}$$

Integrating Eq. (27) w.r.t time and using the integration result from Eq. (17) yields:

$$\Delta i = -\frac{\mu_E}{na^3\sqrt{1-e^2}\sin i}\left(\frac{R_E}{a}\right)^l |F_{lmp}(i)G_{lpq}(e)|J_{[l,m]}\left[q\cos i + m(1-\frac{1}{s_0}\cos i)\right]\left(\frac{2}{kQ}\right)\begin{cases} cn(u_0,\frac{1}{k}) - cn(u,\frac{1}{k}) & |k|>1 \\ dn(u_0,k) - dn(u,k) & |k|<1 \end{cases} \tag{28}$$

Variation of the Argument of Perigee

Lagrange's planetary equation for AoP is given as:

$$\frac{d\omega}{dt} = -\frac{\cos i}{na^2\sqrt{1-e^2}\sin i}\frac{\partial R}{\partial i} + \frac{\sqrt{1-e^2}}{nea^2}\frac{\partial R}{\partial e} \tag{29}$$

Taking partial derivatives of the disturbing function R given in Eq. (7) w.r.t inclination i and eccentricity e, one obtains:

$$\begin{aligned}\frac{d\omega}{dt} = &-\frac{\cos i}{na^2\sqrt{1-e^2}\sin i}\frac{\mu_E}{a}\left(\frac{R_E}{a}\right)^l F'_{lmp}(i)G_{lpq}(e)J_{[l,m]}\cos\psi \\ &+\frac{\sqrt{1-e^2}}{nea^2}\frac{\mu_E}{a}\left(\frac{R_E}{a}\right)^l F_{lmp}(i)G'_{lpq}(e)J_{[l,m]}\cos\psi\end{aligned} \tag{30}$$

Integrating Eq. (30) w.r.t time and using the integration result from Eq. (18) yields:

$$\begin{aligned}\Delta\omega = &\frac{\mu_E}{na^3}\left(\frac{R_E}{a}\right)^l J_{lm}\sigma\left[\frac{\cos i}{\sqrt{1-e^2}}G_{lpq}(e)\frac{F'_{lmp}(i)}{\sin i} - \sqrt{1-e^2}F_{lmp}(i)\right. \\ &\left.\frac{G'_{lpq}(e)}{e}\right]\begin{cases} \frac{2}{Q}[E(u,\frac{1}{k}) - E(u_0,\frac{1}{k})] - \frac{1}{Q}[u-u_0] & |k|>1 \\ \frac{2}{kQ}[E(u,k) - E(u_0,k)] - (\frac{k'^2+1}{kQ})[u-u_0] & |k|<1 \end{cases}\end{aligned} \tag{31}$$

where $\sigma = sign(F_{lmp}(i)G_{lpq}(e))$.

Variation of the Right Ascension of Ascending Node

Lagrange's planetary equation for RAAN is given as:

$$\frac{d\Omega}{dt} = \frac{1}{na^2\sqrt{1-e^2}\sin i}\frac{\partial R}{\partial i} \tag{32}$$

Taking partial derivatives of the disturbing function R given in Eq. (7) w.r.t inclination i, one obtains:

$$\frac{d\Omega}{dt} = \frac{1}{na^2\sqrt{1-e^2}\sin i}\frac{\mu_E}{a}\left(\frac{R_E}{a}\right)^l F'_{lmp}(i)G_{lpq}(e)J_{[l,m]}\cos\psi \tag{33}$$

Integrating Eq. (33) w.r.t time and using the integration result from Eq. (18) yields:

$$\begin{aligned}\Delta\Omega = &-\frac{\mu_E}{na^3\sqrt{1-e^2}}\left(\frac{R_E}{a}\right)^l J_{lm}\sigma G_{lpq}(e)\frac{F'_{lmp}(i)}{\sin i} \\ &\begin{cases} \frac{2}{Q}[E(u,\frac{1}{k}) - E(u_0,\frac{1}{k})] - \frac{1}{Q}[u-u_0] & |k|>1 \\ \frac{2}{kQ}[E(u,k) - E(u_0,k)] - (\frac{k'^2+1}{kQ})[u-u_0] & |k|<1 \end{cases}\end{aligned} \tag{34}$$

A comparison between analytical and numerical orbit propagation is carried out next to demonstrate the importance of tesseral perturbations for a GEO object. The numerical results are obtained via the direct integration of GVE using Dormand and Prince's Runge-Kutta (4,5) ODE solver [39] with relative tolerance of 10^{-12} and absolute tolerance of 10^{-12}. The numerical integration of GVE requires the radial, transverse, and perpendicular components of the tesseral acceleration, which are obtained as follows [41]:

$$[S \;\; T \;\; W]^T = {}^{P}T^{L}\vec{a}_L \tag{35}$$

where, the transformation matrix ${}^{P}T^{L}$ is given as:

$${}^{P}T^{L} = {}^{P}T^{I}\,{}^{I}T^{B}\,{}^{B}T^{L} \tag{36}$$

The transformation matrices in Eq. (36) are given as:

$${}^{P}T^{I} = \begin{bmatrix} \cos\Omega\cos u - \sin\Omega\cos i\sin u & \sin\Omega\cos u + \cos\Omega\cos i\sin u & \sin i\sin u \\ -\cos\Omega\sin u - \sin\Omega\cos i\cos u & -\sin\Omega\sin u + \cos\Omega\cos i\cos u & \sin i\cos u \\ \sin\Omega\sin i & -\cos\Omega\sin i & \cos i \end{bmatrix} \tag{37a}$$

$${}^{I}T^{B} = \begin{bmatrix} \cos GMST & -\sin GMST & 0 \\ \sin GMST & \cos GMST & 0 \\ 0 & 0 & 1 \end{bmatrix} \tag{37b}$$

$${}^{B}T^{L} = \begin{bmatrix} \cos\phi\cos\lambda & -\sin\lambda & -\sin\phi\cos\lambda \\ \cos\phi\sin\lambda & \cos\lambda & -\sin\phi\sin\lambda \\ \sin\phi & 0 & \cos\phi \end{bmatrix} \tag{37c}$$

where Ω, u, i, $GMST$, ϕ, λ represent RAAN, argument of latitude, inclination, Greenwich Mean Sidereal Time, latitude, and longitude, respectively.

The acceleration vector $\vec{a}_L$ in Eq. (35) is given as:

$$\vec{a}_L = \begin{bmatrix} \frac{\mu_E}{r^2}\left(\frac{R_E}{r}\right)^2(-3)\tilde{P}_2^{(2)}(\tilde{C}_{2,2}\cos 2\lambda + \tilde{S}_{2,2}\sin 2\lambda) \\ \frac{\mu_E}{r^2}\left(\frac{R_E}{r}\right)^2(2)\sec\phi\tilde{P}_2^{(2)}(-\tilde{C}_{2,2}\sin 2\lambda + \tilde{S}_{2,2}\cos 2\lambda) \\ \frac{\mu_E}{r^2}\left(\frac{R_E}{r}\right)^2\cos\phi\tilde{P}_2^{(2)'}(\tilde{C}_{2,2}\cos 2\lambda + \tilde{S}_{2,2}\sin 2\lambda) \end{bmatrix} \tag{38}$$

where μ_E, R_E, r, $\tilde{P}_2^{(2)}$, $\tilde{P}_2^{(2)'}$ represent Earth gravitational parameter, equatorial radius of the Earth, object radial distance, normalized Legendre function, and the first derivative of normalized Legendre function w.r.t $\sin\phi$, respectively. $\tilde{C}_{2,2}$ and $\tilde{S}_{2,2}$ are the normalized harmonic coefficients. The normalized Legendre function can be obtained using the following recursive relation:

$$\tilde{P}_n^{(m)} = \begin{cases} Q_1\left[(2n-1)^{\frac{1}{2}}\sin\phi\tilde{P}_{n-1}^{(m)} - Q_2\tilde{P}_{n-2}^{(m)}\right] & m < n \\ \left(\frac{2n+1}{2n}\right)^{\frac{1}{2}}\cos\phi\tilde{P}_{n-1}^{(m-1)} & m = n \\ 0 & m > n \end{cases} \tag{39a}$$

where,

$$Q_1 = \left[\frac{2n+1}{(n+m)(n-m)}\right]^{\frac{1}{2}} \tag{40}$$

$$Q_2 = \left[\frac{(n+m-1)(n-m-1)}{2n-3}\right]^{\frac{1}{2}} \tag{41}$$

and the recursion is initiated using $\tilde{P}_0^{(0)} = 1$, $\tilde{P}_1^{(0)} = \sqrt{3}\sin\phi$, $\tilde{P}_1^{(1)} = \sqrt{3}\cos\phi$.

In Eq. (38), the derivative $\tilde{P}_n^{(m)'}$ is obtained using:

$$\tilde{P}_n^{(m)'} = \frac{1}{\cos^2\phi}\left[-n\sin\phi\tilde{P}_n^{(m)} + \left(\frac{(2n+1)(n+m)(n-m)}{2n-1}\right)^{\frac{1}{2}}\tilde{P}_{n-1}^{(m)}\right] \tag{42}$$

Fig. 2.2 shows the effect of Earth gravitational perturbations for the same set-up as that of Table 1. Figs. 2.2(a), 2.2(c), 2.2(e), 2.2(g), 2.2(i) consider both zonal and tesseral perturbations whereas Figs. 2.2(b), 2.2(d), 2.2(f), 2.2(h), 2.2(j) consider only the zonal perturbations. The scales in the y-axes are kept the same for corresponding zonal and combined zonal-tesseral plots in order to highlight the importance of tesseral resonance. The semi-major axis amplitude in Fig. 2.2(a) (relative to initial value) is roughly of the order of 25 kilometers. The inclination amplitude (relative to initial value) in Fig. 2.2(e) is roughly four times that of Fig. 2.2(f). Figs. 2.2(g) and 2.2(i) establish that the effects of $J_{[2,2]}$ perturbations on argument of perigee and RAAN are much smaller compared to that of other three orbital elements, and it can effectively be ignored. Even after 15 years of propagation, for the combined zonal and tesseral perturbations, the maximum eccentricity

difference between analytical and numerical simulations is around .00002, the maximum inclination difference is merely around .00015 degrees, the maximum argument of perigee difference is around .25 degrees, and the maximum difference for RAAN is around .05 degrees. For semi-major axis, the maximum difference stands at mere .0059% of the initial value. Since these difference values are acceptably small, it justifies and validates the usage of Lane's analytical formulas.

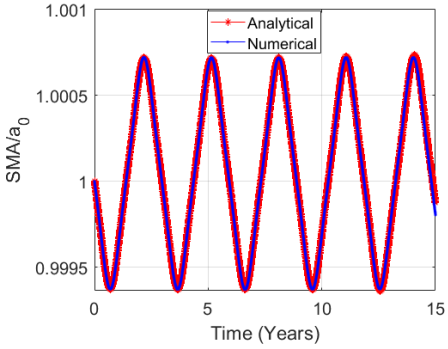

(a) SMA (Zonal+Tesseral).

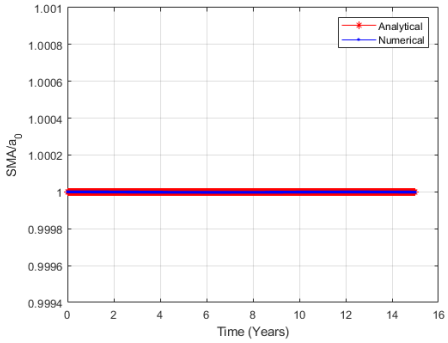

(b) SMA (Zonal).

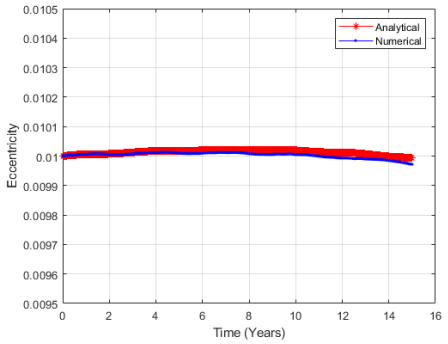

(c) Ecc. (Zonal+Tesseral).

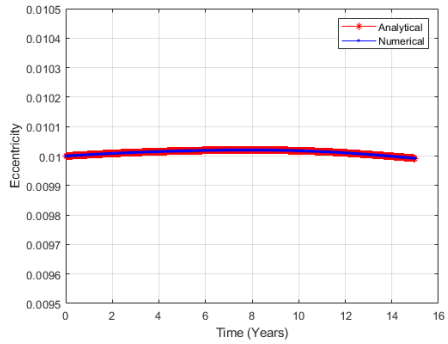

(d) Ecc. (Zonal).

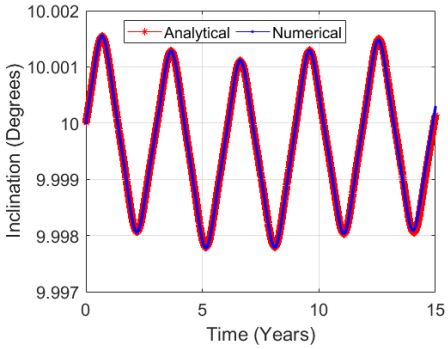

(e) Incl. (Zonal+Tesseral).

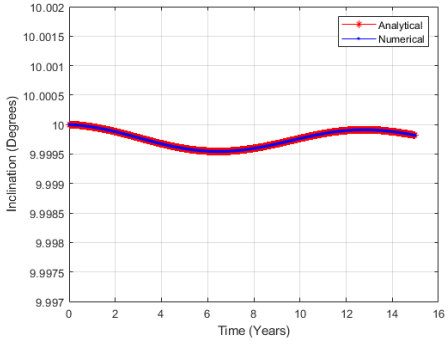

(f) Incl. (Zonal).

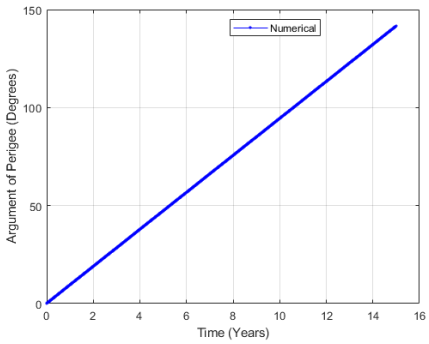

(g) AoP (Zonal+Tesseral).

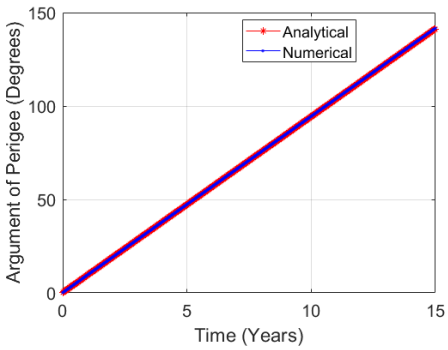

(h) AoP (Zonal).

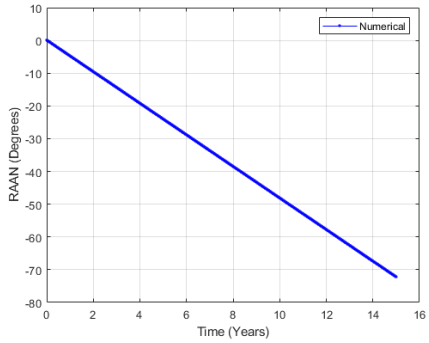

(i) RAAN (Zonal+Tesseral).

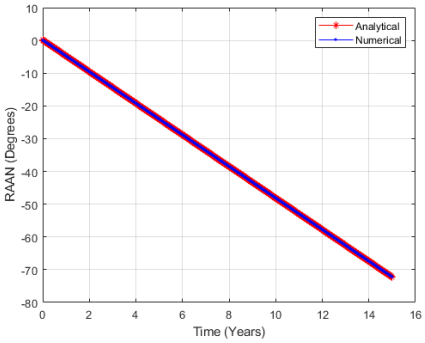

(j) RAAN (Zonal).

Figure 2.2: Effect of tesseral harmonics on perturbation of orbital elements for GEO.

2.2 Modeling Third-Body Gravitational Perturbations

In this research work, only the gravitational perturbations due to the Sun and the Moon are considered; it is assumed that the perturbation effects of all other third bodies are negligible. In the low Earth orbit (LEO) region, the magnitudes of accelerations due to Sun and Moon gravitational forces are much smaller compared to the magnitude of the acceleration due to higher harmonics of Earth's gravity. In the GEO region, however, the third body perturbations are comparable to that of zonal and tesseral perturbations. This research work modifies Cook's analytical theory [15] for third body perturbations. Cook's theory is a 'first-order' theory [3] and does not capture the evolution of eccentricity

[3]The term 'first-order theory' refers to (r/r_d) and higher-order terms being ignored in the expressions for S, T, W, with r being the radial distance of the object from Earth's center and r_d

and argument of perigee correctly. A higher-order theory is hence required for eccentricity and argument of perigee. The Second-order expression for $\Delta\omega$ is provided as additional information in Cook [15]. The Second-order expression for Δe has been derived as part of this research work. The assumptions and derivation of perturbation in eccentricity are discussed next. Derivations for analytic expressions for semi-major axis, inclination, AoP, and RAAN perturbations are excluded from here for brevity and can be found in Cook [15].

Variation of the Eccentricity

The disturbing function for third body perturbations is given as [15]:

$$R = GM_d\left(\frac{1}{\Delta} - \frac{xx_d + yy_d + zz_d}{r_d^3}\right) \tag{43}$$

where (x, y, z) represents the Earth-centered inertial (ECI) position of the space object, (x_d, y_d, z_d) represents the ECI position of the disturbing body (i.e., the Sun or the Moon), G represents universal gravitational constant, M_d represents the mass of the disturbing body, r_d represents the distance of the disturbing body from the Earth's center, and Δ represents the distance between the space object and the disturbing body, i.e., $\Delta = \sqrt{(x - x_d)^2 + (y - y_d)^2 + (z - z_d)^2}$.

The partial derivatives of the disturbing function R w.r.t the ECI coordinates (x, y, z) are given as:

$$\frac{\partial R}{\partial x} = -GM_d\left(\frac{x - x_d}{\Delta^3} + \frac{x_d}{r_d^3}\right) \tag{44a}$$

$$\frac{\partial R}{\partial y} = -GM_d\left(\frac{y - y_d}{\Delta^3} + \frac{y_d}{r_d^3}\right) \tag{44b}$$

$$\frac{\partial R}{\partial z} = -GM_d\left(\frac{z - z_d}{\Delta^3} + \frac{z_d}{r_d^3}\right) \tag{44c}$$

The direction cosines for a line parallel to the direction in which S is defined in GVE [Eq. (1)] are given as:

$$l_1 = \cos\Omega\cos u - \sin\Omega\sin u\cos i \tag{45a}$$

being the radial distance of Sun/Moon from Earth's center

$$m_1 = \sin\Omega\cos u + \cos\Omega\sin u\cos i \tag{45b}$$

$$n_1 = \sin u\sin i \tag{45c}$$

where Ω, u, i represent RAAN, argument of latitude, and inclination, respectively, of the space object orbit.

The direction cosines for a line parallel to the direction in which T is defined in GVE [Eq. (1)] are given as:

$$l_2 = -\cos\Omega\sin u - \sin\Omega\cos u\cos i \tag{46a}$$

$$m_2 = -\sin\Omega\sin u + \cos\Omega\cos u\cos i \tag{46b}$$

$$n_2 = \cos u\sin i \tag{46c}$$

The direction cosines for a line parallel to the direction in which W is defined in GVE [Eq. (1)] are given as:

$$l_3 = \sin\Omega\sin i \tag{47a}$$

$$m_3 = -\cos\Omega\sin i \tag{47b}$$

$$n_3 = \cos i \tag{47c}$$

With the help of the direction cosines in the radial direction [Eq. (45)], one can write the coordinates of the space object and coordinates of the disturbing body as:

$$x = rl_1 = r(\cos\Omega\cos u - \sin\Omega\sin u\cos i) \tag{48a}$$

$$y = rm_1 = r(\sin\Omega\cos u + \cos\Omega\sin u\cos i) \tag{48b}$$

$$z = rn_1 = r\sin u\sin i \tag{48c}$$

$$x_d = r_d l_d = r_d(\cos\Omega_d\cos u_d - \sin\Omega_d\sin u_d\cos i_d) \tag{48d}$$

$$y_d = r_d m_d = r_d(\sin\Omega_d\cos u_d + \cos\Omega_d\sin u_d\cos i_d) \tag{48e}$$

$$z_d = r_d n_d = r_d\sin u_d\sin i_d \tag{48f}$$

where Ω_d, u_d, i_d represent RAAN, argument of latitude, and inclination, respectively, of the disturbing body orbit. l_d, m_d, n_d represent direction cosines for the disturbing body radial vector.

If ϕ denotes the angle between object radial vector and disturbing body radial vector, then using the Law of Cosines, one can write:

$$\Delta^2 = r^2 + r_d^2 - 2rr_d\cos\phi \tag{49}$$

$$\frac{1}{\Delta^3} = \frac{1}{r_d^3}\left(1 + \left(\frac{r}{r_d}\right)^2 - 2\left(\frac{r}{r_d}\right)\cos\phi\right)^{-\frac{3}{2}} \tag{50}$$

Using Taylor series expansion on Eq. (50) and ignoring the terms of the order $(r/r_d)^3$ and higher,

$$\frac{1}{\Delta^3} = \frac{1}{r_d^3}\left[1 + 3\left(\frac{r}{r_d}\right)\cos\phi + \left(-\frac{3}{2} + \frac{15}{2}\cos^2\phi\right)\left(\frac{r}{r_d}\right)^2\right] \tag{51}$$

Since ϕ is the angle between object radial vector and disturbing body radial vector, it can also be written as:

$$\cos\phi = \frac{[x \;\; y \;\; z]\cdot[x_d \;\; y_d \;\; z_d]}{rr_d} = \frac{xx_d + yy_d + zz_d}{rr_d} \tag{52}$$

Substituting the expressions for x, y, z, x_d, y_d, z_d from Eq. (48) into Eq. (52) results in:

$$\cos\phi = A\cos u + B\sin u \tag{53}$$

where,

$$A = \cos u_d\cos(\Omega - \Omega_d) + \sin u_d\cos i_d\sin(\Omega - \Omega_d) \tag{54a}$$

$$B = \cos i[-\sin(\Omega - \Omega_d)\cos u_d + \cos i_d\sin u_d\cos(\Omega - \Omega_d)] + \sin i\sin u_d\sin i_d \tag{54b}$$

Substituting Eqs. (48) and (51) into Eq. (44) results in:

$$\begin{aligned}\frac{\partial R}{\partial x} = -\frac{GM_d r}{r_d^3}\Bigg[l_1 + 3\left(l_1\frac{r}{r_d} - l_d\right)\cos\phi + \frac{3}{2}l_d\frac{r}{r_d}(1 - 5\cos^2\phi) \\ - \frac{3}{2}l_1\left(\frac{r}{r_d}\right)^2(1 - 5\cos^2\phi)\Bigg]\end{aligned} \tag{55a}$$

$$\frac{\partial R}{\partial y} = -\frac{GM_d r}{r_d^3}\left[m_1 + 3\left(m_1\frac{r}{r_d} - m_d\right)\cos\phi + \frac{3}{2}m_d\frac{r}{r_d}(1-5\cos^2\phi) - \frac{3}{2}m_1\left(\frac{r}{r_d}\right)^2(1-5\cos^2\phi)\right] \tag{55b}$$

$$\frac{\partial R}{\partial z} = -\frac{GM_d r}{r_d^3}\left[n_1 + 3\left(n_1\frac{r}{r_d} - n_d\right)\cos\phi + \frac{3}{2}n_d\frac{r}{r_d}(1-5\cos^2\phi) - \frac{3}{2}n_1\left(\frac{r}{r_d}\right)^2(1-5\cos^2\phi)\right] \tag{55c}$$

The radial, transverse, and perpendicular components of the perturbation acceleration in GVE [Eq. (1)] can be computed using:

$$S = l_1\frac{\partial R}{\partial x} + m_1\frac{\partial R}{\partial y} + n_1\frac{\partial R}{\partial z} \tag{56a}$$

$$T = l_2\frac{\partial R}{\partial x} + m_2\frac{\partial R}{\partial y} + n_2\frac{\partial R}{\partial z} \tag{56b}$$

$$W = l_3\frac{\partial R}{\partial x} + m_3\frac{\partial R}{\partial y} + n_3\frac{\partial R}{\partial z} \tag{56c}$$

Substituting Eq. (55) into Eq. (56a), and noting that $l_1^2+m_1^2+n_1^2 = 1$, $l_1l_d+m_1m_d+n_1n_d = \cos\phi$, one obtains:

$$S = -Kr\left[1 + 3\left(\frac{r}{r_d} - \cos\phi\right)\cos\phi + \frac{3}{2}\left(\frac{r}{r_d}\right)(1-5\cos^2\phi)\cos\phi - \frac{3}{2}\left(\frac{r}{r_d}\right)^2(1-5\cos^2\phi)\right] \tag{57}$$

where $K = \frac{GM_d}{r_d^3}$.

Cook's first order theory [15] ignores both (r/r_d) and $(r/r_d)^2$ terms in Eq. (57). Here, only $(r/r_d)^2$ term will be ignored. Using Eq. (53) in Eq. (57) and making use of the identity $(1/2)(A^2+B^2) + AB\sin 2u + (1/2)(A^2-B^2)\cos 2u = \cos^2\phi$, one obtains:

$$S = -Kr\left[1 - \frac{3}{2}(A^2+B^2) - 3AB\sin 2u - \frac{3}{2}(A^2-B^2)\cos 2u + \frac{3}{2}\left(\frac{r}{r_d}\right)(A\cos u + B\sin u)(3 - 5(A\cos u + B\sin u)^2)\right] \tag{58}$$

Substituting Eq. (55) into Eq. (56b), and noting that $l_1 l_2 + m_1 m_2 + n_1 n_2 = 0$, one obtains:

$$T = 3Kr(l_2 l_d + m_2 m_d + n_2 n_d)\left[\cos\phi - \frac{1}{2}\left(\frac{r}{r_d}\right)(1 - 5\cos^2\phi)\right] \tag{59}$$

Using Eqs. (46) and (48), one can write:

$$l_2 l_d + m_2 m_d + n_2 n_d = -A\sin u + B\cos u \tag{60}$$

where A and B are defined in Eq. (54).

Substituting Eqs. (60) and (53) into Eq. (59), and making use of the identity $AB\cos 2u - \frac{1}{2}(A^2 - B^2)\sin 2u = (A\cos u + B\sin u)(-A\sin u + B\cos u)$, one obtains:

$$\begin{aligned} T = 3Kr\Bigg[&AB\cos 2u - \frac{1}{2}(A^2 - B^2)\sin 2u \\ &+ \frac{1}{2}\left(\frac{r}{r_d}\right)(A\sin u - B\cos u)\Big(1 - 5(A\cos u + B\sin u)^2\Big)\Bigg] \end{aligned} \tag{61}$$

Cook's first order theory [15] ignores the (r/r_d) term in Eq. (61). In the second order theory presented here, the (r/r_d) term is retained.

Substituting Eq. (55) into Eq. (56c), and noting that $l_1 l_3 + m_1 m_3 + n_1 n_3 = 0$, one obtains:

$$W = 3Kr(l_3 l_d + m_3 m_d + n_3 n_d)\left[\cos\phi - \frac{1}{2}\left(\frac{r}{r_d}\right)(1 - 5\cos^2\phi)\right] \tag{62}$$

Using Eqs. (47), (48), one can write an expression for $C = l_3 l_d + m_3 m_d + n_3 n_d$ as:

$$\begin{aligned} l_3 l_d + m_3 m_d + n_3 n_d = \sin i[&\cos u_d \sin(\Omega - \Omega_d) \\ &- \cos i_d \sin u_d \cos(\Omega - \Omega_d)] + \cos i \sin i_d \sin u_d \end{aligned} \tag{63}$$

Substituting Eqs. (63) and (53) into Eq. (62), one obtains:

$$W = 3KrC\left[A\cos u + B\sin u - \frac{1}{2}\left(\frac{r}{r_d}\right)(1 - 5(A\cos u + B\sin u)^2)\right] \tag{64}$$

Using the first order approximation $\frac{dt}{df} = (1/n)(r/a)^2(1/\sqrt{1-e^2})$, the GVE for eccentricity [Eq. (1b)] can be written as:

$$\frac{de}{df} = \frac{r^2}{n^2 a^3}\Big[S\sin f + T(\cos f + \cos E)\Big] \tag{65}$$

Substituting expressions for radial and transverse acceleration components from Eqs. (58) and (61) into Eq. (65) and using the relation $\cos E = (\cos f + e)/(1 + e\cos f)$ results in:

$$\begin{aligned}\frac{de}{df} = \frac{Kr^3}{n^2 a^3}\Bigg(&-\sin f\Big[1 - \frac{3}{2}(A^2 + B^2) - 3AB\sin 2u - \frac{3}{2}(A^2 - B^2)\\ &\cos 2u + \frac{3}{2}(\frac{r}{r_d})(A\cos u + B\sin u)(3 - 5(A\cos u + B\sin u)^2)\Big]\\ &+ 3\Bigg(\cos f + \frac{\cos f + e}{1 + e\cos f}\Bigg)\Big[AB\cos 2u - \frac{1}{2}(A^2 - B^2)\sin 2u\\ &+ \frac{1}{2}\Big(\frac{r}{r_d}\Big)(A\sin u - B\cos u)\Big(1 - 5(A\cos u + B\sin u)^2\Big)\Big]\Bigg)\end{aligned} \tag{66}$$

From Cook's theory [15], the integration of the first-order part (i.e., non (r/r_d) terms) of Eq. (66) over one orbit results in:

$$(\Delta e)_{first\ order} = -\frac{15\pi K e\sqrt{1 - e^2}}{n^2}\Big[AB\cos 2\omega - \frac{1}{2}(A^2 - B^2)\sin 2\omega\Big] \tag{67}$$

The second-order part of Eq. (66) that is not captured in Cook's theory is:

$$\begin{aligned}\Big(\frac{de}{df}\Big)_{second\ order} = \frac{Kr^3}{n^2 a^3}\Big[&-\sin f(\frac{3r}{2r_d})(A\cos u + B\sin u)(3 - 5(A\cos u\\ &+ B\sin u)^2) + 3\Big(\cos f + \frac{\cos f + e}{1 + e\cos f}\Big)\frac{1}{2}\Big(\frac{r}{r_d}\Big)\\ &(A\sin u - B\cos u)\Big(1 - 5(A\cos u + B\sin u)^2\Big)\Big]\end{aligned} \tag{68}$$

Using the orbit mechanics conic equation $r = a(1 - e^2)/(1 + e\cos f)$ and noting that $u = \omega + f$, Eq. (68) can be written as:

$$\left(\frac{de}{df}\right)_{second\ order} = \frac{K}{n^2}\frac{(1-e^2)^4}{(1+e\cos f)^4}\left(\frac{3a}{2r_d}\right)\Bigg[-\sin f(A(\cos f\cos\omega - \sin f\sin\omega) + B(\sin f\cos\omega + \cos f\sin\omega))$$
$$(3 - 5(A(\cos f\cos\omega - \sin f\sin\omega) + B(\sin f\cos\omega + \cos f\sin\omega))^2) + \left(2\cos f + e\left(\frac{1+\cos 2f}{2}\right) + e\right)\left(\frac{1}{1+e\cos f}\right)(A(\sin f\cos\omega + \cos f\sin\omega)$$
$$- B(\cos f\cos\omega - \sin f\sin\omega))(1 - 5(A(\cos f\cos\omega - \sin f\sin\omega) + B(\sin f\cos\omega + \cos f\sin\omega))^2)\Bigg] \tag{69}$$

After much simplification of Eq. (69) using trigonometric identities (steps not shown for brevity), one obtains:

$$\left(\frac{de}{df}\right)_{second\ order} = -\frac{K}{n^2}\frac{(1-e^2)^4}{(1+e\cos f)^4}\left(\frac{3a}{4r_d}\right)(K_1\cos 2f + K_2\cos 4f + K_3) + \frac{K}{n^2}\frac{(1-e^2)^4}{(1+e\cos f)^5}\left(\frac{3a}{4r_d}\right)(K_4\cos f + K_5\cos 2f + K_6\cos 3f + K_7\cos 4f + K_8\cos 5f + K_9) + zero\ integrands \tag{70}$$

where *zero integrands* refer to integrands of the form:

$$zero\ integrands \equiv constant \times \frac{sin(\alpha f)}{(1+e\cos f)^\beta} \tag{71}$$

where α and β are some positive integers. Integration of *zero integrands* (w.r.t true anomaly) from 0 to 2π leads to zero and hence they are not written out explicitly in Eq. (70).

The parameters K_1 through K_9 in Eq. (70) are given as:

$$K_1 = 3(A\sin\omega - B\cos\omega) - 15AB^2\sin^2\omega\cos\omega + 15A^2B\sin^2\omega\cos\omega - 5A^3\sin^3\omega - \frac{5B^3}{2}\cos\omega(-2+3\sin^2\omega) \tag{72a}$$

$$K_2 = \frac{15AB^2}{4}\sin 3\omega + \frac{15A^2B}{4}\cos 3\omega - \frac{5A^3}{4}\sin 3\omega - \frac{5B^3}{4}\cos 3\omega \tag{72b}$$

$$K_3 = 3(B\cos\omega - A\sin\omega) + \frac{15AB^2}{4}\sin\omega - \frac{15A^2B}{4}\cos\omega + \frac{15A^3}{4}\sin\omega - \frac{15B^3}{4}\cos\omega \tag{72c}$$

$$K_4 = e(A\sin\omega - B\cos\omega)\Big[-5(A^2-B^2)\cos 2\omega - 10AB\sin 2\omega + \frac{7}{2} - \frac{35}{4}(A^2+B^2)\Big] + e(A\cos\omega + B\sin\omega)\Big(-\frac{15}{2}\Big)\Big[-\Big(\frac{A^2-B^2}{2}\Big)\sin 2\omega + AB\cos 2\omega\Big] \tag{72d}$$

$$K_5 = 2(A\sin\omega - B\cos\omega)[1 - 5(A\cos\omega + B\sin\omega)^2] \tag{72e}$$

$$K_6 = \Big(\frac{e}{2}\Big)(A\sin\omega - B\cos\omega)\Big[-\frac{35}{2}\Big(\Big(\frac{A^2-B^2}{2}\Big)\cos 2\omega + AB\sin 2\omega\Big) + 1 - \frac{5}{2}(A^2+B^2)\Big] + \frac{25e}{4}(A\cos\omega + B\sin\omega)\Big(-\Big(\frac{A^2-B^2}{2}\Big)\sin 2\omega + AB\cos 2\omega\Big) \tag{72f}$$

$$K_7 = -5(A\sin\omega - B\cos\omega)\Big[\Big(\frac{A^2-B^2}{2}\Big)\cos 2\omega + AB\sin 2\omega\Big] + 5(A\cos\omega + B\sin\omega)\Big[-\Big(\frac{A^2-B^2}{2}\Big)\sin 2\omega + AB\cos 2\omega\Big] \tag{72g}$$

$$K_8 = -\frac{5e}{4}(A\sin\omega - B\cos\omega)\left[\left(\frac{A^2-B^2}{2}\right)\cos 2\omega + AB\sin 2\omega\right] + \frac{5e}{4}(A\cos\omega + B\sin\omega)\left[-\left(\frac{A^2-B^2}{2}\right)\sin 2\omega + AB\cos 2\omega\right] \tag{72h}$$

$$K_9 = (A\sin\omega - B\cos\omega)\left[-\frac{5}{2}(A^2-B^2)\cos 2\omega - 5AB\sin 2\omega + 2 - 5(A^2+B^2)\right] - 5(A\cos\omega + B\sin\omega)\left[-\left(\frac{A^2-B^2}{2}\right)\sin 2\omega + AB\cos 2\omega\right] \tag{72i}$$

Integration of Eq. (70) w.r.t the independent variable f over one orbit results in:

$$(\Delta e)_{second\ order} = -\frac{K}{n^2}(1-e^2)^4\left(\frac{3a}{4r_d}\right)([K_1 f_1(e) + K_2 f_2(e) + K_3 f_3(e)] - [K_4 f_4(e) + K_5 f_5(e) + K_6 f_6(e) + K_7 f_7(e) + K_8 f_8(e) + K_9 f_9(e)]) \tag{73}$$

The eccentricity functions f_j in Eq. (73) are given as:

$$f_1(e) = \int_0^{2\pi} \frac{\cos 2\nu}{(1+e\cos\nu)^4} d\nu = g_1 + h_1 \tag{74a}$$

$$f_2(e) = \int_0^{2\pi} \frac{\cos 4\nu}{(1+e\cos\nu)^4} d\nu = \begin{cases} g_2 + h_2 & for\ \ e \geq .05 \\ \mathcal{P}_9 & for\ \ e < .05 \end{cases} \tag{74b}$$

$$f_3(e) = \int_0^{2\pi} \frac{1}{(1+e\cos\nu)^4} d\nu = g_3 + h_3 \tag{74c}$$

$$f_4(e) = \int_0^{2\pi} \frac{cos(\nu)}{(1+e\cos\nu)^5} d\nu = g_4 + h_4 \tag{74d}$$

$$f_5(e) = \int_0^{2\pi} \frac{cos(2\nu)}{(1+e\cos\nu)^5} d\nu = g_5 + h_5 \tag{74e}$$

$$f_6(e) = \int_0^{2\pi} \frac{cos(3\nu)}{(1+e\cos\nu)^5} d\nu = g_6 + h_6 \tag{74f}$$

$$f_7(e) = \int_0^{2\pi} \frac{cos(4\nu)}{(1+e\cos\nu)^5} d\nu = g_7 + h_7 \tag{74g}$$

$$f_8(e) = \int_0^{2\pi} \frac{cos(5\nu)}{(1+e\cos\nu)^5} d\nu = \begin{cases} g_8 + h_8 & for \;\; e \geq .1 \\ \tilde{\mathcal{P}}_9 & for \;\; e < .1 \end{cases} \tag{74h}$$

$$f_9(e) = \int_0^{2\pi} \frac{1}{(1+e\cos\nu)^5} d\nu = g_9 + h_9 \tag{74i}$$

where the analytical expressions for eccentricity-dependent functions g_j (the integrand being integrated from 0 to π) and h_j (the integrand being integrated from π to 2π) are obtained using Matlab's [4] symbolic integration and are given in Appendix A. MATLAB's symbolic integrator performs wrong evaluations of the functions f_2 and f_8 for low eccentricity, and hence, a split-wise function is defined for f_2 and f_8. Terms $\mathcal{P}_9$ and $\tilde{\mathcal{P}}_9$ are 9^{th} order polynomial fits used to approximate f_2 and f_8, respectively, for small eccentricity, and are given in Appendix A.

A comparison between analytical and numerical orbit propagation for Moon third-body perturbation is carried out next for a GEO object. The numerical results are obtained via the direct integration of GVE using Dormand and Prince's Runge-Kutta (4,5) ODE solver [39] with relative tolerance of 10^{-12} and absolute tolerance of 10^{-12}. For the numerical integration of GVE, the radial (S), transverse (T), and perpendicular (W) components of the third body perturbations are obtained using Eqs. (56) and (44) without any approximation for the $1/\Delta^3$ term. For the same set up as that of Table 1, Fig. 2.3 shows the comparison between Cook's first-order theory and numerical results for an object perturbed by Moon gravity. In Fig. 2.3a, the blue curve corresponds to analytical results and the orange curve corresponds to the numerical results. Fig. 2.3b shows the difference between numerical and analytical eccentricity values.

Fig. 2.4 shows the comparison between second-order analytical theory developed here and numerical results for Moon perturbation. In Fig. 2.4a, the blue curve corresponds to analytical results and the orange curve corresponds to the numerical results. Fig. 2.4b

[4]MATLAB version 9.4.0.813654 (R2018a), The MathWorks, Inc., Natick, Massachusetts, United States

shows the difference between numerical and analytical eccentricity values. There is one order of magnitude improvement in Δe values for the second-order theory as compared to the first-order theory. Since the second-order analytical theory is able to follow numerical results for the 15-year period to an accuracy of the order of 10^{-5}, a higher-order theory is not sought after.

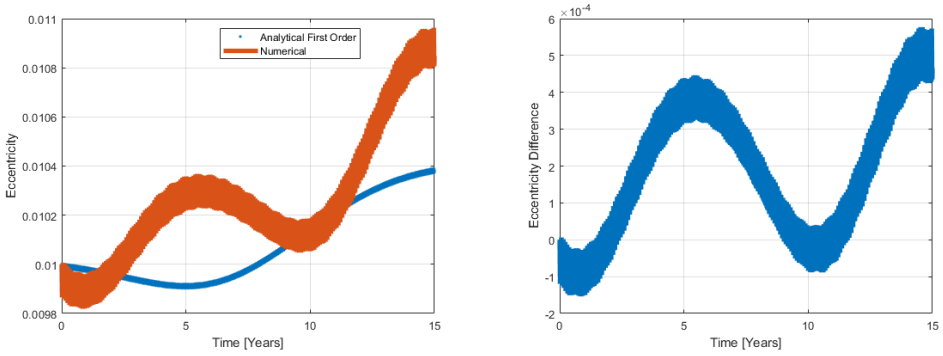

(a) Eccentricity. **(b)** Δ Eccentricity.

Figure 2.3: Effect of Moon third-body perturbation on eccentricity of a GEO object using first order theory.

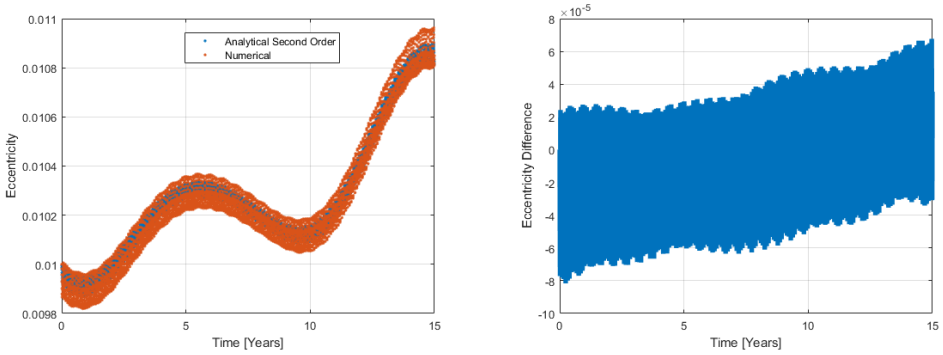

(a) Eccentricity. **(b)** Δ Eccentricity.

Figure 2.4: Effect of Moon third-body perturbation on eccentricity of a GEO object using second order theory.

2.3 Modeling Perturbations Due to Direct Solar Radiation Pressure

Solar radiation pressure (SRP) is the pressure exerted on an object resulting from the momentum exchange between solar photons and the object. For low area-to-mass ratio (LAMR) objects, solar radiation pressure (SRP) is smaller than gravitational perturbation

forces in both LEO and GEO regions. However, for HAMR objects in the GEO region, SRP is one of the most dominant perturbing forces resulting in large perturbations, which lead to difficulties in the detection and tracking of these HAMR objects. Modeling SRP can be difficult in situations that involve self-shadowing or complicated body geometry. The simplest SRP model, called 'cannonball model,' assumes a body as a sphere that is rotationally invariant with the same optical properties for the entire surface. This research work assumes all objects to be simple spheres, and hence the 'cannonball model' is applicable. Under the cannonball model, acceleration due to SRP is given as [42]:

$$\vec{F}_{rad} = -\frac{A}{m}\frac{E}{c}\frac{A_{\oplus}^2}{|\vec{r}-\vec{r}_{\odot}|^2}\left(\frac{1}{4}+\frac{1}{9}C_d\right)\hat{\mathbf{S}} \tag{75}$$

where A represents the surface area of the body, m represents the total mass of the body, E represents solar flux, c represents the speed of light, $A_{\oplus}$ represents the astronomical unit, and C_d represents the diffuse reflection coefficient. $\vec{r}$, $\vec{r}_{\odot}$, $\hat{\mathbf{S}}$ represent geocentric position of object, geocentric position of the sun, and direction of radiation source respectively.

This work uses Cook's analytical theory [15] for SRP perturbations. A cylindrical shadow model for the Earth is assumed, and the algorithm for computing the same is taken from [43]. Cook's analytical perturbations diverge over time, and hence a modified update scheme is used in this research work. The assumptions and derivation of Cook's analytical theory are discussed next.

Cook's analytical theory is based on the following assumptions:

1. As the distance of the Sun from the Earth or the object is large compared to the distance of the object from the Earth, the magnitude of solar radiation pressure will be assumed to be independent of the object-Sun distance i.e., a constant value for the object-sun distance will be assumed during one orbital period.

2. It is assumed that the SRP magnitude is independent of body orientation. A suitable average value for magnitude is taken for the entire orbital period.

If F represents the magnitude of the SRP acceleration given in Eq. (75), ϕ represents the angle between radial vector to the object and radial vector to the Sun, β represents the angle

between $\hat{\theta}$ (unit vector along the perpendicular direction to object radial vector and lying in the orbital plane) and radial vector to the Sun, and γ represents the angle between $\hat{h}$ (unit vector along the normal direction to the object orbital plane) and radial vector to the Sun, then the radial, transverse, and perpendicular components of perturbation acceleration can be written as:

$$S = F\cos\phi \tag{76a}$$

$$T = F\cos\beta \tag{76b}$$

$$W = F\cos\gamma \tag{76c}$$

Expression for $\cos\phi$ is given in earlier seen Eq. (53).

Expression for $\cos\beta$ can be obtained with the help of Eqs. (46) and (48) as:

$$\cos\beta = l_2 l_d + m_2 m_d + n_2 n_d \tag{77}$$

$$\begin{aligned}\cos\beta = {} & (-\cos\Omega\sin u - \sin\Omega\cos u\cos i)(\cos\Omega_d\cos u_d \\ & - \sin\Omega_d\sin u_d\cos i_d) + (-\sin\Omega\sin u + \cos\Omega\cos u\cos i) \\ & (\sin\Omega_d\cos u_d + \cos\Omega_d\sin u_d\cos i_d) + (\cos u\sin i)(\sin u_d\sin i_d)\end{aligned} \tag{78}$$

$$\cos\beta = -A\sin u + B\cos u \tag{79}$$

where the expressions for A and B are given in Eq. (54).

Expression for $\cos\gamma$ can be obtained with the help of Eqs. (47) and (48) as:

$$\cos\gamma = l_3 l_d + m_3 m_d + n_3 n_d \tag{80}$$

$$\begin{aligned}\cos\gamma = {} & \sin\Omega\sin i(\cos\Omega_d\cos u_d - \sin\Omega_d\sin u_d\cos i_d) \\ & - \cos\Omega\sin i(\sin\Omega_d\cos u_d + \cos\Omega_d\sin u_d\cos i_d) \\ & + \cos i\sin u_d\sin i_d = C\end{aligned} \tag{81}$$

Substituting Eqs. (53), (79), (81) into Eq. (76) results in:

$$S = F(A\cos u + B\sin u) \tag{82a}$$

$$T = F(-A\sin u + B\cos u) \tag{82b}$$

$$W = FC \tag{82c}$$

Variation of the Semi-major Axis

Using the first order approximation $\frac{dt}{df} = (1/n)(r/a)^2(1/\sqrt{1-e^2})$, the GVE for semi-major axis [Eq. (1a)] can be written as:

$$\frac{da}{df} = \frac{2r^2}{n^2a^2(1-e^2)}(Se\sin f + T(1+e\cos f)) \tag{83}$$

Substituting expressions for radial and transverse components of perturbation acceleration from Eq. (82) into Eq. (83) results in:

$$\begin{aligned}\frac{da}{df} = \frac{2r^2}{n^2a^2(1-e^2)}&(F(A\cos u + B\sin u)e\sin f \\ &+ F(-A\sin u + B\cos u)(1+e\cos f))\end{aligned} \tag{84}$$

Substituting $r = a(1-e^2)/(1+e\cos f)$, $u = \omega + f$ into Eq. (84) and simplifying, one obtains:

$$\begin{aligned}\frac{da}{df} = -\frac{2F(1-e^2)}{n^2(1+e\cos f)^2}&\Big[(A\sin\omega - B\cos\omega)(e+\cos f) \\ &+ (A\cos\omega + B\sin\omega)\sin f\Big]\end{aligned} \tag{85}$$

Integrating Eq. (85) over one orbital period and keeping in mind that that the solar radiation pressure is zero when the object is in Earth's shadow, one obtains:

$$\begin{aligned}\Delta a = -\frac{2F}{n^2a}&\Big[(A\sin\omega - B\cos\omega)(r_A\sin\theta_A^* - r_D\sin\theta_D^*) \\ &+ (A\cos\omega + B\sin\omega)\left(\frac{r_A - r_D}{e}\right)\Big]\end{aligned} \tag{86}$$

where r_D and r_A are the radial distances of the object at departure from Earth's shadow and arrival to Earth's shadow, respectively. θ_D^* and θ_A^* are the true anomaly values at departure from Earth's shadow and arrival to Earth's shadow, respectively.

It is to be noted that the solar radiation pressure, under the aforementioned model results in net zero change in energy or semi-major axis over one orbital period, if the object never enters the Earth's shadow region. Neglecting the orbital changes caused by other perturbations, only when an object passes through the shadow region, SRP results in net semi-major axis perturbation over an orbital period.

Variation of the Eccentricity

From Eq. (65), Gauss's variational equation for eccentricity is:

$$\frac{de}{df} = \frac{r^2}{n^2 a^3}\Big[S\sin f + T(\cos f + \cos E)\Big] \tag{87}$$

Substituting expressions for radial and transverse components of perturbation acceleration from Eq. (82) into Eq. (87) results in:

$$\begin{aligned}\frac{de}{df} = \frac{Fr^2}{\mu}\Bigg[&\sin f(A\cos u + B\sin u)\\ &+ \frac{1}{ae}\left(a(1+e\cos f) - \frac{a(1-e^2)}{1+e\cos f}\right)(-A\sin u + B\cos u)\Bigg]\end{aligned} \tag{88}$$

where $\mu = n^2a^3$.

Substituting $u = \omega + f$ and simplifying Eq. (88), one obtains:

$$\begin{aligned}\frac{de}{df} = &\frac{Fr^2(-A\sin\omega + B\cos\omega)(1 + 2e\cos f + \cos^2 f)}{\mu(1+e\cos f)}\\ &- \frac{Fr^2(A\cos\omega + B\sin\omega)\sin f(e + \cos f)}{\mu(1+e\cos f)}\end{aligned} \tag{89}$$

Let $S_p = F(A\cos\omega + B\sin\omega)$ and $T_p = F(-A\sin\omega + B\cos\omega)$, where the subscript p indicates that S_p and T_p will denote radial and transverse SRP accelerations at perigee, respectively, when the perigee position is not located inside Earth's shadow. With the help

of these new definitions, and using the orbit mechanics conic equation, one can re-write Eq. (89) as:

$$\begin{aligned}\frac{de}{df} = \frac{T_p}{\mu}\left[\frac{a^2(1-e^2)^2(1+2e\cos f+\cos^2 f)}{(1+e\cos f)^3}\right] \\ - \frac{S_p}{2\mu}\left[\frac{2a^2(1-e^2)^2\sin f(e+\cos f)}{(1+e\cos f)^3}\right]\end{aligned} \tag{90}$$

Integrating Eq. (90) over one orbital period and keeping in mind that that the solar radiation pressure is zero when the object is in Earth's shadow, one obtains:

$$\begin{aligned}\Delta e = \frac{T_p}{\mu}\Bigg[3a^2(1-e^2)^{\frac{1}{2}}\Bigg(\tan^{-1}\left[\frac{(1-e^2)^{\frac{1}{2}}\tan\frac{\theta_A^*}{2}}{1+e}\right] \\ - \tan^{-1}\left[\frac{(1-e^2)^{\frac{1}{2}}\tan\frac{\theta_D^*}{2}}{1+e}\right]\Bigg) - \frac{1}{2e}\big(r_A^2\sin\theta_A^* - r_D^2\sin\theta_D^*\big) \\ + \frac{a}{2e}(1-4e^2)\big(r_A\sin\theta_A^* - r_D\sin\theta_D^*\big)\Bigg] - \frac{S_p}{2\mu}\Bigg[(r_A^2 - r_D^2) \\ + \frac{a(1-e^2)}{e^2}(r_A - r_D) + \frac{1}{e}(r_A^2\cos\theta_A^* - r_D^2\cos\theta_D^*)\Bigg]\end{aligned} \tag{91}$$

Variation of the Inclination

Using the first order approximation $\frac{dt}{df} = (1/n)(r/a)^2(1/\sqrt{1-e^2})$, the GVE for inclination [Eq. (1c)] can be written as:

$$\frac{di}{df} = \frac{r^2}{na^2\sqrt{1-e^2}}\frac{r\cos(f+\omega)}{na^2\sqrt{1-e^2}}W \tag{92}$$

Using the relation $\mu = n^2a^3$ and the orbit mechanics conic equation $r = a(1-e^2)/(1+e\cos f)$ in Eq. (92), one obtains:

$$\frac{di}{df} = \frac{W}{\mu}\left[\left(\frac{a^2(1-e^2)^2\cos f}{(1+e\cos f)^3}\right)\cos\omega - \left(\frac{a^2(1-e^2)^2\sin f}{(1+e\cos f)^3}\right)\sin\omega\right] \tag{93}$$

Integrating Eq. (93) over one orbital period and keeping in mind that that the solar radiation pressure is zero when the object is in Earth's shadow, one obtains:

$$\Delta i = \frac{W}{\mu}\Bigg[\Bigg(\frac{1}{2(1-e^2)}(r_A^2\sin\theta_A^* - r_D^2\sin\theta_D^*) + \frac{a(1+2e^2)}{2(1-e^2)} (r_A\sin\theta_A^* - r_D\sin\theta_D^*) - \frac{3a^2e}{(1-e^2)^{\frac{1}{2}}}\Bigg(\tan^{-1}\left[\frac{(1-e^2)^{\frac{1}{2}}\tan\frac{\theta_A^*}{2}}{1+e}\right] - \tan^{-1}\left[\frac{(1-e^2)^{\frac{1}{2}}\tan\frac{\theta_D^*}{2}}{1+e}\right]\Bigg)\Bigg)\cos\omega - \frac{1}{2e}(r_A^2 - r_D^2)\sin\omega\Bigg] \tag{94}$$

Variation of the Right Ascension of the Ascending Node

Using the first order approximation $\frac{dt}{df} = (1/n)(r/a)^2(1/\sqrt{1-e^2})$, the GVE for RAAN [Eq. (1d)] can be written as:

$$\frac{d\Omega}{df} = \frac{r^3\sin(\omega+f)}{n^2a^4(1-e^2)\sin i}W \tag{95}$$

Using the relation $\mu = n^2a^3$ and the orbit mechanics conic equation $r = a(1-e^2)/(1+e\cos f)$ in Eq. (95), one obtains:

$$\frac{d\Omega}{dt} = \frac{W}{\mu\sin i}\Bigg[a^2(1-e^2)^2\sin\omega\frac{\cos f}{(1+e\cos f)^3} + a^2(1-e^2)^2\cos\omega\frac{\sin f}{(1+e\cos f)^3}\Bigg] \tag{96}$$

Integrating Eq. (96) over one orbital period, one obtains:

$$\Delta\Omega = \frac{W}{\mu\sin i}\Bigg[\frac{(r_A^2 - r_D^2)}{2e}\cos\omega + \Bigg[\frac{r_A^2\sin\theta_A^* - r_D^2\sin\theta_D^*}{2(1-e^2)} + \frac{1+2e^2}{2(1-e^2)}(ar_A\sin\theta_A^* - ar_D\sin\theta_D^*) - \frac{3a^2e}{\sqrt{1-e^2}} \Bigg(\tan^{-1}\left[\frac{\sqrt{1-e^2}\tan\frac{\theta_A^*}{2}}{1+e}\right] - \tan^{-1}\left[\frac{\sqrt{1-e^2}\tan\frac{\theta_D^*}{2}}{1+e}\right]\Bigg)\Bigg]\sin\omega\Bigg] \tag{97}$$

Variation of the Argument of Perigee

Using the first order approximation $\frac{dt}{df} = (1/n)(r/a)^2(1/\sqrt{1-e^2})$, the GVE for AoP [Eq. (1e)] can be written as:

$$\frac{d\omega}{df} = \frac{r^2}{n^2a^3e}\Bigg[-S\cos f + T\left(1+\frac{r}{p}\right)\sin f\Bigg] - \cos i\frac{d\Omega}{df} \tag{98}$$

Substituting expressions for radial and transverse components of perturbation acceleration from Eq. (82) into Eq. (98) results in:

$$\begin{aligned}\frac{d\omega}{df} = -\frac{Fr^2}{\mu e}\left[A\cos\omega + B\sin\omega + (A\sin u - B\cos u)\frac{\sin f}{1+e\cos f}\right] \\ - \cos i\frac{d\Omega}{df}\end{aligned} \tag{99}$$

Substituting orbit mechanics conic equation into Eq. (99) and simplifying, one obtains:

$$\begin{aligned}\frac{d\omega}{df} = \frac{T_P}{\mu e}\left[\frac{a^2(1-e^2)^2\sin f\cos f}{(1+e\cos f)^3}\right] \\ - \frac{S_P}{\mu e}\left[\frac{a^2(1-e^2)^2(1+e\cos f+\sin^2 f)}{(1+e\cos f)^3}\right] - \cos i\frac{d\Omega}{df}\end{aligned} \tag{100}$$

where $S_p = F(A\cos\omega + B\sin\omega)$ and $T_p = F(-A\sin\omega + B\cos\omega)$.

Integrating Eq. (100) over one orbital period and keeping in mind that that the solar radiation pressure is zero when the object is in Earth's shadow, one obtains:

$$\begin{aligned}\Delta\omega = -\frac{S_p}{\mu e}\Bigg[3a^2\sqrt{1-e^2}\Bigg(\tan^{-1}\Big(\frac{\sqrt{1-e^2}\tan\frac{\theta_A^*}{2}}{1+e}\Big) - \\ \tan^{-1}\Big(\frac{\sqrt{1-e^2}\tan\frac{\theta_D^*}{2}}{1+e}\Big)\Bigg) + \frac{1}{2e}(r_A^2\sin\theta_A^* - r_D^2\sin\theta_D^*) \\ - \frac{a}{2e}(1+2e^2)(r_A\sin\theta_A^* - r_D\sin\theta_D^*)\Bigg] + \frac{T_p}{2\mu e^3} \\ \Bigg[e(r_A^2\cos\theta_A^* - r_D^2\cos\theta_D^*) + a(1-e^2)(r_A - r_D)\Bigg] - \Delta\Omega\cos i\end{aligned} \tag{101}$$

Valk's algorithm for computation of shadow entry and exit true anomalies [43] has some typos. Expressions for the corrected parameters are as follows (for the definition of these parameters, look at [43]):

$$a_2(y) = p^2\beta^2 + R_\oplus^2 k_e^2 \tag{102a}$$

$$a_1(y) = 2p^2\beta\xi y + 2k_e R_\oplus^2 + 2k_e h_e R_\oplus^2 y \tag{102b}$$

$$a_0(y) = p^2\xi^2 y^2 + R_\oplus^2 + R_\oplus^2 h_e^2 y^2 + 2h_e y R_\oplus^2 - p^2 \tag{102c}$$

$$\begin{aligned} A_0 = {} & R_\oplus^4 k_e^4 - 2R_\oplus^4 k_e^2 + R_\oplus^4 + 2R_\oplus^2\beta^2 k_e^2 p^2 + 2R_\oplus^2\beta^2 p^2 \\ & - 2R_\oplus^2 k_e^2 p^2 - 2R_\oplus^2 p^2 + \beta^4 p^4 - 2\beta^2 p^4 + p^4 \end{aligned} \tag{102d}$$

$$\begin{aligned} A_1 = {} & -4R_\oplus^4 h_e k_e^2 + 4R_\oplus^4 h_e + 4R_\oplus^2\beta^2 h_e p^2 - 8R_\oplus^2\beta k_e p^2\xi \\ & - 4R_\oplus^2 h_e p^2 \end{aligned} \tag{102e}$$

$$\begin{aligned} A_2 = {} & -2R_\oplus^4 h_e^2 k_e^2 + 6R_\oplus^4 h_e^2 - 2R_\oplus^4 k_e^4 + 2R_\oplus^4 k_e^2 + 2R_\oplus^2\beta^2 h_e^2 p^2 \\ & - 4R_\oplus^2\beta^2 k_e^2 p^2 - 2R_\oplus^2\beta^2 p^2 - 8R_\oplus^2\beta h_e k_e p^2\xi - 2R_\oplus^2 h_e^2 p^2 \\ & + 2R_\oplus^2 k_e^2 p^2\xi^2 + 2R_\oplus^2 k_e^2 p^2 + 2R_\oplus^2 p^2\xi^2 - 2\beta^4 p^4 \\ & - 2\beta^2 p^4\xi^2 + 2\beta^2 p^4 - 2p^4\xi^2 \end{aligned} \tag{102f}$$

$$\begin{aligned} A_3 = {} & 4R_\oplus^4 h_e^3 + 4R_\oplus^4 h_e k_e^2 - 4R_\oplus^2\beta^2 h_e p^2 + 8R_\oplus^2\beta k_e p^2\xi \\ & + 4R_\oplus^2 h_e p^2\xi^2 \end{aligned} \tag{102g}$$

$$\begin{aligned} A_4 = {} & R_\oplus^4 h_e^4 + 2R_\oplus^4 h_e^2 k_e^2 + R_\oplus^4 k_e^4 - 2R_\oplus^2\beta^2 h_e^2 p^2 + 2R_\oplus^2\beta^2 k_e^2 p^2 \\ & + 8R_\oplus^2\beta h_e k_e p^2\xi + 2R_\oplus^2 h_e^2 p^2\xi^2 - 2R_\oplus^2 k_e^2 p^2\xi^2 + \beta^4 p^4 \\ & + 2\beta^2 p^4\xi^2 + p^4\xi^4 \end{aligned} \tag{102h}$$

A simulation comparing numerical and analytical orbital evolution is carried out for a GEO object perturbed by SRP for the set-up given in Table 2.

Table 2: Simulation parameters for comparison between numerical and analytical methods for SRP perturbation.

Parameter	Value
Initial Semi-major Axis	42164 km
Initial Eccentricity	0.1
Initial Inclination	10^0
Initial AoP	$.1^0$
Initial RAAN	$.1^0$
Initial Epoch	2437582.5 JD
Propagation Period	30 years
Area	1 m^2
AMR	50 m^2/kg
Diffuse Reflection Coefficient (C_d)	.035

The numerical results are obtained via the direct integration of GVE using Dormand and Prince's Runge-Kutta (4,5) ODE solver [39] with relative tolerance of 10^{-12} and absolute tolerance of 10^{-12}. For the numerical integration of GVE, the radial (S), transverse (T), and perpendicular (W) components of the SRP perturbations are obtained using Eq. (82) without assuming F, A, B, C as constants. Fig. 2.5(a) shows the comparison for the eccentricity and Fig. 2.5(b) shows the comparison for the argument of perigee, where the red plot belongs to the analytical method, and the blue plot belongs to the numerical method. The plots demonstrate how the error between numerical and analytical results grows rapidly with progress in time. The amplitude of the difference between numerical and analytical eccentricities increases to about .07 for a propagation period of 30 years, whereas the amplitude of difference increases to about 30 degrees for the argument of perigee.

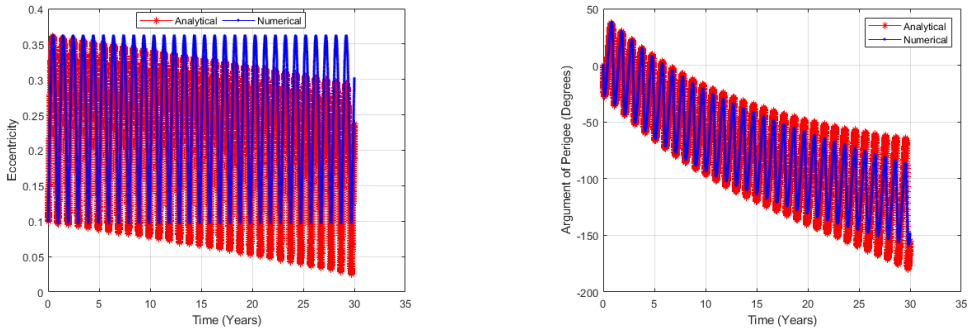

(a) Eccentricity. **(b)** Argument of Perigee.

Figure 2.5: Eccentricity and AoP divergence due to Cook's analytical expressions.

In order to overcome the divergence issue, Cook's update scheme need modification. In this research work, Cook's update scheme:

$$x_{t+1} = x_t + \Delta x(a_t, e_t, i_t, \omega_t, \Omega_t, \vec{r}_{sun_t}) \tag{103}$$

is replaced with a modified update scheme:

$$x_{t+1} = x_t + \Delta x(a_t, e_t, i_t, \omega_t, \Omega_t, \vec{r}_{sun_t}) \tag{104a}$$

$$x_{t+1} = .5x_{t+1} + .5x_t + .5\Delta x(a_{t+1}, e_{t+1}, i_{t+1}, \omega_{t+1}, \Omega_{t+1}, \vec{r}_{sun_{t+1}}) \tag{104b}$$

where x represents the Keplerian elements, the subscripts t and t+1 represent the corresponding quantities at times t and t+T_{period} respectively, $\vec{r}_{sun_t}$ represents Sun position at time t. Δx (which is a function of parameters in parenthesis) represents Cook's [15] analytical perturbation for one orbital period. In essence, we are replacing an Euler-like scheme with a Strong-Stability Preserving Runge-Kutta (SSP-RK)-like scheme of order 2.

Fig. 2.6 shows the comparison between numerical and analytical results obtained using the modified update scheme. The amplitude of difference between numerical and analytical results for eccentricity is mere .002 even after 30 years of propagation, and the amplitude of difference is only 2 degrees for argument of perigee.

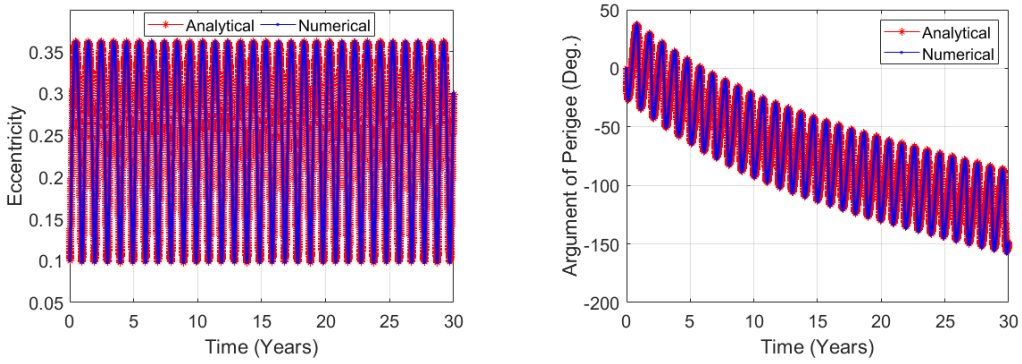

(a) Eccentricity. **(b)** Argument of Perigee.

Figure 2.6: Eccentricity and argument of perigee evolution with modified update scheme.

All the analytical results discussed so far have been compared against numerical integration results generated using Dormand and Prince's Runge-Kutta (4,5) ODE solver. Hence, a

discussion on the rationale behind the selection of Dormand and Prince's Runge-Kutta (4,5) ODE solver over other readily available numerical solvers in Matlab is carried out next.

2.4 Comparison of Numerical Solvers

To compare various numerical techniques, a dummy dynamics model that has an exact analytical solution (i.e., "truth") will be used. This dynamics model is similar in structure to the actual perturbation model, but not the same. Let the dummy dynamics model be given by the following equations [44]:

$$\dot{x} = v_x \tag{105}$$

$$\dot{y} = v_y \tag{106}$$

$$\dot{z} = v_z \tag{107}$$

$$\dot{v}_x = -Dv_x - \frac{K}{R^3}x + \left(\frac{5}{1000}\right)\sin\left(\frac{t}{1000}\right) \tag{108}$$

$$\dot{v}_y = -Dv_y - \frac{K}{R^3}y + \left(\frac{5}{1000}\right)\cos\left(\frac{t}{1000}\right) \tag{109}$$

$$\dot{v}_z = -Dv_z - \frac{K}{R^3}z + \left(\frac{5}{1000}\right)\sin\left(\frac{t}{1000}\right) \tag{110}$$

where, x, y, z are the satellite coordinates relative to Earth's center, $\dot{v}_x$, $\dot{v}_y$, $\dot{v}_z$ are the satellite velocity components, $K = 3.986004415\times10^{14}\ m^3/s^2$ is the gravitational parameter, $D = 5 \times 10^{-9}\ s^{-1}$ is the coefficient of atmospheric drag, $R = 6.65256 \times 10^6\ m$ represents object distance from center of Earth. The first term in each acceleration equation simulates drag, the second term simulates Keplerian term, and the third term simulates all other perturbations. The initial state for the dynamical model is taken as:

$$\begin{bmatrix} x(0) \\ y(0) \\ z(0) \\ v_x(0) \\ v_y(0) \\ v_z(0) \end{bmatrix} = \begin{bmatrix} R \\ 0 \\ 0 \\ 0 \\ v_0 \\ 0 \end{bmatrix} = \begin{bmatrix} 6.65256 \times 10^6 m \\ 0 \\ 0 \\ 0 \\ 7740.6\frac{m}{s} \\ 0 \end{bmatrix} \tag{111}$$

The exact analytical solution for the dummy dynamical model is given by the following equations [44] [5]:

$$x(t) = e^{\alpha t}(C_1 \cos(\beta t) + C_2 \sin(\beta t)) + A_1 \cos\left(\frac{t}{1000}\right) + B_1 \sin\left(\frac{t}{1000}\right) \tag{112}$$

$$y(t) = e^{\alpha t}(C_3 \cos(\beta t) + C_4 \sin(\beta t)) + A_2 \cos\left(\frac{t}{1000}\right) + B_2 \sin\left(\frac{t}{1000}\right) \tag{113}$$

$$z(t) = e^{\alpha t}(C_5 \cos(\beta t) + C_6 \sin(\beta t)) + A_1 \cos\left(\frac{t}{1000}\right) + B_1 \sin\left(\frac{t}{1000}\right) \tag{114}$$

$$v_x(t) = e^{\alpha t}[C_1(\alpha \cos(\beta t) - \beta \sin(\beta t)) + C_2(\beta \cos(\beta t) + \alpha \sin(\beta t))] - \frac{A_1}{1000} \sin\left(\frac{t}{1000}\right) + \frac{B_1}{1000} \cos\left(\frac{t}{1000}\right) \tag{115}$$

$$v_y(t) = e^{\alpha t}[C_3(\alpha \cos(\beta t) - \beta \sin(\beta t)) + C_4(\beta \cos(\beta t) + \alpha \sin(\beta t))] - \frac{A_2}{1000} \sin\left(\frac{t}{1000}\right) + \frac{B_2}{1000} \cos\left(\frac{t}{1000}\right) \tag{116}$$

$$v_z(t) = e^{\alpha t}[C_5(\alpha \cos(\beta t) - \beta \sin(\beta t)) + C_6(\beta \cos(\beta t) + \alpha \sin(\beta t))] - \frac{A_1}{1000} \sin\left(\frac{t}{1000}\right) + \frac{B_1}{1000} \cos\left(\frac{t}{1000}\right) \tag{117}$$

[5] [44] has some typos in its analytical solutions, which have been corrected here

where,

$$\alpha = Re\left(\frac{-D+\sqrt{D^2-\frac{4K}{R^3}}}{2}\right) \tag{118}$$

$$\beta = Im\left(\frac{-D+\sqrt{D^2-\frac{4K}{R^3}}}{2}\right) \tag{119}$$

$$A_1 = -\frac{5DR^6\times 10^6}{(K\times 10^6-R^3)^2+D^2R^6\times 10^6} \tag{120}$$

$$B_1 = 1000\times\frac{5R^3(K\times 10^6-R^3)}{(K\times 10^6-R^3)^2+D^2R^6\times 10^6} \tag{121}$$

$$A_2 = B_1 \tag{122}$$

$$B_2 = -A_1 \tag{123}$$

$$C_1 = x(0)-A_1 \tag{124}$$

$$C_2 = \frac{1}{\beta}\left(v_x(0)-C_1\alpha-\frac{B_1}{1000}\right) \tag{125}$$

$$C_3 = y(0)-A_2$$

$$C_4 = \frac{1}{\beta}\left(v_y(0)-C_3\alpha-\frac{B_2}{1000}\right) \tag{126}$$

$$C_5 = z(0)-A_1 \tag{127}$$

$$C_6 = \frac{1}{\beta}\left(v_z(0)-C_5\alpha-\frac{B_1}{1000}\right) \tag{128}$$

where Re and Im denote the real and imaginary parts, respectively.

Matlab has following readily available ODE solvers:

1. ode45: According to Mathworks, ode45 is based on explicit Runge-Kutta (4,5) formula [39], which means it combines a fourth-order method and a fifth-order method, both of which are similar to the classical fourth-order Runge-Kutta (RK) method [45]. The modified RK varies the step size, choosing the step size at each step in an attempt to achieve the desired accuracy. It is a single-step solver in computing $\mathrm{y}(t_n)$, it needs only the solution at the immediately preceding time point, $\mathrm{y}(t_{n-1})$.

2. ode23: According to Mathworks, ode23 is an implementation of an explicit Runge-Kutta (2,3) pair of Bogacki and Shampine [46]. It may be more efficient than ode45 at

crude tolerances and in the presence of moderate stiffness. In ode23, two simultaneous single-step formulas, one of second-order and one of the third order, are involved.

3. ode113: According to Mathworks, ode113 is a variable-step, variable-order (VSVO) Adams-Bashforth-Moulton PECE solver of orders 1 to 13 [47]. The highest order used appears to be 12, however, a formula of order 13 is used to form the error estimate and the function does local extrapolation to advance the integration at order 13. ode113 may be more efficient than ode45 at stringent tolerances or if the ODE function is particularly expensive to evaluate. ode113 is a multistep solver, it normally needs the solutions at several preceding time points to compute the current solution.

4. ode15s: According to Mathworks, ode15s is a variable-step, variable-order (VSVO) solver based on the numerical differentiation formulas (NDFs) of orders 1 to 5. Optionally, it can use the backward differentiation formulas (BDFs, also known as Gear's method) that are usually less efficient. Like ode113, ode15s is a multistep solver. One may use ode15s if ode45 fails or is very inefficient and if one suspects that the problem is stiff, or, when solving a differential-algebraic equation (DAE) [48, 49].

5. ode23s: According to Mathworks, ode23s is based on a modified Rosenbrock formula of order 2. Because it is a single-step solver, it may be more efficient than ode15s at solving problems that permit crude tolerances or problems with solutions that change rapidly. It can solve some kinds of stiff problems for which ode15s is not effective [48].

6. ode23t: According to Mathworks, ode23t is an implementation of the trapezoidal rule using a free interpolant. This solver is preferred over ode15s if the problem is only moderately stiff and you need a solution without numerical damping. ode23t can also solve differential-algebraic equations (DAEs) [49, 50].

7. ode23tb: According to Mathworks, ode23tb is an implementation of TR-BDF2, an implicit Runge-Kutta formula with a trapezoidal rule step as its first stage and a backward differentiation formula of order two as its second stage. By construction, the same iteration matrix is used in evaluating both stages. Like ode23s and ode23t,

this solver may be more efficient than ode15s for problems with crude tolerances [50, 51].

For each of the aforementioned numerical ODE solvers, the dummy dynamical system is integrated and the following three characteristics are investigated:

1. Stability.
2. Accuracy.
3. Computational cost.

1. Stability Analysis:

For the stability analysis, two orbits with slightly different initial states are integrated w.r.t time. The initial state of the first orbit is given by Eq. (111), and the initial state of the second orbit is .00005% offset from the initial state of the first orbit, i.e., $\vec{X}(0)_{second\ orbit} = \vec{X}(0)_{firs\ orbit} \pm (.00005/100) \times \vec{X}(0)_{first\ orbit}$. The distance between the two orbits for various integration techniques is plotted in Fig. 2.7. Fig. 2.7(a) shows the difference between reference orbit and orbit with .00005% increment in the initial state and Fig. 2.7(b) shows the difference between reference orbit and orbit with .00005% decrement in the initial state. The green plot corresponds to the exact or analytical method.

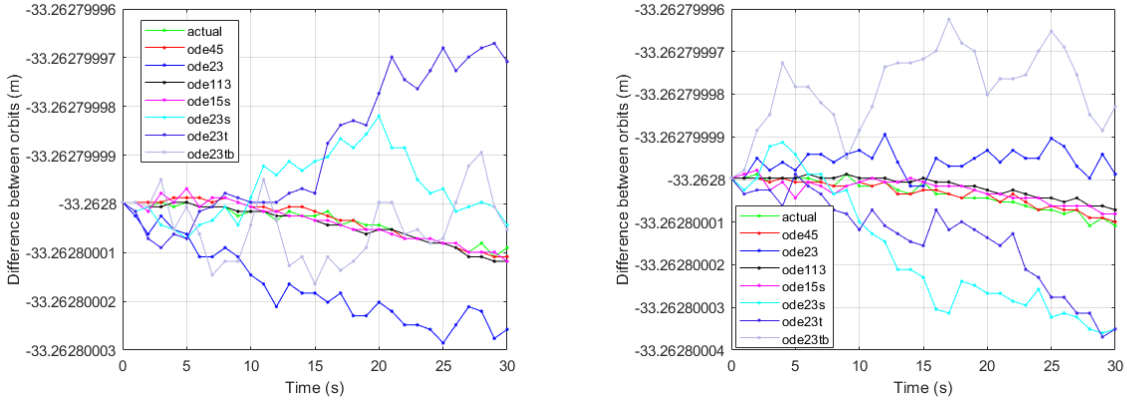

(a) .00005% Increment. **(b)** .00005% Decrement.

Figure 2.7: Comparison of various integration techniques for stability analysis.

A small change is magnified much more quickly by ode23, ode23t, ode23tb, ode23s when compared to ode45 or ode113 or ode15s. This implies that ode23, ode23t, ode23tb, ode23s are the least stable ones. The relative tolerance and absolute tolerance are taken as $[10^{-12}; 10^{-12}]$ for all the integration techniques.

2. Accuracy Analysis:

For determining accuracy, the difference between true (analytical) and numerical solutions are investigated. The initial state is given by Eq. (111). Fig. 2.8(a) plots the difference for all the integration techniques and Fig. 2.8(b) plots the difference for all but ode15s. Orbit obtained through ode15s is the least accurate one. The orbits obtained using ode45 and ode113 have the best accuracy results. The relative tolerance and absolute tolerance are taken as $[10^{-12}; 10^{-12}]$ for all the integration techniques.

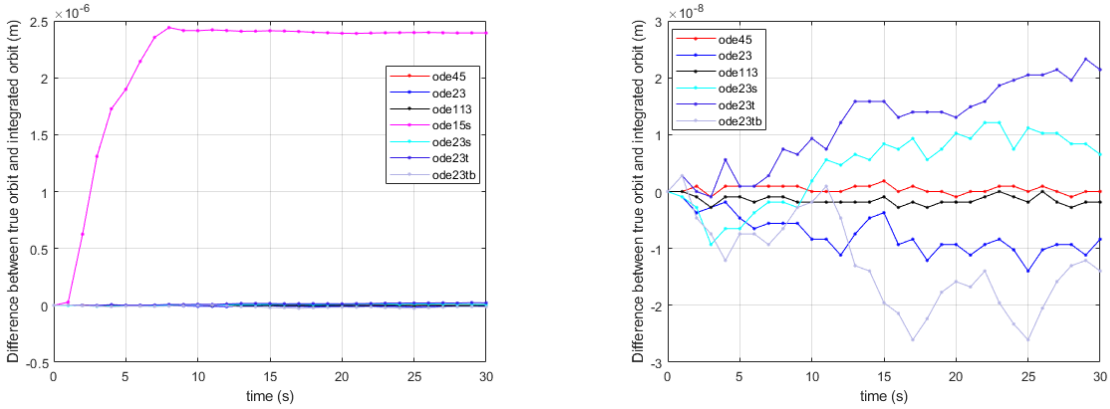

(a) All Integration Techniques. **(b)** All But ode15s.

Figure 2.8: Accuracy of various integration techniques.

3. Computational Cost Analysis:

Five iterations are run for each integration scheme, and the average run-time for each is plotted in Fig. 2.9.

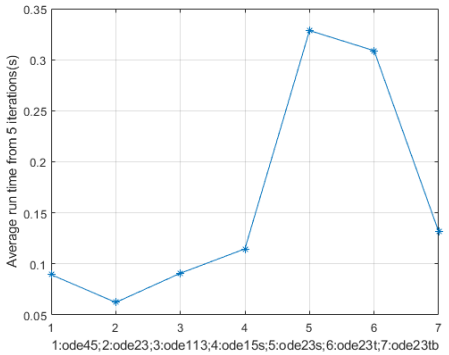

Figure 2.9: Average run-time of various integration techniques.

From Fig. 2.9, ode23s and ode23t are the worst integrators in terms of run-time. ode45, ode23, and ode 113 are the best integrators in terms of run-time.

From the stability, accuracy, and run-time analysis, the best integrators (from among the ones readily available with Matlab) are ode45 and ode113. Between the two, ode45 is selected because of its popularity.

2.5 Concluding Remarks

To conclude, the analytical developments in this chapter serve to provide a more accurate solution for orbit propagation of near-Earth objects. The lesser the object distance from the Earth-center compared to the disturbing body distance, the more relevant is the third-body perturbation improvements made in this chapter. The improvement made in solar radiation pressure perturbations is most relevant when the propagation period is relatively large (of the order of decades).

3 MODELING LORENTZ FORCE PERTURBATIONS

This chapter is dedicated to studying Lorentz force and orbital perturbations because of the Lorentz force. Since the Lorentz force is not well-studied, a comprehensive numerical study is first carried out before moving on to the development of analytical perturbation theory. The numerical study carried out in section 3.1 uses Cartesian coordinates and is a full-model study, i.e., all GEO-relevant perturbation forces are considered.

3.1 Full-Model Numerical Investigation of the Effect of Lorentz Force

Since the space debris is modeled as a sphere in this research work, a 3-DoF equation of motion holds for center of mass, which is given in Cartesian coordinates as:

$$\ddot{\vec{x}} = -GM_{\oplus}\nabla V(\vec{x}) - G\sum_{k=1,2} M_k \left[\frac{\vec{x}-\vec{x}_k}{|\vec{x}-\vec{x}_k|^3} + \frac{\vec{x}_k}{x_k^3}\right] + \sum_l \vec{a}_l \tag{129}$$

where $\vec{x}$ is the geocentric position of the object, G the gravitational constant, $M_{\oplus}$ the Earth-mass, and $V(\vec{x})$ the Earth gravitational potential. The formulation of Pines [52] has been implemented for the gravitational potential representations. The third body gravitational perturbations of the Sun and Moon (k=1,2) with the states $\vec{x}_k$ are modeled via their center of mass. The Sun and Moon masses are represented by M_k (k=1,2). Finally, $\sum \vec{a}_l$ is the sum over non-gravitational accelerations of solar radiation pressure, atmospheric drag, and Lorentz force.

The acceleration due to solar radiation pressure is modeled using cannonball model (Eq. (75)) and the acceleration due to atmospheric drag force is modeled as:

$$\vec{a}_{drag} = -\frac{1}{2}\frac{\tilde{c}_D A_{ref}\rho|\vec{v}_{rel}|\vec{v}_{rel}}{m} \tag{130}$$

where $\tilde{c}_D$ is drag coefficient, A_{ref} is reference area, ρ is atmospheric density and $\vec{v}_{rel}$ is velocity of body relative to atmosphere. A_{ref} is taken as spherical cross-sectional area i.e., πr^2. The atmosphere is assumed to be co-rotating with Earth. The density ρ is obtained using GOST model [37].

3.1.1 Lorentz Force

A charge q that moves through the Earth's magnetosphere with a velocity $\vec{v}_{rel}$ relative to the magnetic field $\vec{B}$, experiences Lorentz force,

$$\vec{F}_{charge} = q\vec{v}_{rel} \times \vec{B} \tag{131}$$

where the charge q can be obtained from the potential ϕ of the space object and body capacitance C using:

$$q = C\phi \tag{132}$$

For solving the body potential ϕ, Kirchoff's current equation needs to be solved. Assuming that an object in space behaves like a node in an electric circuit, Kirchoff's current law under equilibrium condition gives [34]:

$$\sum_j I_j(\phi) = I_i + I_e + I_{ph} + I_{se} + I_{bsc} + I_{misc} = 0 \tag{133}$$

where I_i is plasma ion current, I_e is plasma electron current, I_{ph} is photoelectric current, I_{se} is secondary electron current, I_{bsc} is backscattered current and I_{misc} is miscellaneous current. Miscellaneous current includes all currents apart from ones mentioned until now, and it will be neglected in all the theoretical developments and simulations in this work. The ϕ in parenthesis indicates that the currents are a function of body potential. In this work, the charging time scale is much smaller compared to orbit propagation time steps, and hence the assumption of equilibrium current condition can be used.

3.1.2 Earth Magnetosphere

Lorentz force depends upon the selection of Earth's magnetosphere model. Typically, magnetosphere models can be grouped into two classes: statistical and physics-based. The Physics-based models are computationally expensive and difficult to solve as they require solving numerically several nonlinear partial differential equations on a three-dimensional grid of points. They take magnetohydrodynamic (MHD) flows of the plasma into consideration for simulating the magnetic field. Statistical models, on the other hand, are based on

empirical formulations. Early magnetosphere models were primarily physics-based due to the unavailability of sufficient space-data, but over the last three decades, with the availability of the huge amount of data from satellites and space-instruments, the trend has shifted towards the use of statistical models [53, 54, 55].

The work carried out in this research uses the empirical dipole magnetic field model. The model is a first-order approximation of Earth's actual magnetic field. The implementation of the dipole model is simple and is particularly accurate at low Earth altitudes. GEO magnetic field can be much more accurately simulated using a complex model like the Tsyganenko magnetic field model, but it is harder and slower to implement and is not part of this work. Eqs. (134), (135), (136) represent the dipole model [56], where the parameters η, ξ, ζ represent geocentric distance, co-elevation and East longitude from Greenwich, respectively. r_E is the equatorial radius of Earth. The parameters g_i^j and h_i^j are IGRF coefficients and can be obtained from data released by IAGA [57].

$$B_\eta = 2\left(\frac{r_E}{\eta}\right)^3\left[g_1^0\cos\xi + (g_1^1\cos\zeta + h_1^1\sin\zeta)\sin\xi\right] \tag{134}$$

$$B_\xi = \left(\frac{r_E}{\eta}\right)^3\left[g_1^0\sin\xi - (g_1^1\cos\zeta + h_1^1\sin\zeta)\cos\xi\right] \tag{135}$$

$$B_\zeta = \left(\frac{r_E}{\eta}\right)^3\left[g_1^1\sin\zeta - h_1^1\cos\zeta\right] \tag{136}$$

3.1.3 Space-Plasma Environment

Body charge depends on longitude, local time, and altitude, because of varying plasma conditions [34]. The numerical simulations carried out here focus on low Earth altitudes (up to an altitude of 2000 Km) and geosynchronous region only. In the current work, for the low Earth regions, local time and longitudinal variations of plasma data are neglected, focusing only on altitude dependent effects as they appear to be the most crucial ones. For the geosynchronous region, only the local time variations are considered because of limitations in data availability. Plasma at low Earth orbits is usually of low energy (typically less than .1 eV energy) and high density (typically $10^5\ cm^{-3}$ or higher) [34]. At geosynchronous altitudes, the plasma density is relatively small (around 1 cm^{-3}), but plasma energy is high,

typically around 100 eV, often reaching KeV ranges during geomagnetic storm activities [34]. A geomagnetic storm is a space weather phenomenon resulting from a rapid increase in energy transfer from Sun to Earth's magnetosphere and typically caused by solar coronal mass ejections (CME). Bodies in geosynchronous orbit typically get positively charged in sunlight due to the emission of photo-electrons. The photoelectric current in the geosynchronous region is of similar order as that of the dominant plasma electron current and hence it is a major contributor to body charge. For the low Earth region, the photoelectric current is relatively insignificant as plasma currents are much larger than photoelectric current. However, under certain conditions, like when an object is inside the auroral oval, the photoelectric current might play an important role. In the geosynchronous shadow region and all of the low Earth regions, bodies are typically negatively charged because of the dominant plasma electron current. Once the voltage is determined from the current equilibrium, the charge can be determined using capacitance. The capacitance is both object geometry dependent and plasma dependent. The plasma dependence is characterized using the so-called Debye length, which is a density-dependent quantity. Debye length is roughly the distance from the body at which the electrostatic effect of the body is completely shielded by the plasma particles surrounding it [58].

3.1.4 Modeling of Current

In the following sections, plasma electron and ion currents, secondary electron and ion currents, backscattered electron current, and photoelectric current are modeled using a steady-state approach [34].

3.1.4.1 Plasma Electron and Ion Currents

Depending on whether a particular kind (polarity) of plasma species is attracted or repelled, plasma current expression can be different.

3.1.4.1.1 Plasma Flux for Repelled Particles

This section introduces analytical expression for the flux of particles repelled by the polarity of the space object in low Earth and geosynchronous orbits. It will be assumed that

the plasma particles follow Maxwell-Boltzmann distribution under the thermal equilibrium condition. The assumption is usually valid for a calm environment. In actuality, no single distribution can accurately model the plasma particles because of various disturbances.

For a spacecraft charged to a potential ϕ, the flux is given as [59]:

$$\tilde{\phi} = e^{-\frac{\tilde{q}\phi}{kT}}\phi_0 \tag{137}$$

where $\tilde{q}$ is particle charge, k is Boltzmann constant, and T is plasma distribution temperature. ϕ_0 is the flux in absence of spacecraft charging, and is given as:

$$\phi_0 = n\sqrt{\frac{kT}{2\pi\tilde{m}}} \tag{138}$$

where n and $\tilde{m}$ represent particle number density and particle mass, respectively.

The current density to an uncharged body can then be written in terms of flux as:

$$J_0 = \tilde{q}\phi_0 = n\tilde{q}\sqrt{\frac{kT}{2\pi\tilde{m}}} = \frac{1}{2}n\tilde{q}\sqrt{\frac{2kT}{\pi\tilde{m}}} \tag{139}$$

And, the current density to a body charged to a potential ϕ is given as:

$$J = \tilde{q}\tilde{\phi} = e^{-\frac{\tilde{q}\phi}{kT}}\tilde{q}\phi_0 = e^{-\frac{\tilde{q}\phi}{kT}}J_0 \tag{140}$$

3.1.4.1.2 Plasma Flux for Attracted Particles

This section introduces flux for particles attracted by body polarity. In the geosynchronous region, where the plasma density is low, the incoming current density collected by a perfectly absorbing spherical or infinitely long cylindrical body from a collisionless, stationary, isotropic plasma is limited by the particles' orbital angular momenta. This current is known as orbit-limited current [60]. For orbit-limited sphere, for an attracted particle approaching the body from infinity, conservation of energy and angular momentum results in the following total current density striking the body surface [59],

$$J(\phi) = J_0(1 - \frac{\tilde{q}\phi}{kT}) \tag{141}$$

where J_0 is ambient current density outside the sheath and is given by Eq. (139).

In Eq. (141), the velocity of the body is not taken into consideration, i.e., it is assumed that the body is at rest compared to plasma velocities. At geosynchronous altitudes, plasma energy is high. The average kinetic energy of particles is much larger than the orbital speed, and the body is essentially at rest compared to plasma particles and hence Eq. (141) is valid.

At a low Earth orbit regime, the body gets negatively charged, i.e., an ion is the attracted species. However, at low Earth orbit, the plasma sheath is thin such that thick sheath theories do not apply here. Also, the orbital velocity is larger than the average kinetic energy of ions. Hence, Eq. (141) becomes invalid for ions in low Earth orbits.

For low Earth orbits, under low-charge plasma conditions, as ions are relatively at rest, they are assumed to be ramming into the body surface, and the ion current is approximately given as [35]:

$$I = en_i V_{sc} A_i \tag{142}$$

where e is elementary charge, n_i is free plasma ion density, V_{sc} is inertial object velocity, and A_i is projected ion collection area. For a sphere of radius r, the projected ion collection area is $A_i = \pi r^2$.

For low Earth orbits, under high-charge plasma conditions, voltage dependence needs to be considered, and the ion current is approximately given as [59]:

$$I = en_i V_{sc} A_i \left(1 - \frac{\tilde{q}\phi}{E_c}\right) \tag{143}$$

where E_c represents ion kinetic energy in the frame of spacecraft.

3.1.4.2 Secondary Electron Current Model

The expression for secondary electron current can be found using yield, i.e., the number of secondary electrons generated per incident projectile particle. Yield expressions can be multiplied with incident plasma ion and electron currents to find the value of secondary

electron current. The secondary electron currents due to hitting ions and electrons are given as:

$$I_{sec_i} = (< \Delta_i >) I_i \tag{144}$$

$$I_{sec_e} = (< \Delta_e >) I_e \tag{145}$$

where the subscripts i and e denote impacting particles as ions and electrons, respectively. I_i and I_e represent plasma ion and electron currents, respectively. It will be assumed that all the incident electrons and ions get absorbed and contribute to secondary electron emission process. The $< \Delta >$ symbol signifies averaged yield value, averaged over all energies, and is given as [34]:

$$< \Delta >= \frac{\int_{E_l}^{E_u} \tilde{E} f(\tilde{E}) \Delta(\tilde{E}) d\tilde{E}}{\int_{E_l}^{E_u} \tilde{E} f(\tilde{E}) d\tilde{E}} \tag{146}$$

where $\tilde{E}$ represents energy, $f(\tilde{E})$ represents the Maxwell-Boltzmann distribution function representing incoming electrons or ions. The integral limits E_l and E_u in Eq. (146) represent lower and upper energy bounds of the impacting particles. In absence of precise information, E_l and E_u are taken as 0 and ∞, respectively. In more advanced modeling, E_l and E_u can be modeled as functions of spacecraft energy, but that aspect is not considered in this work. $\Delta(\tilde{E})$ represents the secondary electron yield corresponding to the particular energy $\tilde{E}$ of the impacting particle. f($\tilde{E}$) is given as:

$$f(\tilde{E}) = n \left(\frac{\tilde{m}}{2\pi k T} \right)^{\frac{1}{2}} e^{-\frac{\tilde{E}}{kT}} \tag{147}$$

3.1.4.2.1 Secondary Electron Yield, $\Delta(\tilde{E})$

The yield Δ can be obtained using Sternglass's theory [61],

$$\Delta = \frac{1}{2} \frac{1}{\bar{E}_0} \left\langle \frac{dE_i}{dx} \right\rangle_{Av} \tau A L_s (1 + \tilde{F}(v_i)) \tag{148}$$

where $\bar{E}_0$ represents mean energy loss per secondary electron formed. Its value is approximately 25 eV for solids. τ is the surface transmission coefficient, and A is a constant that

depends upon the distribution of initial velocities of secondary electrons and the ratio of mean free path for absorption to mean free path for inelastic collisions; $\tau A \approx .5$. The parameter L_s is a characteristic length and is of the order of the distance between inelastic collisions. L_s is given by the following equation:

$$L_s = (\alpha' N \sigma_g)^{-1} \tag{149}$$

where the constant α' is approximately .23 for metals, N is the number of atoms per unit volume, and σ_g is the geometrical area of the outermost filled electron shells. σ_g is given as: $\sigma_g = 1.6 Z^{\frac{1}{3}} \times 10^{-16}$, where Z is the atomic number of the substrate.

In Eq. (148), $\left\langle \frac{dE_i}{dx} \right\rangle_{Av}$ represents total energy loss per unit length and it is given as:

$$\left\langle \frac{dE_i}{dx} \right\rangle_{av} = 2\pi N e^4 z_i^2 \left[\frac{Z}{E_{eq}} ln\left(\frac{4E_{eq}}{\bar{I}} \right) \right] \tag{150}$$

where e represents the electronic charge, z_i represents the charge of incident particle, and $\bar{I}$ represents mean excitation potential of the atom. $E_{eq} = (m_0/\tilde{m})\tilde{E}$ with m_0, $\tilde{m}$, and $\tilde{E}$ being electronic mass, mass of incident particle, and energy of incident particle, respectively. There is a minimum energy requirement for incident particles, and it comes from the condition of positive argument for logarithm function in Eq. (150).

For lighter elements ($Z < 30$), the function $\tilde{F}(v_i)$ in Eq. (148) is given as:

$$\tilde{F}(v_i) \approx \left(1 + \frac{E_{eq}}{100} \right)^{-1} \tag{151}$$

where E_{eq} is expressed in electronvolts.

For heavier elements ($Z \geq 30$), the function $\tilde{F}(v_i)$ in Eq. (148) is given as:

$$\tilde{F}(v_i) \approx \left(\left(1 + \frac{E_{eq}}{100} \right)^{-1} + \tilde{f} \right) \left(1 + \tilde{f} \right)^{-1} \tag{152}$$

Experimental values for the parameter $\tilde{f}$ range typically from .05 for aluminum to .25 for gold. A linear variation of this quantity with atomic number will be assumed in this work.

3.1.4.3 Backscattering Current Model

Backscattering current can be obtained with the help of backscattering yield, i.e., the number of backscattered particles per incident particle. The backscattering of electrons is more important than the backscattering of ions. Usually, the backscattering yield is much smaller compared to the secondary yield. Backscattering electron current is given as:

$$I_{bsc} = r_{bsc} I_e \tag{153}$$

where r_{bsc} represents backscattering yield and I_e represents plasma electron current.

3.1.4.3.1 Backscattering Yield, r_{bsc}

There are two models (diffusion model and elastic collision model) that Archard [62] used for explaining backscattering. Neither of the models single-handedly explains the backscattering, but a combination of the two models explains the backscattering over the entire atomic number range.

In the diffusion model, it is assumed that electrons travel straight into the target up to a certain specified distance, after which they diffuse evenly in all directions. This model assumes that an electron exhibits completely random motion after multiple collisions. It ignores the possibility of an electron undergoing large single elastic reflections between the surface and the depth of complete diffusion.

In the elastic collision model [63], it is assumed that electrons travel straight into the target, suffering retardation according to Thomson-Whiddington law. Also, the electrons undergo elastic collisions per Rutherford's law of scattering. This model acknowledges the presence of electrons that are elastically scattered through large angles, but ignores the diffusion effect of multiple collisions. All electrons that are not turned through more than a right angle are assumed not to have turned at all.

At a low atomic number (Z), the ratio of the depth of complete diffusion x_d to the full range x_R is large, such that there is a great chance of large elastic collisions before diffusion sets in, hence elastic collision model is used. For high Z, $\frac{x_d}{x_R}$ is small, so diffusion sets in

almost immediately long before any elastic collision may take place, so the diffusion model is applicable. In the intermediate region, both models are applicable, and a weighted average of both is used. The following piece-wise model can be assumed for a substrate with the atomic number Z:

For $Z < 11$,

$$r_{bsc} = \frac{a - 1 + .5^a}{a + 1} \tag{154}$$

For $Z > 60$,

$$r_{bsc} = \frac{7Z - 80}{14Z - 80} \tag{155}$$

For $11 \leq Z \leq 60$

$$r_{bsc} = \frac{x_d}{x_R}\left(\frac{a - 1 + .5^a}{a + 1}\right) + \frac{x_R - x_d}{x_R}\left(\frac{7Z - 80}{14Z - 80}\right) \tag{156}$$

where the value of parameter a is approximately taken as .045. The ratio $\frac{x_d}{x_R}$ is approximated as $\frac{x_d}{x_R} \approx \frac{40}{7Z}$ if the average energy of incoming particles is less than 100 KeV. For higher energetic particles, it is approximated as $\frac{x_d}{x_R} \approx \frac{40}{6Z}$.

3.1.4.4 Photoelectron Current Model

Photoelectron current is one of the significant currents in GEO. Photoelectron current density (divided by elementary charge) is given as [34]:

$$J_{ph} = \int_0^\infty f_s Y d\omega \tag{157}$$

where f_s is the number of photons per unit area per unit time per unit photon energy, and it is a function of photon energy, ω. Y is the yield, i.e., the number of photoelectrons per incident photon and is a function of ω and angle of incidence, θ_i. The yield is given as:

$$Y[\omega, R(\omega)] = Y^\star[\omega, R(\omega, \theta_i)][1 - R(\omega, \theta_i)] \tag{158}$$

where R is reflectance and $Y^\star$ is yield per absorbed photon, which can be approximated as [34, 64]:

$$Y^\star[\omega, R(\omega, \theta_i)] \approx \frac{Y^\star[\omega, R(\omega, 0)]}{cos\theta_i} \tag{159}$$

Laboratory measurements [34, 65, 66] show:

$$1 - R(\omega, \theta_i) \approx [1 - R(\omega, 0)]cos(\theta_i) \tag{160}$$

Thus, from the product of $Y^\star$ and $(1-R)$, there is no θ_i dependence of Y. The only incident angle dependence of the photoelectric current stems from the factor $\cos\theta_i$, which results from effective surface area on which light is incident. Photoelectrons can be assumed to follow Maxwellian distribution for positive body potentials with characteristic temperature ranging 1eV-2eV [34]. The characteristic temperature T_{ph} will be taken as 1.5 eV in this work. This leads to:

$$I_{ph} = eJ_{ph}(0)A_{body}cos\theta_i \equiv eJ_{ph}(0)A_\perp \quad if\ \phi \leq 0 \tag{161}$$

and,

$$I_{ph} = eJ_{ph}(0)A_\perp e^{-\frac{\phi}{T_{ph}}} \quad if\ \phi > 0 \tag{162}$$

where the neutral current density $J_{ph}(0)$ is given as:

$$J_{ph}(0) = \int_0^\infty f_s(\omega)Y^*(\omega)[1 - R(\omega)]d\omega \tag{163}$$

In Eqs. (161) and (162), e represents elementary charge, $A_\perp$ represents projected area of the body and ϕ represents the body potential.

In the sections to follow, methods for obtaining quantities appearing in Eq. (163) are stated. The number of photons per unit area per unit time per unit photon energy (f_s) will be obtained from AM 0 solar spectral irradiance. Yield per absorbed photon (Y^*) will be obtained using Fowler's method for near-threshold frequencies and assumed constant for higher frequencies. Fowler's yield depends upon absolute body temperature, which will be

obtained using the thermal equilibrium equation. Reflectance (R) will be obtained using Fresnel's equation. Fresnel's equation depends upon the refractive index, which will be computed using Brendel and Bormann model.

3.1.4.4.1 Solar Photon Flux Data f_s

AM 0 or ASTM E-490 spectrum provides solar spectral irradiance ($\frac{W}{m^2 nm^{-1}}$) data and is based on data collected from several satellites, space shuttles, high altitude aircrafts, solar telescopes.

Spectral irradiance (power per unit area per unit wavelength) S_λ can be used to obtain the number of photons per unit area per unit time per unit photon energy f_s using [67]:

$$f_s = \frac{\lambda^3}{(hc)^2} S_\lambda \tag{164}$$

where λ, h, c represent light wavelength, Plank's constant, and speed of light, respectively.

3.1.4.4.2 Fowler's Yield Per Absorbed Photon Y^*

Photoelectron yield per absorbed photon (Y^*) for frequencies near the threshold frequency of the body material can be obtained using Fowler's yield [68]. It is given as:

$$Y^* = K_P \frac{T_B^2}{(\chi_0 - h\nu)^{\frac{1}{2}}} \varkappa\left(\frac{h\nu - \chi}{kT_B}\right) \tag{165}$$

where the parameter K_P is a proportionality constant, T_B is absolute body temperature, h is Plank's constant, ν is photon frequency, χ is work function, and k is Boltzmann constant. $\chi_0 = \chi + \epsilon^*$ where ϵ^* is Fermi energy. Fowler assumed that for frequencies near threshold, $(\chi_0 - h\nu)^{\frac{1}{2}}$ is constant. According to Fowler, at $h\nu \approx \chi$, $(\chi_0 - h\nu) \approx \epsilon^\star$, so if ν changes by 15%, (with ν_0 of the order of 4 eV and $\chi_0 - h\nu$ of the order of 10 volts), $(\chi_0 - h\nu)$ changes by 6% and $(\chi_0 - h\nu)^{\frac{1}{2}}$ changes by only 3%. This implies approximately a constant $(\chi_0 - h\nu)^{\frac{1}{2}}$. In this work, the upper and lower limit on variation of photon frequency ν from threshold frequency ν_0 would correspond to 3% variation of $(\chi_0 - h\nu)^{\frac{1}{2}}$ from its nominal value $(\chi_0 - \chi)^{\frac{1}{2}}$. Thus,

$$Y^* = K_P' T_B^2 \varkappa(\mu) \tag{166}$$

where K'_P is new constant of proportionality, and $\mu = \frac{h\nu - \chi}{kT_B}$. The function $\varkappa$ is defined as:

$$\varkappa(\mu) = e^{\mu} - \frac{e^{2\mu}}{2^2} + \frac{e^{3\mu}}{3^2} \ldots \qquad for \quad \mu \leq 0 \tag{167}$$

$$\varkappa(\mu) = \frac{\pi^2}{6} + \frac{1}{2}\mu^2 - (e^{-\mu} - \frac{e^{-2\mu}}{2^2} + \frac{e^{-3\mu}}{3^2} - \ldots) \qquad for \quad \mu > 0 \tag{168}$$

The value of the constant K'_P has to be found from the experimental values of the photoelectric yield. For aluminum (the material used in this work), if absolute body temperature is expressed in terms of equivalent electronvolts, K'_P can be taken as .0038 eV^{-2}. For frequencies that have energy values lower than the proposed 3% range, it will be assumed that there is no photoelectron emission. For all frequencies that have energy values higher than this range, the yield will be taken as constant.

Eq. (166) requires absolute body temperature T_B, which can be obtained from thermal equilibrium:

$$T_B = \left(\frac{(1 - a_{lb})E}{4\sigma} \right)^{\frac{1}{4}} \tag{169}$$

where a_{lb} is the albedo, r is radius of the body, E is solar constant, and σ is Stefan's constant. As an approximation in this work, albedo is taken as a summation of diffuse and specular reflectances.

3.1.4.4.3 Reflectance R

Reflectance (for thick materials), under the assumption of unpolarized sunlight and zero angle of incidence, is given as [69, 70]:

$$R = \frac{k_2^2 + (n_1 - n_2)^2}{k_2^2 + (n_1 + n_2)^2} \tag{170}$$

where n_1 and n_2 are the refractive indices of the medium in which incident light is present and the object medium, respectively. k_2 represents an optical parameter. It is safe to assume $n_1 = 1$, which corresponds to the vacuum. The next objective is to determine the refractive index of the second medium n_2 as a function of light wavelength or frequency,

and the optical parameter k_2.

Brendel and Bormann [71] proposed a modified version of the classical Lorentz-Drude model. According to the modified model, the complex dielectric function is given as:

$$\hat{\epsilon}_r(\tilde{\omega}) = 1 - \frac{\Omega_p^2}{\tilde{\omega}(\tilde{\omega} - i\Gamma_0)} + \sum_{j=1}^{l} \chi_j(\tilde{\omega}) \tag{171}$$

$$\chi_j(\tilde{\omega}) = \frac{1}{\sqrt{2\pi}\sigma_j} \int_{-\infty}^{\infty} e^{-\frac{(x-\omega_j)^2}{2\sigma_j^2}} \frac{f_j \omega_p^2}{(x^2 - \tilde{\omega}^2) + i\tilde{\omega}\Gamma_j} dx \tag{172}$$

where $\omega_p = \sqrt{\frac{\tilde{N}e^2}{\epsilon_0 m_0}}$ is plasma frequency, with $\tilde{N}$, e, ϵ_0, m_0 being number of conduction electrons per unit volume, electronic charge, permittivity of vacuum, and electronic mass, respectively. l is the number of oscillators with frequency ω_j, strength f_j, and lifetime $1/\Gamma_j$, and $\Omega_p = \sqrt{f_0}\omega_p$ is plasma frequency associated with intraband transitions with oscillator strength f_0 and damping constant Γ_0. σ_j is standard deviation associated with the Gaussian modelling of the dielectric function and its value is experimentally obtained. $\tilde{\omega}$ is angular frequency of light.

Rakic [72] has given experimental tables for Brendel-Bormann model parameters f_0, f_j, Γ_0, Γ_j, ω_j, σ_j for some commonly used materials. For Aluminum, $[f_0, f_1, f_2, f_3, f_4] = [.526, .213, .060, .182, .014]$, $[\Gamma_0, \Gamma_1, \Gamma_2, \Gamma_3, \Gamma_4] = [.047, .312, .315, 1.587, 2.145]\ eV$, $[\omega_1, \omega_2, \omega_3, \omega_4] = [.163, 1.561, 1.827, 4.495]\ eV$, $[\sigma_1, \sigma_2, \sigma_3, \sigma_4] = [.013, .042, .256, 1.735]\ eV$.

Analytical solution for $\chi_j(\tilde{\omega})$ exists and is given as:

$$\chi_j = \frac{i f_j \omega_p^2}{2\sqrt{2} a_j \sigma_j} \left(U\left[1/2, 1/2, -\left(\frac{a_j - \omega_j}{\sqrt{2}\sigma_j}\right)^2\right] + U\left[1/2, 1/2, -\left(\frac{a_j + \omega_j}{\sqrt{2}\sigma_j}\right)^2\right] \right) \tag{173}$$

U is known as Kummer function of second kind and $U(1/2, 1/2, z^2) = \sqrt{\pi} e^{z^2} erfc(z)$, where $erfc(x) = \frac{2}{\sqrt{\pi}} \int_x^{\infty} e^{-t^2} dt$ is the complementary error function. The parameter a_j is given by its real and imaginary parts:

$$a_j = a_j' + i a_j'' \tag{174}$$

where,

$$a'_j = \frac{\tilde{\omega}}{\sqrt{2}}\left((1+(\Gamma_j/\tilde{\omega})^2)^{1/2}+1\right)^{1/2} \tag{175}$$

$$a''_j = \frac{\tilde{\omega}}{\sqrt{2}}\left((1+(\Gamma_j/\tilde{\omega})^2)^{1/2}-1\right)^{1/2} \tag{176}$$

Now, the complex refractive index is given as:

$$\tilde{n} = n_2 - ik_2 \tag{177}$$

where n_2 is the usual real refractive index and k_2 is the extinction coefficient. Now, the square of amplitude of this complex refractive index $(\tilde{n})^2 = (n_2^2 - k_2^2) - 2ik_2n_2$ is equal to the complex dielectric function.

Thus, if complex dielectric function $\hat{\epsilon}_r(\tilde{\omega}) = \epsilon_{r_1} - i\epsilon_{r_2}$, then from $\hat{\epsilon}_r(\tilde{\omega}) = (\tilde{n})^2$,

$$\epsilon_{r_1} = n_2^2 - k_2^2 \tag{178}$$

$$\epsilon_{r_2} = 2k_2n_2 \tag{179}$$

Solving Eqs. (178) and (179), one obtains:

$$n_2 = \frac{1}{\sqrt{2}}\sqrt{\epsilon_{r_1} + \sqrt{\epsilon_{r_1}^2 + \epsilon_{r_2}^2}} \tag{180}$$

$$k_2 = \frac{1}{\sqrt{2}}\sqrt{-\epsilon_{r_1} + \sqrt{\epsilon_{r_1}^2 + \epsilon_{r_2}^2}} \tag{181}$$

3.1.5 Capacitance Modeling

To compute object charge from voltage, one requires body capacitance, whose modeling depends upon the orbit regime. The primary reason for the difference in capacitance modeling arises from the difference in Debye length relative to body dimension. For an object with dimension ranging from tens of centimeters to few meters, Debye length is much larger than body dimension in the GEO region, whereas Debye length is much smaller than body dimension in the LEO region. As a consequence of this, certain first-order approximations

can be made in the capacitance formulation.

For two concentric conducting spheres having radii a_1 and b_1, respectively, the potential difference is given as:

$$\Delta\phi = \frac{q}{4\pi\epsilon_0}\left(\frac{1}{a_1} - \frac{1}{b_1}\right) \tag{182}$$

where ϵ_0 is vacuum permittivity. Thus, the capacitance C is:

$$C = \frac{4\pi\epsilon_0}{(\frac{1}{a_1} - \frac{1}{b_1})} \tag{183}$$

At GEO altitude, with $a_1 = r$ and $b_1 = L$, where r is radius of the body and L is the Debye length, using the approximation $\frac{r}{L} << 1$ in Eq. (183) results in:

$$C = 4\pi\epsilon_0 r \tag{184}$$

For LEO, with $a_1 = r$ and $b_1 = (r + L)$, and using the approximation $\frac{r}{L} >> 1$, Eq. (183) results in:

$$C = \frac{4\pi\epsilon_0 r^2}{L} \tag{185}$$

The Debye length L can be obtained from the following equation:

$$\frac{1}{L^2} = \sum_j \left(\frac{n_j \tilde{q}_j^2}{\epsilon_0 k T_j}\right) \tag{186}$$

where n_j, $\tilde{q}_j$, T_j, k denote number density of plasma particles, charge of particle, characteristic temperature of particle distribution, and Boltzmann constant, respectively, for particle type j.

3.1.6 GEO Numerical Simulation For Different Orbital Parameters, Area-To-Mass Ratios, and Plasma Conditions

For all the simulation cases, an aluminum sphere of 1 m^2 surface area is considered. Simulation time is taken as four days, and the initial epoch is set to 12:00:00 UTC, March 21, 2000. Earth's gravity, Luni-Solar gravity, direct solar radiation pressure, and Lorentz force

are included in the modeling. The gravitational potential is modeled up to degree and order 12, the atmospheric drag coefficient is taken as two, and the SRP diffuse reflection coefficient is taken as .035. The dipole model has been chosen for Earth's magnetic field. Earth's shadow is modeled as a cylinder. Plasma electrons and ions are assumed to be collected over the entire surface area, whereas photons are assumed to be collected over the frontal surface area. Two area-to-mass ratio objects are investigated, one corresponds to general satellites with low area-to-mass ratio (LAMR) of .02 m^2/kg, and the other corresponds to a high area-to-mass ratio (HAMR) of 23.6 m^2/kg. Orbit propagation is performed using the integrator 'dop853' (Runge-Kutta method of order 8(5,3) due to Dormand and Prince) available with the Python class scipy.integrate.ode.

Three different groups of geosynchronous orbits are considered: the first GEO group is characterized by low initial inclination ($.1^0$) and small initial eccentricity (.001), the second GEO group is characterized by initial inclination of 15^0 and initial eccentricity of .015, and the third GEO group is characterized by initial inclination of 40^0 and initial eccentricity of .015. The initial true anomaly values are taken such that the initial longitude value is 75^0 E (GEO libration point). The GEO cases are described in Table 3.

Table 3: The GEO cases (a_i = 42164 km, $\omega_i = 30^0$, $\Omega_i = 60^0$).

GEO group 1	GEO group 2	GEO group 3
($i_i = .1^0$,	($i_i = 15^0$,	($i_i = 40^0$,
$e_i = .001$,	$e_i = .015$,	$e_i = .015$,
$\nu_i = 344.15^0$)	$\nu_i = 344.6^0$)	$\nu_i = 349^0$)
AMR = .02 m^2/kg	AMR = .02 m^2/kg	AMR = .02 m^2/kg
AMR = 23.6 m^2/kg	AMR = 23.6 m^2/kg	AMR = 23.6 m^2/kg

Two different plasma conditions are simulated, one corresponding to low-charge conditions and the other corresponding to high-charge conditions. Denton [73] provides GEO plasma parameters for three classes of particles: hot electrons (30 eV to 45 KeV), hot protons (100 eV to 45 KeV), and low protons (1 eV to 100 eV). Data corresponding to one-solar-cycle

(1990 - 2001) averaged low proton density, hot proton density, hot electron density, hot proton perpendicular and parallel temperatures, hot electron perpendicular and parallel temperatures (Maxwellian temperatures for distributions in the perpendicular and parallel directions of the magnetic field, respectively) can be obtained from Denton [73]. The net temperature for the overall distribution is then taken as:

$$T = \frac{2}{3}T_{\perp} + \frac{1}{3}T_{\parallel} \tag{187}$$

Temperature distribution for low protons is not given by Denton. An assumption of 50 eV (corresponding to mid-value of the energy range) is used for the low proton temperature. Once the data is extracted from Denton for a particular turbulence level (decided by geomagnetic K_p index value), an interpolation surface is fit through the data from which plasma parameters can be obtained for any orbit local time. The low-charge plasma condition is simulated using Denton's data for $K_p = 1$. For simulating high-charge plasma condition, high-flux ATS-6 data [74] given in Table 4 is used.

Table 4: High-charge plasma environment for GEO.

Particles	Number Density (m^{-3})	Energy (eV)
Electrons	2.36×10^5	16000
Protons	2.36×10^5	2.95×10^4

Figs. 3.1(a) and 3.1(b) show voltage and equilibrium currents, respectively, of a GEO body under low-charge plasma condition, where PEC, PIC, SEC, BEC, PC stand for plasma electron current, plasma ion current, secondary electron current, backscattered electron current, and photoelectric current, respectively. In GEO, the photoelectric current is one of the major contributors, and its absence in the shadow region results in a large dip in voltage. The body potential is a few positive volts in sunlight. On the other hand, for the high-charge plasma condition described by Table 4, body voltage is 2.293 volts under sunlit condition, and it is approximately -40 kV, when in Earth's shadow.

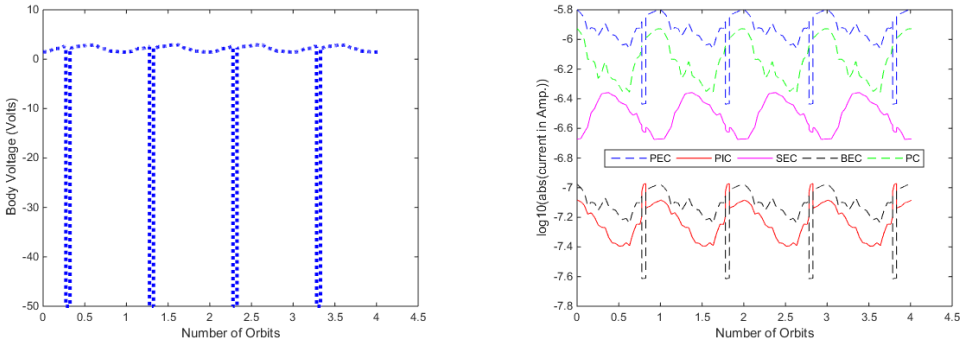

(a) Body Voltage.

(b) Logarithm of Absolute Value of Current.

Figure 3.1: Charging characteristic of GEO group 1 (LAMR, low-charge plasma condition).

Fig. 3.2 shows the logarithm of magnitudes of perturbing accelerations for GEO orbits. For the LAMR objects, higher harmonics of Earth's gravity and Sun/Moon third body gravitational perturbations are the dominant contributors to perturbing acceleration; for the HAMR objects, however, solar radiation pressure also becomes one of the major contributors. Lorentz force is still the least dominating factor affecting perturbing acceleration. The sudden jumps in Lorentz perturbation in Fig. 3.2(a) implies that the object is in Earth's shadow. The jumps in Lorentz perturbation in Figs. 3.2(b), 3.2(c) are because of magnetic field vector nearly aligning up with the relative velocity vector.

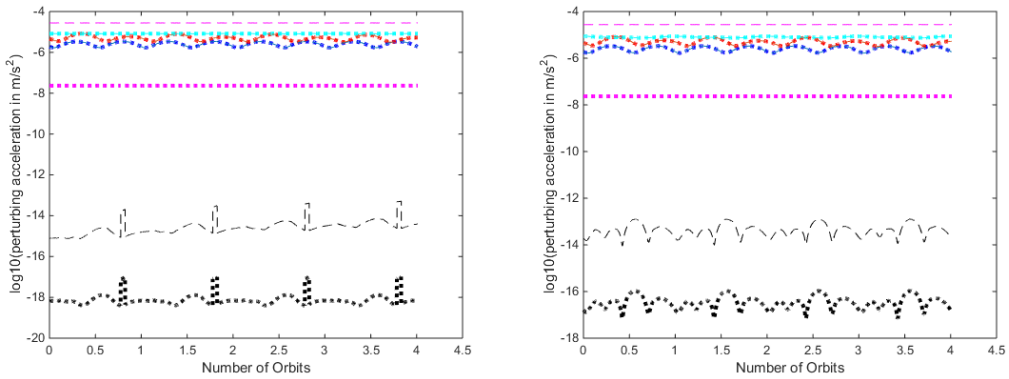

(a) GEO Group 1.

(b) GEO Group 2.

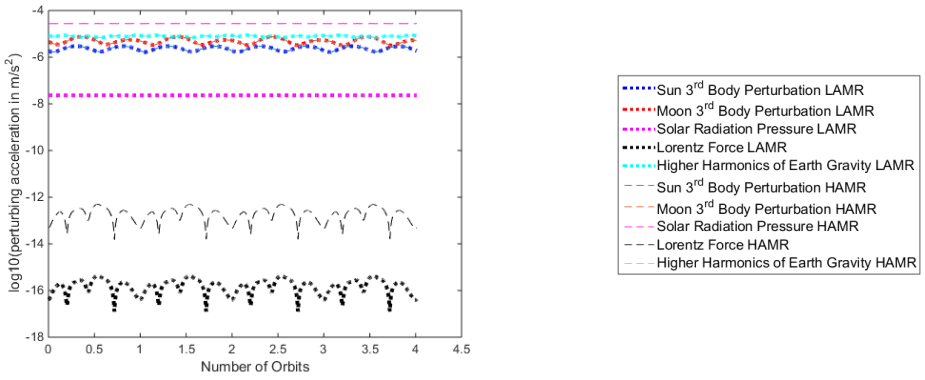

(c) GEO Group 3.

Figure 3.2: Common logarithm of perturbing acceleration magnitudes for GEO orbits, low-charge plasma condition.

To investigate the importance of Lorentz force, the difference between Lorentz force included orbit and Lorentz force excluded orbit is plotted. The projection of displacement vector, i.e., the position vector in Lorentz force included orbit minus position vector in Lorentz force excluded orbit, along the tangential or velocity vector direction of the Lorentz force excluded orbit is defined as the in-track perturbation, the projection along the radial direction is defined as the radial perturbation, and the projection along orbit-plane normal is defined as the cross-track perturbation. For clarification, the definition of in-track and radial perturbations are shown in Fig. 3.3.

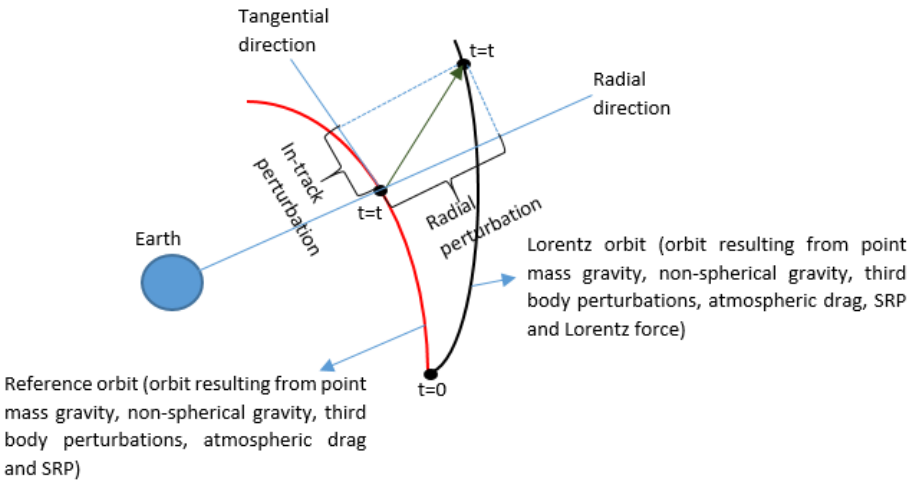

Figure 3.3: Definition of in-track and radial perturbations.

Figs. 3.4, 3.5, 3.6 show in-track, cross-track, and radial perturbations of Lorentz force included orbit relative to Lorentz force excluded orbit, respectively, for HAMR objects. Figs. 3.4(a), 3.4(b) show the in-track perturbations corresponding to low-charge and high-charge plasma conditions, respectively. Under both low-charge and high-charge plasma conditions, all the orbit groups exhibit a secular decreasing trend in in-track plots. In addition to the secular trend, the in-track perturbations also exhibit a short periodic variation with a period of one day. The decreasing secular trend in in-track perturbation arises because of the increasing semi-major axis of Lorentz force included orbit relative to Lorentz force excluded orbit. Since the in-track perturbations are mostly negative, the object in Lorentz force included orbit, on an average, lags behind the object in Lorentz force excluded orbit. For group 1 orbit under low-charge plasma conditions, the order of in-track perturbations is 10^{-4} m, whereas it is an order higher for group 2 and group 3 orbits. Under high-charge plasma conditions, for group 1 orbit, the order of in-track perturbations is 10^{-1} m, which is two orders of magnitude higher than group 2 and group 3 orbits. This opposite trend for group 1 orbit under high-charge plasma condition is due to body voltage reaching approximately -40 kV in the shadow under high-charge plasma condition; as the simulations are run near the equinox, higher inclined orbits do not enter Earth's shadow region and hence do not see a surge in Lorentz force values.

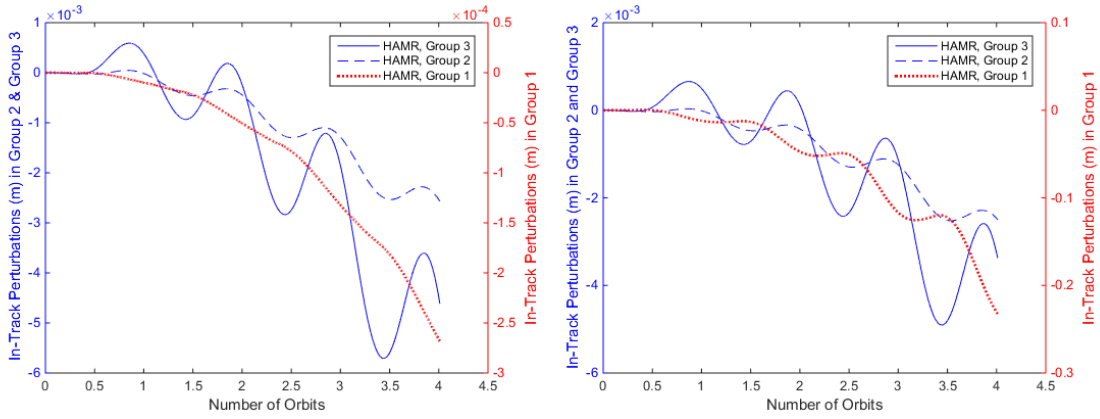

(a) In-Track Perturbations, Low-Charge Condition.

(b) In-Track Perturbations, High-Charge Condition.

Figure 3.4: In-track perturbations for Lorentz force perturbed orbit relative to Lorentz force excluded orbit (HAMR object).

Figs. 3.5(a), 3.5(b) show cross-track perturbations of Lorentz force included orbit relative to Lorentz force excluded orbit under low-charge and high-charge plasma conditions, respectively. The cross-track perturbation plots nearly exhibit a zero-mean periodic variation with an approximate period of one day. The zero-mean periodic behavior implies that, on average, there is no change in the orbital plane due to Lorentz force. The amplitudes of the periodic variations in the cross-track perturbations increase with time, and a factor responsible for this increasing behavior is the decreasing RAAN of the Lorentz force included orbit relative to Lorentz force excluded orbit. Among group 2 and group 3 orbits, group 3 orbits exhibit larger amplitudes of variations because of higher inclination. For low-charge plasma conditions, cross-track perturbations are of the order of 10^{-6} m for lowly inclined group 1 orbit, whereas it is two orders of magnitude higher for higher inclined group 2 and group 3 orbits. For group 1 orbit under high-charge plasma conditions, cross-track perturbations are of the order of 10^{-3} m, which is one order of magnitude higher than group 2 and group 3 orbits. The sharp change in the slope of group 1 orbit under high-charge plasma condition (near .3 orbital period epoch) corresponds to the body entering Earth's shadow region for the first time.

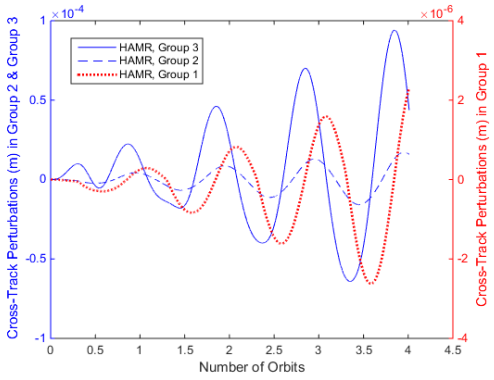

(a) Cross-Track Perturbations, Low-Charge Condition.

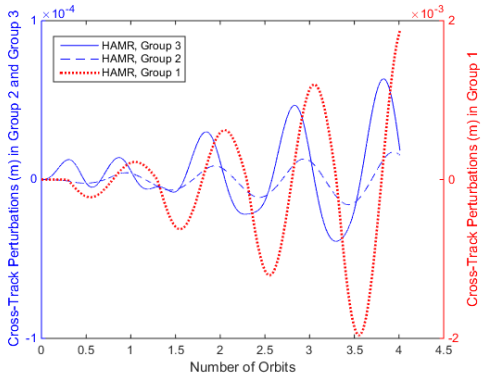

(b) Cross-Track Perturbations, High-Charge Condition.

Figure 3.5: Cross-track perturbations for Lorentz force perturbed GEO relative to Lorentz force excluded orbit (HAMR object).

Figs. 3.6(a), 3.6(b) show radial perturbations of Lorentz force included orbit relative to Lorentz force excluded orbit under low-charge and high-charge plasma conditions, respectively. Group 1 radial perturbation plots exhibit an increasing secular trend superimposed

with a periodic variation. The secular trend arises out of the increasing semi-major axis of Lorentz force included orbit relative to Lorentz force excluded orbit. The periodic variation in radial perturbations of group 1 orbit has a time-scale of approximately one day, and the amplitude of variation increases over time. Higher inclined group 2 and group 3 orbits have a small secular (increasing) trend because of increasing relative semi-major axis. Group 2 and group 3 orbits also have a periodic variation of one-day period with increasing amplitude. Also, group 3 orbits have larger amplitudes of variations compared to group 2 orbits. Under low-charge plasma conditions, group 1 orbit has radial perturbations of the order of 10^{-6} m, which is three orders of magnitude smaller than higher inclined group 2 and group 3 orbits. On the contrary, under high-charge plasma conditions, group 1 orbit has perturbations of the order of 10^{-2} m, which is an order of magnitude larger than higher inclined groups.

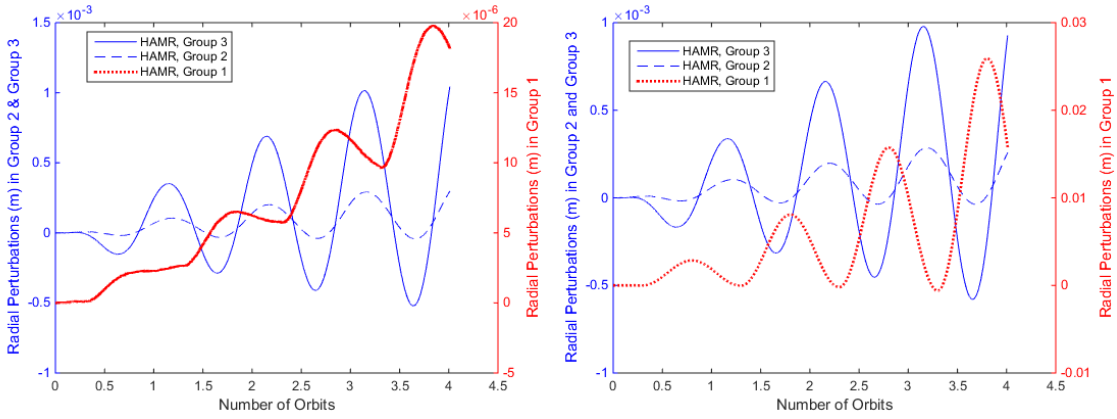

(a) Radial Perturbations, Low-Charge Condition.

(b) Radial Perturbations, High-Charge Condition.

Figure 3.6: Radial perturbations for Lorentz force perturbed orbit relative to Lorentz force excluded orbit (HAMR object).

Plots corresponding to LAMR objects in GEO are not included here because of their relatively small perturbation values when compared to that of HAMR objects. Table 5, however, lists the orders of in-track, cross-track, and radial perturbations of the Lorentz force included orbit relative to Lorentz force excluded orbit for LAMR objects.

Table 5: Orders of magnitude for in-track, cross-track and radial perturbations for LAMR objects in GEO over a period of four days.

GEO group	In-track Perturbations (m)	Cross-Track Perturbations (m)	Radial Perturbations (m)
Group 1	10^{-7}	10^{-9}	10^{-7}
Group 2	10^{-6}	10^{-7}	10^{-7}
Group 3	10^{-6}	10^{-7}	10^{-6}

3.2 Modeling Analytical Lorentz Force Perturbations in Keplerian Orbital Elements

Peng and Gao [21] proposed an elegant analytical technique for obtaining Lorentz perturbations using multiple coordinate frame transformations. Their closed-form expressions were derived by integrating GVE over one orbital period using a tilted magnetic dipole model under the assumption that the components of the dipole in the equatorial plane remain constant during one orbital period. This simplification makes their expressions valid only for low Earth orbit (LEO) region, where the orbital period is typically much smaller than the dipole rotation period of 24 hours. For the set-up given in Table 6, a comparison between Peng's analytical results and numerical results is shown in Fig. 3.7.

The research work carried out here extends the work by Peng and Gao [21]. New analytical formulas for Lorentz force perturbations are developed here that applies to both the LEO and higher Earth orbit regions, with special focus on geosynchronous Earth orbit (GEO) region. Two sets of formulas are derived, one that is applicable for small eccentric orbits and one that is applicable for large eccentric orbits.

Table 6: Simulation parameters for comparison between numerical and analytical methods for Lorentz force perturbation.

Parameter	Value
Initial Semi-major Axis	42164 km
Initial Eccentricity	.01
Initial Inclination	10^0
Initial AoP	$.1^0$
Initial RAAN	$.1^0$
Initial Epoch	2437582.5 JD
Propagation Period	15 years
Area	1 m^2
AMR	50 m^2/kg
Voltage	10^4 V
Capacitance	3.1387×10^{-11} F

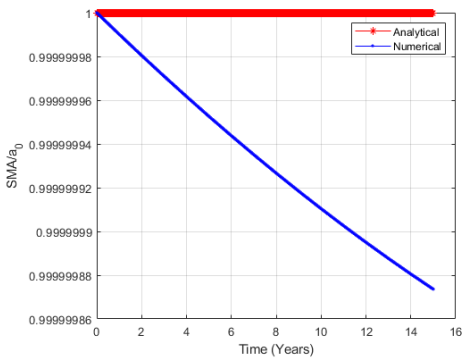

(a) Semi-Major Axis.

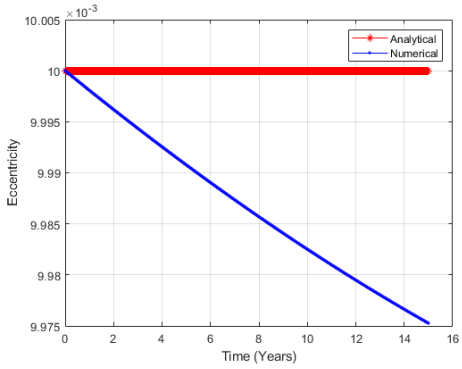

(b) Eccentricity.

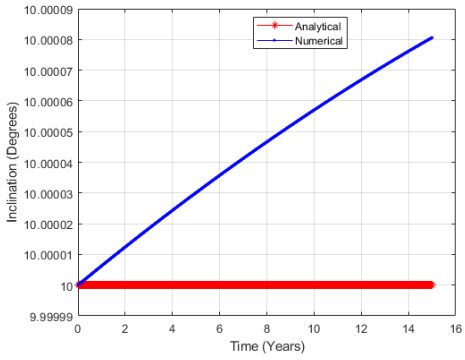

(c) Inclination.

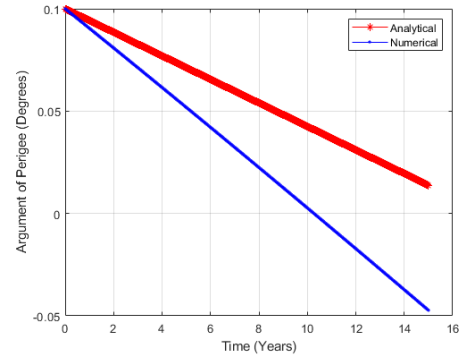

(d) Argument of Perigee.

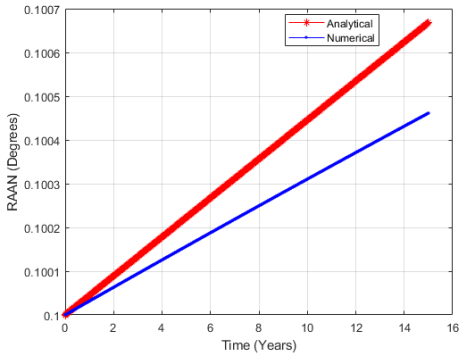

(e) RAAN.

Figure 3.7: Peng's analytical results versus numerical results for a GEO object subjected to Lorentz force perturbations.

3.2.1 Analytical Lorentz Perturbations for Small Eccentricities

The integration of GVEs requires the expressions for Lorentz acceleration components S, T, W, which can be obtained from Peng and Gao [21]. In their derivation, the authors start with the the expression for Lorentz acceleration, which is given by Eq. (131) (divided by object mass). Substituting for relative velocity expression into the definition of Lorentz acceleration, one obtains:

$$\vec{a}_L = \left(\frac{q}{m}\right)(-(\vec{\omega}_e \times \vec{r}) \times \vec{B} + \dot{\vec{r}} \times \vec{B}) \tag{188}$$

where $\vec{\omega}_e$ is the ECI angular velocity vector of Earth, $\vec{r}$ is the ECI position vector of the object, and $\dot{\vec{r}}$ is the ECI velocity vector of the object. q is the object charge, m is the object mass, and $\vec{B}$ represents the Earth magnetic field in ECI coordinates. Substituting the ECI magnetic field vector, angular velocity vector, position vector, dipole-direction unit vector ($\hat{\vec{N}}$), velocity vector, radial-direction unit vector ($\hat{\vec{r}}$) expressions:

$$\vec{B} = \frac{B_0}{r^3}\left[3(\hat{\vec{N}} \cdot \hat{\vec{r}})\hat{\vec{r}} - \hat{\vec{N}}\right] \tag{189a}$$

$$\vec{\omega}_e = [0 \;\; 0 \;\; \omega_e]^T \tag{189b}$$

$$\vec{r} = [x \;\; y \;\; z]^T \tag{189c}$$

$$\hat{\vec{N}} = [\hat{N}_x \;\; \hat{N}_y \;\; \hat{N}_z]^T \tag{189d}$$

$$\dot{\vec{r}} = [\dot{x} \;\; \dot{y} \;\; \dot{z}]^T \tag{189e}$$

$$\hat{\vec{r}} = \left[\frac{x}{r} \;\; \frac{y}{r} \;\; \frac{z}{r}\right]^T \tag{189f}$$

into Eq. (188), Peng and Gao [21] obtains the ECI components of Lorentz acceleration. In Eq. (189a), B_0 represents magnetic dipole moment of Earth, and in Eq. (189b), ω_e represents the angular rotational speed of the Earth. Subsequently, the authors perform two coordinate transformations to convert the ECI acceleration components to S-T-W acceleration components. The first transformation is performed from the ECI coordinate system to an intermediate frame, and the second transformation is performed from the intermediate frame to the S-T-W frame. The expressions for S, T, W, as obtained by Peng and Gao [21] after the transformations are as follows:

$$\begin{aligned} S = {} & \left(\frac{q}{m}\right) B_0 \left[- \frac{\omega_e}{r^2} (\sin u \cos u \sin i) \right] \hat{N}_x(t) + \left(\frac{q}{m}\right) B_0 \Bigg(\frac{na}{r^3 \sqrt{1-e^2}} \\ & [\sin i (1 + e \cos f)] - \frac{\omega_e}{r^2} (\sin^2 u \sin i \cos i) \Bigg) \hat{N}_y(t) + \left(\frac{q}{m}\right) B_0 \\ & \left(- \frac{na}{r^3 \sqrt{1-e^2}} [\cos i (1 + e \cos f)] + \frac{\omega_e}{r^2} (1 - \sin^2 u \sin^2 i) \right) \hat{N}_z \end{aligned} \tag{190a}$$

$$\begin{aligned} T = {} & \left(\frac{q}{m}\right) B_0 \left(\frac{\omega_e}{r^2} (2 \cos^2 u \sin i) \right) \hat{N}_x(t) + \left(\frac{q}{m}\right) B_0 \\ & \left(\frac{na}{r^3 \sqrt{1-e^2}} (-e \sin i \sin f) + \frac{\omega_e}{r^2} (\sin 2u \sin i \cos i) \right) \hat{N}_y(t) \\ & + \left(\frac{q}{m}\right) B_0 \left(\frac{na}{r^3 \sqrt{1-e^2}} (e \cos i \sin f) + \frac{\omega_e}{r^2} (\sin 2u \sin^2 i) \right) \hat{N}_z \end{aligned} \tag{190b}$$

$$\begin{aligned} W = {} & \left(\frac{q}{m}\right) B_0 \Bigg(\frac{na(-3e \cos u \cos f - 2 \cos u + e \cos \omega)}{r^3 \sqrt{1-e^2}} \\ & + \frac{\omega_e (2 \cos u \cos i)}{r^2} \Bigg) \hat{N}_x(t) + \left(\frac{q}{m}\right) B_0 \Bigg(\frac{na}{r^3 \sqrt{1-e^2}} \cos i \\ & (-3e \sin u \cos f - 2 \sin u + e \sin \omega) + \frac{\omega_e}{r^2} (2 \sin u \cos^2 i) \Bigg) \hat{N}_y(t) \\ & + \left(\frac{q}{m}\right) B_0 \Bigg(- \frac{na \sin i [e \sin \omega + 4 \sin u + 3e \sin (u + f)]}{2r^3 \sqrt{1-e^2}} \\ & + \frac{\omega_e (\sin 2i \sin u)}{r^2} \Bigg) \hat{N}_z \end{aligned} \tag{190c}$$

where u is the argument of latitude, i.e., the summation of the argument of perigee and true anomaly. The components of the dipole-direction unit vector in Eq. (190) are obtained via the use of following equations [21, 56]:

$$[\hat{N}_x \;\; \hat{N}_y \;\; \hat{N}_z]^T = [\sin\theta_m \cos\alpha_m \;\; \sin\theta_m \sin\alpha_m \;\; \cos\theta_m]^T \tag{191a}$$

$$\cos\theta_m = \frac{g_1^0}{\sqrt{(g_1^0)^2 + (g_1^1)^2 + (h_1^1)^2}} \tag{191b}$$

$$\alpha_m = \alpha_{G0} + \omega_e t + \phi_m - \Omega \tag{191c}$$

$$\tan\phi_m = \frac{h_1^1}{g_1^1} \tag{191d}$$

where θ_m represents the angle between dipole north pole and geographic north pole, α_{G0} represents the right ascension of Greenwich at reference time, which is set as the beginning of integration period in this research, ϕ_m represents the east longitude of the dipole, and g_1^0, g_1^1, h_1^1 represent 12th Generation International Geomagnetic Reference Field (IGRF) coefficients [75]. The magnetic dipole moment can be obtained from the IGRF coefficients as [56]:

$$B_0 = R_E^3 \sqrt{(g_1^0)^2 + (g_1^1)^2 + (h_1^1)^2} \tag{192}$$

where R_E is the equatorial radius of the Earth. As a final step, Peng and Gao [21] substitute back the expressions for Lorentz acceleration components from Eq. (190) into the GVEs [Eq. (1)] to obtain their closed-form perturbation expressions.

In their integration of GVEs, Peng and Gao [21] assumed that the equatorial components of the dipole-direction unit vector, i.e., $\hat{N}_x(t)$ and $\hat{N}_y(t)$ remain constant during the integration period. The rationale behind the approximation is that, for low Earth orbits, the orbital periods are much smaller compared to Earth rotation period, and hence, one can roughly state that the dipole does not rotate at all in the inertial space during the integration period of one orbital period. This assumption is not valid for higher Earth orbits (orbits beyond LEO), where the orbital periods are of the same or larger orders as compared to the Earth orbital period. This research work gets rid of the aforementioned approximation, and hence, provides closed-form expressions valid for both low Earth orbit and higher Earth

orbit regions. To facilitate analytical integrability, following two approximations are made:

1. Eccentricity is assumed to be small, which leads to the approximation of time in terms of mean motion and true anomaly as:

$$t \approx \frac{f}{n} \tag{193}$$

The above assumption comes from discarding the eccentricity terms in the Fourier expansion of true anomaly [76]:

$$f = M + \left(2e - \frac{1}{4}e^3\right)\sin M + \frac{5}{4}e^2 \sin 2M + \frac{13}{12}e^3 \sin 3M + \mathcal{O}(e^4) \tag{194}$$

where mean anomaly $M = nt$.

2. Since eccentricity is assumed to be small, the factor $(1+e\cos f)^{-1}$, which is introduced in the derivation via the conic or orbit equation, can be approximated using Taylor series of order two as:

$$\frac{1}{1+e\cos f} \approx 1 - e\cos f + e^2 \cos^2 f \tag{195}$$

The other approximations which are assumed in this research work (as well as in [21]) are - (1) charge-to-mass ratio, q/m, is constant (2) the orbital elements $[a, e, i, \omega, \Omega]$ remain constant during the integration period. For the integrations of GVEs, the independent variable of choice is taken as true anomaly. Hence, it is imperative to change the independent variable in GVEs from time to true anomaly. This is obtained using the following relations:

$$\Delta x = \int_0^{2\pi} \left(\frac{dx}{dt}\frac{dt}{df}\right) df \quad ; \quad x :: [a, e, i, \omega, \Omega] \tag{196a}$$

$$\frac{dt}{df} = \frac{1}{n}\left(\frac{r}{a}\right)^2 \frac{1}{\sqrt{1-e^2}} \tag{196b}$$

It is to be noted that in Eq. (196b) one should ideally include the explicit effects of Lorentz acceleration, but the errors introduced due to this approximation are of second or higher orders, and hence, the approximation is justifiable. The elegance of the assumed approx-

imations is that all the integrands can be written nicely as sine and cosine trigonometric functions of the independent variable using little trigonometric manipulations. Further simplification is obtained as a result of the integration limits being from 0 to 2π, which pushes many periodic sine and cosine terms to zero. After much simplification in the integration process, the following simple expressions are obtained for orbital element changes over one period:

$$\begin{aligned}\Delta a = C_{80}\Big[\sin\left(2\omega - \alpha_{G0} - \frac{2\pi\omega_e}{n} + \Omega - \phi_m\right) - \sin\left(2\omega - \alpha_{G0} + \Omega - \phi_m\right)\Big] \\ + C_{81}\Big[\sin(2\omega + \alpha_{G0} + \frac{2\pi\omega_e}{n} - \Omega + \phi_m) - \sin\left(2\omega + \alpha_{G0} - \Omega + \phi_m\right)\Big] \\ + C_{82}\Big[\sin\left(\alpha_{G0} + \frac{2\pi\omega_e}{n} - \Omega + \phi_m\right) - \sin\left(\alpha_{G0} - \Omega + \phi_m\right)\Big] \quad (197)\end{aligned}$$

$$\begin{aligned}\Delta e = D_{110}\Big[\sin\left(2\omega + \alpha_{G0} + \frac{2\pi\omega_e}{n} - \Omega + \phi_m\right) - \sin\left(2\omega + \alpha_{G0} - \Omega + \phi_m\right)\Big] \\ + D_{111}\Big[\sin(2\omega - \alpha_{G0} - \frac{2\pi\omega_e}{n} + \Omega - \phi_m) - \sin\left(2\omega - \alpha_{G0} + \Omega - \phi_m\right)\Big] \\ + D_{112}\Big[\sin\left(\alpha_{G0} + \frac{2\pi\omega_e}{n} - \Omega + \phi_m\right) - \sin\left(\alpha_{G0} - \Omega + \phi_m\right)\Big] \\ + \frac{D_{105_4}\pi}{na^2\sqrt{1-e^2}}\sin 2\omega \quad (198)\end{aligned}$$

$$\begin{aligned}\Delta i = J_1\Big[\sin\left(2\omega + \alpha_{G0} + \frac{2\pi\omega_e}{n} - \Omega + \phi_m\right) - \sin\left(2\omega + \alpha_{G0} - \Omega + \phi_m\right)\Big] \\ + J_2\Big[\sin(2\omega - \alpha_{G0} - \frac{2\pi\omega_e}{n} + \Omega - \phi_m) - \sin\left(2\omega - \alpha_{G0} + \Omega - \phi_m\right)\Big] \\ + J_3\Big[\sin\left(\alpha_{G0} + \frac{2\pi\omega_e}{n} - \Omega + \phi_m\right) - \sin\left(\alpha_{G0} - \Omega + \phi_m\right)\Big] \\ + H_4\Big[\cos\left(\omega + \alpha_{G0} + \frac{2\pi\omega_e}{n} - \Omega + \phi_m\right) - \cos\left(\omega + \alpha_{G0} - \Omega + \phi_m\right)\Big] \\ + H_5\Big[\cos(\omega - \alpha_{G0} - \frac{2\pi\omega_e}{n} + \Omega - \phi_m) - \cos\left(\omega - \alpha_{G0} + \Omega - \phi_m\right)\Big] \\ + E_{202}\Big[\sin\left(\omega + \alpha_{G0} + \frac{2\pi\omega_e}{n} - \Omega + \phi_m\right) - \sin\left(\omega + \alpha_{G0} - \Omega + \phi_m\right)\Big] \\ + E_{203}\Big[\sin\left(\omega - \alpha_{G0} - \frac{2\pi\omega_e}{n} + \Omega - \phi_m\right) - \sin\left(\omega - \alpha_{G0} + \Omega - \phi_m\right)\Big]\end{aligned}$$

$$+\frac{\pi\sin 2\omega}{na^2\sqrt{1-e^2}}I_{12} \quad (199)$$

$$\begin{aligned}
\Delta\omega = {} & Q_{142}\left[\cos\left(2\omega+\alpha_{G0}+\frac{2\pi\omega_e}{n}-\Omega+\phi_m\right)-\cos\left(2\omega+\alpha_{G0}-\Omega+\phi_m\right)\right] \\
& + Q_{143}\left[\cos(2\omega-\alpha_{G0}-\frac{2\pi\omega_e}{n}+\Omega-\phi_m)-\cos\left(2\omega-\alpha_{G0}+\Omega-\phi_m\right)\right] \\
& + Q_{144}\left[\cos\left(\alpha_{G0}+\frac{2\pi\omega_e}{n}-\Omega+\phi_m\right)-\cos\left(\alpha_{G0}-\Omega+\phi_m\right)\right]+ \\
& Q_{145}\left[\cos\left(\omega+\alpha_{G0}+\frac{2\pi\omega_e}{n}-\Omega+\phi_m\right)-\cos\left(\omega+\alpha_{G0}-\Omega+\phi_m\right)\right] \\
& + Q_{146}\left[\cos(\omega-\alpha_{G0}-\frac{2\pi\omega_e}{n}+\Omega-\phi_m)-\cos\left(\omega-\alpha_{G0}+\Omega-\phi_m\right)\right] \\
& + Q_{147}\left[\sin\left(\omega+\alpha_{G0}+\frac{2\pi\omega_e}{n}-\Omega+\phi_m\right)-\sin\left(\omega+\alpha_{G0}-\Omega+\phi_m\right)\right] \\
& + Q_{148}\left[\sin\left(\omega-\alpha_{G0}-\frac{2\pi\omega_e}{n}+\Omega-\phi_m\right)-\sin\left(\omega-\alpha_{G0}+\Omega-\phi_m\right)\right] \\
& + \frac{Q_{149}\pi}{na^2\sqrt{1-e^2}}\left[K_{11}+K_{13}\sin\omega\right]+\frac{2\pi Q_{150}}{na^2\sqrt{1-e^2}}\left[\frac{K_{12}}{2}+K_2\sin\omega+K_{14}\sin^2\omega\right] \\
& + \frac{\pi Q_{151}}{na^2\sqrt{1-e^2}}\left[K_{15}-K_{11}\cos 2\omega+K_{13}\sin\omega\right] \\
& + \frac{\pi}{na^2\sqrt{1-e^2}}\left[Q_{43}+Q_{131}Q_{133}+\frac{Q_{131}Q_{134}e}{2}+Q_{132}Q_{134}\cos 2\omega\right] \quad (200)
\end{aligned}$$

$$\begin{aligned}
\Delta\Omega = {} & N_1\left[\cos\left(2\omega+\alpha_{G0}+\frac{2\pi\omega_e}{n}-\Omega+\phi_m\right)-\cos\left(2\omega+\alpha_{G0}-\Omega+\phi_m\right)\right] \\
& + N_2\left[\cos(2\omega-\alpha_{G0}-\frac{2\pi\omega_e}{n}+\Omega-\phi_m)-\cos\left(2\omega-\alpha_{G0}+\Omega-\phi_m\right)\right] \\
& + N_3\left[\cos\left(\alpha_{G0}+\frac{2\pi\omega_e}{n}-\Omega+\phi_m\right)-\cos\left(\alpha_{G0}-\Omega+\phi_m\right)\right] \\
& + L_{177}\left[\cos\left(\omega+\alpha_{G0}+\frac{2\pi\omega_e}{n}-\Omega+\phi_m\right)-\cos\left(\omega+\alpha_{G0}-\Omega+\phi_m\right)\right]
\end{aligned}$$

$$+ L_{178}\left[\cos(\omega - \alpha_{G0} - \frac{2\pi\omega_e}{n} + \Omega - \phi_m) - \cos(\omega - \alpha_{G0} + \Omega - \phi_m)\right]$$
$$+ J_{180}\left[\sin(\omega + \alpha_{G0} + \frac{2\pi\omega_e}{n} - \Omega + \phi_m) - \sin(\omega + \alpha_{G0} - \Omega + \phi_m)\right]$$
$$+ J_{181}\left[\sin(\omega - \alpha_{G0} - \frac{2\pi\omega_e}{n} + \Omega - \phi_m) - \sin(\omega - \alpha_{G0} + \Omega - \phi_m)\right]$$
$$+ \frac{K_6\pi}{na^2\sqrt{1-e^2}}\left[K_{11} + K_{13}\sin\omega\right] + \frac{2\pi K_9}{na^2\sqrt{1-e^2}}\left[\frac{K_{12}}{2} + K_2\sin\omega + K_{14}\sin^2\omega\right]$$
$$+ \frac{\pi K_{10}}{na^2\sqrt{1-e^2}}\left[K_{15} - K_{11}\cos 2\omega + K_{13}\sin\omega\right] \quad (201)$$

where the expressions for the coefficients appearing in Eqs. (197)-(201) are given in Appendix B. Some of the coefficients blow up for the exact geostationary altitude. The presence of the term $(\omega_e/n - 1)$ in the denominator can be solved by obtaining the limiting value:

$$[\Delta x]_{GEO} = \lim_{n\to\omega_e} \Delta x \quad ; \quad x :: [a, e, i, \omega, \Omega] \quad (202)$$

The limiting expressions for geostationary altitude are given as:

$$\Delta a_{GEO} = B_0\pi\left(\frac{q}{m}\right)\frac{\omega_e a \sin i \sin\theta_m \cos^2\frac{i}{2} e}{\mu(1-e^2)}\cos(2\omega - \alpha_{G0} + \Omega - \phi_m)$$
$$+ B_0\pi\left(\frac{q}{m}\right)\frac{\sin i \sin\theta_m e}{na^2(1-e^2)}(2 - \cos i)\cos(\alpha_{G0} - \Omega + \phi_m)$$
$$- \frac{1}{2}B_0\pi\left(\frac{q}{m}\right)\frac{\sin i \sin\theta_m e^3}{na^2(1-e^2)^{\frac{5}{2}}}\cos(\alpha_{G0} - \Omega + \phi_m) \quad (203)$$

$$\Delta e_{GEO} = B_0\pi\left(\frac{q}{m}\right)\frac{\omega_e \sin i \sin\theta_m \sin^2\frac{i}{2} e^2}{4\mu}\cos(2\omega + \alpha_{G0} - \Omega + \phi_m)$$
$$- \frac{B_0\pi}{\mu}\left(\frac{q}{m}\right)\sin i \sin\theta_m \cos^2\frac{i}{2}\omega_e\left(\frac{e^2}{4} - \frac{3}{2}\right)\cos(2\omega - \alpha_{G0} + \Omega - \phi_m)$$
$$+ \frac{B_0\pi}{a^3 n(1-e^2)^{\frac{3}{2}}}\left(\frac{q}{m}\right)\sin i \sin\theta_m\left(1 - e^2 - \frac{e^4}{4}\right)\cos(\alpha_{G0} - \Omega + \phi_m)$$
$$- \frac{B_0\pi}{a^3 n}\left(\frac{q}{m}\right)\sin i \sin\theta_m\left(\frac{e^2}{4} - 2 + \frac{\cos i}{2}\right)\cos(\alpha_{G0} - \Omega + \phi_m)$$
$$- \frac{B_0\omega_e}{\mu}\frac{q}{m}\cos\theta_m \sin^2 i\left(-e^3 + \frac{e}{2}\right)\pi\sin 2\omega \quad (204)$$

$$\Delta i_{GEO} = -B_0\pi\left(\frac{q}{m}\right)\frac{\sin\theta_m e^3\sin^2\frac{i}{2}}{4a^3n(1-e^2)^{\frac{3}{2}}}\cos\left(2\omega+\alpha_{G0}-\Omega+\phi_m\right)$$
$$-\left(\frac{B_0\pi q}{m}\right)\frac{\sin\theta_m\cos^2\frac{i}{2}e(\cos i\left(-\frac{e^2}{2}+\frac{3}{2}\right)+\frac{3e^2}{4}+\frac{3}{2})}{2a^3n(1-e^2)^{\frac{3}{2}}\cos^2\frac{i}{2}}\cos\left(2\omega-\alpha_{G0}+\Omega-\phi_m\right)$$
$$-B_0\pi\left(\frac{q}{m}\right)\frac{\sin\theta_m\cos i\cos^2\frac{i}{2}\omega_e e}{a^3n^2}\cos\left(2\omega-\alpha_{G0}+\Omega-\phi_m\right)$$
$$-B_0\pi\left(\frac{q}{m}\right)\frac{3\sin\theta_m e\left(1+\frac{e^2}{2}\right)}{2a^3n(1-e^2)^{\frac{3}{2}}}\cos\left(\alpha_{G0}-\Omega+\phi_m\right)$$
$$-B_0\pi\left(\frac{q}{m}\right)\frac{\sin\theta_m\cos i\omega_e e}{a^3n^2}\cos\left(\alpha_{G0}-\Omega+\phi_m\right)$$
$$-B_0\pi\left(\frac{q}{m}\right)\frac{e\cos i\sin\omega\sin\theta_m}{a^3n(1-e^2)^{\frac{3}{2}}}\sin\left(\omega-\alpha_{G0}+\Omega-\phi_m\right)$$
$$+B_0\pi\left(\frac{q}{m}\right)\frac{e\cos\omega\sin\theta_m}{a^3n(1-e^2)^{\frac{3}{2}}}\cos\left(\omega-\alpha_{G0}+\Omega-\phi_m\right)$$
$$+B_0\pi\left(\frac{q}{m}\right)\frac{\sin\left(2\omega\right)e^2\cos\theta_m}{4a^3n}\left[-\frac{3e^2\sin i}{2(1-e^2)^{\frac{3}{2}}}+\sin\left(2i\right)\right] \quad (205)$$

$$\Delta\Omega_{GEO} = -\frac{\pi B_0 e^3 q\sin\theta_m\sin^2\frac{i}{2}}{4a^3mn\sin i(1-e^2)^{\frac{3}{2}}}\sin\left(2\omega+\alpha_{G0}-\Omega+\phi_m\right)$$
$$-\frac{3\pi B_0 eq\sin\theta_m\cos^2\frac{i}{2}(1+\frac{e^2}{2})}{2a^3mn\sin i(1-e^2)^{\frac{3}{2}}}\sin\left(2\omega-\alpha_{G0}+\Omega-\phi_m\right)$$
$$-\frac{\pi B_0 eq\sin\theta_m\cos i\cos^2\frac{i}{2}}{a^3mn\sin i}\sin\left(2\omega-\alpha_{G0}+\Omega-\phi_m\right)$$
$$-\frac{3\pi B_0 eq\sin\theta_m\cos i(1+\frac{e^2}{2})}{2a^3mn\sin i(1-e^2)^{\frac{3}{2}}}\sin\left(\alpha_{G0}-\Omega+\phi_m\right)$$
$$-\frac{\pi B_0 eq\sin\theta_m\cos^2 i}{a^3mn\sin i}\sin\left(\alpha_{G0}-\Omega+\phi_m\right)$$
$$+\frac{\pi B_0 eq\cos\omega\sin\theta_m}{a^3mn\sin i(1-e^2)^{\frac{3}{2}}}\sin\left(\omega-\alpha_{G0}+\Omega-\phi_m\right)$$
$$+\frac{\pi B_0 eq\cos i\sin\omega\sin\theta_m}{a^3mn\sin i(1-e^2)^{\frac{3}{2}}}\cos\left(\omega-\alpha_{G0}+\Omega-\phi_m\right)$$
$$-\frac{(\frac{e^2}{2}+1)\pi B_0 q\cos\theta_m}{na^3m(1-e^2)^{\frac{3}{2}}}\left[2+\frac{3e^2}{4}-2\cos i(1-e^2)^{\frac{3}{2}}+\frac{e^2\sin^2\omega}{2}\right]$$
$$+\frac{\pi e^2 B_0 q\cos\theta_m}{2na^3m(1-e^2)^{\frac{3}{2}}}\left[\frac{5}{2}+3\sin^2\omega\right]$$

$$- \frac{\pi e^2 B_0 q \cos\theta_m}{4na^3 m(1-e^2)^{\frac{3}{2}}}\left[\frac{3e^2}{4} - 2\cos 2\omega - \frac{3e^2\cos 2\omega}{4} + 2\cos i(1-e^2)^{\frac{3}{2}}\cos 2\omega + \frac{e^2\sin^2\omega}{2}\right] \quad (206)$$

$$\begin{aligned}
\Delta\omega_{GEO} = & -\frac{B_0 q e\pi \sin\theta_m \sin^2\frac{i}{2}}{4a^3 mn}\left(-\frac{e^2\cos i}{\sin i(1-e^2)^{\frac{3}{2}}} + \sin i\right) \\
& \sin(2\omega + \alpha_{G0} - \Omega + \phi_m) + \frac{2\pi B_0 q \sin\theta_m \cos^2\frac{i}{2}}{a^3 mn}\left[\frac{3e\cos i(1+\frac{e^2}{2})}{4\sin i(1-e^2)^{\frac{3}{2}}} + \frac{e\cos^2 i}{2\sin i}\right. \\
& \left. - \frac{(3+\frac{e^2}{2})\sin i}{4e}\right]\sin(2\omega - \alpha_{G0} + \Omega - \phi_m) - \frac{2\pi B_0 q\sin\theta_m}{a^3 mn}\sin(\alpha_{G0} - \Omega + \phi_m) \\
& \left[-\frac{3e\cos^2 i(1+\frac{e^2}{2})}{4\sin i(1-e^2)^{\frac{3}{2}}} - \frac{e\cos^3 i}{2\sin i} + \frac{\sin i(\frac{e^3}{8}+e+\frac{1}{e})}{2(1-e^2)^{\frac{3}{2}}} + \frac{\sin i(\frac{e^2}{4}+2-\frac{\cos i}{2})}{2e}\right] \\
& - \frac{\pi B_0 eq\cos\omega\sin\theta_m\cos i}{a^3 mn\sin i(1-e^2)^{\frac{3}{2}}}\sin(\omega - \alpha_{G0} + \Omega - \phi_m) \\
& - \frac{\pi B_0 eq\cos^2 i\sin\omega\sin\theta_m}{a^3 mn\sin i(1-e^2)^{\frac{3}{2}}}\cos(\omega - \alpha_{G0} + \Omega - \phi_m) \\
& + \frac{(\frac{e^2}{2}+1)\pi B_0 q\cos\theta_m\cos i}{na^3 m(1-e^2)^{\frac{3}{2}}}\left[2 + \frac{3e^2}{4} - 2\cos i(1-e^2)^{\frac{3}{2}} + \frac{e^2\sin^2\omega}{2}\right] \\
& - \frac{\pi e^2 B_0 q\cos\theta_m\cos i}{2na^3 m(1-e^2)^{\frac{3}{2}}}\left[\frac{5}{2} + 3\sin^2\omega\right] + \frac{\pi e^2 B_0 q\cos\theta_m\cos i}{4na^3 m(1-e^2)^{\frac{3}{2}}}\left[\frac{3e^2}{4} - 2\cos 2\omega\right. \\
& \left. - \frac{3e^2\cos 2\omega}{4} + 2\cos i(1-e^2)^{\frac{3}{2}}\cos 2\omega + \frac{e^2\sin^2\omega}{2}\right] \\
& + \frac{\pi B_0 q\cos\theta_m}{na^3 m(1-e^2)^{\frac{3}{2}}}\left[4\cos i - \frac{\cos 2\omega\sin^2 i(1-e^2)^{\frac{3}{2}}}{2}\right] \quad (207)
\end{aligned}$$

Although not included here, simplified formulas can also be obtained for low Earth orbits by using the approximations $\omega_e << n$ and $e^2 << 1$ in Eqs. (197)-(201).

Fig. 3.8 shows how the analytical results developed here compare to the numerical simulation for the set-up given in Table 6. Figs. 3.8(a)-(b) compare the temporal evolution of semi-major axis, Figs. 3.8(c)-(d) compare eccentricity, Figs. 3.8(e)-(f) compare inclination, Figs. 3.8(g)-(h) compare argument of perigee, and Figs. 3.8(i)-(j) compare RAAN. The analytical semi-major axis, eccentricity, inclination, argument of perigee, and RAAN are

able to follow the secular trend of the numerical orbital elements within an accuracy of the order of 10^{-4} km, 10^{-8}, 10^{-8} degrees, 10^{-5} degrees, 10^{-5} degrees, respectively, for the assumed period.

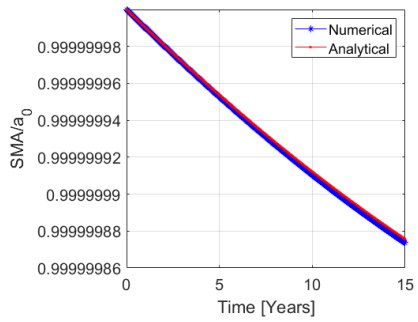

(a) Semi-Major Axis.

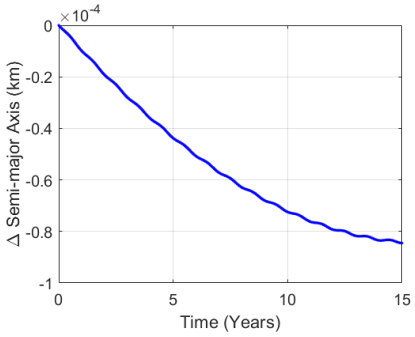

(b) Δ Semi-Major Axis.

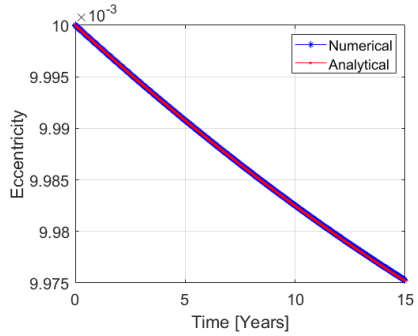

(c) Eccentricity.

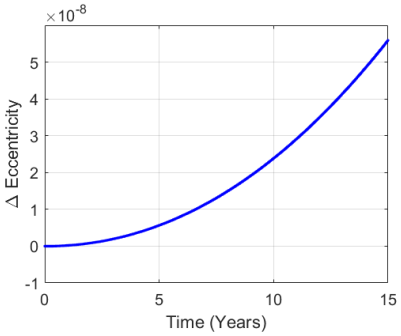

(d) Δ Eccentricity.

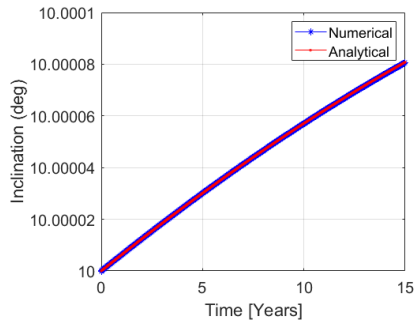

(e) Inclination.

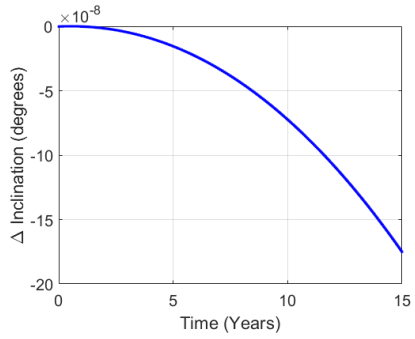

(f) Δ Inclination.

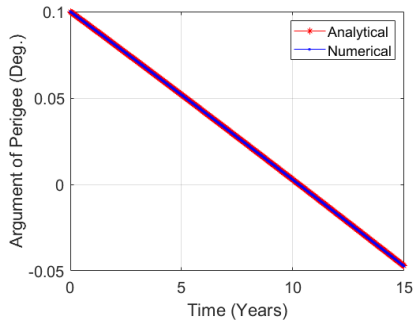

(g) Argument of Perigee.

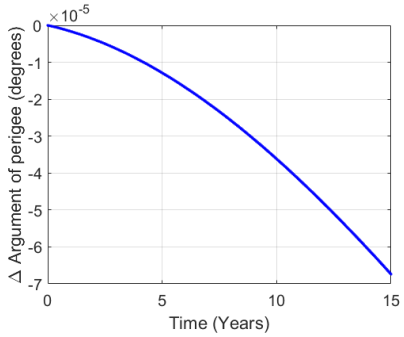

(h) Δ Argument of Perigee.

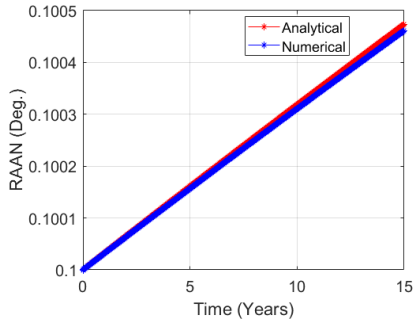

(i) RAAN

ytically

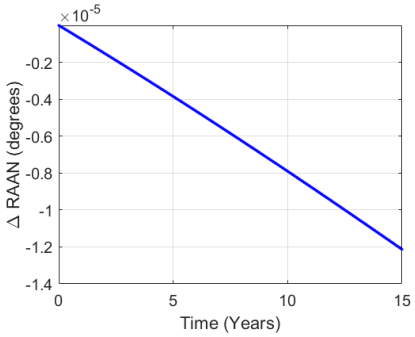

(j) Δ RAAN

Figure 3.8: Comparison between analytical and numerical simulations for a Keplerian orbit perturbed by Lorentz force.

3.2.2 Analytical Lorentz Perturbations for Large Eccentricities

The analytical formulas developed in section 3.2.1 are based on the assumption of near-zero eccentricity. This section is devoted to the development of analytical formulas applicable to all eccentricity values. Explicit expressions for the perturbations in orbital elements are not given here, and only the procedure for the derivation is discussed.

If one were to substitute the expressions for GVEs [Eq. (1)] into Eq. (196) with S, T, W given by Eq. (190), and simplify, one would eventually arrive at integrals of the form:

$$I = \int_0^{2\pi} \cos\left(\aleph_1 + \aleph_2 f \pm \omega_e t\right) df \tag{208}$$

where $\aleph_j$ $(j = 1 : 2)$ are parameters that can be assumed constant over the integration period, ω_e represents Earth rotation rate, t represents time, and f represents true anomaly.

For analytically integrating the integrand in Eq. 208, the time t needs to be written as a function of independent variable f. Integration of Eq. (196b) w.r.t. the independent variable f, after some trigonometric manipulation, results in:

$$t = \frac{2}{n}\Bigg[\tan^{-1}\left(\sqrt{\frac{1+e}{1-e}}\tan\frac{f}{2}\right) - e\sin\left(\tan^{-1}\left(\sqrt{\frac{1+e}{1-e}}\tan\frac{f}{2}\right)\right) \cos\left(\tan^{-1}\left(\sqrt{\frac{1+e}{1-e}}\tan\frac{f}{2}\right)\right)\Bigg] \tag{209}$$

When substituting Eq. (209) into Eq. (208), it is important to take the quadrant ambiguity of inverse tangent function into consideration. Eq. (208) can thus be re-written as:

$$I = \int_0^{2\pi} \cos\Bigg(\aleph_1 + \aleph_2 f \pm \omega_e \cdot \frac{2}{n}\Bigg[\pi \cdot floor\left(\frac{f}{\pi+\epsilon}\right) + \tan^{-1}\left(\sqrt{\frac{1+e}{1-e}}\tan\frac{f}{2}\right) - e\sin\left(\tan^{-1}\left(\sqrt{\frac{1+e}{1-e}}\tan\frac{f}{2}\right)\right) \cos\left(\tan^{-1}\left(\sqrt{\frac{1+e}{1-e}}\tan\frac{f}{2}\right)\right)\Bigg]\Bigg) df \tag{210}$$

where ϵ is an arbitrarily selected positive number and $\epsilon \to 0$. Floor(x) is a function that rounds the input x to the nearest integer towards $-\infty$. The above integral is then approximated using 12^{th} order Legendre-Gauss quadrature rule [6] as given in Eq. (211). A quadrature order analysis starting from 1^{st} order up to 15^{th} order is carried out for determining the optimal order.

$$I = \int_0^{2\pi} F(f)df = \sum_{k=1}^{12} w_k F(f_k) \tag{211}$$

where F represents the integrand in Eq. (210). The weights w_k and the true anomaly values f_k (nodes) between 0 and 2π at which the integrand is evaluated are listed in Table 7.

A 15-year simulation is carried out for a uniform spherical GEO object in the presence of the Lorentz perturbation force. Orbital elements' evolution from the analytical technique is compared to the numerical results for validation. Table 8 lists the orbital, charging, and

[6] Winckel, G. von, "Legendre-gauss Quadrature Weights and Nodes," 2004 (available online)

Table 7: Weights and nodes for the Legendre-Gauss quadrature rule.

w_k	f_k (degrees)
0.1482	356.6809
0.3360	342.7411
0.5029	318.5825
0.6383	285.7172
0.7335	246.2097
0.7827	202.5420
0.7827	157.4580
0.7335	113.7903
0.6383	74.2828
0.5029	41.4175
0.3360	17.2589
0.1482	3.3191

design parameters used in the simulation.

Table 8: Orbital, charging, and design parameters

Parameter	Value
Initial Semi-Major Axis	42164 km
Initial Eccentricity	.4
Initial Inclination	10^0
Initial AoP	$.1^0$
Initial RAAN	$.1^0$
Object Capacitance	3.1387×10^{-11} F
Voltage	10^4 V
Object Area	1 m^2
AMR	50 m^2/kg
Initial Epoch	2437582.5 JD
Propagation Period	15 Years

Fig. 3.9 shows how the analytical results compare to the numerical simulation for large eccentric orbit. Figs. 3.9(a)-(b) compare the temporal evolution of semi-major axis, Figs. 3.9(c)-(d) compare the temporal evolution of eccentricity, Figs. 3.9(e)-(f) compare the temporal evolution of inclination, Figs. 3.9(g)-(h) compare the temporal evolution of argument of perigee, and Figs. 3.9(i)-(j) compare the temporal evolution of RAAN.

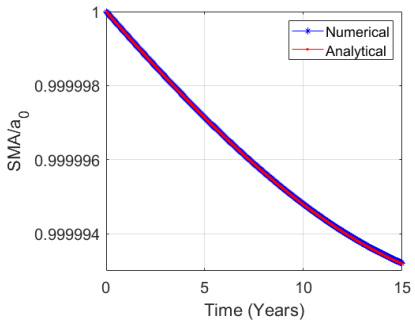

(a) Semi-Major Axis.

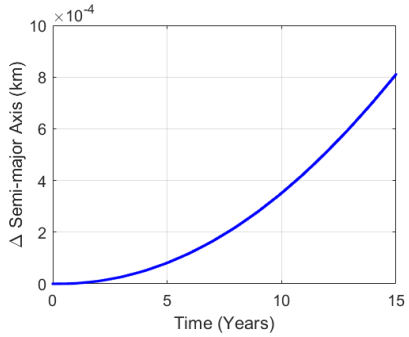

(b) Δ Semi-Major Axis.

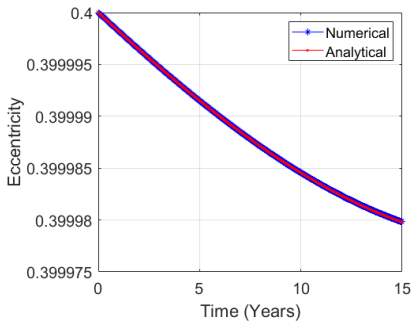

(c) Eccentricity.

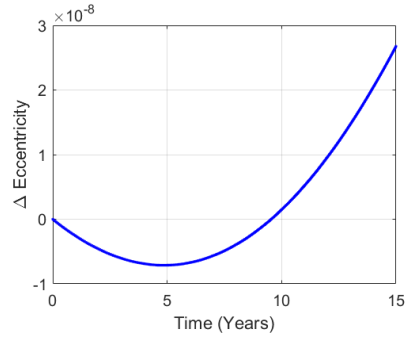

(d) Δ Eccentricity.

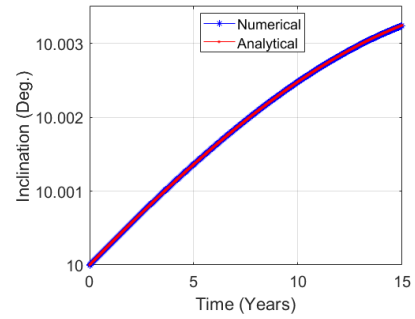

(e) Inclination.

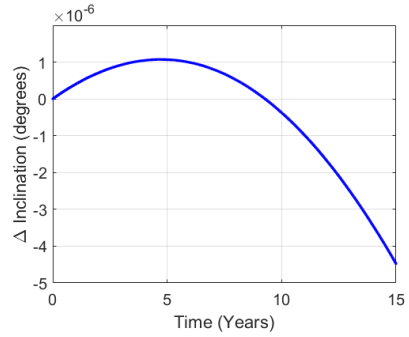

(f) Δ Inclination.

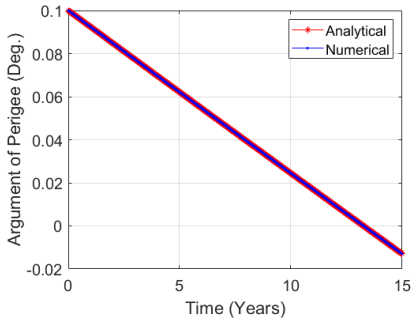

(g) Argument of Perigee.

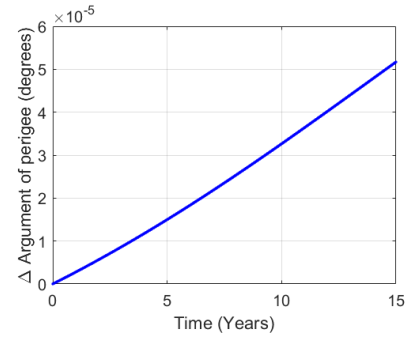

(h) Δ Argument of Perigee.

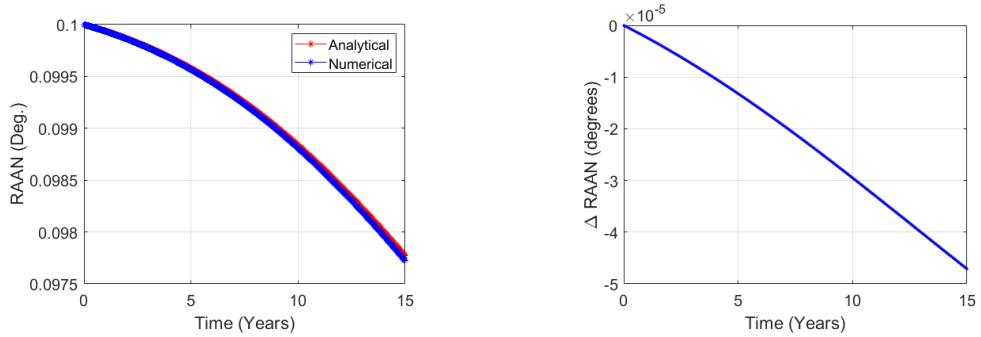

(i) RAAN. **(j)** Δ RAAN.

Figure 3.9: Comparison between analytical and numerical simulations for a Keplerian orbit perturbed by Lorentz force (large eccentricity).

3.3 Concluding Remarks

To conclude, the Lorentz perturbations exhibit secular or additive behavior in the long-term (order of decades). In a high-charge environment, the additive effect is significant and cannot be ignored whereas in a calm low-charge environment, the effects of Lorentz force on orbital elements can be ignored depending upon the accuracy level sought for the application. Especially, non-conservative perturbation forces like Lorentz force are important for objects with a high area-to-mass ratio. The main gains from this chapter are a comprehensive methodology for determining object charge and an analytical set of formulas for computing Lorentz perturbations for both the important LEO and GEO regions.

4 ANALYTICAL UNCERTAINTY PROPAGATION

Investigation of long-term orbital evolution can be a challenging task as parameters have uncertainty. To add to the uncertainty problem, orbit propagation itself is a non-linear process where Gaussianity is not preserved. Monte Carlo (MC) particle approach is the most precise for capturing and propagating the uncertainty as it can capture higher moments too. However, MC based propagation is costly as it requires a large number of particles. An alternative to the MC particle approach is the use of unscented transformation (UT) based sigma points [30]. UT approach is remarkably advantageous over the Monte Carlo approach as it requires much fewer points. But, are sigma points sufficiently accurate to solve the problem at hand? Thus, this section performs: (a) long-term propagation of geosynchronous space objects using analytical methods to investigate the evolution of orbital uncertainties (b) a comparison between UT propagation and MC propagation to quantify the accuracy of sigma points. Additionally, a discussion on the Gaussian uncertainty characterization is carried out.

4.1 Sigma Points

For an n-dimensional system, the minimum number of sigma points to capture the mean and covariance is (n+1). However, this set of points is asymmetric in the state space, and as such, they have significant skew. This particular skew changes with change in orientation of the sigma points. So, if the underlying distribution is Gaussian, it is wiser to choose the zero skew (2n+1) sigma points over the skewed (n+1) sigma points to capture the behavior of the probability distribution correctly. Mathematically, for an n-dimensional system, the sigma points are given as [30]:

$$\S_0 = \bar{\mathbf{x}}(t) \tag{212a}$$

$$\S_j = \bar{\mathbf{x}}(t) + (\sqrt{n+\lambda})\left[\sqrt{\mathbf{P}(t)}\right]_j \qquad for \;\; j = 1, 2, 3, ..., n \tag{212b}$$

$$\S_{j+n} = \bar{\mathbf{x}}(t) - (\sqrt{n+\lambda})\left[\sqrt{\mathbf{P}(t)}\right]_j \qquad for \;\; j = 1, 2, 3, ..., n \tag{212c}$$

where $\bar{\mathbf{x}}(t)$ is the mean state vector, $\mathbf{P}$ is the state covariance matrix, $\left[\cdot\right]_j$ is the j_{th} column of matrix, λ is a scaling parameter and is given as $\lambda = \alpha^2(n+\kappa) - n$, with α and κ

being parameters that determine the spread of sigma points around the state mean vector. These sigma points are then transformed via the associated system non-linear equation to obtain the transformed points $\S_{0p}$, $\S_{1p}$, $\S_{2p}$,.....,$\S_{2np}$. The transformed sigma points do not contribute equally towards computation of mean or covariance, and hence, they have associated weights.

The weights for the computation of mean, are given as:

$$w_0^m = \frac{\lambda}{n+\lambda} \tag{213a}$$

$$w_j^m = \frac{1}{2(n+\lambda)} \qquad for \;\; j = 1, 2, 3, ..., 2n \tag{213b}$$

where the superscript m stands for mean.

The weights for the computation of covariance, are given as:

$$w_0^c = \frac{\lambda}{n+\lambda} + (1 - \alpha^2 + \beta) \tag{214a}$$

$$w_j^c = \frac{1}{2(n+\lambda)} \qquad for \;\; j = 1, 2, 3, ..., 2n \tag{214b}$$

where the superscript c stands for covariance. After the non-linear transformation, the UT based mean and covariance are computed as:

$$\bar{\mathbf{x}}_{UTp} = w_0^m \S_{0p} + w_1^m \S_{1p} + w_2^m \S_{2p} + ... + w_{2n}^m \S_{2np} \tag{215a}$$

$$\begin{aligned}\mathbf{P}_{UTp} = {} & w_0^c(\S_{0p} - \bar{\mathbf{x}}_{UTp})(\S_{0p} - \bar{\mathbf{x}}_{UTp})^T + w_1^c(\S_{1p} - \bar{\mathbf{x}}_{UTp})(\S_{1p} - \bar{\mathbf{x}}_{UTp})^T + \\ & w_2^c(\S_{2p} - \bar{\mathbf{x}}_{UTp})(\S_{2p} - \bar{\mathbf{x}}_{UTp})^T + ... + w_{2n}^c(\S_{2np} - \bar{\mathbf{x}}_{UTp})(\S_{2np} - \bar{\mathbf{x}}_{UTp})^T\end{aligned} \tag{215b}$$

The effect of the parameters α, κ, and β on the selection of sigma points, and the transformation needs further discussion.

A two-dimensional example, a three-dimensional example, and a six-dimensional example are shown for different values of α in Fig. 4.1. From the plots, it can be seen that increasing α increases the distance of the symmetrically distributed sigma

points from the mean without changing the direction of the points from the mean. When there are strong non-linearities, it is best to keep α small to avoid sampling the non-local effects. The standard practice is to keep α less than one but greater than 10^{-4}. For each of the examples, the parameter κ is kept constant with a value equal to $3 - dimension$.

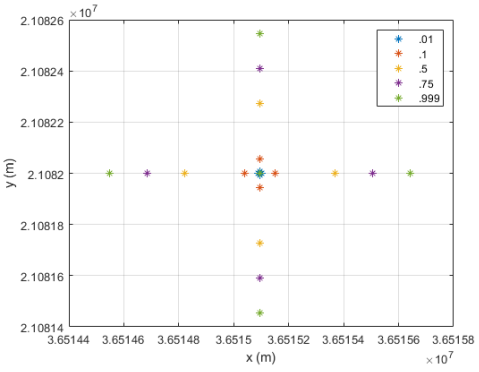

(a) Distribution of σ Points (n=2).

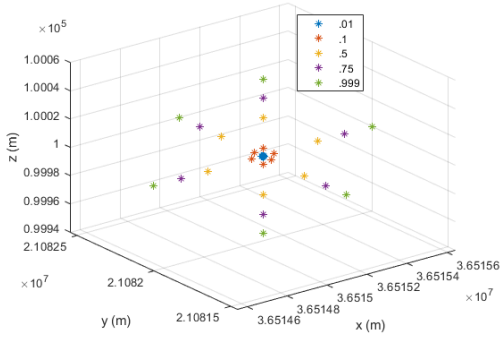

(b) Distribution of σ Points (n=3).

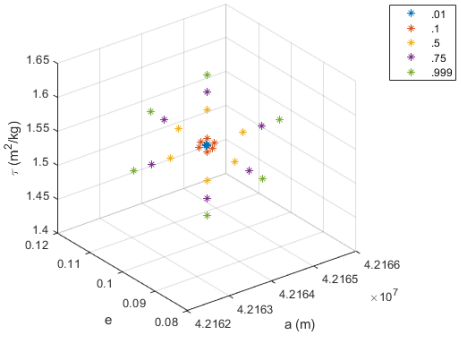

(c) Distribution of σ Points (n=6); First 3 Elements.

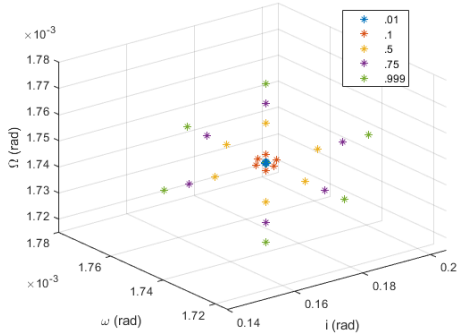

(d) Distribution of σ Points (n=6); Remaining 3 Elements.

Figure 4.1: Effect of the parameter α on the distribution of σ points.

Just like α, the parameter κ is also a scaling factor. A two-dimensional example and a six-dimensional example are shown for different values of κ in Fig. 4.2. The value of κ is varied between 0 and $3 - n$. The parameter α is taken as 0.5 for all the plots. As can be seen from the plots, larger the value of κ (including sign), further are the

sigma points away from the mean. Additionally, changing κ changes the sigma points by a smaller amount when compared to the effect of changing α.

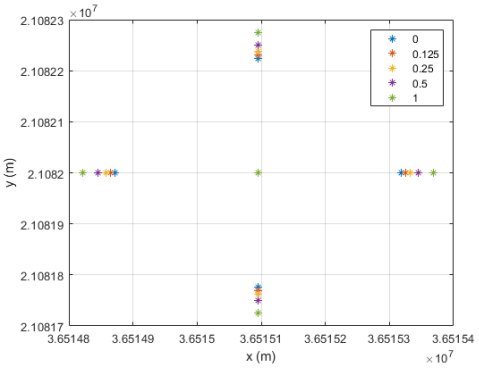

(a) Distribution of σ points (n=2).

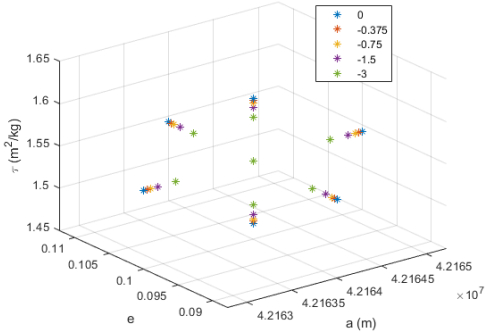

(b) Distribution of σ Points (n=6); First 3 Elements.

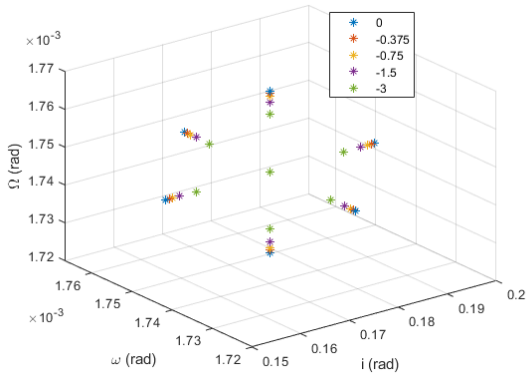

(c) Distribution of σ Points (n=6); Remaining 3 Elements.

Figure 4.2: Effect of the parameter κ on the distribution of σ points.

For $n = 3$, a couple of simulations are run with a range of β values: $[0, 1, 2, 5]$. Two different non-linear transformations (sine and squared sine) of σ points are carried out. The UT weights are then used to compute the transformed mean and covariance. Of course, β has no effect on the mean as the weights for the mean are not dependent on β, but changing β changes the covariance. Figs. 4.3 and 4.4 show the $3-\sigma$ ellipsoids and semi-axes for different values of β for the two non-linear transformations. It is

hard to deduce any specific trend or pattern from the different β value plots. Thus, if one has any prior knowledge about the concerned variable, β is used to incorporate that knowledge.

In this research work, the parameters α and κ are taken as 0.5 and 3-n, respectively from standard SSA practices. The value of β is taken as 2, which is optimal for Gaussian distributions.

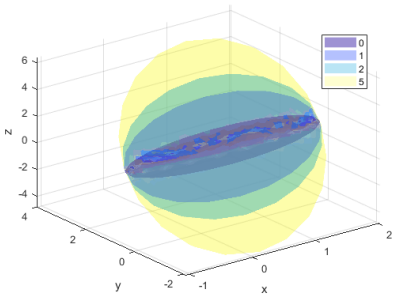

(a) 3-Sigma Ellipsoid.

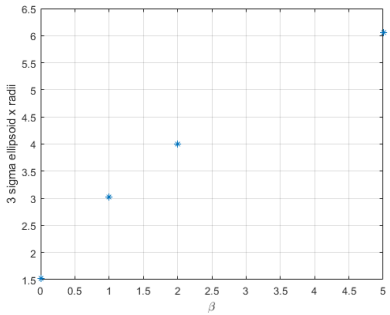

(b) X-Radius of the Ellipsoid.

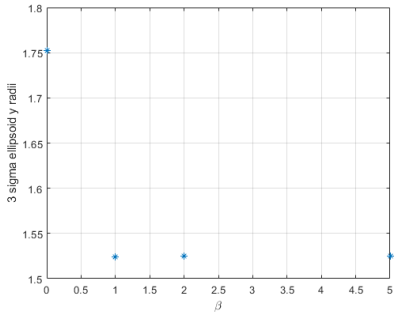

(c) Y-Radius of the Ellipsoid.

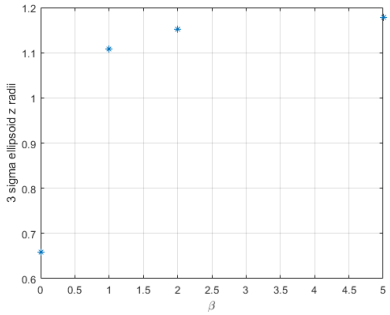

(d) Z-Radius of the Ellipsoid.

Figure 4.3: β-analysis corresponding to the sine-squared non-linear transformation.

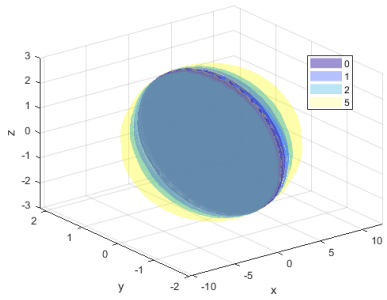

(a) 3-Sigma Ellipsoid.

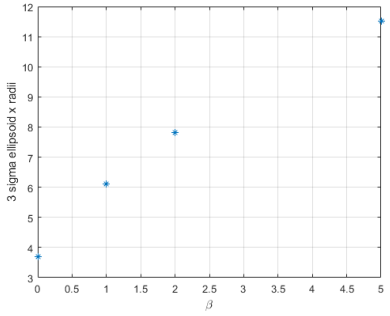

(b) X-Radius of the Ellipsoid.

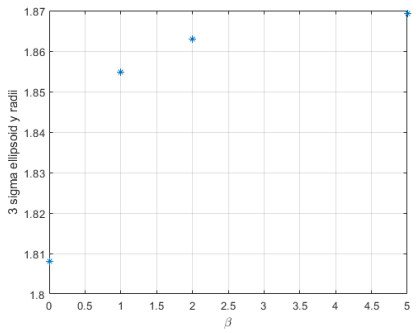

(c) Y-Radius of the Ellipsoid.

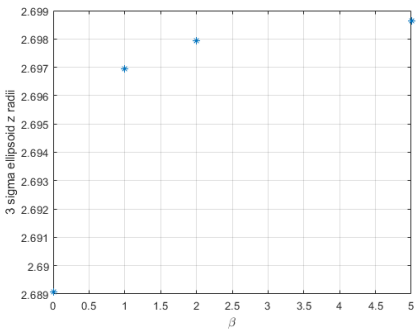

(d) Z-Radius of the Ellipsoid.

Figure 4.4: β-analysis corresponding to the sine non-linear transformation.

4.2 Uncertainty Propagation of Testbed HAMR Objects

The uncertainty propagation carried out in this section lays the necessary background for the propagation of HAMR objects for sensor tasking purposes discussed in the next chapter. As a testbed for investigating uncertainty evolution, it is assumed that the following elements have initial value uncertainty: semi-major axis, eccentricity, inclination, AoP, RAAN, area-to-mass ratio, and diffuse reflection coefficient. Uncertainty in the last two elements is realized through the product $\zeta = AMR(.25 + \frac{1}{9}C_d)$, where AMR is the area-to-mass ratio, and C_d is the diffuse reflection coefficient. With the focus of this research being the investigation of objects that are prone to large perturbations, 11 HAMR objects are assumed to be initially located in a geosynchronous orbit with near-uniform spacing as given in Table 9. The selected area-to-mass ratio values motivate from commonly used space materials that lead to the birth of HAMR objects as well as the intention to span a wide range of area-to-mass ratio values. A multivariate normal distribution with a diagonal variance-covariance matrix is chosen for the uncertain parameters. The mean and standard deviations representing the initial uncertainty are described in Table 10. A 15-years propagation is carried out in the presence of perturbations due to Earth tesseral and zonal harmonics, Sun gravity, Moon gravity, and solar radiation pressure.

Table 9: Initial true anomaly and area-to-mass ratio values.

True Anomaly (Degrees)	AMR (m^2/kg)
0	23
33	35
66	5
99	4
132	32
165	47
198	57
231	8
264	35
297	29
330	1

Table 10: Initial distribution of the uncertain parameters.

Initial Mean	Initial Standard Deviation
$\mu_a = 42164 \ \ Km$	$\sigma_a = 1 \ \ Km$
$\mu_e = .1$	$\sigma_e = .01$
$\mu_i = 10^0$	$\sigma_i = 1^0$
$\mu_\omega = .1^0$	$\sigma_\omega = .001^0$
$\mu_\Omega = .1^0$	$\sigma_\Omega = .001^0$
$\mu_\zeta = \mu_{AMR} \times (.25 + .5625/9) \ \ \frac{m^2}{kg}$	$\sigma_\zeta = .06 \ \ \frac{m^2}{kg}$

For the Monte Carlo approach, a rule of thumb states that each of the 11 objects is represented by 10^6 points, but propagating such a large number of points, even using the analytical technique, is beyond the capacity of the computing machine used in this research work. Perhaps, a more realizable estimate of the number of points can be obtained as [77]:

$$n_{sample} = 1 + 2\left(\frac{Z_\beta}{\epsilon}\right)^2 \tag{216}$$

$$\beta = \frac{1}{2}[1 - (1-\alpha)^{\frac{1}{n}}] \tag{217}$$

where Z_β is obtained from the standard normal table, α is decided by the confidence level sought, ϵ is a small number, and n is the dimension. Assuming $\alpha = .05$ (95% confidence interval) and $\epsilon = .1$ results in $n_{sample} \approx 1384$. Rounding it to the nearest multiple of 500 gives 1500 points. Thus, for the Monte Carlo approach, each of the objects is approximated using 1500 points.

Fig. 4.5 compares semi-major axes for populations propagated through UT and MC schemes, respectively. Each sub-figure contains histogram plot of MC population, and

histogram plot of UT population. Each sub-figure also contains two normal fits: the blue-colored probability density function (pdf) plot is created using sample mean and standard deviation of the propagated MC points, and the magenta-colored pdf plot is created using mean and standard deviation obtained from weighted propagated UT points.

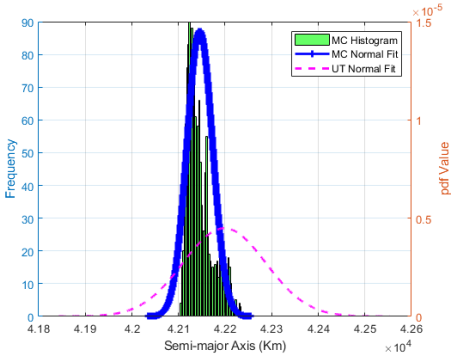

(a) AMR = 23 m^2/kg, $\nu_0 = 0^0$.

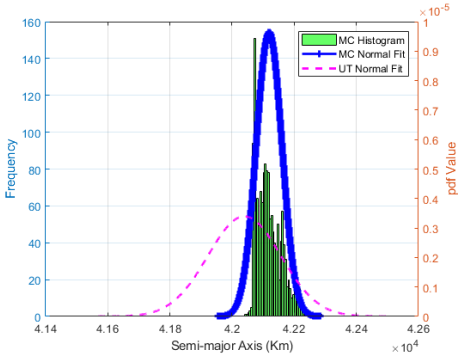

(b) AMR = 35 m^2/kg, $\nu_0 = 33^0$.

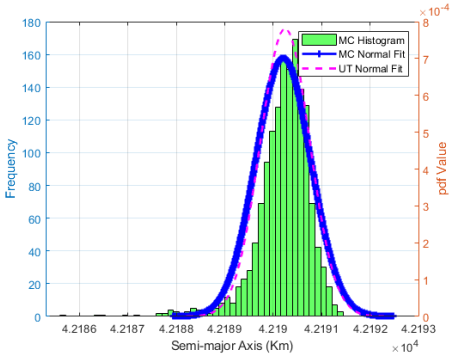

(c) AMR = 5 m^2/kg, $\nu_0 = 66^0$.

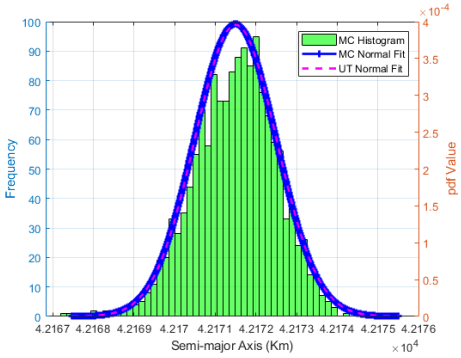

(d) AMR = 4 m^2/kg, $\nu_0 = 99^0$.

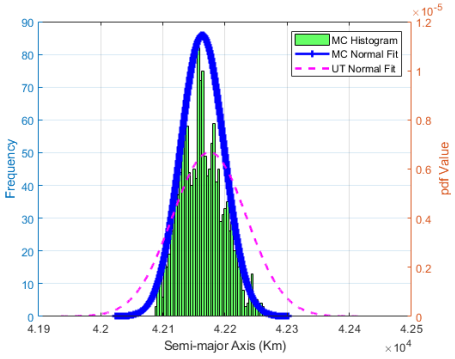

(e) AMR = 32 m^2/kg, $\nu_0 = 132^0$.

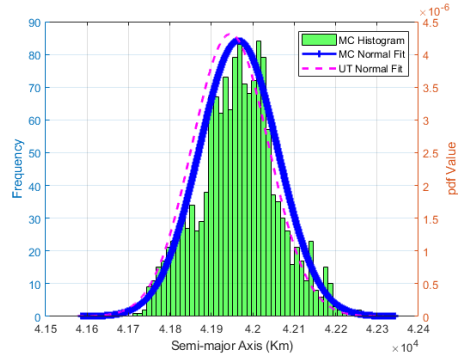

(f) AMR = 47 m^2/kg, $\nu_0 = 165^0$.

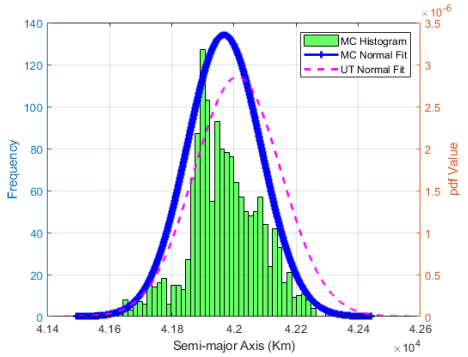

(g) AMR $= 57\ m^2/\text{kg}$, $\nu_0 = 198^0$.

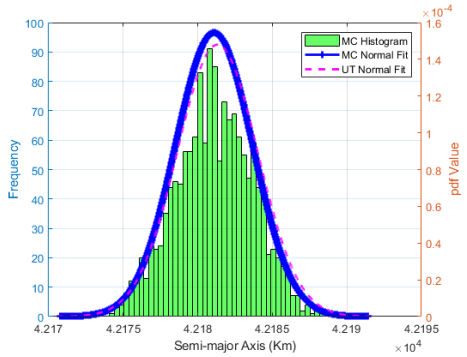

(h) AMR $= 8\ m^2/\text{kg}$, $\nu_0 = 231^0$.

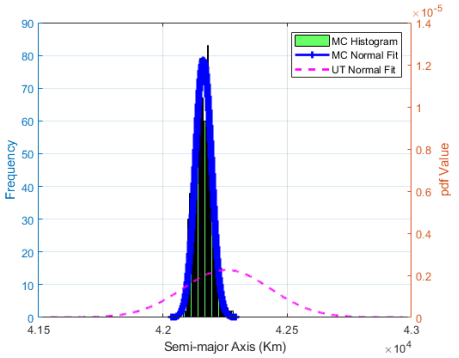

(i) AMR $= 35\ m^2/\text{kg}$, $\nu_0 = 264^0$.

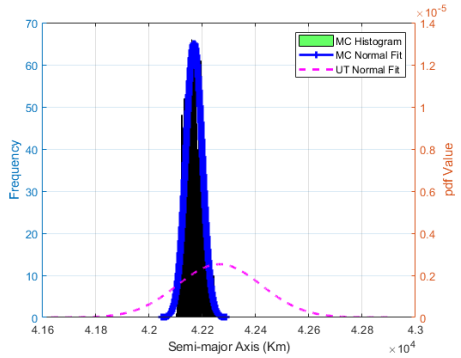

(j) AMR $= 29\ m^2/\text{kg}$, $\nu_0 = 297^0$.

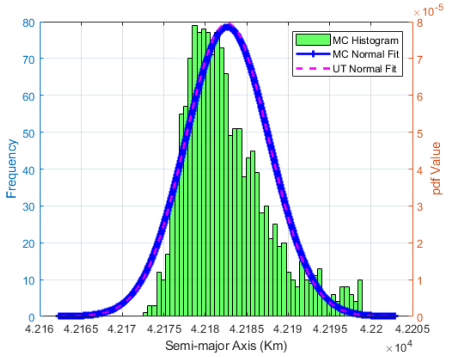

(k) AMR $= 1\ m^2/\text{kg}$, $\nu_0 = 330^0$.

Figure 4.5: Comparison of MC and UT based methods for semi-major axis.

Comparisons for other orbital elements are given in Figs. 4.6-4.9.

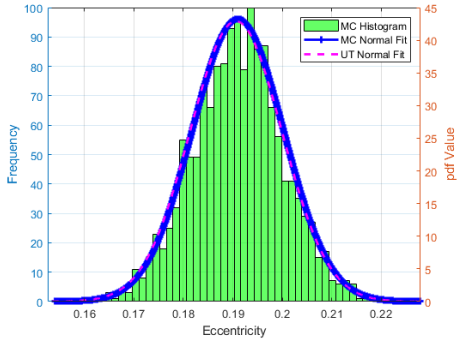

(a) AMR $= 23\ m^2/\text{kg}$, $\nu_0 = 0^0$.

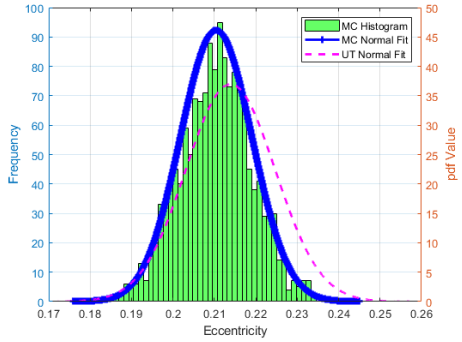

(b) AMR $= 35\ m^2/\text{kg}$, $\nu_0 = 33^0$.

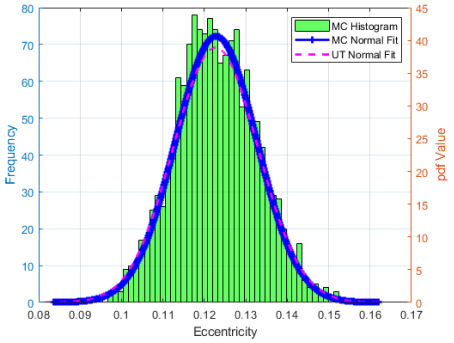

(c) AMR $= 5\ m^2/\text{kg}$, $\nu_0 = 66^0$.

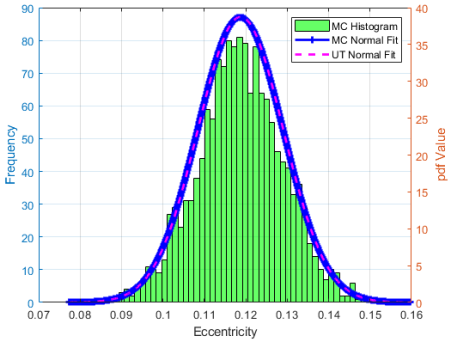

(d) AMR $= 4\ m^2/\text{kg}$, $\nu_0 = 99^0$.

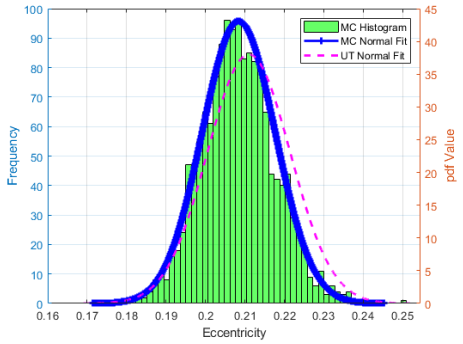

(e) **AMR $= 32\ m^2/\text{kg}$,** $\nu_0 = 132^0$

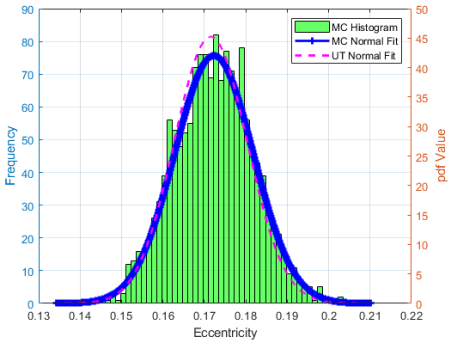

(f) AMR $= 47\ m^2/\text{kg}$, $\nu_0 = 165^0$.

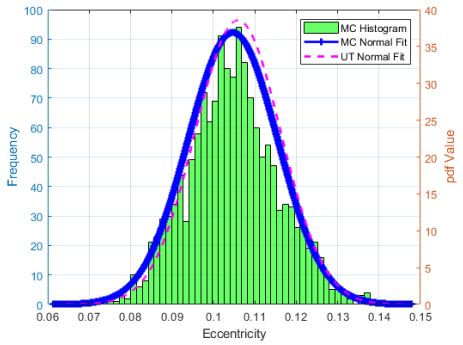

(g) AMR $= 57\ m^2/\text{kg}$, $\nu_0 = 198^0$.

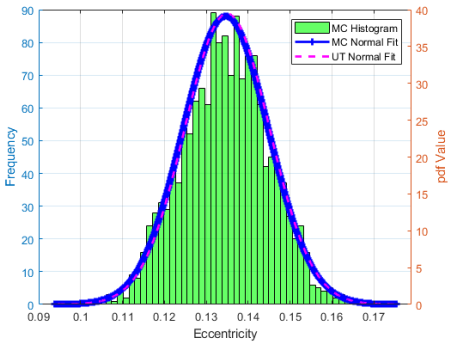

(h) AMR $= 8\ m^2/\text{kg}$, $\nu_0 = 231^0$.

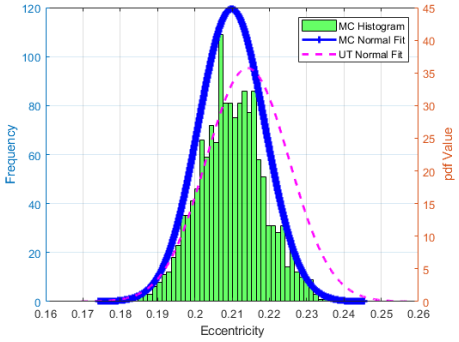

(i) AMR = 35 m^2/kg, $\nu_0 = 264^0$.

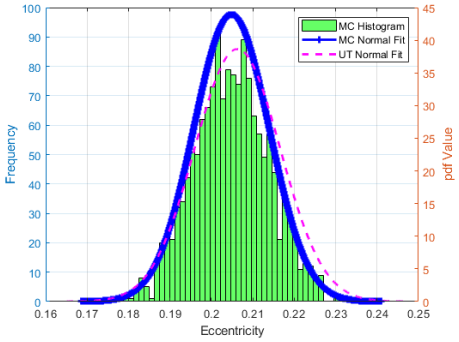

(j) AMR = 29 m^2/kg, $\nu_0 = 297^0$.

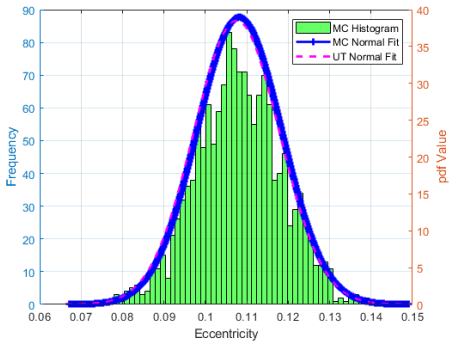

(k) AMR = 1 m^2/kg, $\nu_0 = 330^0$.

Figure 4.6: Comparison of MC and UT based methods for eccentricity.

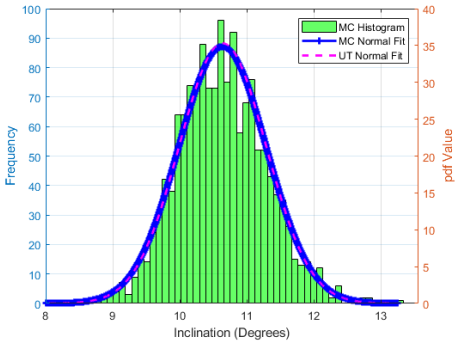

(a) AMR = 23 m^2/kg, $\nu_0 = 0^0$.

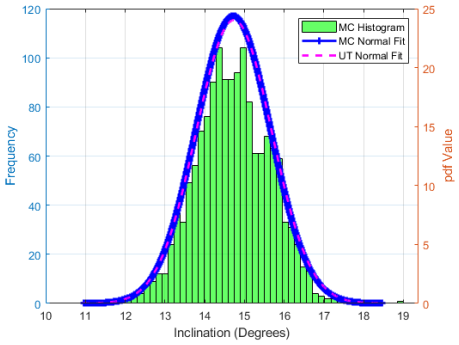

(b) AMR = 35 m^2/kg, $\nu_0 = 33^0$.

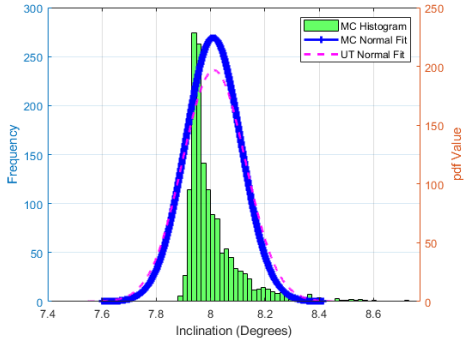

(c) AMR $= 5\ m^2/\text{kg}$, $\nu_0 = 66^0$.

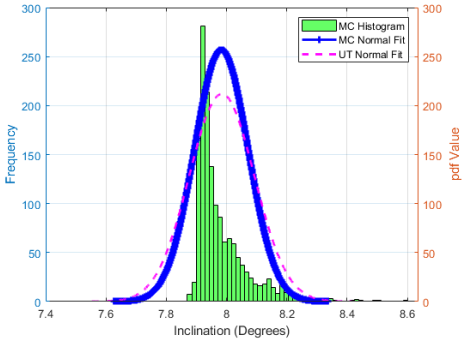

(d) AMR $= 4\ m^2/\text{kg}$, $\nu_0 = 99^0$.

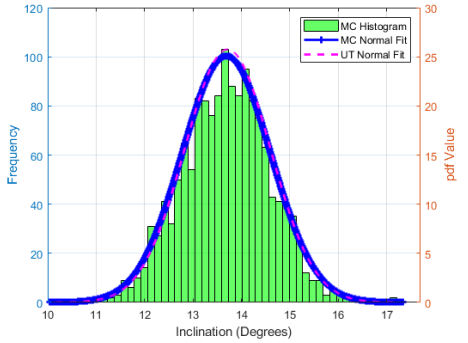

(e) AMR $= 32\ m^2/\text{kg}$, $\nu_0 = 132^0$.

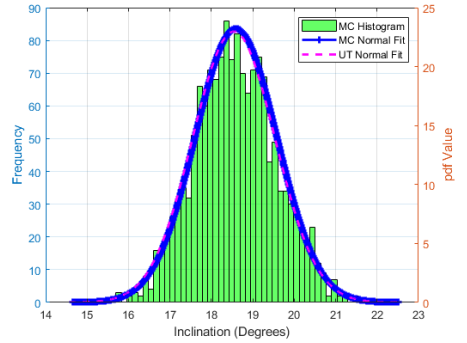

(f) AMR $= 47\ m^2/\text{kg}$, $\nu_0 = 165^0$.

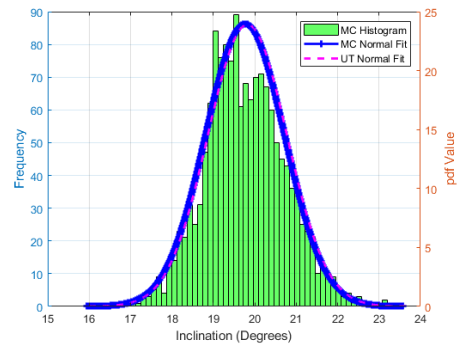

(g) AMR $= 57\ m^2/\text{kg}$, $\nu_0 = 198^0$.

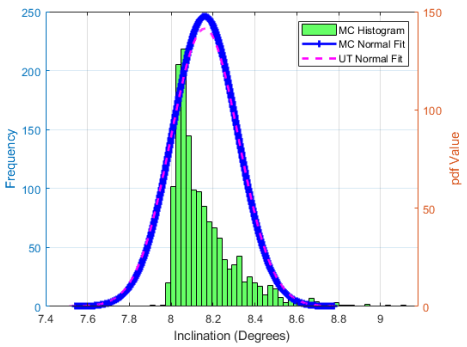

(h) AMR $= 8\ m^2/\text{kg}$, $\nu_0 = 231^0$.

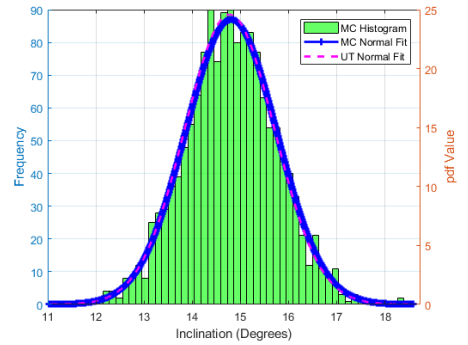

(i) AMR $= 35\ m^2/\text{kg}$, $\nu_0 = 264^0$.

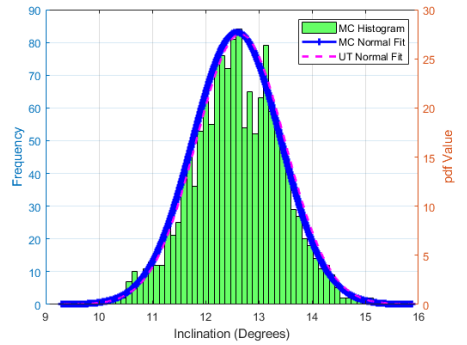

(j) AMR $= 29\ m^2/\text{kg}$, $\nu_0 = 297^0$.

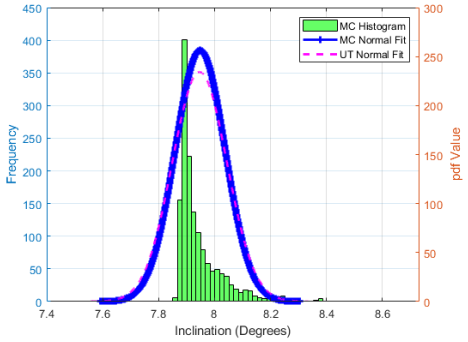

(k) AMR = 1 m^2/kg, $\nu_0 = 330^0$.

Figure 4.7: Comparison of MC and UT based methods for inclination.

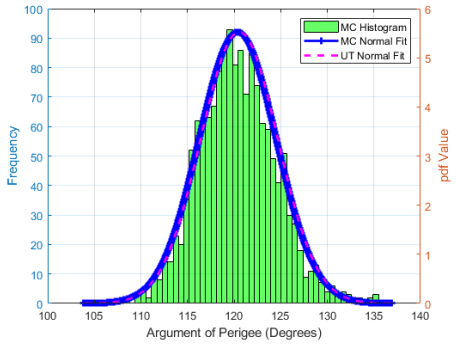

(a) AMR = 23 m^2/kg, $\nu_0 = 0^0$.

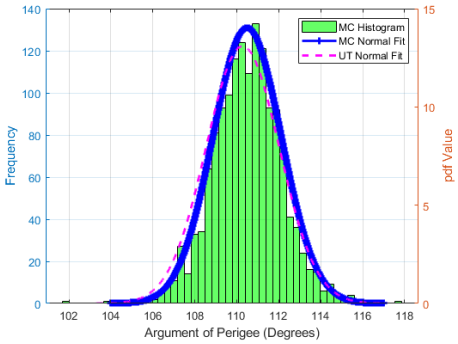

(b) AMR = 35 m^2/kg, $\nu_0 = 33^0$.

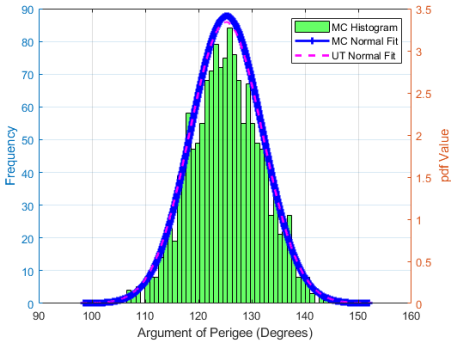

(c) AMR = 5 m^2/kg, $\nu_0 = 66^0$.

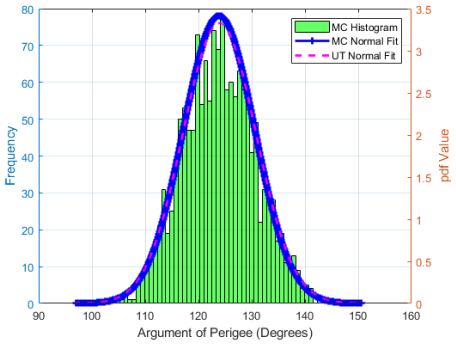

(d) AMR = 4 m^2/kg, $\nu_0 = 99^0$.

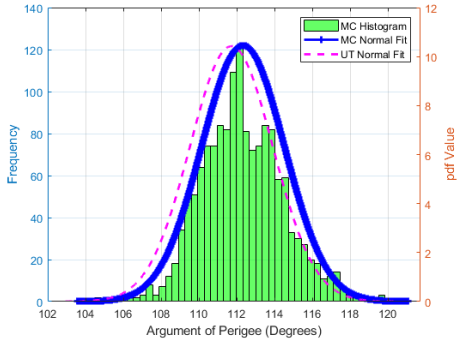

(e) AMR $= 32\ m^2/\text{kg}$, $\nu_0 = 132^0$.

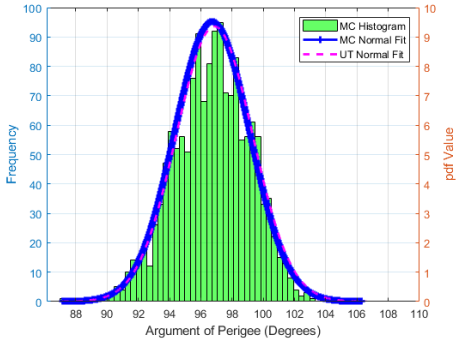

(f) AMR $= 47\ m^2/\text{kg}$, $\nu_0 = 165^0$.

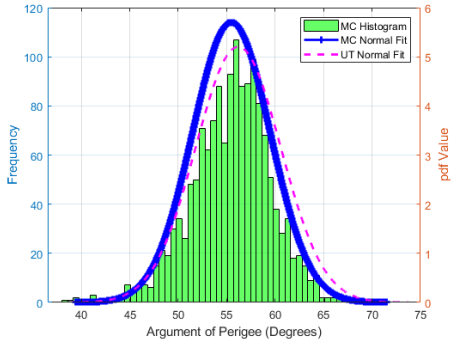

(g) AMR $= 57\ m^2/\text{kg}$, $\nu_0 = 198^0$.

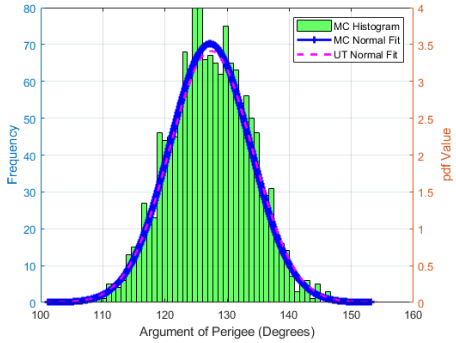

(h) AMR $= 8\ m^2/\text{kg}$, $\nu_0 = 231^0$.

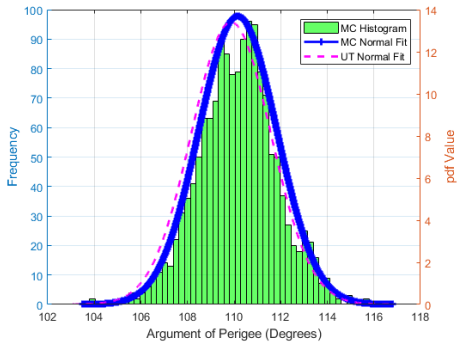

(i) AMR $= 35\ m^2/\text{kg}$, $\nu_0 = 264^0$.

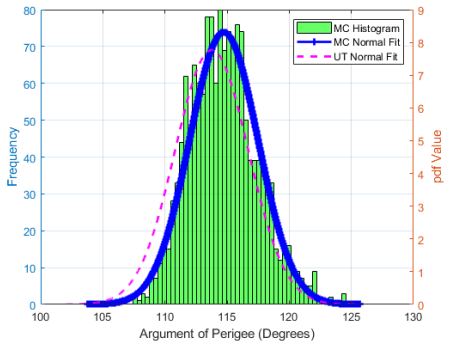

(j) AMR $= 29\ m^2/\text{kg}$, $\nu_0 = 297^0$.

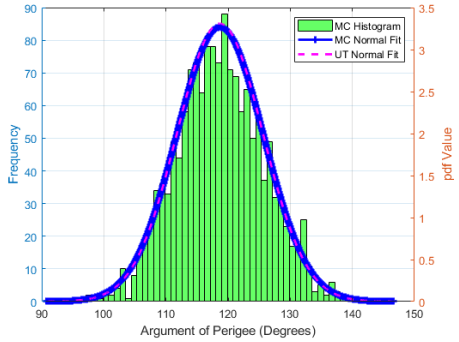

(k) AMR = 1 m^2/kg, $\nu_0 = 330^0$.

Figure 4.8: Comparison of MC and UT based methods for argument of perigee.

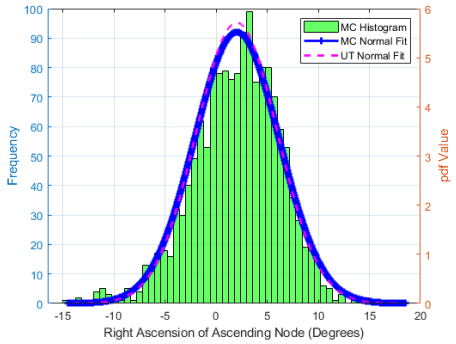

(a) AMR = 23 m^2/kg, $\nu_0 = 0^0$.

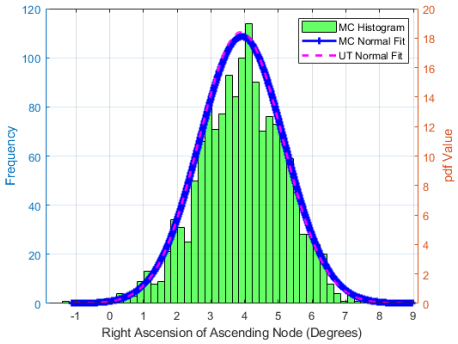

(b) AMR = 35 m^2/kg, $\nu_0 = 33^0$.

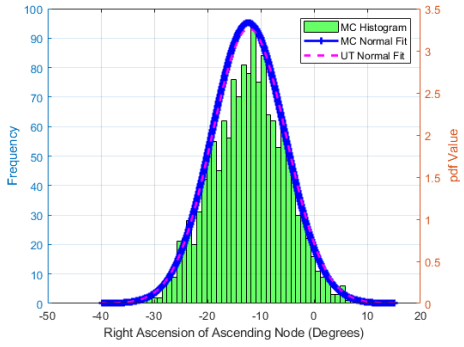

(c) AMR = 5 m^2/kg, $\nu_0 = 66^0$.

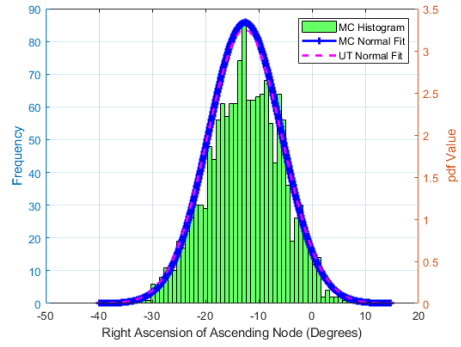

(d) AMR = 4 m^2/kg, $\nu_0 = 99^0$.

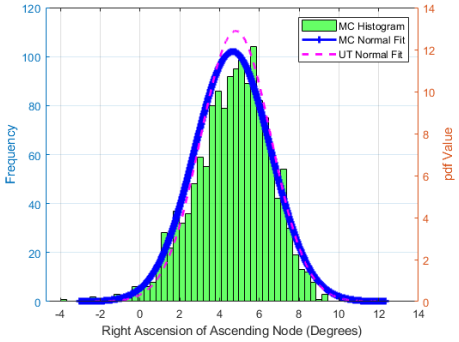

(e) AMR $= 32\ m^2/\text{kg}$, $\nu_0 = 132^0$.

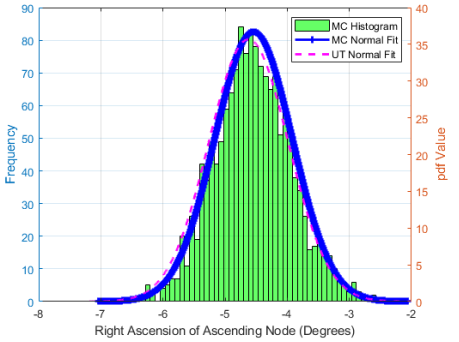

(f) AMR $= 47\ m^2/\text{kg}$, $\nu_0 = 165^0$.

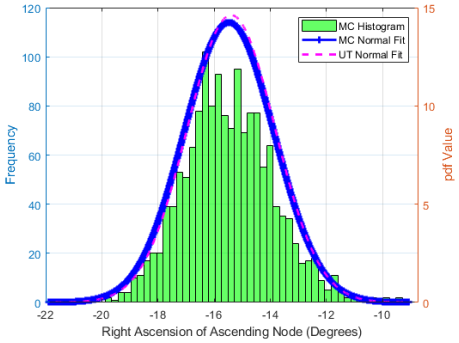

(g) AMR $= 57\ m^2/\text{kg}$, $\nu_0 = 198^0$.

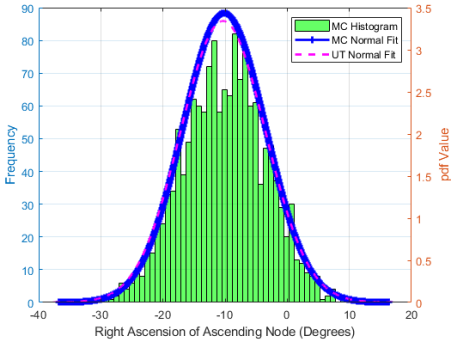

(h) AMR $= 8\ m^2/\text{kg}$, $\nu_0 = 231^0$.

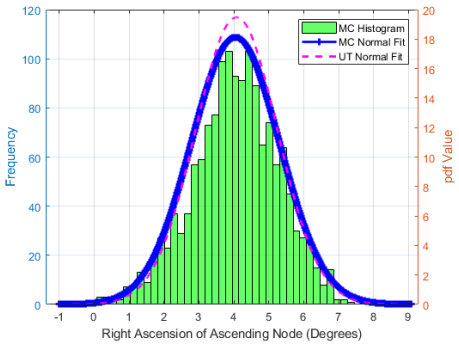

(i) AMR $= 35\ m^2/\text{kg}$, $\nu_0 = 264^0$.

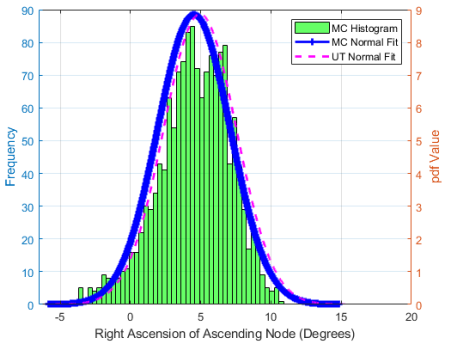

(j) AMR $= 29\ m^2/\text{kg}$, $\nu_0 = 297^0$.

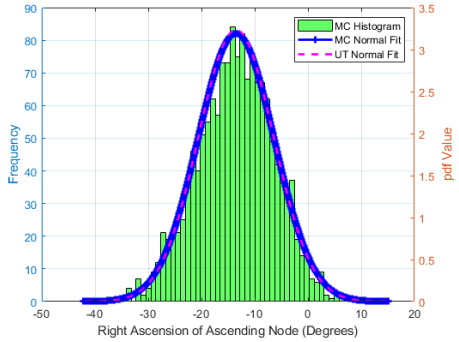

(k) AMR = 1 m^2/kg, $\nu_0 = 330^0$.

Figure 4.9: Comparison of MC and UT based methods for right ascension of ascending node.

Few interesting observations can be made from Figs. 4.5-4.9. Among the five plotted orbital elements, the sigma points were able to follow the Monte Carlo points for eccentricity, inclination, argument of perigee, and right ascension of ascending node, as evident from the closely located blue and magenta pdf plots. For quantification, this is also shown in the (log) Kullback-Leibler divergence plots for eccentricity, inclination, argument of perigee, and RAAN (Figs. 4.10(b)-(e)), where the values are negative (less than -1.5). For semi-major axis, however, a reasonable agreement between UT and MC propagation is achieved mostly when the area-to-mass ratio is relatively low (AMR = $1m^2/kg$, $4m^2/kg$, $5m^2/kg$, $8m^2/kg$). To quantify, the (log) KL divergences are positive for semi-major axis (Fig. 4.10(a)) for many of the relatively high area to mass ratios, thereby implying a poor agreement. This shows that the effect of non-linearity is most prominent for the semi-major axis, especially for those objects that have relatively high area-to-mass ratios. For semi-major axis and inclination, the pdf values are at least an order of magnitude smaller for relatively high AMRs as compared to the pdf values for relatively low area-to-mass ratios. This implies that the variances in semi-major axis and inclination are much smaller for relatively low AMRs compared to relatively high AMRs. An interesting pattern that cannot be figured out from Figs. 4.5-4.9 but can be figured out from Fig. 4.10 is that there is roughly an average increasing trend in KL divergences with area-to-mass ratios for

semi-major axis, eccentricity, argument of perigee, and RAAN, whereas, there is a decreasing trend for inclination.

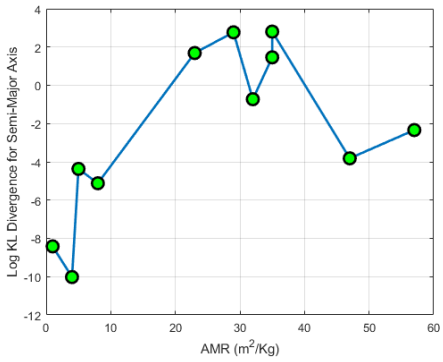

(a) KL Divergence for SMA.

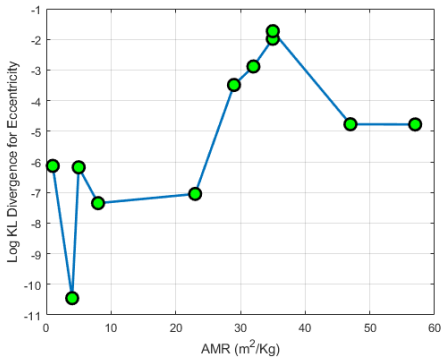

(b) KL Divergence for Eccentricity.

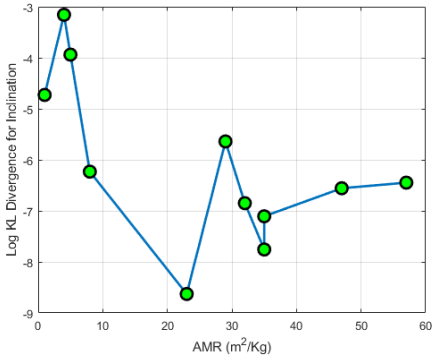

(c) KL Divergence for Inclination.

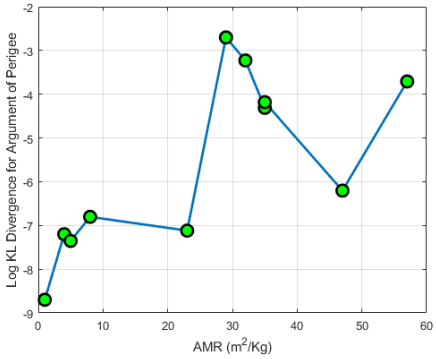

(d) KL Divergence for AoP.

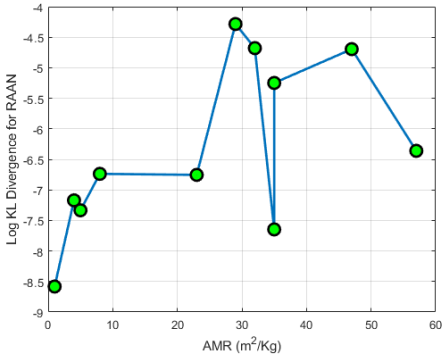

(e) KL Divergence for RAAN.

Figure 4.10: Logarithm of Kullback-Leibler divergence from Monte Carlo based normal distribution to Unscented Transformation based normal distribution.

Correct modeling of uncertainties in orbital and design parameters is an essential part of space situational awareness, and it is important to discuss the Gaussian distribution assumption that has been adopted for the parameters in this work. The next section sheds light on the cyclical and truncated natures of some of these parameters.

4.3 Important Considerations in the Uncertainty Quantification of Space Objects

Two foremost concerns need to be discussed - (1) the parameters semi-major axis, eccentricity, and $\tau = AMR(1/4 + C_d/9)$ can only take values in the range of $[0, +\infty]$, $[0, 1]$, and $[0, +\infty]$, respectively, whereas Gaussian distribution spans the entire range of real numbers (both positive and negative) (2) the parameters inclination, argument of perigee, and right ascension of ascending node are cyclic parameters, i.e., two particular values θ and $(\theta + 2\pi k)$, where k is some integer and $\theta \in [0, 2\pi)$, should have same probability density, but Gaussian distribution does not consider the cyclic repetition.

The first concern can be addressed by using truncated Gaussian distribution. Obtaining expressions for mean and covariance for 1D truncated Gaussian distribution is relatively straight forward, and they are given in John Burkardt's presentation titled "The Truncated Normal Distribution" (available online). However, the interest here lies in the multivariate truncated normal distribution, and obtaining expressions for mean and covariance for the multivariate case is more involved. Based on the work in [78, 79, 80, 81, 82], Stephan Wilhelm wrote a library in R called "tmvtnorm" (available online), that can be used to compute mean and covariance matrix for the truncated multivariate normal distribution. The inputs required for $mtmvnorm.R$ (the specific R function in the "tmvtnorm" library that computes the mean and covariance) are the lower truncation limit, upper truncation limit, mean and covariance of the non-truncated multivariate Gaussian distribution. To investigate the error incurred because of Gaussian approximation, objects with area-to-mass

ratio values of 1 m^2/kg and 57 m^2/kg are tested. The lower truncation limit for $(a, e, i, \omega, \Omega, \tau)$ is taken as $(0, 0, -\infty, -\infty, -\infty, 0)$ and the upper truncation limit is taken as $(+\infty, 1, +\infty, +\infty, +\infty, +\infty)$. The obtained results for the error (the difference between the multivariate normal distribution and the truncated multivariate normal distribution) in the mean and covariance matrix for the two AMR values are:

$$\begin{aligned}\Delta\vec{\mu}_{(AMR=1m^2/kg)} = 10^{-6} \cdot [0\ km\ \ 0\ \ 0.275052231520219^0 \\ 0.042857567967164^0\ \ 0.042857567967164^0 \\ 0.030801045269868\ m^2/kg]\end{aligned} \tag{218}$$

$$\begin{aligned}\Delta P_{(AMR=1m^2/kg)} = Diagonal([0\ \ 0\ \ 0.542101086242752e-19 \\ 0\ \ 0\ \ -0.962532759529386e-8])\ \ (SI\ units)\end{aligned} \tag{219}$$

$$\begin{aligned}\Delta\vec{\mu}_{(AMR=57m^2/kg)} = 10^{-6} \cdot [0\ km\ \ 0\ \ 0.275052231520219^0 \\ 0.042857567967164^0\ \ 0.042857567967164^0 \\ 0\ m^2/kg]\end{aligned} \tag{220}$$

$$\begin{aligned}\Delta P_{(AMR=57m^2/kg)} = Diagonal([0\ \ 0\ \ 0.542101086242752e-19 \\ 0\ \ 0\ \ 0])\ \ (SI\ units)\end{aligned} \tag{221}$$

These difference values are much smaller compared to the absolute mean and covariance values, and hence, for the numerical values used in this work, it is justified to use a multivariate Gaussian distribution instead of the truncated multivariate normal distribution.

The second concern can be addressed by using a distribution that uses circular space instead of the linear space for the circular variables. One such distribution is the so-called "Partially Wrapped Normal or PWN" distribution [83], which wraps a normal distribution around a circle. The authors in [83] defined a distribution combining one angular variable and two linear variables. Here, it is extended to three angular

variables (ω, Ω, i) and three linear variables (a, e, τ). The PWN distribution for 3 angular and 3 linear variables is given as:

$$f(\bar{x};\bar{\mu},\boldsymbol{C}) = \sum_{k_1=-\infty}^{\infty}\sum_{k_2=-\infty}^{\infty}\sum_{k_3=-\infty}^{\infty}\mathcal{N}(\bar{x}+[2\pi k_1 \quad 2\pi k_2 \quad 2\pi k_3 \quad 0 \quad 0 \quad 0]^T;\bar{\mu},\boldsymbol{C}) \tag{222}$$

with, $\bar{x} \in [0,2\pi)^3 \times \mathbb{R}^3$, location parameter $\bar{\mu} \in [0,2\pi)^3 \times \mathbb{R}^3$, and symmetric positive definite uncertainty parameter $\boldsymbol{C} \in \mathbb{R}^{6\times 6}$.

$$\bar{\mu} = \begin{bmatrix}\mu_1 & \mu_2 & \mu_3 & \mu_4 & \mu_5 & \mu_6\end{bmatrix}^T \tag{223}$$

$$\boldsymbol{C} = \begin{bmatrix} C_{11} & C_{12} & C_{13} & C_{14} & C_{15} & C_{16} \\ \star & C_{22} & C_{23} & C_{24} & C_{25} & C_{26} \\ \star & \star & C_{33} & C_{34} & C_{35} & C_{36} \\ \star & \star & \star & C_{44} & C_{45} & C_{46} \\ \star & \star & \star & \star & C_{55} & C_{56} \\ \star & \star & \star & \star & \star & C_{66} \end{bmatrix} \tag{224}$$

where, μ_1 is the circular mean of the first periodic variable, μ_2 is the circular mean of the second periodic variable, μ_3 is the circular mean of the third periodic variable, μ_4 is the mean of the first linear variable, μ_5 is the mean of the second linear variable, μ_6 is the mean of the third linear variable, and $\star$ represents the symmetric entries. The matrix

$$C_{circ} = \begin{bmatrix} C_{11} & C_{12} & C_{13} \\ \star & C_{22} & C_{23} \\ \star & \star & C_{33} \end{bmatrix} \tag{225}$$

represents the covariance of the circular part. C_{14}, C_{15}, C_{16}, C_{24}, C_{25}, C_{26}, C_{34}, C_{35}, C_{36} represent the circular-linear correlation, and the matrix

$$C_{lin} = \begin{bmatrix} C_{44} & C_{45} & C_{46} \\ \star & C_{55} & C_{56} \\ \star & \star & C_{66} \end{bmatrix} \tag{226}$$

represents the covariance of the linear part. The first hybrid moment of a partially wrapped random variable $\bar{X}$ on $\mathbb{S}_3 \times \mathbb{R}^3$ (where $\mathbb{S}_3 := [0, 2\pi)^3$) is defined as [83]:

$$\begin{aligned} \bar{m}_1 = E([cos(X_1) \quad sin(X_1) \quad cos(X_2) \quad sin(X_2) \quad cos(X_3) \\ sin(X_3) \quad X_4 \quad X_5 \quad X_6]^T) \qquad \in \mathbb{R}^9 \end{aligned} \tag{227}$$

The second hybrid moment $\boldsymbol{m}_2 \in \mathbb{R}^{9\times 9}$ of a partially wrapped random variable $\bar{X}$ on $\mathbb{S}_3 \times \mathbb{R}^3$ is defined as [83]:

$$\begin{aligned} \boldsymbol{m}_2 = E(([cos(X_1) \quad sin(X_1) \quad cos(X_2) \quad sin(X_2) \quad cos(X_3) \\ sin(X_3) \quad X_4 \quad X_5 \quad X_6]^T - \bar{m}_1)([cos(X_1) \quad sin(X_1) \\ cos(X_2) \quad sin(X_2) \quad cos(X_3) \quad sin(X_3) \quad X_4 \quad X_5 \\ X_6]^T - \bar{m}_1)^T) \end{aligned} \tag{228}$$

Following the same derivation procedure as [83], the analytic expression for the first hybrid moment is obtained as:

$$\begin{aligned} \bar{m}_1 = [\cos\mu_1 exp(-C_{11}/2) \quad \sin\mu_1 exp(-C_{11}/2) \\ \cos\mu_2 exp(-C_{22}/2) \quad \sin\mu_2 exp(-C_{22}/2) \\ \cos\mu_3 exp(-C_{33}/2) \quad \sin\mu_3 exp(-C_{33}/2) \\ \mu_4 \quad \mu_5 \quad \mu_6]^T \end{aligned} \tag{229}$$

One can use the knowledge of the characteristic function and obtain the analytic expression for the second hybrid moment. The expressions for the 45 entries of the second hybrid moment (in actuality, there are 81 entries, since it is a 9×9 matrix but 36 of those entries are symmetric) are derived in this research work, and they are given in Appendix C. The simulation scenario involving 11 objects is re-run, this time

using the PWN distribution for capturing the initial uncertainty of the parameters. $\bar{\mu}$ is taken as same as earlier, the diagonal entries of the uncertainty parameter $\boldsymbol{C}$ are also taken as same as earlier, and the non-diagonal entries taken as zero. One possible way to sample the sigma points would be to select 19 sigma points ($2 \times 9D + 1$) representative of each object from the distribution of:

$$\bar{X} = [cos(i) \quad sin(i) \quad cos(\omega) \quad sin(\omega) \quad cos(\Omega) \quad sin(\Omega) \quad a \quad e \quad \tau] \tag{230}$$

and then convert these sigma points from the above 9D space to 6D space of $[a, e, i, \omega, \Omega, \tau]$ and subsequently propagate these 19 sigma points. An alternative way to sampling and propagation would be to first compute the mean and covariance of $[a, e, i, \omega, \Omega, \tau]$ from the 19 sigma points using UT weights and then use that mean and covariance to compute a new set of 13 sigma points ($2 \times 6D + 1$) and subsequently propagate those 13 sigma points. It is found that for the numerical values that are used in this work, there is a negligible difference between the final distribution of propagated sigma points resulting from multivariate Gaussian distribution and the final distribution of propagated sigma points resulting from PWN distribution. For the sake of brevity, only a semi-major axis comparison for the object with an initial true anomaly value of 231^0 and AMR of 8 m^2/kg is shown in Fig. 4.11. Since there is little difference between the three cases, this justifies the use of multivariate normal distribution instead of a (hybrid) circular distribution.

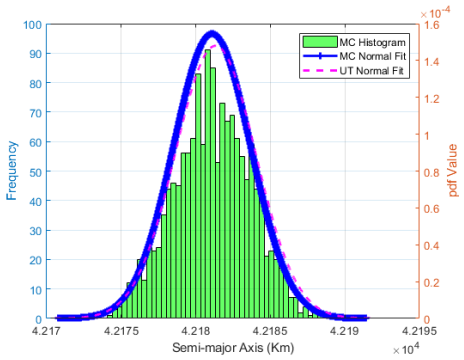

(a) MC vs Gaussian UT.

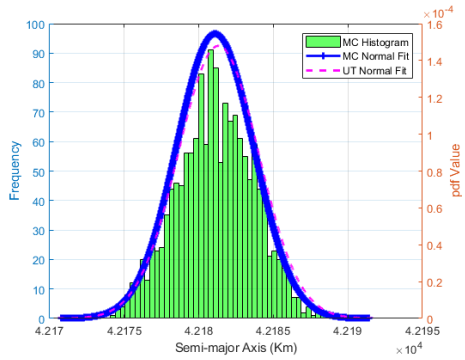

(b) MC vs PWN (13 σ Points).

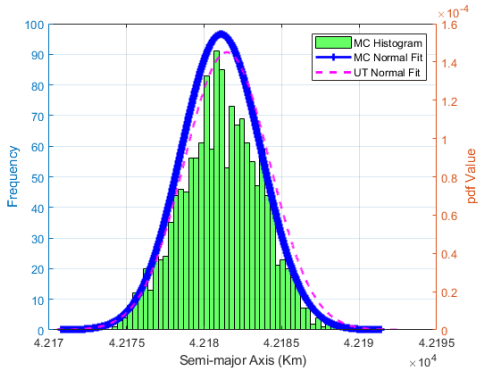

(c) MC vs PWN (19 σ Points).

Figure 4.11: Comparison of semi-major axis for propagated object with $\nu_0 = 231^0$, $AMR = 8 \ \ m^2/kg$.

4.4 Concluding Remarks

To conclude, a combination of the simga points and analytical methods can be used for uncertainty propagation in a much more computationally efficient manner compared to traditional methods. The only limitation is the loss of information on higher moments while using $(2n + 1)$ (n is the dimension) sigma points.

5 SPACE SITUATIONAL AWARENESS APPLICATION: SENSOR TASKING FOR OBJECT DETECTION

An important part of space situational awareness is the detection of new space debris population for which no a priori orbital information is at our disposal. Because of limited resources (e.g., number of sensors and sensor observation time) and the sheer number of known objects that also need observation time, the detection of these uncatalogued objects must be carried out in an optimal and efficient manner by carefully tasking the sensors. Sensor tasking strategies can broadly be classified into survey and follow-up [84, 85, 86]. Survey is the systematic way to scan the visible sky for the detection of objects with no a priori information, whereas follow-up refers to observation strategy meticulously designed for objects with already available orbital information. Whether one performs just survey or performs both survey and follow-up depends on the objective that the observer is trying to accomplish. The primary focus of this chapter is the survey of unknown high area-to-mass ratio GEO objects. The survey of high area-to-mass ratio objects is preceded by a testbed case of survey cum follow-up for the detection of known low area-to-mass ratio GEO objects.

5.1 Sensor Tasking as an Optimization Problem

In this work, sensor tasking is posed as an optimization problem [36]:

$$\max A = \sum_{g=1}^{l} \sum_{h=1}^{r_g} \sum_{f=1}^{m_g} \sum_{t_{g,f}=1}^{j_g} \Big[\Big(\sum_{i=1}^{n} \mu_{\text{past}}(\alpha_i(t_{g,f}), \delta_i(t_{g,f})) \cdot p(\alpha_i(t_{g,f}), \delta_i(t_{g,f}), \mathbf{o}, t_{g,f}) \cdot d(\alpha_{f,g}, \delta_{f,g}, \alpha_i, \delta_i, t_{g,f}) \Big) + w \cdot k(\alpha_{f,g}, \delta_{f,g}, t_{g,f}) \Big] \quad (231)$$

with the following constraints:

$$\alpha_{f,g} - \frac{1}{2}\text{FOV} - \alpha_i(t_{g,f}) \leq 0 \quad (232)$$

$$-\alpha_{f,g} - \frac{1}{2}\text{FOV} + \alpha_i(t_{g,f}) \leq 0 \quad (233)$$

$$\delta_{f,g} - \frac{1}{2}\mathrm{FOV} - \delta_i(t_{g,f}) \leq 0 \tag{234}$$

$$-\delta_{f,g} - \frac{1}{2}\mathrm{FOV} + \delta_i(t_{g,f}) \leq 0 \tag{235}$$

$$\mathbf{R} - \sigma(\alpha_i, \dot{\alpha}_i, \delta_i, \dot{\delta}_i, \rho_i, \dot{\rho}_i, \nu) \leq 0 \tag{236}$$

where A is the cost function that needs to be maximized. In the cost function, the sum runs over l different survey sensors, employed at r_g observation intervals. Only a specific number of viewing directions m_g can be visited, assuming a steady repositioning time independently of the actual slewing distance. Right ascension $\alpha_i(t_{g,f})$ and declination $\delta_i(t_{g,f})$ specify viewing direction of a particular sensor. The parameter j_g represents the number of exposures that are made for each viewing direction. The first part of the summation is based on concrete object information when state information is known a priori. The quantity $p(\alpha_i(t_{g,f}), \delta_i(t_{g,f}), \mathbf{o}, t_{g,f})$ represents the probability of detection, where the argument $\mathbf{o}$ shows the dependence of the detection probability on the object orientation and the argument $t_{g,f}$ shows the explicit time dependence. The function $\mu_{\mathrm{past}}(\alpha_i(t_{g,f}), \delta_i(t_{g,f}))$ gives weightage to the observations made in the past. It is responsible to trigger a good anomaly spread in the observations. The parameter $d(\alpha_{f,g}, \delta_{f,g}, \alpha_i, \delta_i, t_{g,f})$ represents the object count. The first four constraints imply that only the objects which are in the field of view (FOV) for given viewing directions are counted. The last constraint implies that an object contributes to the count d only if its covariance σ is above a certain threshold $\mathbf{R}$. The purpose of the last constraint is to avoid objects being observed too frequently. The count d can be understood as a probabilistic measure, the integrated probability density functions that overlap with the FOV. The second half of the summation comprises of the weight w and the surface function $k(\alpha_{f,g}, \delta_{f,g}, t_{g,f})$; they establish viewing direction values that are independent of concrete object information.

5.1.1 Hypothesis Surface or Surface-k

The hypothesis surface or surface-k, in the second part of Eq. (231), is used before any object information is gathered. Traditionally, without any prior information on the objects being tracked, if the interest lies in tracking objects that are not listed in any existing catalogs, the usual observation strategy for optical sensors is to do an exhaustive or brute-force search of the space. However, this strategy may not be efficient. Hence, an optimal or pseudo-optimal mechanism needs to be in place that guides an observer to look at specific directions or regions; the hypothesis surface precisely provides that mechanism. In this thesis, a number of hypothesis objects resembling actual catalog objects or possible actual objects will be generated. Since it is assumed that these objects have uncertainties in their initial states and design parameters, each of them will be simulated using a number of particles in order to capture their probability distribution; the number of particles will depend on whether Monte Carlo approach is used (more particles) or whether UT approach is used (fewer particles). Each object (represented by a number of particles) is then propagated over a long period using analytic formulas in order to obtain its final state and the uncertainty surrounding that final state. For generating the surface k appearing in Eq. (231), each final state along with its uncertainty will then be propagated over a 24-hour period numerically in order to obtain an array of states and uncertainties corresponding to an array of sample times. The mean and uncertainty values will then be used to fill out grids in an appropriate coordinate system. The optical sensors can then be pointed towards specific grid directions based on grid or surface values and constraints for better chances of detecting objects.

5.2 Sensor Tasking for Testbed LAMR Objects

A hypothesis for the generation of LAMR objects is proposed roughly based on the publicly available GEO catalog [7]. From the GEO catalog, the number of objects

[7]United States Space Command (USSPACECOM) provides orbital information on GEO objects via `www.space-track.org`

is plotted against the launch year (the red plot in Fig. 5.1), and a linear-curve is fitted through these points (green plot in Fig. 5.1). The equation of the fitted line is $y = .3823(year) - 749.4$. Hypothesis LAMR objects are created for each year starting from 1964 up until 2016. The number of LAMR objects generated each year is taken as $y' = ceiling(y)$, where the mathematical function *ceiling* gives the integer greater than or equal to the input y. The total number of LAMR objects thus generated is 629. The black plot in Fig. 5.1 shows the number of LAMR objects generated using the described hypothesis.

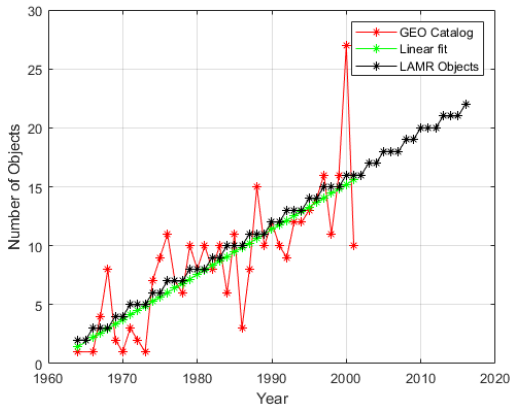

Figure 5.1: LAMR object-generation hypothesis. In red: number of GEO catalog objects versus launch year; in green: a linear-fit through the data points in red; in black: number of proposed hypothesis objects versus launch year.

The initial mean and standard deviations of the hypothesis objects are shown in Table 11.

Table 11: Initial distribution for LAMR objects.

Parameters	Mean	Standard Deviation
semi-major Axis	42164 km	1 km
eccentricity	.1	.01
inclination	$.1^0$	$.001^0$
argument of peri.	$.1^0$	$.001^0$
RAAN	$.1^0$	$.001^0$
$\zeta = AMR(\frac{1}{4} + \frac{C_d}{9})$	$\mu_{AMR}(\frac{1}{4} + \frac{.5625}{9})\ \frac{m^2}{kg}$	$1.2 \times 10^{-4}\ \frac{m^2}{kg}$

The mean area-to-mass ratio values for the 629 objects are sampled from a piece-wise

function:

$$\mu_{AMR}(j) = \begin{cases} \mathcal{U}(.0001\frac{m^2}{kg}, .01\frac{m^2}{kg}) & for\ \ 500\ \ objects \\ \mathcal{U}(.01\frac{m^2}{kg}, .02\frac{m^2}{kg}) & for\ \ 100\ \ objects \\ \mathcal{U}(.02\frac{m^2}{kg}, .1\frac{m^2}{kg}) & for\ \ 29\ \ objects \end{cases} \tag{237}$$

where $\mathcal{U}(\cdot, \cdot)$ represents the uniform distribution function. The initial true anomaly value is taken as 0^0 for all objects. These objects are propagated from their birth epoch until June 12, 2017, 00:00:00 UTC using analytic propagation. The propagated objects are finally placed within the orbit using a random distribution for true anomaly values. It is important to compare the propagated hypothesis LAMR objects with actual GEO catalog objects to ensure that a realistic object population hypothesis has been proposed. Fig. 5.2 compares the mean of propagated LAMR objects with the GEO catalog population on June 12, 2017. Fig. 5.2(a) shows the comparison with the full GEO catalog (all GEO catalog objects) and Fig. 5.2(b) shows the comparison with the assumed inactive GEO catalog (i.e., objects that were launched before 2002). As seen from Fig. 5.2, the two populations have good coherence.

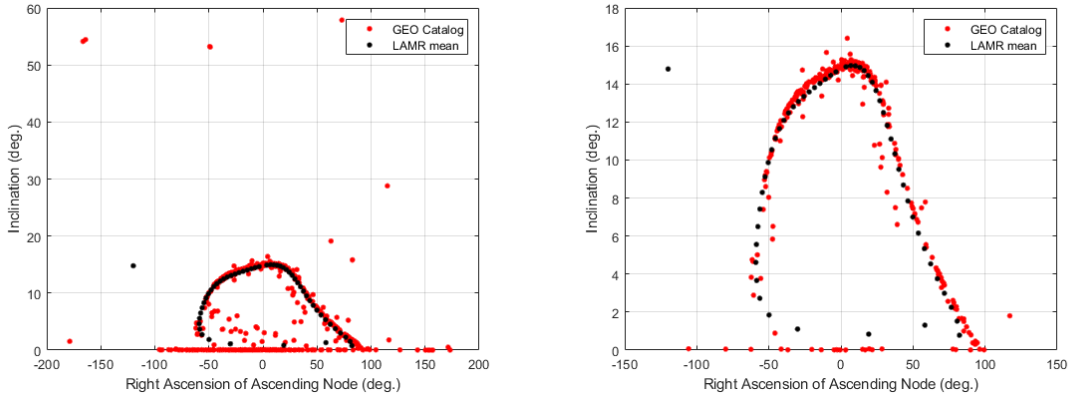

(a) LAMR Objects Vs. Full GEO Catalog. **(b)** LAMR Objects Vs. Inactive Catalog.

Figure 5.2: Inclination-right ascension of ascending node comparison between GEO catalog and LAMR population.

The tasking goal here is to detect as many objects as possible from the GEO cata-

log (treating them as un-tracked objects) under the applicable constraints using the hypothesis surface. For generating the LAMR hypothesis surface, the propagated objects (where each object is represented by a group of sigma points) at June 12, 2017, 00:00:00 UTC are further propagated using numerical methods over an "averaging" period (24 hours), and their positions are sampled every "time-step" (1 hour). For each object, at each time-step, over the averaging period, the mean azimuth-elevation (AZ-EL) and the corresponding covariance matrix are obtained by first computing the AZ-EL values from the positions of the sigma points and then taking UT based weighted averages. The normal cumulative distribution function (CDF) value for each of these AZ-EL pairs is then computed for different bins. The bins are created by dividing the AZ-EL observation space into grids the size of the telescope field-of-view. Each grid represents a particular viewing direction. The total CDF value corresponding to a particular bin is the summation of CDF values resulting from each object at each time-step. The CDF values are then normalized with respect to the averaging period and time-step, in order to obtain the bin value or the surface value. Fig. 5.3(a) shows the k-surface for the LAMR objects in the azimuth-elevation reference frame created from the CDF values of the propagated objects, where the observer is assumed to be located at Bern, Switzerland. A similar surface is also shown in Fig. 5.3(b) where the bins are filled with the number of objects (object mean) instead of the CDF values. Fig. 5.3(c) shows the surface created using inactive GEO catalog objects. Comparison of the LAMR surface and the GEO catalog population is done in Figs. 5.3(d) and 5.3(e). Fig. 5.3(d) plots the positive difference between LAMR mean surface and inactive GEO catalog mean surface, whereas Fig. 5.3(e) plots the negative difference between LAMR mean surface and inactive GEO catalog mean surface. The number of colored grid fields in Figs. 5.3(d) and 5.3(e) are not drastically different, thereby implying that the LAMR surface can be used for sensor tasking leading to the detection of catalog objects. The same mechanism can also be followed for any other coordinates; the azimuth-elevation coordinate pair is just

one such example. Figs. 5.3(d) and 5.3(e) also point to the astrodynamic feature that objects in real life often reside in groups or cliques (e.g., because of a break-up), which is not considered in the modeling of hypothesis objects.

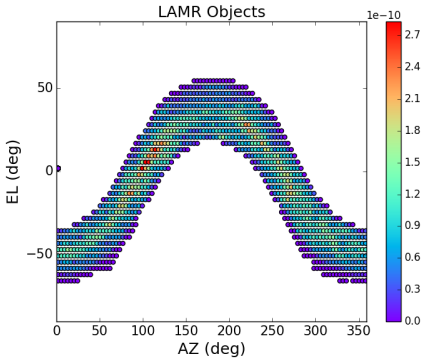

(a) LAMR Surface (Created From CDF).

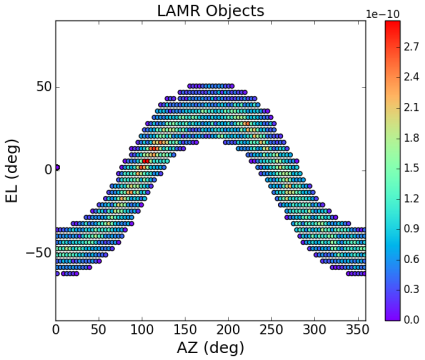

(b) LAMR Surface (Created from Counting the Means).

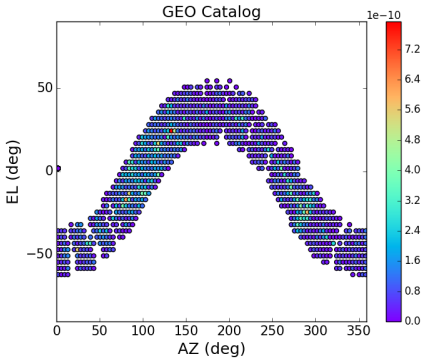

(c) GEO Catalog Mean Surface.

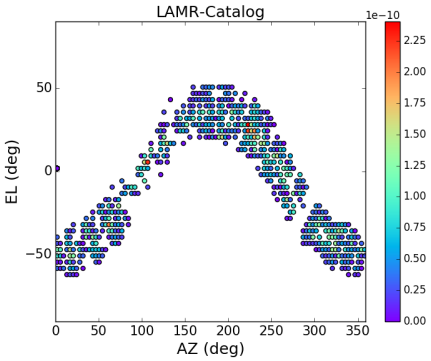

(d) Overestimation Map.

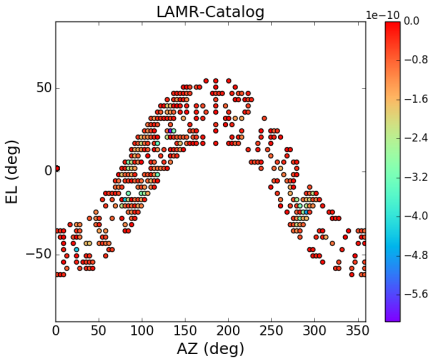

(e) Underestimation Map.

Figure 5.3: k-Surface for LAMR population in the azimuth-elevation reference frame and its comparison with GEO catalog.

To test the surface generated from the LAMR objects, a set of 614 objects from the publicly available TLE catalog (semi-major axis value is constrained between 41,700 km and 42,300 km for obtaining the set) are used to generate truth object orbits. The initial states for the truth orbits are generated by propagation with SGP4 to one hour before the start of the observation window (19:58:00 UTC, June 12, 2017) and are sampled from the SGP4 state and a diagonal covariance with position uncertainties $\sigma_x = \sigma_y = \sigma_z = 50km$ and velocity uncertainties $\sigma_{\dot{x}} = \sigma_{\dot{y}} = \sigma_{\dot{z}} = 1m/s$. These objects are then propagated under two-body motion for the remainder of the simulations. The observer in this scenario is located in Bern, Switzerland (Lat: 46.9° E, Long: 7.5° N). The observer FOV is assumed to be 3° square, and a minimum elevation constraint of 12° is imposed. The observer's Field of Regard is discretized into 3023 possible pointing directions based on the minimum elevation and FOV size [87].

The LAMR surface provides a value for every possible pointing direction that estimates the likelihood that objects will be observed at the pointing direction during a 24 hour period. In this scenario, the LAMR surface is mapped into the Local Meridian Equatorial reference frame (τ, δ) [87], where the telescope pointing directions are defined; the angles are given by:

$$\tau = \tan^{-1}\left(\frac{u_x \sin\theta - u_y \cos\theta}{u_x \cos\theta + u_y \sin\theta}\right) \tag{238a}$$

$$\delta = \sin^{-1}(u_z) \tag{238b}$$

where θ is the local mean sidereal time of the observer location, and $[u_x,\ u_y,\ u_z]^T$ is the unit (pointing) vector of the telescope. Figure 5.4 shows the LAMR grid plotted against the possible pointing directions for the observer in the LME reference frame [87]; the pointing directions with no color have a value of zero, indicating that they are unlikely to produce observations of objects.

At each observation time, the optimizer will select a pointing direction. If a truth object is detected, a candidate orbit is generated [8]; for simplicity, it is assumed that

[8]The follow-up part for detection of GEO catalog objects is done in collaboration with Bryan Little (Ph.D., AAE, Purdue University)

every detection is correctly associated with the truth object (no mistagging). The initial candidates assume circular orbits at the GEO altitude; a covariance with the same uncertainties used to initialize the truth orbits is associated with the candidate. These candidates (state and covariance) are propagated under two-body motion in an Extended Kalman Filter framework. At each observation, a cumulative distribution function (CDF) value for the candidate objects is calculated for all of the possible pointing direction; these CDF values are combined with the LAMR surface values, and the optimizer uses the total values to determine which pointing direction to assign for the new observation. Assigning the same pointing direction at every time is undesirable, but because the truth objects may move with respect to the pointing directions, the optimizer may wish to assign the same pointing direction later in the observation window. To accomplish this, the weights in Eq. (231) are used to adjust the influence of the LAMR surface and the candidates; w is a vector of weights that correspond to each of the values in the LAMR surface, while μ is a vector of weights that correspond to each candidate. When a pointing direction is selected, the w value for that pointing direction is set to zero; likewise, after candidate generation, if that candidate is observed again, its μ value is set to zero. These values are then allowed to grow slowly over time, thus allowing the LAMR surface and candidates to be used to re-select pointing directions at a later time.

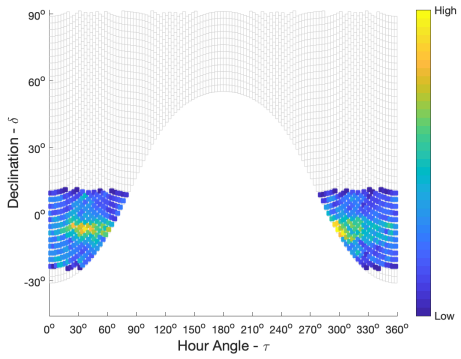

Figure 5.4: The LAMR surface provides values for the pointing directions that the observer may choose.

Over the observation period, 209 of the 614 GEO objects are within the field of regard at some point. However, the objects are distributed across many viewing directions, and there is no guarantee that all of them could be observed by the sensor during the limited number of observations. Using the aforementioned strategy, 46 different grid fields have been selected, observing 69 unique objects, with 36 of the objects observed twice. Fig. 5.5(a) shows the grids or observation directions selected (against the LAMR surface) according to the sensor tasking strategy for a total of 104 observation steps. For better visualization, Fig. 5.5(b) shows just the selected directions without the background LAMR surface. The number of objects detected at each step is shown in Fig. 5.5(c).

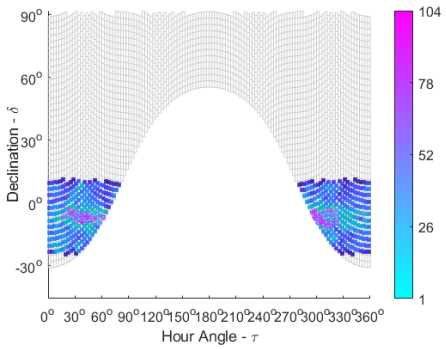

(a) Selected Grids.

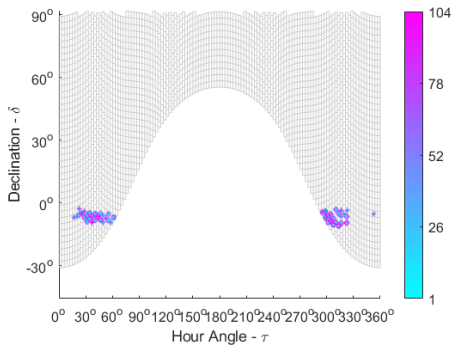

(b) Selected Grids Without LAMR Surface.

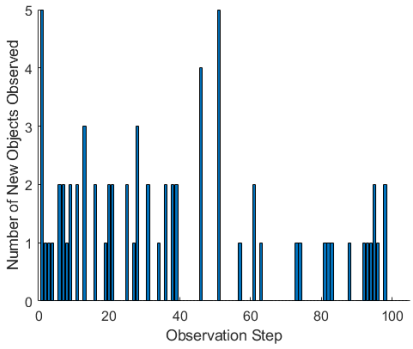

(c) Objects Detected at Each Step.

Figure 5.5: Selected directions obtained using the sensor tasking algorithm.

Next, a comparative investigation is carried out using a combination of different ob-

servation techniques, surface types, and re-observation criteria, and the following six cases have been simulated:

1. Case #1: Using hypothesis LAMR surface for survey + follow-up; re-observation of grid fields allowed
2. Case #2: Using the hypothesis LAMR surface for just survey, with re-observation of grid fields allowed
3. Case #3: Using GEO catalog surface for survey + follow-up; re-observation of grid fields allowed
4. Case #4: Using GEO catalog surface for just survey; re-observation of grid fields allowed
5. Case #5: Using hypothesis LAMR surface for just survey; re-observation of grid fields not allowed
6. Case #6: Using GEO catalog surface for just survey; re-observation of grid fields not allowed

Table 12 lists the important parameters comparing the six cases.

Table 12: Comparison of different sensor tasking strategies.

Case No.	Different Grid Fields Selected	Unique Objects Observed	Objects Observed Twice
1	46	69	36
2	47	72	36
3	26	80	50
4	26	83	50
5	104	92	1
6	104	111	6

From Table 12, case numbers 1 and 2 have fewer unique objects observed as well as objects observed twice when compared to case numbers 3 and 4. Case numbers 5 and 6 perform much better than others for the number of unique objects observed once. However, for case numbers 5 and 6, the number of objects observed twice drops significantly. Observing an object just once in a night may not be ideal unless a follow-up is carried out.

5.3 Sensor Tasking for HAMR Objects

Since the LAMR surface was able to detect a surprisingly large number of GEO catalog objects despite LAMR hypothesis objects being a rough approximation of the true GEO catalog objects, this gives confidence in the usage of k-surface for detection of high area-to-mass ratio objects. A surface-based survey will be carried out for HAMR objects in this section with the future intention of using the surface for actual object detection using an optical telescope. Little information is available for HAMR objects as most of them are not cataloged, and hence, a heuristic method will be followed for the generation of HAMR hypothesis objects.

Satellites are usually thermally insulated using multi-layer insulation (MLI) foil. Because of material deterioration, these MLIs de-laminate over time. It is suspected that these MLI fragments are the main sources of high area-to-mass ratio populations in the geosynchronous region. Several factors determine the deterioration of MLI, for example, outgassing and equivalent solar hour (ESH). ESH is defined as the total number of hours a space object is exposed to solar radiations [88]. As a gross approximation in this work, ESH will be considered as the main driver for delamination. Once the MLI degradation starts, the rate of delamination typically goes up with time [88].

A model for the creation of MLI is presented here. From the publicly available GEO catalog, there are roughly 120 objects launched during 1980-1985, 133 launched during 1985-1990, and 155 launched during 1990-1995. It will be assumed that all launches during 1980-1985 happened in the mid-year of the interval, i.e., 1982. Similarly, it will be assumed that all 133 launches happened in 1987, and 155 launches happened in 1992. It will further be assumed that only 70% of these objects have MLIs. Thus, approximately 285 of these objects will be releasing MLIs. It will further be assumed that the onset of delamination happens 20 years after the launch. Let it also be assumed that MLI coverings deteriorate with time according to a time-increasing

rate-law: the number of MLIs increase by an additional 10% every five years. Let it also be assumed that on the onset of delamination, only one MLI per object is created. Following this strategy, the 1982 launched objects will spew 84 MLIs in 2002, 92 MLIs in 2007, and 101 MLIs in 2012. The 1987 launched objects will spew 93 MLIs in 2007 and 102 MLIs in 2012. The 1992 launched objects will spew 108 objects in 2012. Thus, in total, there will be 580 HAMR objects in the orbit in 2017. The next step is to create a model for their distribution within the orbit and their AMR distribution. Objects with AMR = [23 35 5 4 32 47 57 8 35 29 1] m^2/kg are considered. It will be assumed that the number of objects follows a bi-modal Gaussian function with peaks at 26.30 m^2/kg and 111.11 m^2/kg, with equal amplitudes and standard deviations for the two Gaussian functions. Mathematically,

$$n_{AMR} = \lambda \exp\left(- \frac{(AMR - 26.30)^2}{2(\frac{111.11-26.30}{4})^2} \right) + \lambda \exp\left(- \frac{(AMR - 111.11)^2}{2(\frac{111.11-26.30}{4})^2} \right) \tag{239}$$

where the amplitude λ is to be decided from the total number of objects. Popular materials used as MLIs include PET (AMR=111.11 m^2/kg) and Kapton (AMR=26.30 m^2/kg), which are the inspiration behind the peak values. Using the bi-modal Gaussian function, the distribution for the number of objects resulting from 1982 launched objects is given in Table 13, and the same for 1987 and 1992 launched objects are given in Table 14.

Table 13: HAMR objects spewed off of 1982 launched objects.

AMR (m^2/kg)	2002 $n_{objects}$	2007 $n_{objects}$	2012 $n_{objects}$
23	10	11	12
35	9	10	11
5	6	7	8
4	6	7	7
32	10	11	12
47	7	7	8
57	4	4	5
8	7	8	9
35	9	10	11
29	11	11	12
1	5	6	6
n_{total}	84	92	101

Table 14: HAMR objects spewed off of 1987 and 1992 launched objects.

AMR (m^2/kg)	2007 $n_{objects}$; 1987	2012 $n_{objects}$; 1987	2012 $n_{objects}$; 1992
23	11	12	13
35	10	11	12
5	7	8	8
4	7	7	8
32	11	12	13
47	7	8	8
57	5	5	5
8	8	9	9
35	10	11	12
29	11	13	13
1	6	6	7
n_{total}	93	102	108

The initial distribution for the Keplerian elements, and $\zeta = AMR(.25 + C_d/9)$ are given in Table 15.

Table 15: Initial distribution for HAMR objects.

Initial Mean	Initial Standard Deviation
$\mu_a = 42164 \ \ km$	$\sigma_a = 1 \ \ km$
$\mu_e = .1$	$\sigma_e = .01$
$\mu_i = 10^0$	$\sigma_i = 1^0$
$\mu_\omega = .1^0$	$\sigma_\omega = .001^0$
$\mu_\Omega = .1^0$	$\sigma_\Omega = .001^0$
$\mu_\zeta = \mu_{AMR} \times (.25 + .5625/9) \ \ \frac{m^2}{kg}$	$\sigma_\zeta = .06 \ \ \frac{m^2}{kg}$

For each AMR and spewing year, true anomalies are given by:

$$\nu_{amr,spewingyear} = linspace\big(0, 2\pi - \frac{2\pi}{n_{amr,spewingyear}}, n_{amr,spewingyear}\big) \tag{240}$$

where the function $linspace(n_1,n_2,n_3)$ indicates a row vector of n_3 points linearly spaced between and including n_1 and n_2, i.e., objects with same AMR and delamination year are uniformly spaced within the orbit. In total, 580 HAMR objects are to

be propagated using analytic techniques. Of these, 84 objects are to be propagated for 15 years (start epoch: June 16, 2002, 00:00:00 UTC; end epoch: June 12, 2017, 00:00:00 UTC), 185 objects are to be propagated for 10 years (start epoch: June 15, 2007, 00:00:00 UTC; end epoch: June 12, 2017, 00:00:00 UTC), and 311 objects are to be propagated for 5 years (start epoch: June 13, 2012, 00:00:00 UTC; end epoch: June 12, 2017, 00:00:00 UTC). Figs. 5.6(a), 5.6(b), 5.6(c) show the mean positions of the propagated points in ECI Cartesian coordinate system. There are regions where the objects are more cluttered and then there are regions where the object density is relatively low. To get a more quantitative understanding of the importance of various directions, Fig. 5.6(d) shows the angle histogram for total number of HAMR objects corresponding to ECI-xy projection of the final population. Most number of objects are in the projected angular range $[27.69^0, 41.54^0]$, and least number of objects are in the projected range $[249.23^0, 263.08^0]$. Fig. 5.6(e) gives the angle histogram for relatively high area-to-mass ratio objects ($\geq 20m^2/kg$) in the projected x-y plane. Most number of objects are in the projected angular range $[152.31^0, 166.15^0]$, and least number of objects are in the projected angular range $[180^0, 193.85^0]$. The next task is to apply survey strategy to select the observation directions with higher chances of object detection.

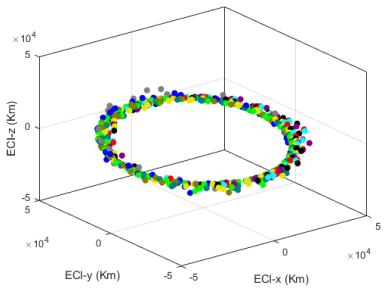

(a) Final Objects in ECI Frame.

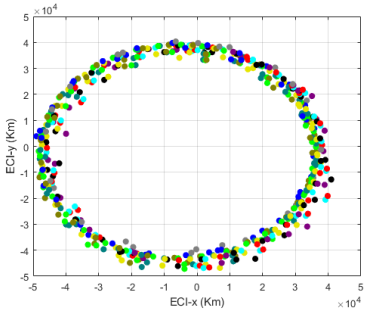

(b) Final Objects Projected into ECI-xy Plane.

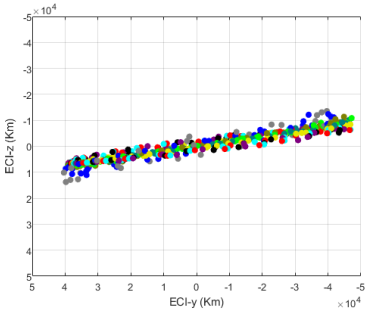

(c) Final Objects Projected Into ECI-yz Plane.

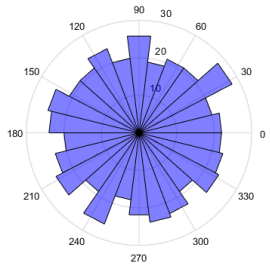

(d) Angle Histogram in the ECI-xy Plane.

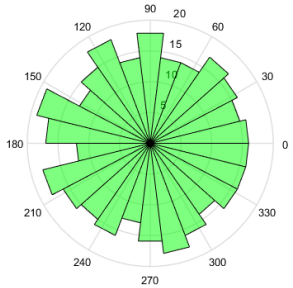

(e) Angle Histogram in the ECI-xy Plane.

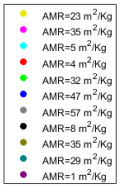

(f) AMR to Color Mapping for Sub-Figures a, b, c

Figure 5.6: Mean final positions of HAMR objects at 00:00:00 UTC, June 12, 2017.

The detection of 508 hypothesis objects is carried out with the help of hypothesis surface k. The hypothesis surface is created using the same procedure as discussed in section 5.2. Once the surface is computed, the observation duration, which is typically dusk-to-dawn, is divided into "steps," which represents the total time it requires for the telescope to observe, process, and move from one-viewing direction to the next. The sensor tasking strategy at each step is to select the viewing direction with the highest surface value. Once a particular direction is selected, it is discarded for further steps. Fig. 5.7(a) shows the generated input surface k. A sensor with 3.77×3.77 degrees field of view located at $[4331.28, 567.55, 4633.14]$ km on the Earth, is used. An exposure time of eight seconds, a readout time of seven seconds, and seven exposures per viewing direction are chosen. A slewing time of 30 seconds is selected for moving the satellite from the center of one viewing direction to the center

of the next viewing direction. Observation is conducted during 12 June 2017 from sunset to sunrise. The minimum elevation for detection is set to 10^0. Fig. 5.7(b) shows chosen directions obtained using the sensor tasking strategy. The color bar represents the bin or surface values.

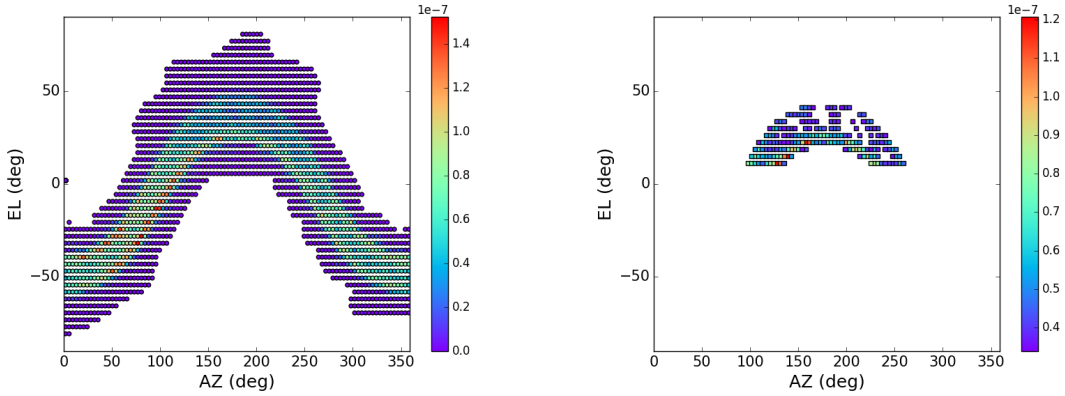

(a) Surface k. **(b)** Chosen Directions.

Figure 5.7: Surface k and chosen directions in the azimuth-elevation frame.

From Fig. 5.7, the minimum and maximum azimuths for the chosen directions are 99.375^0 and 260.625^0, respectively. The minimum and maximum elevations for the chosen directions are 13.125^0 and 43.125^0, respectively. The number of chosen directions in Fig. 5.7 is limited by the total observation period. Also, no direction below the minimum set elevation level is selected.

It needs to be emphasized that the survey results for high area-to-mass ratio objects could not be validated here because of the lack of an actual catalog consisting of high area-to-mass ratio objects. However, the developed methodology serves as a future basis for systematic detection of actual high area-to-mass ratio objects in geosynchronous region using Purdue Optical Ground Station (POGS) telescope.

5.4 Unscented Transformation Based Sensor Tasking Versus Monte Carlo Based Sensor Tasking

Since the construction of the hypothesis surface relies on only the first two moments, the k-surface generation and tasking results should not be significantly affected by the usage of sigma points over Monte Carlo particles. This section investigates sensor tasking result differences between the two uncertainty representation methods.

For the simulation set-up involving 11 HAMR objects given in Tables 9 and 10, k-surface is generated following a similar procedure as the previous section, once using sigma points and once using Monte Carlo points. A greedy algorithm, using the same observation set-up as the previous section, is then applied to the hypothesis surface for selecting the observation directions. Fig. 5.8 compares the k-surfaces computed from sigma points and Monte Carlo particles, respectively.

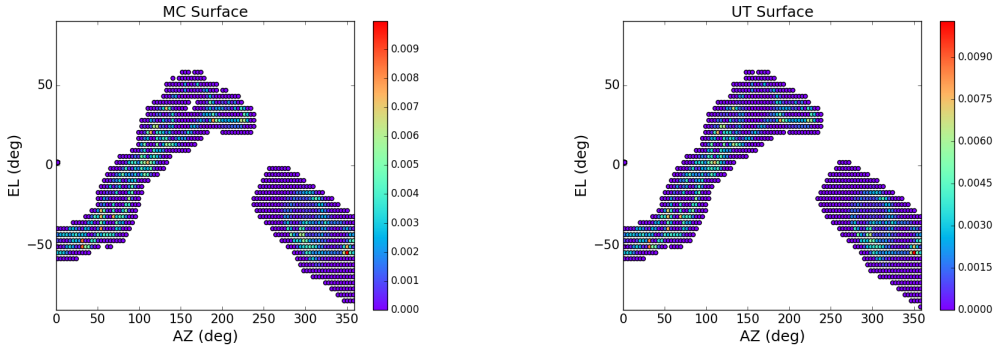

(a) k-Surface (Using Monte Carlo). **(b)** k-Surface (Using Sigma Points).

Figure 5.8: k-surface comparison between Monte Carlo and Unscented Transformation methods.

Fig. 5.9 compares the observation directions selected for the two surfaces using the greedy algorithm. From Fig. 5.9(a), 313 out of 318 selected directions were common between the two surfaces. Similarly, from Fig. 5.9(b), 313 out of 325 selected directions were common between the two surfaces. This demonstrates the earlier made exertion that the usage of computationally inexpensive sigma points in place

of computationally expensive Monte Carlo particles is acceptable for sensor tasking purposes.

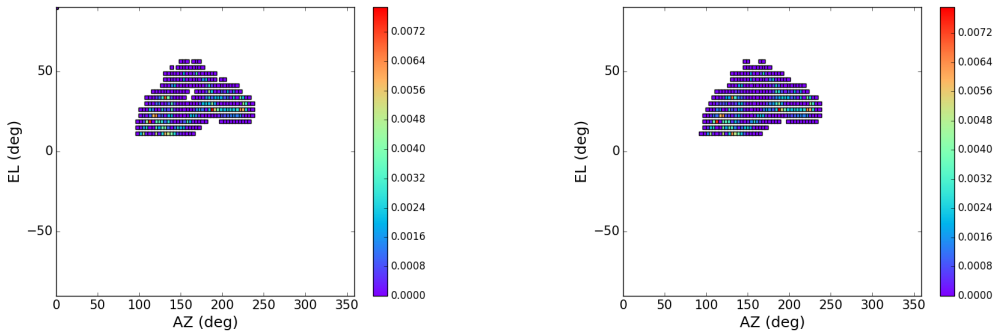

(a) Chosen Directions From Uncertainty Based MC Surface.

(b) Chosen Directions From Uncertainty Based UT Surface.

Figure 5.9: Comparison of chosen directions between Monte Carlo and Unscented Transformation methods.

5.5 Concluding Remarks

To conclude, the LAMR detection algorithm does a good job of detecting catalog objects, especially along a thin declination band close to the exact geostationary curve. This encourages the development of a systematic methodology for future detection of unknown HAMR objects.

6 SPACE SITUATIONAL AWARENESS APPLICATION: CATEGORIZATION OF NEAR-GEO SPACE OBJECTS

In space situational awareness, categorization or classification of space objects based on the similarity of characteristics can be used to optimize efforts or resources used towards object identification, object maintenance, object threat perception, and can enable prediction of future behavior. Several works exist in the literature concerning space object categorization. Wilkins et al. [89] uses a Linnaean approach to categorize resident space objects with the help of external information such as orbit class and manufacturer of the resident space objects. Frueh et al. [90] establishes a categorization system for space objects based on Phylogenetic system using features such as orbital state, attitude, amount of different materials, shape, size, and area-to-mass ratio. Jia et al. [91] uses orbital energy time series, light curve time series, and texture feature information in order to categorize space objects. Rochelle Mellish [92] uses dynamical principles to categorize geosynchronous objects using various clustering algorithms such as k-means, wards linkage method, particle swarm optimization, and density-based spatial clustering of applications with noise (DBSCAN).

This dissertation focuses on combining the knowledge of object dynamics and data-based learning approaches to categorize near-GEO space objects. This chapter is divided into three sections - the first section discusses a dynamical criterion for object categorization, the second section introduces the Neural Network machine learning algorithm, and the third section presents a scheme for long-term categorization of near-GEO objects using a combined data-dynamics approach.

6.1 Categorization of Near-GEO Objects Using Dynamical Characteristics

The dynamical criterion for near-GEO object categorization developed here will be subsequently used for generating the input data for training the Neural Network learning algorithm. The list of objects that are studied here is obtained from the

"January 2019 status report on (near) geosynchronous objects" prepared by ESA Space Debris Office. From among all the objects listed in the ESA report, a subtotal of 1489 objects, which are also publicly listed by USSPACECOM [9] are selected for investigation. Based on the observed dynamical behavior, the ESA report classifies these 1489 objects into eight different categories, which are listed in Table 16. Of these 1489 objects, 365 objects belong to the category $C1$, 108 objects belong to the category $C2$, 696 objects belong to the category D, 112 objects belong to the category $L1$, 41 objects belong to the category $L2$, 18 objects belong to the category $L3$, 20 objects belong to the category I, and 129 objects belong to the category X.

The ESA report categorization for the 1489 objects is based on continuous observation of patterns in the orbital elements. The work carried out in this thesis is focused upon developing a generic criterion for object categorization that does not depend upon continuous observation of orbital elements, but rather upon the availability of orbital data at two different time instances. The procedure for the generation of orbital data is discussed next.

Table 16: Object categorization from ESA 2019 status report on (near) geosynchronous objects.

Category	Description
$C1$	East-west (E-W) and north-south (N-S) controlled objects
$C2$	East-west (E-W) controlled objects
D	Drifting objects
$L1$	Objects librating about the Eastern stable point (75^0 E longitude)
$L2$	Objects librating about the Western stable point (105^0 W longitude)
$L3$	Objects librating about both the Eastern and Western stable points
I	Highly inclined objects (inclination greater than 25^0)
X	Rocket bodies crossing GEO protected region. GEO protected region defined by longitude $\in [-15^0, 15^0]$, altitude $\in [35586, 35986]$ km

[9] United States Space Command (USSPACECOM) provides orbital information on GEO objects via `www.space-track.org`

For those of 1489 objects which have orbital data available close to both initial and final epochs, following orbital data are generated: (i) semi-major axis, eccentricity, inclination, argument of perigee, right ascension of ascending node at an initial epoch t_1 (ii) semi-major axis, eccentricity, inclination, argument of perigee, right ascension of ascending node at a final epoch t_2 (where, $t_2 = t_1 + 1$ year) (iii) changes in semi-major axis, eccentricity, inclination, argument of perigee, right ascension of ascending node values between t_1 and t_2 (iv) object longitude at t_1 (v) object longitude at t_2 (vi) change in longitude value between t_1 and t_2. In the first step of data generation, object orbital information corresponding to a time close to t_1, in the two-line element format, is gathered from USSPACECOM's publicly available TLE catalog [10]. These objects are then propagated from their respective epochs to t_1 epoch using SGP4. The SGP4 output is in True Equator Mean Equinox of date (TEME) frame [93], which is defined as follows: the z-axis is parallel to the Earth's instantaneous North Pole axis, the x-axis points towards average vernal equinox direction, and the y-axis completes the right-handed orthogonal system. The SGP4 output is then converted from TEME frame to the more commonly used mean equator mean equinox frame or J2000 frame [93], with the Earth orientation parameters available at [94]. Similarly, object orbital information corresponding to a time close to t_2 are gathered from TLE catalog. These objects are then propagated to the epoch t_2 using SGP4. From the epoch t_2, a further propagation is carried out using SGP4 such that the final true anomaly values are within 10^{-3} radians of the initial true anomaly values at epoch t_1. The SGP4 output is then converted to J2000 frame. Having nearly the same initial and final true anomaly values ensures that Δa, Δe, Δi, $\Delta\omega$, $\Delta\Omega$ values are independent of true anomaly variations. Orbital data from space-track with the initial epoch of 12:00:00 UTC, 30^{th} December 2018 is processed to generate $\{a_i, e_i, i_i, \omega_i, \Omega_i, a_f, e_f, i_f, \omega_f, \Omega_f, \Delta a, \Delta e, \Delta i, \Delta\omega, \Delta\Omega, longitude_i, longitude_f, \Delta longitude\}$, and a 7-step dynamical criterion is applied for categorizing them:

Step 1. Objective: create a group of objects rich in high inclination or category I objects. Criterion: if the initial inclination is greater than 25^0 and initial eccentricity ≤ 0.3, it is expected that the group will be composed of predominantly category I objects. Since some of the rocket bodies crossing the GEO protected region have high inclination and large

[10] `www.space-track.org`

eccentricity, the eccentricity limit is added to the criterion. Using this criterion, the objects are divided into two groups, which are shown in Fig. 6.1. The percentage composition of each group in terms of ESA status report categorization is also provided. All the 20 category-I objects are present in group 1. The criterion in the next step is applied to the second group of objects.

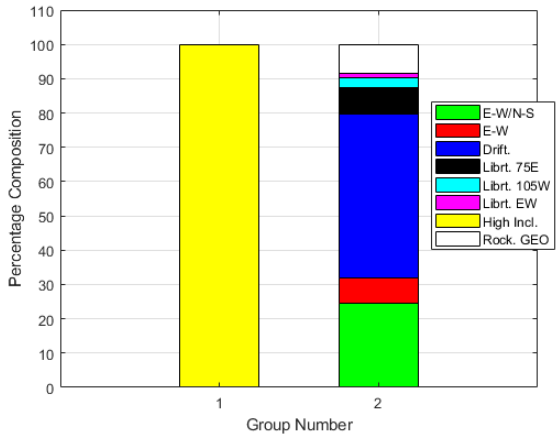

Figure 6.1: Step 1: Separation of high inclination group 1 objects.

Step 2. Objective: create a group of objects rich in rocket bodies crossing GEO protected region or category X objects. Condition: (a) if initial eccentricity ≥ 0.2 (b) if initial eccentricity lies in the range $[0.1, 0.2)$ and initial semi-major axis does not lie in the range $(37500\ km, 48100\ km)$, it is expected that the group will be composed of predominantly category X objects. The semi-major axis limit for the relatively low eccentricity rocket bodies comes from the rationale that a mission would probably want to reduce collision risks with active GEO objects by avoiding the synchronous semi-major axis value of 42164 km. Fig. 6.2 shows the two groups of objects created using the criterion. All the 120 category-X objects are present in group 1. There is also one E-W, N-S controlled object present in group 1 as a pollutant. The criterion in the next step is applied to the second group of objects.

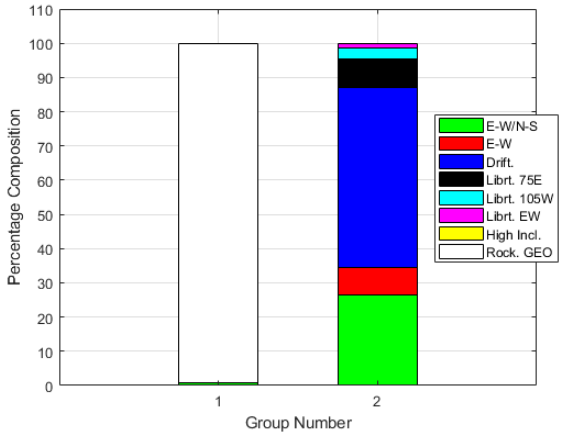

Figure 6.2: Step 2: Separation of a group rich in rocket bodies crossing GEO protected region.

Step 3. Objective: create a group of objects rich in E-W, N-S controlled or category $C1$ objects. Condition: if initial inclination $\leq 1^0$ and final inclination $\leq 1^0$, it is expected that the group will be composed of predominantly category $C1$ objects. The rationale behind the criterion is that when performing N-S control, operators try to keep the inclination low [95]. Fig. 6.3 shows the two groups of objects created using the criterion. 339 out of 350 E-W, N-S controlled objects are present in group 1. There are also 3 E-W controlled and 1 drifting objects present in group 1 as pollutants. The criterion in the next step is applied to the second group of objects.

Step 4: Objective: create a group of objects rich in E-W controlled or category $C2$ objects. Condition: if initial and final semi-major axes $\leq 42168.3\ km$, if initial and final semi-major axes $\geq 42164.1\ km$, if initial and final eccentricities $\leq .05$, it is expected that the group will be composed of predominantly category $C2$ objects. In an E-W control maneuver, operators try to keep the semi-major axis close to the synchronous value and also try to keep the eccentricity small, which is the motivation for the selected criterion. Fig. 6.4 shows the two groups of objects created using the criterion. 89 out of 106 E-W controlled objects are present in group 1. There are also 7 E-W, N-S controlled objects, 6 objects librating about the Eastern stable point, and 9 objects librating about the Western stable point present in group 1 as pollutants. The criterion in the next step is applied to the second group of objects.

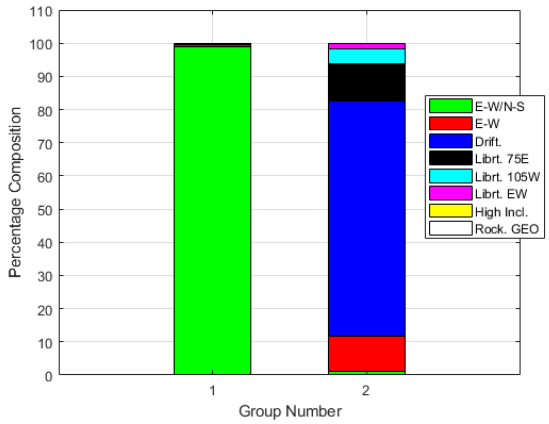

Figure 6.3: Step 3: Separation of a group rich in E-W, N-S controlled objects.

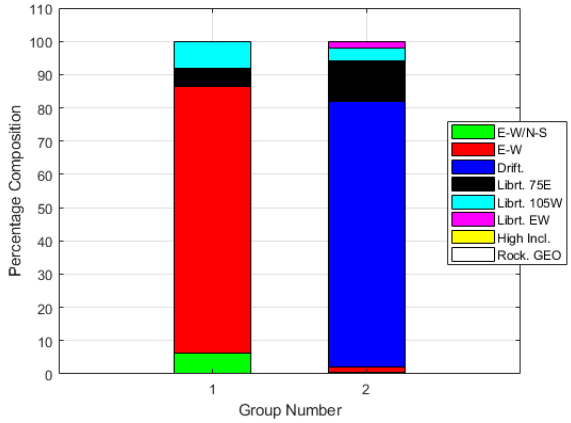

Figure 6.4: Step 4: Separation of a group rich in E-W controlled objects.

Step 5: Objective: create a group of objects rich in drifting or category D objects. Condition: if the initial semi-major axis lies outside the range $(42129\ km, 42200\ km)$, it is expected that the group will be composed of predominantly category D objects. At the beginning of step 5, objects are primarily librating or drifting, and it is known that librating objects have semi-major axis oscillating around the synchronous value, and that is the motivation for the selected criterion. The second group will have some drifting objects, but the advantage of the selected criterion is that the first group will have most of the drifting objects. Fig. 6.5 shows the two groups of objects created using the criterion. 672 out of 689 drifting objects are present in group 1. There are no pollutants present in group 1. Also, the second group is composed of predominantly librating objects. The criterion in the next step is applied to the second group of objects.

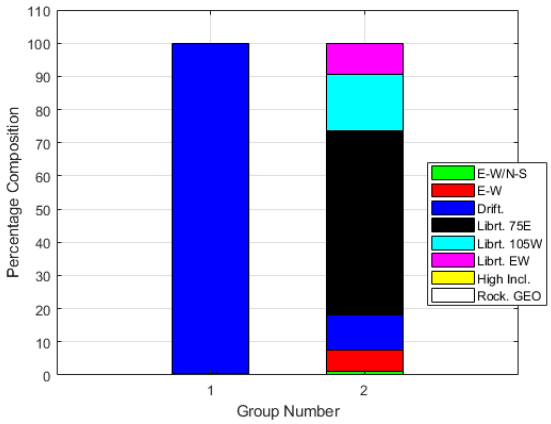

Figure 6.5: Step 5: Separation of a group rich in drifting objects.

Step 6: Objective: create a group of objects rich in category $L1$ objects or objects librating about the Eastern stable point. Condition: if the initial and final longitudes lie in the range $[3^0, 143^0]$, and if Δlongitude lies in the range $(-114^0, 105^0)$, it is expected that the group will be composed of predominantly category $L1$ objects. Since objects librating about the Eastern stable point have their longitudes oscillating about 75^0E, the selected criterion makes sense. Fig. 6.6 shows the two groups of objects created using the selected criterion. 103 out of 111 East-librating objects are present in group 1. 5 E-W controlled objects and 2 objects librating about both the stable points are also present in group 1 as pollutants. The criterion in the next step is applied to the second group of objects.

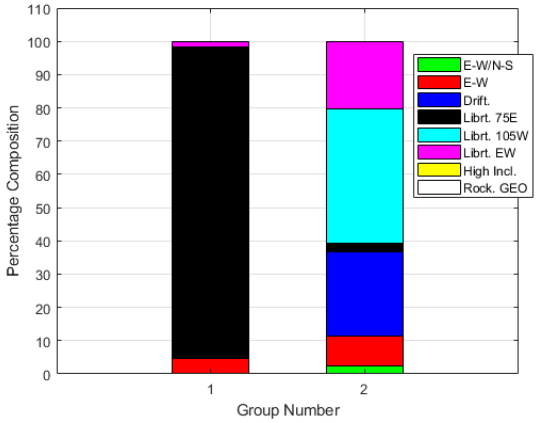

Figure 6.6: Step 6: Separation of a group rich in objects librating about the Eastern stable point.

Step 7: Objective: create a group of objects rich in category $L2$ objects or objects librating about the Western stable point. Condition: if the initial and final longitudes lie in the range $[183^0, 346^0]$, and if Δlongitude lies in the range $(-118^0, 108^0)$, it is expected that the group will be composed of predominantly category $L2$ objects. Since objects librating about the Western stable point have their longitudes oscillating about 105^0W (or 255^0E), the selected criterion makes sense. Fig. 6.7 shows the two groups of objects created using the selected criterion. 32 out of 41 West-librating objects are present in group 1. 3 E-W controlled objects, 2 objects librating about both the stable points, 1 object librating about the Eastern stable point, and 1 E-W, N-S controlled object are also present in group 1 as pollutants. Most of the objects librating about both the stable points are present in group 2, but it is difficult to separate them.

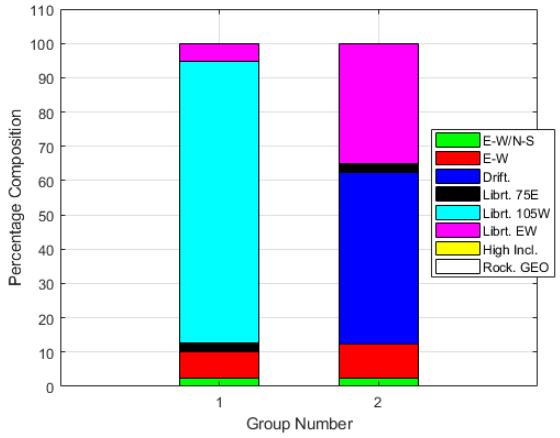

Figure 6.7: Step 7: Separation of a group rich in objects librating about the Western stable point.

Thus, using the knowledge of orbit dynamics, the near-GEO objects are separated into eight different groups - one group rich in category I objects, one group rich in category X objects, one group rich in category $C1$ objects, one group rich in category $C2$ objects, one group rich in category D objects, one group rich in category $L1$ objects, one group rich in category $L2$ objects, and one group which is a motley of different category objects.

6.2 Supervised Machine Learning Using Neural Network

Supervised learning is a machine learning technique in which a function relating an input to an output is learned based on example or training sets of input-output pairs [96]. A supervised machine learning technique that is roughly based on the working of a human brain is the Neural Network. This section describes the Neural Network algorithm [97], which will be used for learning the orbital parameters of space objects and their categorization. The Neural Network algorithm is selected based on its popularity and a comparison of the Neural Network with other existing supervised learning techniques is not a part of this thesis.

A Neural Network is characterized by an input layer, an output layer, and layers in-between called hidden layers. Each layer is composed of neurons or nodes, where a node is "a computational unit that has one or more weighted input connections, a transfer function that combines the inputs in some way, and an output connection" [98]. The number of nodes in the input layer is the same as the dimension of the feature vector. For the object categorization problem, the feature vector comprises of the initial and final semi-major axes, eccentricities, inclinations, AoPs, RAANs, longitudes, change in semi-major axis, eccentricity, inclination, AoP, RAAN, so the number of nodes in the input layer is 18. The number of nodes in the output layer is 1 for binary classification. For multi-class classification, the number of nodes in the output layer is equal to K, the number of classes in the classification problem. For the object categorization problem, $K = 8$ since there are eight different groups, as discussed in the last section. For the object categorization problem, only one hidden layer with 36 nodes (two times the size of the feature vector) is used. The common practice is to use the same number of nodes in all hidden layers, and the number of nodes in a hidden layer is typically taken as two, three, four, or five times the number of nodes in the input layer.

Let s_l denote the number of units or nodes (not counting the bias unit, i.e., an unit with value 1) in layer l, L denote the total number of layers, and $\theta^{(j)}$ denote the matrix of weights controlling function mapping from layer j to layer $(j+1)$, where the dimension of the matrix $\theta^{(j)}$ is $s_{j+1} \times (s_j + 1)$. The depiction of the mapping for a dummy 3-layer case is shown in

Fig. 6.8.

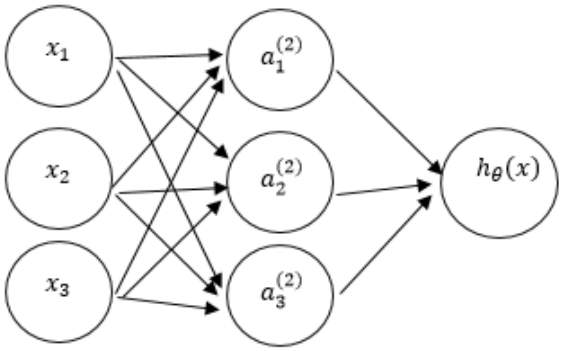

Figure 6.8: Neural Network mapping for a dummy 3-layer case.

The parameters $a_k^{(l)}$ are called activation units. $a^{(1)}$ represents activation for the first layer, $a^{(2)}$ represents activation for the second layer, and so on. The activation units are given as:

$$a_1^{(2)} = g(\theta_{10}^{(1)} x_0 + \theta_{11}^{(1)} x_1 + \theta_{12}^{(1)} x_2 + \theta_{13}^{(1)} x_3) \tag{241a}$$

$$a_2^{(2)} = g(\theta_{20}^{(1)} x_0 + \theta_{21}^{(1)} x_1 + \theta_{22}^{(1)} x_2 + \theta_{23}^{(1)} x_3) \tag{241b}$$

$$a_3^{(2)} = g(\theta_{30}^{(1)} x_0 + \theta_{31}^{(1)} x_1 + \theta_{32}^{(1)} x_2 + \theta_{33}^{(1)} x_3) \tag{241c}$$

where x_0 is the bias unit, i.e., $x_0 = 1$. The function g is some activation function. In this research work, g is taken as the sigmoid function, which is defined as:

$$g(x) = \frac{1}{1 + \exp(-x)} \tag{242}$$

For binary classification, the hypothesis $h_\theta(x)$ is given as:

$$h_\theta(x) = a_1^{(3)} = g(\theta_{10}^{(2)} a_0^{(2)} + \theta_{11}^{(2)} a_1^{(2)} + \theta_{12}^{(2)} a_2^{(2)} + \theta_{13}^{(2)} a_3^{(2)}) \tag{243}$$

where $a_0^{(2)}$ is the bias unit, i.e., $a_0^{(2)} = 1$. The benefit of using the sigmoid function for binary classification is that it restricts the hypothesis value between 0 and 1. For $0 - 1$ binary classification, any suitable threshold T can be selected to predict:

$$Predicted\ \ output = \begin{cases} 1 & if\ \ h_\theta(x) \geq T \\ 0 & if\ \ h_\theta(x) < T \end{cases} \tag{244}$$

T is usually taken as 0.5. However, for the near-GEO object categorization in this work, a slightly different procedure is followed for predicting the output. For the multi-group near-GEO object categorization, the hypothesis is first predicted as:

$$h_\theta(x) = g\Big(\theta^{(L-1)} a^{(L-1)}\Big) \tag{245}$$

The result of the hypothesis is then passed through a Softmax function:

$$\tilde{h}_\theta(x) = \frac{\exp(h_\theta(x))}{\sum_{j=1}^{K}(\exp(h_\theta(x)))_j} \tag{246}$$

where $(\exp(h_\theta(x)))_j$ is the j^{th} component of $\exp(h_\theta(x))$. Denoting the eight category of near-GEO objects by $[1; \mathbf{0}^{7\times1}]$, $[0; 1; \mathbf{0}^{6\times1}]$, $[\mathbf{0}^{2\times1}; 1;\ \mathbf{0}^{5\times1}]$, $[\mathbf{0}^{3\times1}; 1; \mathbf{0}^{4\times1}]$, $[\mathbf{0}^{4\times1}; 1; \mathbf{0}^{3\times1}]$, $[\mathbf{0}^{5\times1}; 1; \mathbf{0}^{2\times1}]$, $[\mathbf{0}^{6\times1}; 1; 0]$, $[\mathbf{0}^{7\times1}; 1]$, the output is then predicted as:

$$\hat{y} = [\mathbf{0}^{(j-1)\times1}; 1; \mathbf{0}^{(8-j)\times1}] \quad if\ \ index(maximum(\tilde{h}_\theta(x))) = j \tag{247}$$

Determination of the mapping parameter Θ (the collection of all $\theta^{(j)}$ is referred to as Θ) is discussed next.

If there are m number of training data sets $\{(x^{(1)}, y^{(1)}), (x^{(2)}, y^{(2)}), ..., (x^{(m)}, y^{(m)})\}$, the cost function for Neural Network is defined as:

$$J(\Theta) = -\frac{1}{m}\Bigg[\sum_{i=1}^{m}\sum_{k=1}^{K} y_k^{(i)} log\big(h_\theta(x^{(i)})\big)_k + \big(1 - y_k^{(i)}\big) log\big(1 - \big(h_\theta(x^{(i)})\big)_k\big)\Bigg] - \frac{\lambda}{2m}\sum_{l=1}^{L-1}\sum_{i=1}^{s_l}\sum_{j=1}^{s_{l+1}}\big(\theta_{ji}^{(l)}\big)^2 \tag{248}$$

where i=0 is not used in the $\big(\theta_{ji}^{(l)}\big)^2$ term because it corresponds to the bias term. The hypothesis $h_\theta(x) \in \mathbb{R}^K$ and $(h_\theta(x))_i = i^{th}$ component of $h_\theta(x)$. λ is known as

the regularization parameter. Regularization parameter controls the trade off between under-fitting and over-fitting. Intuitively, increasing λ will push the hypothesis towards under-fitting and decreasing λ will push the hypothesis towards over-fitting.

The cost function given in Eq. (248) is minimized w.r.t Θ using gradient descent approach in order to obtain the optimal Θ. In gradient descent approach, one iteratively updates Θ according to:

$$\theta_{ij}^{(l)} = \theta_{ij}^{(l)} - \alpha \frac{\partial J(\Theta)}{\partial \theta_{ij}^{(l)}} \tag{249}$$

where α is the learning rate.

In order to find the derivative $\frac{\partial J(\Theta)}{\partial \theta_{ij}^{(l)}}$, two tasks are performed: (1) forward propagation (2) backward propagation. Forward propagation refers to the process of computing the hypothesis values for each training example. In the back-propagation, one starts with the last layer or the output layer and gradually move in towards the input layer. Back-propagation is all about computing $\delta_j^{(l)}$, error of node j in layer l.

An example of forward propagation using one training data set (x, y) and four layers is shown in Table 17.

Table 17: An example of a forward propagation for hypothesis computation.

Step No.	Equation
1	$a^{(1)} = x$
2	$z^{(2)} = \theta^{(1)}[a_0^{(1)}; a^{(1)}]$, where $a_0^{(1)} = 1$
3	$a^{(2)} = g(z^{(2)})$
4	$z^{(3)} = \theta^{(2)}[a_0^{(2)}; a^{(2)}]$, where $a_0^{(2)} = 1$
5	$a^{(3)} = g(z^{(3)})$
6	$z^{(4)} = \theta^{(3)}[a_0^{(3)}; a^{(3)}]$, where $a_0^{(3)} = 1$
7	$a^{(4)} = h_\theta(x) = g(z^{(4)})$

An example of backward propagation using one training data set (x, y) and four layers is shown in Table 18.

Table 18: An example of a backward propagation for error computation.

Step No.	Equation
1	$\delta^{(4)} = a^{(4)} - y$
2	$\delta^{(3)} = \left(\theta^{(3)}\right)^T \delta^{(4)} .* \left(a^{(3)} .* (1 - a^{(3)})\right)$, where $.*$ is element-wise multiplication
3	$\delta^{(2)} = \left(\theta^{(2)}\right)^T \delta^{(3)} .* \left(a^{(2)} .* (1 - a^{(2)})\right)$

The complete algorithm for the computation of the derivatives $\frac{\partial}{\partial \theta_{ij}^{(l)}} J(\Theta)$ is described in Table 19.

Table 19: Algorithm for the computation of $\frac{\partial}{\partial \theta_{ij}^{(l)}} J(\Theta)$.

- Given, training set $\{(x^{(1)}, y^{(1)}), (x^{(2)}, y^{(2)}), ..., (x^{(m)}, y^{(m)})\}$
- Set $\Delta_{ij}^{(l)} = 0$ for all i, j, l

For $i = 1$ to m

- Set $a^{(1)} = x^{(i)}$
- Perform forward propagation to compute $a^{(l)}$ for

  $l = 2, 3, ..., L$
- Using $y^{(i)}$, compute $\delta^{(L)} = a^{(L)} - y^{(i)}$
- Compute $\delta^{(L-1)}, \delta^{(L-2)}, ..., \delta^{(2)}$
- $\Delta_{ij}^{(l)} := \Delta_{ij}^{(l)} + a_j^{(l)} \delta_i^{(l+1)}$

End

- $D_{ij}^{(l)} = \frac{1}{m} \Delta_{ij}^{(l)} + \lambda \theta_{ij}^{(l)}$ if $j \neq 0$
- $D_{ij}^{(l)} = \frac{1}{m} \Delta_{ij}^{(l)}$ if $j = 0$
- $\frac{\partial}{\partial \theta_{ij}^{(l)}} J(\Theta) = D_{ij}^{(l)}$

The learning parameter α for the gradient descent approach cannot be selected randomly. Too small a value of α will lead to extremely slow convergence, and too large a value of α may lead to divergence. A brute force approach, i.e., a series of α values [0.0010 0.1009 0.2008 0.3007 0.4006 0.5004 0.6003 0.7002 0.8001 0.9000] are tried in this research work. For each α, the plot of $J(\Theta)$ versus the number of iterations is investigated, and an α value with a moderate rate of convergence is selected.

If the features are of very different scales (e.g., semi-major axis and eccentricity in the near-GEO object categorization problem), the gradient descent algorithm may perform badly, and hence the features need to be scaled. In this research work, the features are scaled as: $x_i' = \frac{x_i - x_{i,min}}{x_{i,max} - x_{i,min}}$, where $x_{i,max}$ is the largest value that x_i takes among all training data sets and $x_{i,min}$ is the smallest value that x_i takes among all training data sets.

Just like the learning parameter α, the regularization parameter λ appearing in the cost function cannot be selected randomly. In this work, the following strategy for determining λ is used: the data set is divided into three parts - the first part is taken as the training data set, the second part is taken as the cross-validation set, and the third part is taken as the test set. The data set is randomly shuffled before performing this division. A series of λ values [.0007 .003 .005 .007 .05 .1 .5 1] are tried out, and cost function minimized. The value of λ that gives the smallest cross-validation cost function is selected.

6.3 Near-GEO Object Categorization Using Combined Data-Dynamics Approach

A schematic is presented here that would enable one to categorize a near-GEO object whenever a new TLE data is made available. The work here focuses on classifying objects over thirteen years, from 2001 to 2013, using Neural Network and the dynamical criterion discussed earlier. The steps for the categorization are as follows:

Step 1: Generate the Neural Network training data. For classifying any incoming TLE during a particular year 20XY, where XY can vary from '01' to '13', the Neural Network is trained with 2000, 2001, ..., (20XY-1) "one-year gap data". The 20WZ "one-year gap data" refers to the 18-dimensional orbital data and its dynamical categorization as described in section 6.1, where the initial epoch t_1 is taken as 12:00:00 UTC, January 1 20WZ and the final epoch t_2 is close to 12:00:00 UTC, December 30 20WZ.

Step 2: Determine the learning rate α for the Neural Network. As discussed in section 6.2, a series of α values are tried to determine the one with a moderate convergence rate.

Step 3: Determine the regularization parameter β for the Neural Network. As discussed in section 6.2, a series of β values are tried to select the one that results in the smallest cost-function for the cross-validation data set.

Step 4: Train the Neural Network. The Neural Network is trained with the training data according to the algorithm discussed in section 6.2 to learn the optimal mapping function.

Step 5: Categorize any incoming new TLE. Anytime a new TLE appears, a search is made through the TLE database (list of prior TLEs) to find the initial orbital data, which corresponds to an epoch that is roughly one year behind the epoch of the new TLE. The 18-dimensional orbital data is then fed into the learned function in step 4 to determine the object categorization.

Step 6: Update the "near-GEO object categorization grid." The near-GEO object categorization grid is a 39 by 39 grid structure, as shown in Fig. 6.9, where each grid represents one near-GEO object. In this research work, all the 1489 near-GEO

objects are sorted according to their NORAD Catalog Number. Grid (1,1) belongs to the object with the lowest NORAD Catalog Number, grid (1,2) belongs to the object with the second lowest NORAD Catalog Number, all the way up to grid (39,7), which belongs to the object with the largest NORAD Catalog Number. Each grid can have ten different colors: (I) the red color represents that the object belongs to category 1, a category rich in high inclination objects (II) the green color represents that the object belongs to category 2, a category rich in rocket bodies crossing GEO protected region (III) the blue color represents that the object belongs to category 3, a category rich in E-W, N-S controlled objects (IV) the magenta color represents that the object belongs to category 4, a category rich in E-W controlled objects (V) the cyan color represents that the object belongs to category 5, a category rich in drifting objects (VI) the yellow color represents that the object belongs to category 6, a category rich in objects librating about the Eastern stable point (VII) the color with RGB components [0.1 0.2 0.4] represents that the object belongs to category 7, a category rich in objects librating about the Western stable point (VIII) the color with RGB components [0.5 0.5 0.3] represents that the object belongs to category 8, which is a motley of different category objects, but primarily drifting or librating about both stable points, as pointed in section 6.1 (IX) the color with RGB components [0.7 0.3 0.2] represents that the object belongs to category 9, i.e., it has no TLE in the past one year (X) the color with RGB components [0.8 0.6 0.6] represents that the object belongs to category 0, i.e., its categorization is undefined or not clear at this point. The color-coding is shown in Fig. 6.10. Initially, the near-GEO object categorization grid is filled with colors corresponding to the categorization of the training data. Every time a new TLE appears, the color of the grid corresponding to that object is updated with its new categorization.

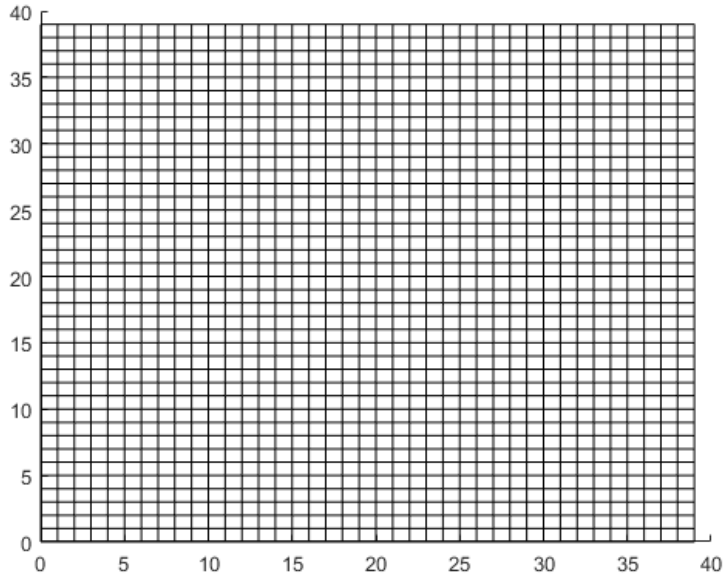

Figure 6.9: 39×39 Grid.

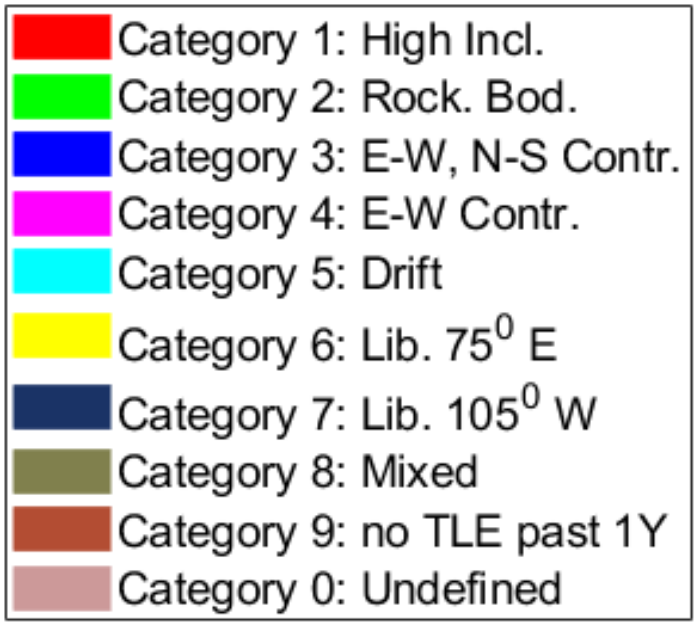

Figure 6.10: Color-coding for object categorization.

The results of the categorization schematic are shown in Figs. 6.11-6.23, where snapshots of the near-GEO object categorization grid corresponding to four random epochs

are shown for each year.

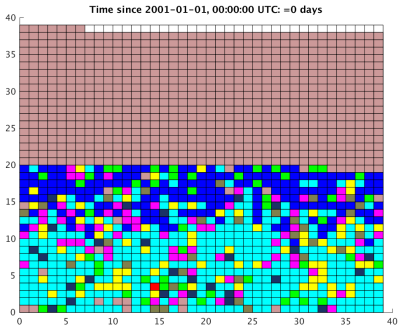

(a) $time_{passed} = 0$ days.

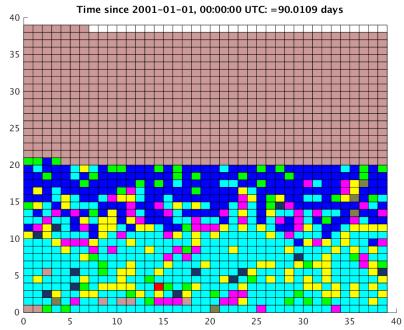

(b) $time_{passed} = 90.0109$ days.

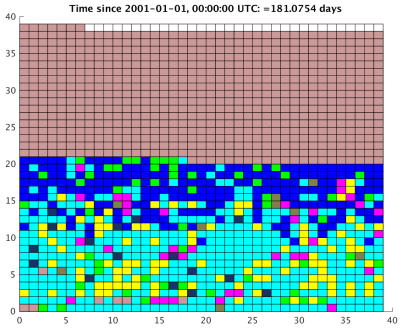

(c) $time_{passed} = 181.0754$ days.

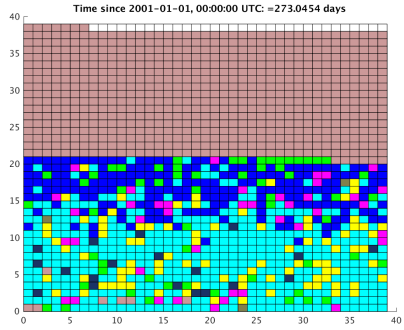

(d) $time_{passed} = 273.0454$ days.

Figure 6.11: Snapshots of near-GEO object categorization grid for the year 2001. $time_{passed}$ is the time passed since 00:00:00 UTC, January 1, 2001.

385 out of 813 objects change their categorization at least once during 2001.

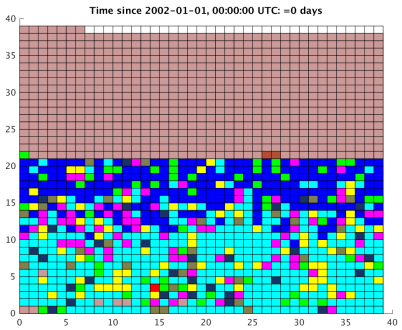

(a) $time_{passed} = 0$ days.

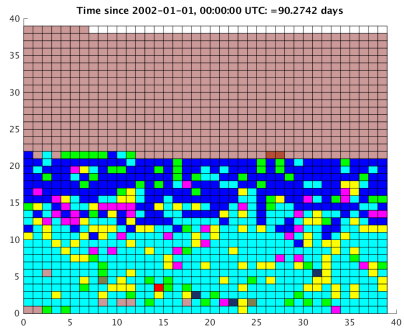

(b) $time_{passed} = 90.2742$ days.

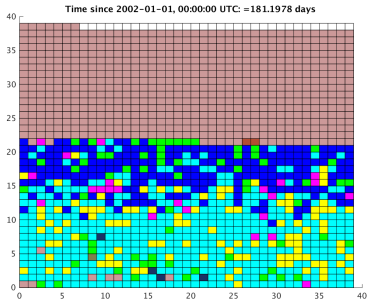

(c) $time_{passed}$ = 181.1978 days.

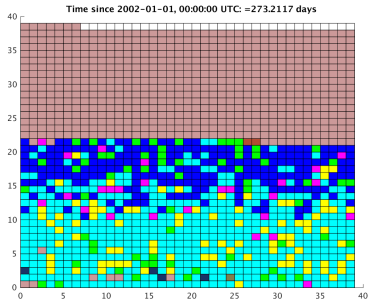

(d) $time_{passed}$ = 273.2117 days.

Figure 6.12: Snapshots of near-GEO object categorization grid for the year 2002. $time_{passed}$ is the time passed since 00:00:00 UTC, January 1, 2002.

364 out of 840 objects change their categorization at least once during 2002.

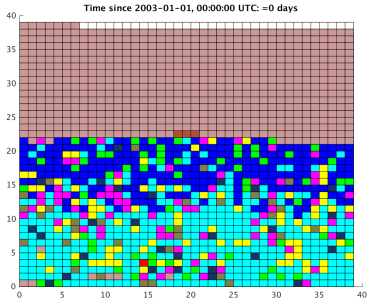

(a) $time_{passed}$ = 0 days.

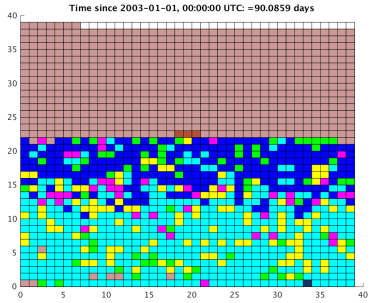

(b) $time_{passed}$ = 90.0859 days.

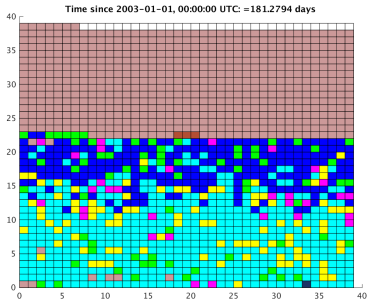

(c) $time_{passed}$ = 181.2794 days.

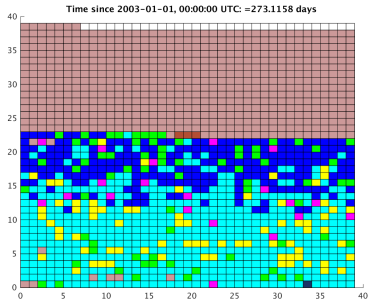

(d) $time_{passed}$ = 273.1158 days.

Figure 6.13: Snapshots of near-GEO object categorization grid for the year 2003. $time_{passed}$ is the time passed since 00:00:00 UTC, January 1, 2003.

369 out of 870 objects change their categorization at least once during 2003.

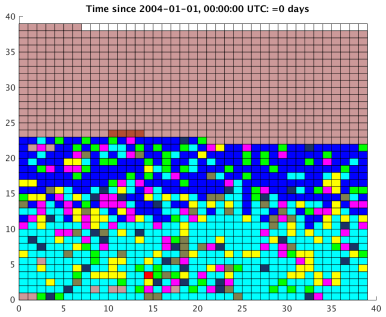

(a) $time_{passed} = 0$ days.

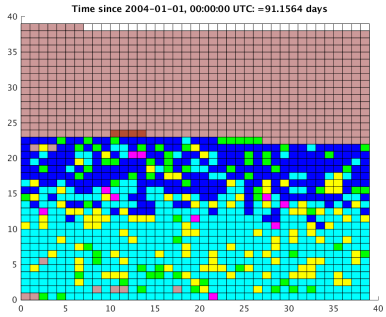

(b) $time_{passed} = 91.1564$ days.

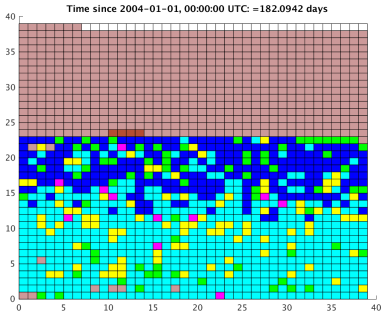

(c) $time_{passed} = 182.0942$ days.

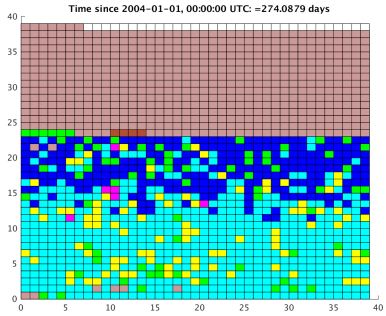

(d) $time_{passed} = 274.0879$ days.

Figure 6.14: Snapshots of near-GEO object categorization grid for the year 2004. $time_{passed}$ is the time passed since 00:00:00 UTC, January 1, 2004.

443 out of 905 objects change their categorization at least once during 2004.

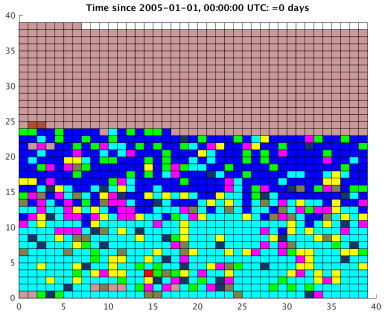

(a) $time_{passed} = 0$ days.

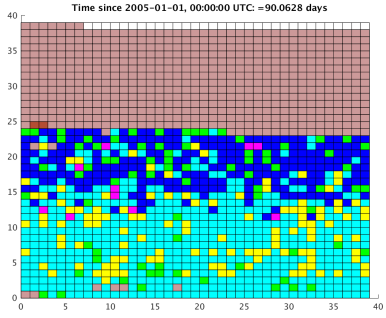

(b) $time_{passed} = 90.0628$ days.

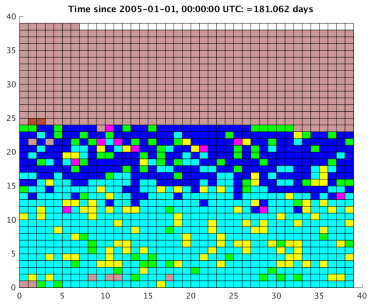

(c) $time_{passed}$ = 181.062 days.

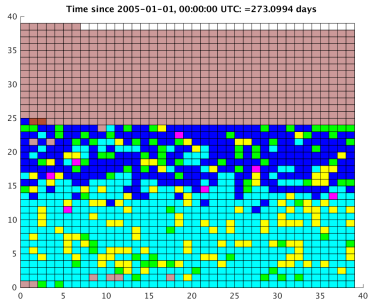

(d) $time_{passed}$ = 273.0994 days.

Figure 6.15: Snapshots of near-GEO object categorization grid for the year 2005. $time_{passed}$ is the time passed since 00:00:00 UTC, January 1, 2005.

451 out of 931 objects change their categorization at least once during 2005.

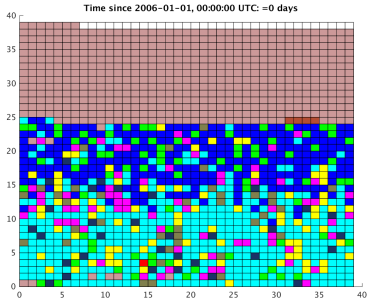

(a) $time_{passed}$ = 0 days.

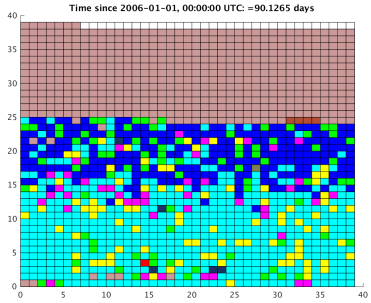

(b) $time_{passed}$ = 90.1265 days.

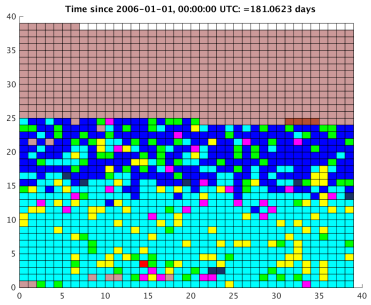

(c) $time_{passed}$ = 181.0623 days.

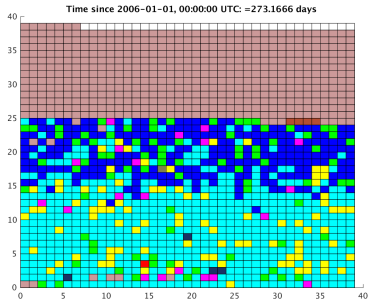

(d) $time_{passed}$ = 273.1666 days.

Figure 6.16: Snapshots of near-GEO object categorization grid for the year 2006. $time_{passed}$ is the time passed since 00:00:00 UTC, January 1, 2006.

320 out of 961 objects change their categorization at least once during 2006.

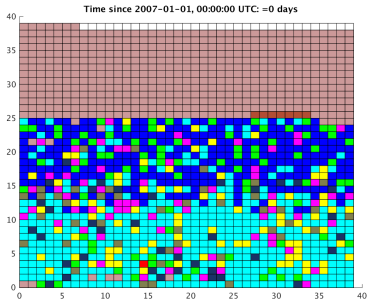

(a) $time_{passed} = 0$ days.

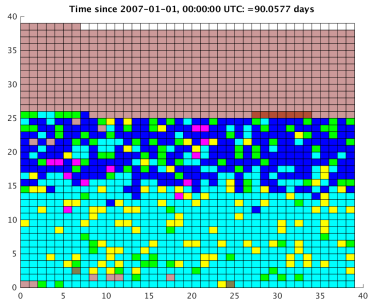

(b) $time_{passed} = 90.0577$ days.

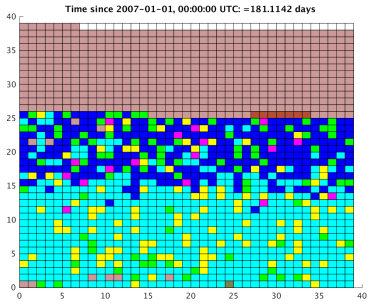

(c) $time_{passed} = 181.1142$ days.

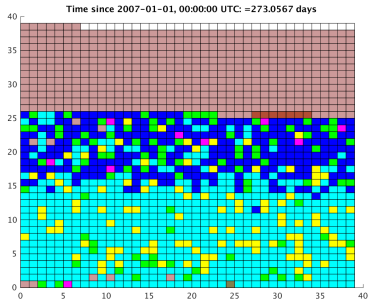

(d) $time_{passed} = 273.0567$ days.

Figure 6.17: Snapshots of near-GEO object categorization grid for the year 2007. $time_{passed}$ is the time passed since 00:00:00 UTC, January 1, 2007.

476 out of 1001 objects change their categorization at least once during 2007.

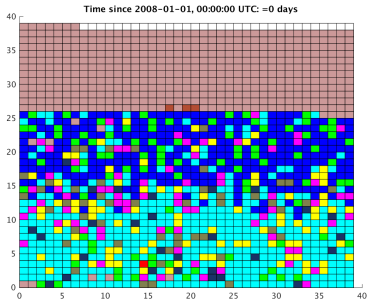

(a) $time_{passed} = 0$ days.

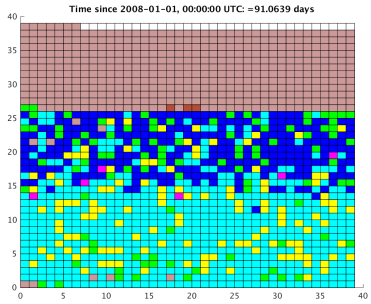

(b) $time_{passed} = 91.0639$ days.

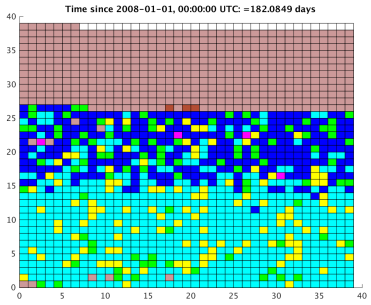

(c) $time_{passed}$ = 182.0849 days.

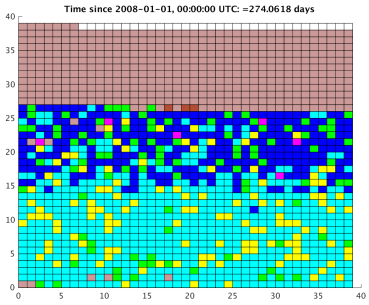

(d) $time_{passed}$ = 274.0618 days.

Figure 6.18: Snapshots of near-GEO object categorization grid for the year 2008. $time_{passed}$ is the time passed since 00:00:00 UTC, January 1, 2008.

490 out of 1028 objects change their categorization at least once during 2008.

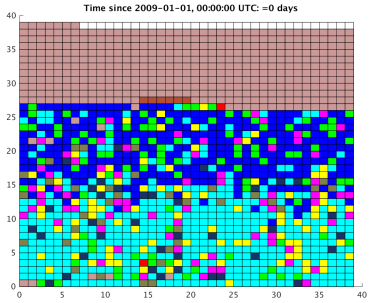

(a) $time_{passed}$ = 0 days.

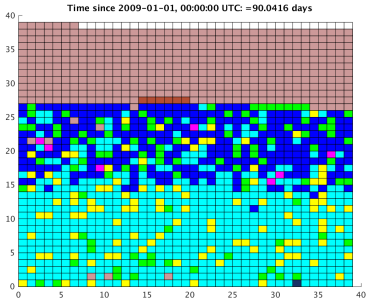

(b) $time_{passed}$ = 90.0416 days.

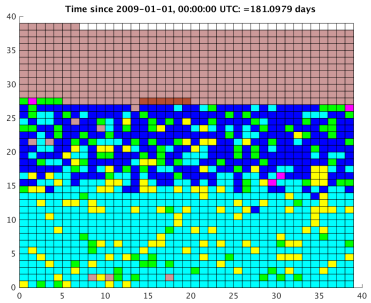

(c) $time_{passed}$ = 181.0979 days.

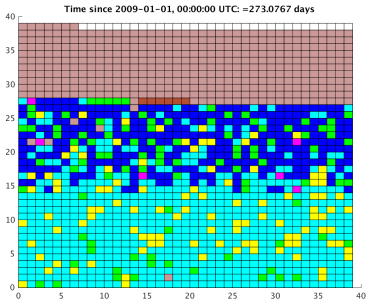

(d) $time_{passed}$ = 273.0767 days.

Figure 6.19: Snapshots of near-GEO object categorization grid for the year 2009. $time_{passed}$ is the time passed since 00:00:00 UTC, January 1, 2009.

538 out of 1069 objects change their categorization at least once during 2009.

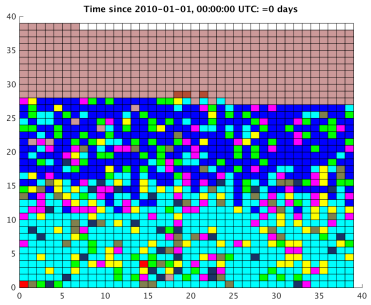

(a) $time_{passed} = 0$ days.

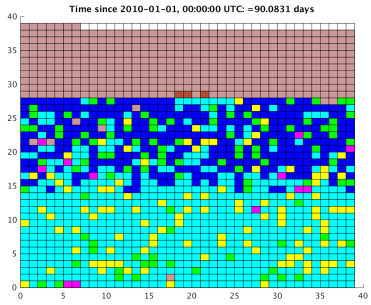

(b) $time_{passed} = 90.0831$ days.

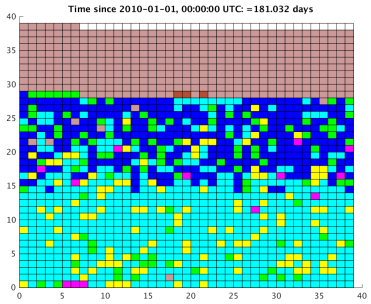

(c) $time_{passed} = 181.032$ days.

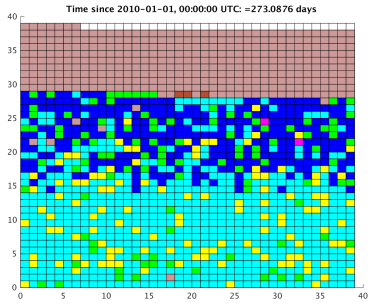

(d) $time_{passed} = 273.0876$ days.

Figure 6.20: Snapshots of near-GEO object categorization grid for the year 2010. $time_{passed}$ is the time passed since 00:00:00 UTC, January 1, 2010.

553 out of 1108 objects change their categorization at least once during 2010.

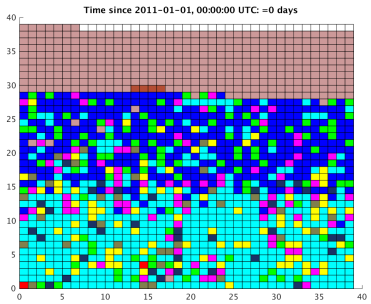

(a) $time_{passed} = 0$ days.

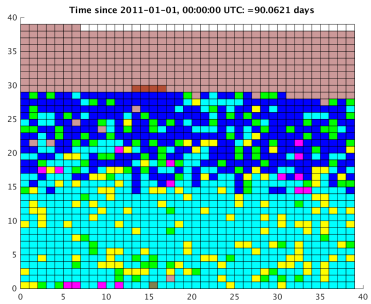

(b) $time_{passed} = 90.0621$ days.

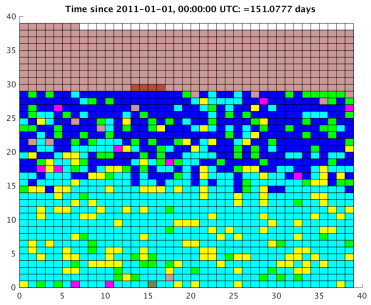

(c) $time_{passed}$ = 151.0777 days.

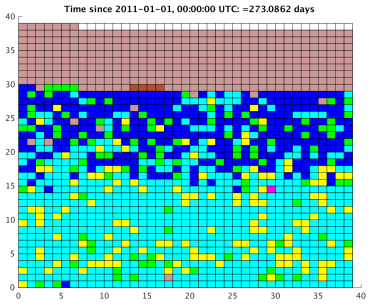

(d) $time_{passed}$ = 273.0862 days.

Figure 6.21: Snapshots of near-GEO object categorization grid for the year 2011. $time_{passed}$ is the time passed since 00:00:00 UTC, January 1, 2011.

569 out of 1140 objects change their categorization at least once during 2011.

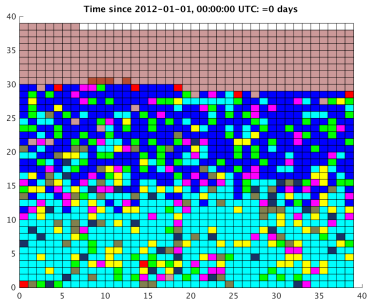

(a) $time_{passed}$ = 0 days.

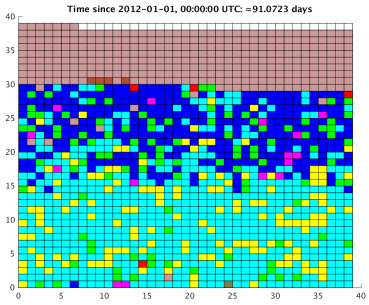

(b) $time_{passed}$ = 91.0723 days.

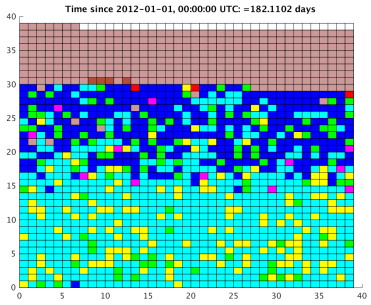

(c) $time_{passed}$ = 182.1102 days.

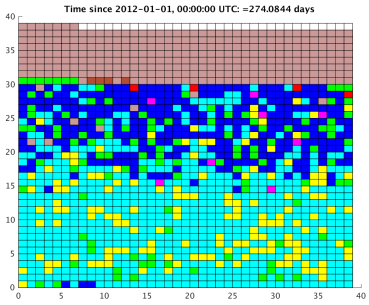

(d) $time_{passed}$ = 274.0844 days.

Figure 6.22: Snapshots of near-GEO object categorization grid for the year 2012. $time_{passed}$ is the time passed since 00:00:00 UTC, January 1, 2012.

598 out of 1176 objects change their categorization at least once during 2012. 612 out of 1230 objects change their categorization at least once during 2013.

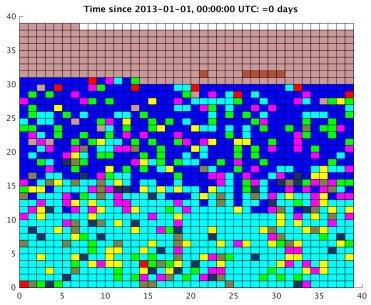

(a) $time_{passed} = 0$ days.

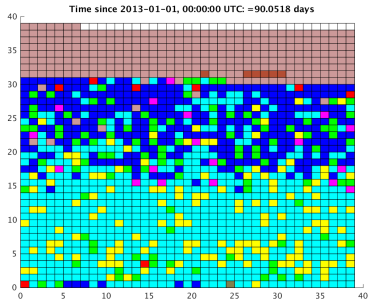

(b) $time_{passed} = 90.0518$ days.

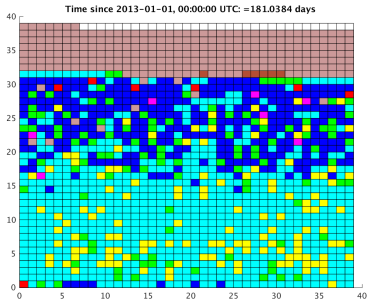

(c) $time_{passed} = 181.0384$ days.

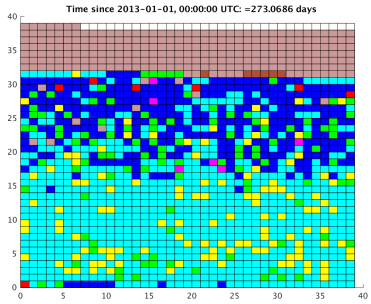

(d) $time_{passed} = 273.0686$ days.

Figure 6.23: Snapshots of near-GEO object categorization grid for the year 2013. $time_{passed}$ is the time passed since 00:00:00 UTC, January 1, 2013.

As can be seen from Figs. 6.11-6.23, object categorization may change not only over a longer period (of the order of years), but it may also change over a shorter duration (less than a year). The figures also show that the learned network classifies most of the catalog objects into three categories - category 3 (rich in E-W, N-S controlled objects), category 5 (rich in drifting objects), and category 6 (rich in objects librating about the Eastern stable point). The categorization scheme presented here, however, is limited by how well the Neural Network can learn the underlying dynamics to predict an object category. The Neural Network is able to categorize objects correctly for roughly 80% of the objects. The Neural Network does a better job in classifying categories 1 through 6 as compared to categories 7 and 8.

The presented scheme is best suitable for SSA purposes where there is too much orbital data for human scrutiny or where only occasional human scrutiny is possible.

Whenever the resources permit, the scheme should be used as a first-assessment tool for object categorization, with manual or human scrutiny as an additional check.

6.4 Concluding Remarks

To conclude, the combination of dynamical knowledge with the Neural Network machine learning technique provides a nice framework for autonomous and large-scale classification of space objects. Although a successful classification rate of roughly 80% is obtained, caution is to be adopted. Most of the objects that do not change category within a year belong to categories 1 through 6. There is a scope for improvement in the learning function or learning technique for classifying categories 7 and 8 objects (category 8 is not surprising since it is composed of objects from different categories).

7 CONCLUSIONS AND RECOMMENDATIONS

7.1 Conclusions

This dissertation performs the following four tasks: (1) investigation of fast analytical techniques for propagation of near-GEO space objects and improving their accuracy (2) analysis of cost-efficient methods to capture initial orbital uncertainties and propagating them using analytical techniques (3) using analytical uncertainty propagation to design a sensor tasking strategy for GEO space objects, with special focus on difficult-to-track high area-to-mass ratio objects (4) categorization of near-GEO space objects using a combined knowledge of dynamics and data-based learning techniques.

In the first task, analytical perturbations due to J_2, J_3, J_4 zonal harmonics of Earth's gravitational potential, $J_{[2,2]}$ tesseral harmonic of Earth's gravitational potential, Sun gravity, Moon gravity, solar radiation pressure, and Lorentz force are investigated. The accuracy of an existing analytical theory for third body perturbations is improved. This is achieved by retaining the r/r_d terms (r is the object distance from Earth's center and r_d is the third body distance from Earth's center) in acceleration components and integrating Gauss's variational equations. Following a 15-year simulation for a GEO object with just the Moon third body perturbations, it is demonstrated that the accuracy in eccentricity improves by one order of magnitude. The accuracy of an existing analytical theory for solar radiation pressure perturbations is improved. This is achieved by using the Strong-Stability Preserving Runge-Kutta scheme of order 2 to update orbital elements instead of a Euler scheme. Following a 30-year simulation for a GEO object with just the solar radiation pressure perturbations, it is demonstrated that the accuracy in eccentricity and argument of perigee improves by one order of magnitude.

An existing analytical theory for Lorentz force perturbations applicable only for low Earth orbits is modified to develop new analytical formulas applicable for both low

Earth and high Earth orbits. Two sets of analytical formulas are developed: one for low eccentric orbits, and one for orbits with any general eccentricity. The first set of analytical formulas (for low eccentric orbits) are developed by integrating Gauss's variational equations using the following two approximations: (I) $t = f/n$ (t is time, f is true anomaly, and n is mean motion) (II) $1/(1+e\cos f)$ (e is eccentricity) is replaced by its second-order Taylor series expansion. The second set of analytical formulas (for any general eccentric orbit) is developed by integrating Gauss's variational equations and using the Legendre-Gauss quadrature rule of order 12 to approximate some of the tricky integrals.

In the second task, GEO space objects with initial uncertainties in semi-major axis, eccentricity, inclination, argument of perigee, right ascension of ascending node, and area-to-mass ratio are propagated over a 15-year period and their distributions are analyzed. A multivariate Gaussian distribution is assumed for the initial distribution of the uncertain parameters. Two methods are used: (I) the initial uncertainty is captured using the traditional Monet Carlo particles and propagated using analytical solutions (II) the initial uncertainty is captured using sigma points and propagated using analytical solutions. The benefit of using the second method is that it requires only $(2 \times dimension + 1)$ sigma points to capture the object mean and co-variance, making it computationally more efficient than the Monte Carlo approach, which requires a large number of particles. In the Monte Carlo method, each object is represented using 1500 points, and in the Unscented Transformation method, each object is represented using 13 sigma points. The Monte Carlo based final distribution is then compared to the distribution obtained through the propagation of sigma points. It is demonstrated that the distribution from sigma points is able to follow the distribution from Monte Carlo points for eccentricity, inclination, argument of perigee, and right ascension of ascending node up to a logarithmic Kullback-Leibler divergence value of roughly -2, -3, -3, -4, respectively. For semi-major axis, the sigma points are able to follow the Monte Carlo points for relatively low area-to-mass ratios. Since Gaussian

distribution does not take into account the circular behavior of the parameters or the truncation in the range of the parameters, an investigation is carried out to assess the effect of the Gaussian assumption. It is found that for the numerical values considered in this work, the circular or the truncation behavior is not relevant to the uncertainty propagation problem.

The third task focuses on sensor tasking for the detection of unknown object classes. High area-to-mass ratio objects are one such class of objects that is focused upon in this dissertation. They are important because there is no catalog information available for high area-to-mass ratio objects because of their susceptibility to large perturbations from non-conservative perturbation forces. As a testbed case, a survey and follow-up of low area-to-mass ratio GEO objects using the so-called hypothesis surface are first carried out. This surface is generated by long-term propagation of hypothesis objects via analytic propagation techniques. A model, approximately mimicking the publicly available GEO catalog, is proposed for the generation of low area-to-mass ratio hypothesis objects. These hypothesis objects are assumed to have uncertainties, which are propagated from their initial epoch to the observation epoch. The surface is created using cumulative distributive function (CDF) values of the propagated hypothesis objects by dividing the observation space into small grids and subsequently filling them out with averaged CDF values. Initially, without any a priori information of the objects, observation direction is selected based on the surface. A 4-hour observation session is simulated to test the efficacy of the strategy. Over the observation duration, 209 of 614 GEO objects were within the field of regard at some point during that time window. The sensor tasking strategy selected 46 different grid fields observing 69 unique objects, 36 of which have been observed twice. Since the surface strategy produced surprisingly good detection results despite the approximations used in the creation of hypothesis objects, a survey strategy is carried out for difficult-to-detect high area-to-mass ratio objects. A heuristics-based birth-scheme is proposed for the generation of hypothesis high area-to-mass ratio

objects. Similar to low area-to-mass ratio objects, the hypothesis-surface is created using the cumulative distribution functions of the propagated hypothesis objects. A greedy algorithm is then used by the sensor tasking strategy to find directions with higher chances of object detection. Since HAMR objects are currently not in the catalog, the next step for the proposed HAMR detection method would be to run it with Purdue Optical Ground Station (POGS) telescope, and a successful detection would serve as the validation for the proposed method.

In the fourth task, a schematic is developed for the categorization of near-geosynchronous space objects. A dynamical criterion is presented to first categorize objects into eight different groups rich in high inclination objects, rocket bodies crossing GEO protected region, East-West and North-South controlled objects, East-West controlled objects, drifting objects, objects librating about the Eastern stable point, objects librating about the Western stable point, and a mixed group. The criterion is then used to train a Neural Network to categorize any new orbital data. Incoming two-line-element data between the years 2001 and 2013 are classified and represented in a 39×39 grid, which gives a holistic view of the categorization of all near-geosynchronous space objects at any point in time. As demonstrated, the categories of objects can change both over long and short periods of time. Most of the catalog objects are categorized into expected drifting, E-W/N-S controlled, and librating (about 75^0 E) objects. The Neural Network is able to classify objects correctly roughly 80% of the times. The Neural Network does a better job at classifying object categories 1 through 6 when compared to categories 7 and 8, thereby leaving room for improvements. The main advantage of the proposed scheme over a traditional classification scheme is its ability to handle large amount of space data and its ability to categorize any object without having to continuously monitor the orbit of the object.

The improvements made in the analytical perturbation expressions for

Recommendations for future work are provided in the next section.

7.2 Recommendations

Using the analytical orbit propagation techniques developed here, one can perform a variety of other SSA related tasks such as investigating the evolution of debris resulting from an anti-satellite test, investigating the long-term collision risks among various object populations, identification of unknown object classes besides the high area-to-mass ratio objects discussed in this dissertation.

The current analysis uses $(2 \times dimension + 1)$ sigma points to represent the uncertainty in each object. One can also use more number of sigma points per object and compare the propagated distributions resulting from sigma points and Monte Carlo particles, respectively.

The sensor tasking analysis in this dissertation is carried out for near-GEO objects. Using the methodology developed here, one can carry out a similar analysis for objects from low Earth and middle Earth orbital regions. The k-surface designed in this dissertation can be used to detect actual high area-to-mass ratio objects using an actual telescope. Additionally, the current sensor tasking strategy employs only one ground-based optical sensor; the work can be extended to employ multiple ground-based and space-based sensors.

For the object categorization purpose, Neural Network is used as the learning algorithm in this work. One can also try out other learning algorithms for object categorization and carry out a comparison between the results of the different algorithms.

VITA

Smriti Nandan Paul was born and brought up in the State of Assam in India. He attended the Indian Institute of Technology Bombay from 2010 to 2015 for his Dual Degree in Aerospace Engineering. Soon after that, in the year 2015, he joined the Space Information Dynamics group at Purdue University for his Ph.D. program. His research background includes orbital mechanics, space situational awareness, dynamics and control, navigation and guidance, and multi-disciplinary optimization.

REFERENCES

[1] Y. Kozai. The motion of a close earth satellite. *The Astronomical Journal*, 64: 367–377, 1959.

[2] D. Brouwer. Solution of the problem of artificial satellite theory without drag. *The Astronomical Journal*, 64:378–396, 1959.

[3] Y. Kozai. Second-order solution of artificial satellite theory without air drag. *The Astronomical Journal*, 67:446–461, 1962.

[4] R.H. Lyddane. Small eccentricities or inclinations in the brouwer theory of the artificial satellite. *The Astronomical Journal*, 68:555–558, 1963.

[5] D. Brouwer and G.I. Hori. Theoretical evaluation of atmospheric drag effects in the motion of an artificial satellite. *The Astronomical Journal*, 66(5):193–225, 1961.

[6] K. Aksnes. A second-order artificial satellite theory based on an intermediate orbit. *The Astronomical Journal*, 75(9):1066–1076, 1970.

[7] G.I. Hori. Theory of general perturbations with unspecified canonical variables. *Publications of the Astronomical Society of Japan*, 18(4):287–296, 1966.

[8] A. Deprit and A. Rom. The main problem of artificial satellite theory for small and moderate eccentricities. *Celestial Mechanics*, 2(2):166–206, 1970.

[9] A. Deprit. Canonical transformations depending on a small parameter. *Celestial Mechanics*, 1(1):12–30, 1969.

[10] G.E. Cook. Perturbations of satellite orbits by tesseral harmonics in the earth's gravitational potential. *Planet Space Sci.*, 11(7):797–815, 1963.

[11] W.M. Kaula. *Theory of Satellite Geodesy*. Blaisdell, Waltham, MA, 1966.

[12] E. Wnuk. Tesseral harmonic perturbations for high order and degree harmonics. *Celestial Mechanics*, 44:179–191, 1988.

[13] E. Wnuk. Tesseral harmonic perturbations in the keplerian orbital elements. *Acta Astronomica*, 40:191–198, 1990.

[14] M.T. Lane. An analytical treatment of resonance effects on satellite orbits. *Celestial Mechanics*, 42:3–38, 1987.

[15] G.E. Cook. Luni-solar perturbations of the orbit of an earth satellite. *The Geophysical Journal*, 6(3):375–386, 1961.

[16] A.E. Roy. Luni-solar perturbations of an earth satellite. *Astrophysics and Space Science*, 4(4):375–386, 1969.

[17] E.W. Brown. *Tables of the Motion of the Moon.* Yale Univ. Press, New Haven, CT, 1919.

[18] G.E.O. Giacaglia. Lunar perturbations on artificial satellites of the earth. *Celestial Mechanics*, 9(2):239–267, 1974.

[19] Y. Kozai. Effects of solar radiation pressure on the motion of an artificial satellite. *Smithsonian Contributions to Astrophysics*, 6:109–112, 1963.

[20] K. Aksnes. Short-period and long-period perturbations of a spherical satellite due to direct solar radiation. *Celestial Mechanics*, 13:89–104, 1976.

[21] C. Peng and Y. Gao. Lorentz-force-perturbed orbits with application to j2-invariant formation. *Acta Astronautica*, 77:12–28, 2012.

[22] H. Schaub and K. T. Alfriend. j_2 invariant relative orbits for spacecraft formations. *Celestial Mechanics and Dynamical Astronomy*, 79:77–95, 2001.

[23] B. Mahajan, S.R. Vadali, and K.T. Alfriend. Analytic solution for satellite relative motion: The complete zonal gravitational problem. In *Proceedings of the*

26th AAS/AIAA Space Flight Mechanics Meeting, pages 3325–3348. American Astronautical Society, 2016.

[24] A.J. Rosengren and D.J. Scheeres. Long-term propagation of high area-to-mass ratio objects using averaged equations. *Proc. 6th European Conference on Space Debris*, 2013.

[25] A.J. Rosengren and D.J. Scheeres. On the milankovitch orbital elements for perturbed keplerian motion. *Celestial Mechanics and Dynamical Astronomy*, 118(3):197–220, 2014.

[26] A.J. Rosengren and D.J. Scheeres. Long-term dynamics of hamr objects in heo. *AIAA/AAS Astrodynamics Specialist Conference*, 2012.

[27] William E. Wiesel. Relative satellite motion about an oblate planet. *Journal of Guidance, Control, and Dynamics*, 25(4):776–785, 2002.

[28] G. J. Der. An elegant state transition matrix. *American Institute of Aeronautics and Astronautics*, A9634790:776–791, 1996.

[29] G.E. Pollock, J.W. Gangestad, and J.M. Longuski. Analytical solutions for the relative motion of spacecraft subject to lorentz-force perturbations. *Acta Astronautica*, 68(1), 2011.

[30] S.J. Julier and J.K. Uhlmann. A new extension of the kalman filter to nonlinear systems. *The 11th International Symposium on Aerospace/Defence Sensing, Simulation and Controls*, 1997.

[31] T. Schildknecht, R. Musci, M. Ploner, G. Beutler, W. Flury, J. Kuusela, L. Cruz, and F.D. Palmero. Optical observations of space debris in geo and in highly-eccentric orbits. *Advances in Space Research*, 34(5):901–911, 2004.

[32] T. Schildknecht, R. Musci, M. Ploner, W. Flury, J. Kuusela, L. Cruz, and F.D. Palmero. An optical search for small-size debris in geo and gto. *In Proceedings of the AMOS Technical Conference*, 2003.

[33] S.E. DeForest. Spacecraft charging at synchronous orbit. *Journal of Geophysical Research*, 77(4):651–659, 1972.

[34] S.T. Lai. *Fundamentals of Spacecraft Charging: Spacecraft Interactions with Space Plasmas*. Princeton University Press, Princeton, New Jersey, 2012.

[35] P.C. Anderson. Characteristic of spacecraft charging in low earth orbit. *Journal of Geophysical Research*, 117, 2012.

[36] C. Frueh, H. Fiedler, and J. Herzog. Heuristic and optimized sensor tasking observation strategies with exemplification for geosynchronous objects. *Journal of Guidance, Control, and Dynamics*, 41(5):1036–1048, 2018.

[37] D.A. Vallado. *Fundamentals of Astrodnyamics and Applications*. Microcosm Press and Springer, Hawthorne, CA and New York, NY, 2007.

[38] B.J. Cain. Determination of mean elements for brouwer's satellite theory. *The Astronomical Journal*, 67(6):391–392, 1962.

[39] J.R. Dormand and P.J. Prince. A family of embedded runge-kutta formulae. *Journal of Computational and Applied Mathematics*, 6(1):19–26, 1980.

[40] R.H. Merson. The motion of a satellite in an axi-symmetric gravitational field. *Geophysical Journal International*, 4:17–52, 1961.

[41] K.C. Howell, D.J. Grebow, and Z.P. Olikara. Design using gauss' perturbing equations with applications to lunar south pole coverage. *Proceedings of the 17th Spaceflight Mechanics Meeting, American Astronautical Society, Paper 07-143, Sedona, AZ*, 2007.

[42] C. Frueh, T.M. Kelecy, and M.K. Jah. Coupled orbit-attitude dynamics of high area-to-mass ratio (HAMR) objects: Influence of solar radiation pressure, earth's shadow and the visibility in light curves. *Celestial Mechanics and Dynamical Astronomy*, 117:385–404, 2013.

[43] S. Valk and A. Lemaitre. Semi-analytic investigations of high area-to-mass ratio geosynchronous space debris including earth's shadowing effects. *Advances in Space Research*, 42:1429–1443, 2008.

[44] Eric Robinson. Comparing three types of numerical techniques for the integration of perturbed satellite motion. *Lawrence Livermore National Laboratory Report LLNL-TR-438273*, 2010.

[45] David Houcque. Applications of matlab: Ordinary differential equations (ode). *Applied Science Notes from Northwestern University (Available Online).*

[46] P. Bogacki and L.F. Shampine. A 3(2) pair of runge-kutta formulas. *Appl. Math. Letters*, 2:321–325, 1989.

[47] L.F. Shampine and M.K. Gordon. *Computer Solution of Ordinary Differential Equations: The Initial Value Problem.* W.H. Freeman, San Francisco, CA, 1975.

[48] L.F. Shampine and M.W. Reichelt. The matlab ode suite. *SIAM Journal on Scientific Computing*, 18:1–22, 1997.

[49] L.F. Shampine and M.W. Reichelt. Solving index-1 daes in matlab and simulink. *SIAM Review*, 41:538–552, 1999.

[50] L.F. Shampine and M.E. Hosea. Analysis and implementation of tr-bdf2. *Applied Numerical Mathematics 20*, 1996.

[51] R.E. Bank, W.C. Coughran, W. Fichtner, E. Grosse, D. Rose, and R. Smith.

[52] S. Pines. Uniform representation of the gravitational potential and its derivatives. *AIAA Journal*, 11(11):1508–1511, 1973.

[53] J. P. McCollough, J. L. Gannon, D. N. Baker, and M. Gehmeyr. A statistical comparison of commonly used external magnetic field models. *Space Weather*, 6 (10), 2008.

[54] N.A. Tsyganenko. Data-based modelling of the earth's dynamic magnetosphere: a review. *Annales Geophysicae*, 31(10):1745–1772, 2013.

[55] N.A. Tsyganenko. Data-based modeling of the geomagnetosphere with an IMF-dependent magnetopause. *Journal of Geophysical Research: Space Physics*, 119 (1):335–354, 2014.

[56] J.R. Wertz. *Spacecraft Attitude Determination and Control*. Kluwer Academic Publishers, Dordrecht, The Netherlands, 1978.

[57] Erwan Thébault, Christopher C Finlay, Ciarán D Beggan, Patrick Alken, Julien Aubert, Olivier Barrois, Francois Bertrand, Tatiana Bondar, Axel Boness, Laura Brocco, Elisabeth Canet, Aude Chambodut, Arnaud Chulliat, Pierdavide Coïsson, Francois Civet, Aimin Du, Alexandre Fournier, Isabelle Fratter, Nicolas Gillet, Brian Hamilton, Mohamed Hamoudi, Gauthier Hulot, Thomas Jager, Monika Korte, Weijia Kuang, Xavier Lalanne, Benoit Langlais, Jean-Michel Léger, Vincent Lesur, and Frank J Lowes et al. International geomagnetic reference field: The 12th generation. *Earth, Planets and Space*, 67(79), 2015.

[58] Richard Fitzpatrick. *Plasma Physics: An Introduction*. Taylor and Francis, Boca Raton, FL, 2014.

[59] S.N. Paul and C. Frueh. Space-object charging and its effect on orbit evolution. *Journal of Guidance, Control, and Dynamics*, 40(12):3180–3198, 2017.

[60] E.C. Whipple. Potentials of surfaces in space. *Reports on Progress in Physics*, 44(11):1197–1250, 1981.

[61] E.J. Sternglass. Theory of secondary electron emission by high-speed ions. *Physical Review*, 108(1):1–12, 1957.

[62] G.D. Archard. Back scattering of electrons. *Journal of Applied Physics*, 32(8): 1505–1509, 1961.

[63] T.E. Everhart. Simple theory concerning the reflection of electrons from solids. *Journal of Applied Physics*, 31(8):1483–1490, 1960.

[64] J.B. Jeanneret. Photoemission at lhc - a simple model. *CERN/Note 97-48 (AP)*, 1997.

[65] C.J. Powell. Analysis of optical and inelastic electron scattering data, iii: Reflectance data for beryllium, germanium, antimony and bismuth. *Journal of the Optical Society of America*, 60(2):214–220, 1970.

[66] S.T. Lai and M.F. Tautz. Aspects of spacecraft charging in sunlight. *IEEE Transactions on Plasma Science*, 34(5):2053–2061, 2006.

[67] A.S. Blazev. *Photovoltaics for Commercial and Utilities Power Generation*. The Fairmount Press, Inc., Lilburn, GA, 2011.

[68] R.H. Fowler. The analysis of photoelectric sensitivity curves for clean metals at various temperatures. *Physical Review*, 38(1):45–56, 1931.

[69] K.D. Moller. *Optics: Learning by Computing, with Model Examples Using MathCAD, Matlab, Mathematica and Maple*. Springer Science+Business Media, New York, 2007.

[70] L.G. Schulz and F.R. Tangherlini. Optical constants of silver, gold, copper and aluminum, ii: The index of refraction. *Journal of the Optical Society of America*, 44(5):362–368, 1954.

[71] R. Brendel and D. Bormann. An infrared dielectric function model for amorphous solids. *Journal of Applied Physics*, 71(1), 1991.

[72] A.D. Rakic, A.B. Djurisic, J.M. Elazar, and M.L. Majewski. Optical properties of metallic films for vertical-cavity optoelectronic devices. *Applied Optics*, 37 (22):5271–5283, 1998.

[73] M. H. Denton, M. F. Thomsen, Korth H., Lynch S., J. C. Zhang, and M. W. Liemohn. Bulk plasma properties at geosynchronous orbit. *Journal of Geophysical Research*, 110(A7), 2005.

[74] Paul S.N. Frueh, C. Orbit-attitude changes of objects in near earth space induced by natural charging. *AFRL Report AFRL-RV-PS-TR-2017-0007*, 2017.

[75] E. Thébault, C.C. Finlay, C.D. Beggan, P. Alken, J. Aubert, O. Barrois, F. Bertrand, T. Bondar, A. Boness, L. Brocco, and et al. International geomagnetic reference field: the 12th generation. *Earth, Planets and Space*, 67(79), 2015.

[76] A.E. Roy. *Orbital Motion*. A. Hilger, Philadelphia, PA, 1988.

[77] P.L. Gupta and R.D. Gupta. Sample size determination in estimating a covariance matrix. *Computational Statistics and Data Analysis*, 5:185–192, 1987.

[78] G.M. Tallis. The moment generating function of the truncated multinormal distribution. *Journal of the Royal Statistical Society, Series B*, 23(1):223–229, 1961.

[79] N. Johnson and S. Kotz. *Distribution in statistics: continuous multivariate distributions*. Wiley, New York, 1972.

[80] L.-F. Lee. On the first and second moments of the truncated multi-normal distribution and a simple estimator. *Economics Letters*, 3(2):165–169, 1979.

[81] P. Leppard and G.M. Tallis. Evaluation of the mean and covariance of the truncated multinormal. *Journal of the Royal Statistical Society*, 38(3):543–553, 1989.

[82] B.G. Manjunath and S. Wilhelm. Moments calculation for the double truncated multivariate normal density. `https://arxiv.org/abs/1206.5387`. 2012.

[83] G. Kurz, I. Gilitschenski, and U.D. Hanebeck. The partially wrapped normal distribution for se(2) estimation. *IEEE International Conference on Multisensor Fusion and Information Integration, Beijing, China*, 2014.

[84] R. Musci, T. Schildknecht, T. Flohrer, and G. Beutler. Concept for a catalogue of space debris in geo. *Fourth European Conference on Space Debris, pp. 601-606, ESOC, Darmstadt, Germany*, 2005.

[85] R. Musci, T. Schildknecht, M. Ploner, and G. Beutler. Orbit improvement for GTO objects using follow-up obervations. *Advances in Space Research*, 35(7): 1236–1242, 2005.

[86] J. Herzog. Cataloguing of objects on high and intermediate altitude orbits. *PhD dissertation treatise, Astronomical Institute, University of Bern*, 2013.

[87] B.D. Little and C. Frueh. Ssa sensor tasking: comparison of machine learning with classical optimization methods. *Advanced Maui Optical and Space Surveillance (AMOS) Technologies Conference, Maui, HI*, 2018.

[88] S.K. Flegel, J. Gelhaus, M. McKel, C. Wiedemann, H. Krag, H. Klinkrad, P. Vorsmann, and M. Oswald. The master-2009 space debris environment model. *European Space Agency, (Special Publication) ESA SP. 672*, 2009.

[89] M. P. Wilkins, A. Pfeffer, P. W. Schumacher, and M. K. Jah. Towards an artificial space object taxonomy. *Advanced Maui Optical and Space Surveillance Technologies Conference (AMOS), Maui, HI*, 2013.

[90] C. Frueh, M. Jah, E. Valdez, P. Kervin, and T. Kelecy. Taxonomy and classification scheme for artificial space objects. *Advanced Maui Optical and Space Surveillance Technologies Conference (AMOS), Maui, HI*, 2013.

[91] B. Jia, K.D. Pham, E. Blasch, D. Shen, Z. Wang, and G. Chen. Space object classification using fused features of time series data. *Advanced Maui Optical and Space Surveillance Technologies Conference (AMOS), Maui, HI*, 2017.

[92] Rochelle Mellish. An automated space object taxonomy of geostationary objects. *PhD dissertation, School of Aeronautics and Astronautics, Purdue University*, 2017.

[93] T.S. Kelso. Revisiting spacetrack report 3 AIAA 2006-6753. *Available online.*

[94] IERS EOP PC. Interactive search for EOP C04. *Available online.*

[95] Jean Kechichian. Optimal steering for north–south stationkeeping of geostationary spacecraft. *Journal of Guidance, Control, AND Dynamics*, 20(3):435–444, 1997.

[96] S. J. Russell and P. Norvig. *Artificial Intelligence: A Modern Approach.* Prentice Hall, Englewood Cliffs, NJ, 1995.

[97] Andrew Ng. Machine Learning, Stanford University. *Available online.*

[98] Jason Brownlee. How to configure the number of layers and nodes in a neural network (available online). 2018.

A COEFFICIENTS FOR SECOND ORDER PERTURBATIONS IN ECCENTRICITY DUE TO LUNI-SOLAR GRAVITY

Parameter g_1:

$$g_1 = \frac{g_{1_1} + g_{1_2} - g_{1_3}}{g_{1_4} - g_{1,5}} - \frac{g_{1_6}}{g_{1_7}} \tag{250}$$

where,

$$g_{1_1} = \frac{\tan\left(\frac{y}{2}\right)^5 \left(2\,e^3 + e^2 + 6\,e + 2\right)}{(e-1)\,(e+1)^3} \tag{251}$$

$$g_{1_2} = \frac{\tan\left(\frac{y}{2}\right) \left(2\,e^3 - e^2 + 6\,e - 2\right)}{(e+1)\left(e^3 - 3\,e^2 + 3\,e - 1\right)} \tag{252}$$

$$g_{1_3} = \frac{20\,e\tan\left(\frac{y}{2}\right)^3 \left(e^2+1\right)}{3\,(e+1)^2\left(e^2 - 2\,e + 1\right)} \tag{253}$$

$$\begin{aligned} g_{1_4} = 3\,e &- \tan\left(\frac{y}{2}\right)^6 \left(e^3 - 3\,e^2 + 3\,e - 1\right) \\ &+ \tan\left(\frac{y}{2}\right)^2 \left(-3\,e^3 - 3\,e^2 + 3\,e + 3\right) \end{aligned} \tag{254}$$

$$g_{1_5} = \tan\left(\frac{y}{2}\right)^4 \left(-3\,e^3 + 3\,e^2 + 3\,e - 3\right) - 3\,e^2 - e^3 - 1 \tag{255}$$

$$g_{1_6} = 5\,e^2\,\mathrm{atanh}\left(\frac{\tan\left(\frac{y}{2}\right)\left(2\,e-2\right)\left(e^3 - 3\,e^2 + 3\,e - 1\right)}{2\,(e-1)^{7/2}\sqrt{e+1}}\right) \tag{256}$$

$$g_{1_7} = (e-1)^{7/2}\,(e+1)^{7/2} \tag{257}$$

where $y = \pi - \epsilon$, with ϵ being an arbitrary positive number that is extremely close to zero.

Parameter h_1:

$$h_1 = \frac{h_{1_1}}{h_{1_2}} - \frac{h_{1_3} + h_{1_4} - h_{1_5}}{h_{1_6} - h_{1_7} + h_{1_8}} \tag{258}$$

where,

$$h_{1_1} = 5\,e^2\,\text{atanh}\left(\frac{\tan\left(\frac{y}{2}\right)\,\left(2\,e+2\right)\,\left(e^3+3\,e^2+3\,e+1\right)}{2\,\sqrt{e-1}\,\left(e+1\right)^{7/2}}\right) \tag{259}$$

$$h_{1_2} = \left(e-1\right)^{7/2}\left(e+1\right)^{7/2} \tag{260}$$

$$h_{1_3} = \frac{\tan\left(\frac{y}{2}\right)\,\left(2\,e^3+e^2+6\,e+2\right)}{\left(e-1\right)\,\left(e^3+3\,e^2+3\,e+1\right)} \tag{261}$$

$$h_{1_4} = \frac{\tan\left(\frac{y}{2}\right)^5\,\left(2\,e^3-e^2+6\,e-2\right)}{\left(e-1\right)^3\,\left(e+1\right)} \tag{262}$$

$$h_{1_5} = \frac{20\,e\,\tan\left(\frac{y}{2}\right)^3\,\left(e^2+1\right)}{3\,\left(e-1\right)^2\,\left(e^2+2\,e+1\right)} \tag{263}$$

$$h_{1_6} = \tan\left(\frac{y}{2}\right)^6\,\left(e^3+3\,e^2+3\,e+1\right) - 3\,e \tag{264}$$

$$h_{1_7} = \tan\left(\frac{y}{2}\right)^2\,\left(-3\,e^3+3\,e^2+3\,e-3\right) \tag{265}$$

$$h_{1_8} = \tan\left(\frac{y}{2}\right)^4\,\left(-3\,e^3-3\,e^2+3\,e+3\right) + 3\,e^2 - e^3 + 1 \tag{266}$$

where $y = \pi - \epsilon$, with ϵ being an arbitrary positive number that is extremely close to zero.

Parameter g_2:

$$g_2 = \frac{48\,y - g_{2_1} - g_{2_2} + g_{2_3} + g_{2_4}}{6\,e^4} \tag{267}$$

where,

$$g_{2_1} = \frac{\operatorname{atanh}\left(\frac{\tan\left(\frac{y}{2}\right)(e-1)}{\sqrt{e^2-1}}\right)\,\left(210\,e^6 - 420\,e^4 + 336\,e^2 - 96\right)}{\left(e^2-1\right)^{7/2}} \tag{268}$$

$$g_{2_2} = \frac{e\,\sin\left(y\right)\,\left(44\,e^6 - 219\,e^4 + 248\,e^2 - 88\right)}{\left(e\,\cos\left(y\right)+1\right)\,\left(e^2-1\right)^3} \tag{269}$$

$$g_{2_3} = \frac{2\,e\,\sin\left(y\right)\,\left(e^4 - 8\,e^2 + 8\right)}{\left(e\,\cos\left(y\right)+1\right)^3\,\left(e^2-1\right)} \tag{270}$$

$$g_{2_4} = \frac{e\,\sin\left(y\right)\,\left(43\,e^4 - 104\,e^2 + 56\right)}{\left(e\,\cos\left(y\right)+1\right)^2\left(e-1\right)^2\left(e+1\right)^2} \tag{271}$$

where $y = \pi - \epsilon$, with ϵ being an arbitrary positive number that is extremely close to zero.

Parameter h_2:

$$h_2 = \frac{48\,y + h_{2_1} - h_{2_2} + h_{2_3} - h_{2_4}}{6\,e^4} \tag{272}$$

where,

$$h_{2_1} = \frac{\operatorname{atanh}\left(\frac{\tan\left(\frac{y}{2}\right)(e+1)}{\sqrt{e^2-1}}\right)\,\left(210\,e^6 - 420\,e^4 + 336\,e^2 - 96\right)}{\left(e^2-1\right)^{7/2}} \tag{273}$$

$$h_{2_2} = \frac{e\,\sin\left(y\right)\,\left(44\,e^6 - 219\,e^4 + 248\,e^2 - 88\right)}{\left(e\,\cos\left(y\right)-1\right)\,\left(e^2-1\right)^3} \tag{274}$$

$$h_{2_3} = \frac{2\,e\,\sin\left(y\right)\,\left(e^4 - 8\,e^2 + 8\right)}{\left(e\,\cos\left(y\right)-1\right)^3\,\left(e^2-1\right)} \tag{275}$$

$$h_{2_4} = \frac{e\,\sin(y)\,\left(43\,e^4 - 104\,e^2 + 56\right)}{\left(e\,\cos(y) - 1\right)^2\left(e-1\right)^2\left(e+1\right)^2} \tag{276}$$

where $y = \pi - \epsilon$, with ϵ being an arbitrary positive number that is extremely close to zero.

Parameter $\mathcal{P}_9$:

$$\begin{aligned}\mathcal{P}_9 = {} & 56.806e^9 + 106.92e^8 + .40918e^7 + 49.464e^6 + .00038031e^5 \\ & + 13.744e^4 + 5.0353\times10^{-8}e^3 - 2.3907\times10^{-10}e^2 \\ & + 5.0403\times10^{-13}e - 5.694\times10^{-16}\end{aligned} \tag{277}$$

Parameter g_3:

$$g_3 = \frac{g_{3_1} - g_{3_2} + g_{3_3}}{g_{3_4} + g_{3_5} + g_{3_6}} - \frac{\operatorname{atanh}\left(\frac{\tan\left(\frac{y}{2}\right)(2\,e-2)\left(e^3-3\,e^2+3\,e-1\right)}{2\,(e-1)^{7/2}\sqrt{e+1}}\right)\,\left(3\,e^2+2\right)}{\left(e-1\right)^{7/2}\left(e+1\right)^{7/2}} \tag{278}$$

where,

$$g_{3_1} = \frac{\tan\left(\frac{y}{2}\right)\,\left(2\,e^3 - 3\,e^2 + 6\,e\right)}{\left(e+1\right)\,\left(e^3 - 3\,e^2 + 3\,e - 1\right)} \tag{279}$$

$$g_{3_2} = \frac{4\tan\left(\frac{y}{2}\right)^3\,\left(e^3 + 9\,e\right)}{3\left(e+1\right)^2\,\left(e^2 - 2\,e + 1\right)} \tag{280}$$

$$g_{3_3} = \frac{\tan\left(\frac{y}{2}\right)^5\,\left(2\,e^3 + 3\,e^2 + 6\,e\right)}{\left(e-1\right)\,\left(e+1\right)^3} \tag{281}$$

$$g_{3_4} = 3\,e - \tan\left(\frac{y}{2}\right)^6\,\left(e^3 - 3\,e^2 + 3\,e - 1\right) \tag{282}$$

$$g_{3_5} = \tan\left(\frac{y}{2}\right)^2 \left(-3\,e^3 - 3\,e^2 + 3\,e + 3\right) \tag{283}$$

$$g_{3_6} = -\tan\left(\frac{y}{2}\right)^4 \left(-3\,e^3 + 3\,e^2 + 3\,e - 3\right) + 3\,e^2 + e^3 + 1 \tag{284}$$

where $y = \pi - \epsilon$, with ϵ being an arbitrary positive number that is extremely close to zero.

Parameter h_3:

$$h_3 = \frac{h_{3_1}}{h_{3_2}} - \frac{h_{3_3} - h_{3_4} + h_{3_5}}{h_{3_6} - h_{3_7} + h_{3_8}} \tag{285}$$

where,

$$h_{3_1} = \operatorname{atanh}\left(\frac{\tan\left(\frac{y}{2}\right)\,(2\,e+2)\,(e^3 + 3\,e^2 + 3\,e + 1)}{2\,\sqrt{e-1}\,(e+1)^{7/2}}\right)\left(3\,e^2 + 2\right) \tag{286}$$

$$h_{3_2} = (e-1)^{7/2}\,(e+1)^{7/2} \tag{287}$$

$$h_{3_3} = \frac{\tan\left(\frac{y}{2}\right)\,(2\,e^3 + 3\,e^2 + 6\,e)}{(e-1)\,(e^3 + 3\,e^2 + 3\,e + 1)} \tag{288}$$

$$h_{3_4} = \frac{4\tan\left(\frac{y}{2}\right)^3\,(e^3 + 9\,e)}{3\,(e-1)^2\,(e^2 + 2\,e + 1)} \tag{289}$$

$$h_{3_5} = \frac{\tan\left(\frac{y}{2}\right)^5\,(2\,e^3 - 3\,e^2 + 6\,e)}{(e-1)^3\,(e+1)} \tag{290}$$

$$h_{3_6} = \tan\left(\frac{y}{2}\right)^6 \left(e^3 + 3\,e^2 + 3\,e + 1\right) - 3\,e \tag{291}$$

$$h_{3_7} = \tan\left(\frac{y}{2}\right)^2 \left(-3\,e^3 + 3\,e^2 + 3\,e - 3\right) \tag{292}$$

$$h_{3_8} = \tan\left(\frac{y}{2}\right)^4 \left(-3\,e^3 - 3\,e^2 + 3\,e + 3\right) + 3\,e^2 - e^3 + 1 \tag{293}$$

where $y = \pi - \epsilon$, with ϵ being an arbitrary positive number that is extremely close to zero.

Parameter g_4:

$$g_4 = \frac{g_{4_1} - g_{4_2} - g_{4_3} + g_{4_4}}{g_{4_5} + g_{4_6} - g_{4_7} + g_{4_8}} - \frac{5\,e\,\operatorname{atanh}\left(\frac{g_{4_9}}{g_{4_{10}}}\right)\,\left(3\,e^2 + 4\right)}{4\,(e-1)^{9/2}\,(e+1)^{9/2}} \tag{294}$$

where,

$$g_{4_1} = \frac{\tan\left(\frac{y}{2}\right)^5\,\left(40\,e^4 + 27\,e^3 + 336\,e^2 + 36\,e + 72\right)}{12\,(e+1)^3\,\left(e^2 - 2\,e + 1\right)} \tag{295}$$

$$g_{4_2} = \frac{\tan\left(\frac{y}{2}\right)^3\,\left(40\,e^4 - 27\,e^3 + 336\,e^2 - 36\,e + 72\right)}{12\,(e+1)^2\,\left(e^3 - 3\,e^2 + 3\,e - 1\right)} \tag{296}$$

$$g_{4_3} = \frac{\tan\left(\frac{y}{2}\right)^7\,\left(8\,e^4 + 17\,e^3 + 48\,e^2 + 12\,e + 8\right)}{(4\,e-4)\,(e+1)^4} \tag{297}$$

$$g_{4_4} = \frac{\tan\left(\frac{y}{2}\right)\,\left(8\,e^4 - 17\,e^3 + 48\,e^2 - 12\,e + 8\right)}{(4\,e+4)\,\left(e^4 - 4\,e^3 + 6\,e^2 - 4\,e + 1\right)} \tag{298}$$

$$g_{4_5} = 4\,e + \tan\left(\frac{y}{2}\right)^8 \left(e^4 - 4\,e^3 + 6\,e^2 - 4\,e + 1\right) \tag{299}$$

$$g_{4_6} = \tan\left(\frac{y}{2}\right)^2 \left(-4\,e^4 - 8\,e^3 + 8\,e + 4\right) \tag{300}$$

$$g_{4_7} = \tan\left(\frac{y}{2}\right)^6 \left(4\,e^4 - 8\,e^3 + 8\,e - 4\right) \tag{301}$$

$$g_{4_8} = \tan\left(\frac{y}{2}\right)^4 \left(6\,e^4 - 12\,e^2 + 6\right) + 6\,e^2 + 4\,e^3 + e^4 + 1 \tag{302}$$

$$g_{4_9} = e \tan\left(\frac{y}{2}\right) \left(2\,e - 2\right) \left(3\,e^2 + 4\right) \left(e^4 - 4\,e^3 + 6\,e^2 - 4\,e + 1\right) \tag{303}$$

$$g_{4_{10}} = \left(6\,e^3 + 8\,e\right) \left(e - 1\right)^{9/2} \sqrt{e + 1} \tag{304}$$

where $y = \pi - \epsilon$, with ϵ being an arbitrary positive number that is extremely close to zero.

Parameter h_4:

$$h_4 = \frac{h_{4_1} - h_{4_2} + h_{4_3} - h_{4_4}}{h_{4_5} - h_{4_6} + h_{4_7} + h_{4_8}} + \frac{5\,e\,\operatorname{atanh}\left(\frac{h_{4_9}}{h_{4_{10}}}\right) \left(3\,e^2 + 4\right)}{4\left(e - 1\right)^{9/2} \left(e + 1\right)^{9/2}} \tag{305}$$

where,

$$h_{4_1} = \frac{\tan\left(\frac{y}{2}\right)^5 \left(40\,e^4 - 27\,e^3 + 336\,e^2 - 36\,e + 72\right)}{12\left(e - 1\right)^3 \left(e^2 + 2\,e + 1\right)} \tag{306}$$

$$h_{4_2} = \frac{\tan\left(\frac{y}{2}\right)^3 \left(40\,e^4 + 27\,e^3 + 336\,e^2 + 36\,e + 72\right)}{12\left(e - 1\right)^2 \left(e^3 + 3\,e^2 + 3\,e + 1\right)} \tag{307}$$

$$h_{4_3} = \frac{\tan\left(\frac{y}{2}\right) \left(8\,e^4 + 17\,e^3 + 48\,e^2 + 12\,e + 8\right)}{\left(4\,e - 4\right) \left(e^4 + 4\,e^3 + 6\,e^2 + 4\,e + 1\right)} \tag{308}$$

$$h_{4_4} = \frac{\tan\left(\frac{y}{2}\right)^7 \left(8\,e^4 - 17\,e^3 + 48\,e^2 - 12\,e + 8\right)}{4\left(e - 1\right)^4 \left(e + 1\right)} \tag{309}$$

$$h_{4_5} = \tan\left(\frac{y}{2}\right)^8 \left(e^4 + 4\,e^3 + 6\,e^2 + 4\,e + 1\right) - 4\,e \tag{310}$$

$$h_{4_6} = \tan\left(\frac{y}{2}\right)^2 \left(4\,e^4 - 8\,e^3 + 8\,e - 4\right) \tag{311}$$

$$h_{4_7} = \tan\left(\frac{y}{2}\right)^6 \left(-4\,e^4 - 8\,e^3 + 8\,e + 4\right) \tag{312}$$

$$h_{4_8} = \tan\left(\frac{y}{2}\right)^4 \left(6\,e^4 - 12\,e^2 + 6\right) + 6\,e^2 - 4\,e^3 + e^4 + 1 \tag{313}$$

$$h_{4_9} = e\tan\left(\frac{y}{2}\right) (2\,e + 2)\left(3\,e^2 + 4\right)\left(e^4 + 4\,e^3 + 6\,e^2 + 4\,e + 1\right) \tag{314}$$

$$h_{4_{10}} = \left(6\,e^3 + 8\,e\right)\sqrt{e-1}\,(e+1)^{9/2} \tag{315}$$

where $y = \pi - \epsilon$, with ϵ being an arbitrary positive number that is extremely close to zero.

Parameter g_5:

$$g_5 = \frac{5\,e^2\,\mathrm{atanh}\left(\frac{g_{5_1}}{g_{5_2}}\right)(e^2+6)}{4\,(e-1)^{9/2}\,(e+1)^{9/2}} - \frac{g_{5_3} + g_{5_4} - g_{5_5} - g_{5_6}}{g_{5_7} + g_{5_8} - g_{5_9} + g_{5_{10}}} \tag{316}$$

where,

$$g_{5_1} = e^2\tan\left(\frac{y}{2}\right)(2\,e-2)\left(e^2+6\right)\left(e^4 - 4\,e^3 + 6\,e^2 - 4\,e + 1\right) \tag{317}$$

$$g_{5_2} = \left(2\,e^4 + 12\,e^2\right)(e-1)^{9/2}\sqrt{e+1} \tag{318}$$

$$g_{5_3} = \frac{\tan\left(\frac{y}{2}\right)^5 (33\,e^4 + 288\,e^3 + 6\,e^2 + 160\,e + 24)}{12\,(e+1)^3\,(e^2 - 2\,e + 1)} \tag{319}$$

$$g_{5_4} = \frac{\tan\left(\frac{y}{2}\right)^3 (33\,e^4 - 288\,e^3 + 6\,e^2 - 160\,e + 24)}{12\,(e+1)^2\,(e^3 - 3\,e^2 + 3\,e - 1)} \tag{320}$$

$$g_{5_5} = \frac{\tan\left(\frac{y}{2}\right)^7 (3\,e^4 + 32\,e^3 + 18\,e^2 + 32\,e + 8)}{(4\,e-4)\,(e+1)^4} \tag{321}$$

$$g_{5_6} = \frac{\tan\left(\frac{y}{2}\right)(3\,e^4 - 32\,e^3 + 18\,e^2 - 32\,e + 8)}{(4\,e+4)\,(e^4 - 4\,e^3 + 6\,e^2 - 4\,e + 1)} \tag{322}$$

$$g_{5_7} = 4\,e + \tan\left(\frac{y}{2}\right)^8 \left(e^4 - 4\,e^3 + 6\,e^2 - 4\,e + 1\right) \tag{323}$$

$$g_{5_8} = \tan\left(\frac{y}{2}\right)^2 \left(-4\,e^4 - 8\,e^3 + 8\,e + 4\right) \tag{324}$$

$$g_{5_9} = \tan\left(\frac{y}{2}\right)^6 \left(4\,e^4 - 8\,e^3 + 8\,e - 4\right) \tag{325}$$

$$g_{5_{10}} = \tan\left(\frac{y}{2}\right)^4 \left(6\,e^4 - 12\,e^2 + 6\right) + 6\,e^2 + 4\,e^3 + e^4 + 1 \tag{326}$$

where $y = \pi - \epsilon$, with ϵ being an arbitrary positive number that is extremely close to zero.

Parameter h_5:

$$h_5 = \frac{h_{5_1} + h_{5_2} - h_{5_3} - h_{5_4}}{h_{5_5} - h_{5_6} + h_{5_7} + h_{5_8}} - \frac{5\,e^2\,\mathrm{atanh}\left(\frac{h_{5_9}}{h_{5_{10}}}\right)\,(e^2+6)}{4\,(e-1)^{9/2}\,(e+1)^{9/2}} \tag{327}$$

where,

$$h_{5_1} = \frac{\tan\left(\frac{y}{2}\right)^5\,(33\,e^4 - 288\,e^3 + 6\,e^2 - 160\,e + 24)}{12\,(e-1)^3\,(e^2 + 2\,e + 1)} \tag{328}$$

$$h_{5_2} = \frac{\tan\left(\frac{y}{2}\right)^3\,(33\,e^4 + 288\,e^3 + 6\,e^2 + 160\,e + 24)}{12\,(e-1)^2\,(e^3 + 3\,e^2 + 3\,e + 1)} \tag{329}$$

$$h_{5_3} = \frac{\tan\left(\frac{y}{2}\right)\,(3\,e^4 + 32\,e^3 + 18\,e^2 + 32\,e + 8)}{(4\,e-4)\,(e^4 + 4\,e^3 + 6\,e^2 + 4\,e + 1)} \tag{330}$$

$$h_{5_4} = \frac{\tan\left(\frac{y}{2}\right)^7\,(3\,e^4 - 32\,e^3 + 18\,e^2 - 32\,e + 8)}{4\,(e-1)^4\,(e+1)} \tag{331}$$

$$h_{5_5} = \tan\left(\frac{y}{2}\right)^8 \left(e^4 + 4\,e^3 + 6\,e^2 + 4\,e + 1\right) - 4\,e \tag{332}$$

$$h_{5_6} = \tan\left(\frac{y}{2}\right)^2 \left(4\,e^4 - 8\,e^3 + 8\,e - 4\right) \tag{333}$$

$$h_{5_7} = \tan\left(\frac{y}{2}\right)^6 \left(-4\,e^4 - 8\,e^3 + 8\,e + 4\right) \tag{334}$$

$$h_{5_8} = \tan\left(\frac{y}{2}\right)^4 \left(6\,e^4 - 12\,e^2 + 6\right) + 6\,e^2 - 4\,e^3 + e^4 + 1 \tag{335}$$

$$h_{5_9} = e^2 \tan\left(\frac{y}{2}\right) \left(2\,e + 2\right) \left(e^2 + 6\right) \left(e^4 + 4\,e^3 + 6\,e^2 + 4\,e + 1\right) \tag{336}$$

$$h_{5_{10}} = \left(2\,e^4 + 12\,e^2\right) \sqrt{e - 1}\,(e + 1)^{9/2} \tag{337}$$

where $y = \pi - \epsilon$, with ϵ being an arbitrary positive number that is extremely close to zero.

Parameter g_6:

$$g_6 = -\frac{g_{6_1} - g_{6_2} - g_{6_3} + g_{6_4}}{g_{6_5} + g_{6_6} - g_{6_7} + g_{6_8}} - \frac{35\,e^3\,\mathrm{atanh}\left(\frac{g_{6_9}}{g_{6_{10}}}\right)}{4\,(e - 1)^{9/2}\,(e + 1)^{9/2}} \tag{338}$$

where,

$$g_{6_1} = \frac{\tan\left(\frac{y}{2}\right)^7 \left(8\,e^4 - 3\,e^3 + 48\,e^2 + 32\,e + 8\right)}{\left(4\,e - 4\right) \left(e + 1\right)^4} \tag{339}$$

$$g_{6_2} = \frac{7\tan\left(\frac{y}{2}\right)^5 \left(24\,e^4 + 9\,e^3 + 48\,e^2 - 8\right)}{12\,(e + 1)^3 \left(e^2 - 2\,e + 1\right)} \tag{340}$$

$$g_{6_3} = \frac{\tan\left(\frac{y}{2}\right) \left(8\,e^4 + 3\,e^3 + 48\,e^2 - 32\,e + 8\right)}{\left(4\,e + 4\right) \left(e^4 - 4\,e^3 + 6\,e^2 - 4\,e + 1\right)} \tag{341}$$

$$g_{6_4} = \frac{7\tan\left(\frac{y}{2}\right)^3 \left(24\,e^4 - 9\,e^3 + 48\,e^2 - 8\right)}{12\,(e + 1)^2 \left(e^3 - 3\,e^2 + 3\,e - 1\right)} \tag{342}$$

$$g_{6_5} = 4\,e + \tan\left(\frac{y}{2}\right)^8 \left(e^4 - 4\,e^3 + 6\,e^2 - 4\,e + 1\right) \tag{343}$$

$$g_{6_6} = \tan\left(\frac{y}{2}\right)^2 \left(-4\,e^4 - 8\,e^3 + 8\,e + 4\right) \tag{344}$$

$$g_{6_7} = \tan\left(\frac{y}{2}\right)^6 \left(4\,e^4 - 8\,e^3 + 8\,e - 4\right) \tag{345}$$

$$g_{6_8} = \tan\left(\frac{y}{2}\right)^4 \left(6\,e^4 - 12\,e^2 + 6\right) + 6\,e^2 + 4\,e^3 + e^4 + 1 \tag{346}$$

$$g_{6_9} = \tan\left(\frac{y}{2}\right) \left(2\,e - 2\right) \left(e^4 - 4\,e^3 + 6\,e^2 - 4\,e + 1\right) \tag{347}$$

$$g_{6_{10}} = 2\,(e-1)^{9/2}\,\sqrt{e+1} \tag{348}$$

where $y = \pi - \epsilon$, with ϵ being an arbitrary positive number that is extremely close to zero.

Parameter h_6:

$$h_6 = \frac{h_{6_1} + h_{6_2} - h_{6_3} - h_{6_4}}{h_{6_5} - h_{6_6} + h_{6_7} + h_{6_8}} + \frac{35\,e^3\,\operatorname{atanh}\left(\frac{h_{6_9}}{h_{6_{10}}}\right)}{4\,(e-1)^{9/2}\,(e+1)^{9/2}} \tag{349}$$

where,

$$h_{6_1} = \frac{7\tan\left(\frac{y}{2}\right)^5 \left(24\,e^4 - 9\,e^3 + 48\,e^2 - 8\right)}{12\,(e-1)^3\,\left(e^2 + 2\,e + 1\right)} \tag{350}$$

$$h_{6_2} = \frac{\tan\left(\frac{y}{2}\right) \left(8\,e^4 - 3\,e^3 + 48\,e^2 + 32\,e + 8\right)}{(4\,e-4)\,\left(e^4 + 4\,e^3 + 6\,e^2 + 4\,e + 1\right)} \tag{351}$$

$$h_{6_3} = \frac{7\tan\left(\frac{y}{2}\right)^3 \left(24\,e^4 + 9\,e^3 + 48\,e^2 - 8\right)}{12\,(e-1)^2\,\left(e^3 + 3\,e^2 + 3\,e + 1\right)} \tag{352}$$

$$h_{6_4} = \frac{\tan\left(\frac{y}{2}\right)^7 \left(8\,e^4 + 3\,e^3 + 48\,e^2 - 32\,e + 8\right)}{4\,(e-1)^4\,(e+1)} \tag{353}$$

$$h_{6_5} = \tan\left(\frac{y}{2}\right)^8 \left(e^4 + 4\,e^3 + 6\,e^2 + 4\,e + 1\right) - 4\,e \tag{354}$$

$$h_{6_6} = \tan\left(\frac{y}{2}\right)^2 \left(4\,e^4 - 8\,e^3 + 8\,e - 4\right) \tag{355}$$

$$h_{6_7} = \tan\left(\frac{y}{2}\right)^6 \left(-4\,e^4 - 8\,e^3 + 8\,e + 4\right) \tag{356}$$

$$h_{6_8} = \tan\left(\frac{y}{2}\right)^4 \left(6\,e^4 - 12\,e^2 + 6\right) + 6\,e^2 - 4\,e^3 + e^4 + 1 \tag{357}$$

$$h_{6_9} = \tan\left(\frac{y}{2}\right) (2\,e + 2) \left(e^4 + 4\,e^3 + 6\,e^2 + 4\,e + 1\right) \tag{358}$$

$$h_{6_{10}} = 2\sqrt{e-1}\,(e+1)^{9/2} \tag{359}$$

where $y = \pi - \epsilon$, with ϵ being an arbitrary positive number that is extremely close to zero.

Parameter g_7:

$$g_7 = \frac{g_{7_1} + g_{7_2} + g_{7_3} - g_{7_4}}{g_{7_5} + g_{7_6} - g_{7_7} + g_{7_8}} + \frac{35\,e^4\,\operatorname{atanh}\left(\frac{g_{7_9}}{g_{7_{10}}}\right)}{4\,(e-1)^{9/2}\,(e+1)^{9/2}} \tag{360}$$

where,

$$g_{7_1} = \frac{7\tan\left(\frac{y}{2}\right)^5 \left(15\,e^4 - 96\,e^3 - 48\,e^2 + 32\,e + 24\right)}{12\,(e+1)^3\,(e^2 - 2\,e + 1)} \tag{361}$$

$$g_{7_2} = \frac{7\tan\left(\frac{y}{2}\right)^3 \left(15\,e^4 + 96\,e^3 - 48\,e^2 - 32\,e + 24\right)}{12\,(e+1)^2\,(e^3 - 3\,e^2 + 3\,e - 1)} \tag{362}$$

$$g_{7_3} = \frac{\tan\left(\frac{y}{2}\right)^7 \left(-27\,e^4 + 32\,e^3 + 48\,e^2 + 32\,e + 8\right)}{(4\,e - 4)\,(e+1)^4} \tag{363}$$

$$g_{7_4} = \frac{\tan\left(\frac{y}{2}\right) \left(27\,e^4 + 32\,e^3 - 48\,e^2 + 32\,e - 8\right)}{(4\,e + 4)\,\left(e^4 - 4\,e^3 + 6\,e^2 - 4\,e + 1\right)} \tag{364}$$

$$g_{7_5} = 4\,e + \tan\left(\frac{y}{2}\right)^8 \left(e^4 - 4\,e^3 + 6\,e^2 - 4\,e + 1\right) \tag{365}$$

$$g_{7_6} = \tan\left(\frac{y}{2}\right)^2 \left(-4\,e^4 - 8\,e^3 + 8\,e + 4\right) \tag{366}$$

$$g_{7_7} = \tan\left(\frac{y}{2}\right)^6 \left(4\,e^4 - 8\,e^3 + 8\,e - 4\right) \tag{367}$$

$$g_{7_8} = \tan\left(\frac{y}{2}\right)^4 \left(6\,e^4 - 12\,e^2 + 6\right) + 6\,e^2 + 4\,e^3 + e^4 + 1 \tag{368}$$

$$g_{7_9} = \tan\left(\frac{y}{2}\right) (2\,e - 2)\,\left(e^4 - 4\,e^3 + 6\,e^2 - 4\,e + 1\right) \tag{369}$$

$$g_{7_{10}} = 2\,(e-1)^{9/2}\,\sqrt{e+1} \tag{370}$$

where $y = \pi - \epsilon$, with ϵ being an arbitrary positive number that is extremely close to zero.

Parameter h_7:

$$h_7 = -\frac{h_{7_1} + h_{7_2} + h_{7_3} - h_{7_4}}{h_{7_5} - h_{7_6} + h_{7_7} + h_{7_8}} - \frac{35\,e^4\,\operatorname{atanh}\left(\frac{h_{7_9}}{h_{7_{10}}}\right)}{4\,(e-1)^{9/2}\,(e+1)^{9/2}} \tag{371}$$

where,

$$h_{7_1} = \frac{7\tan\left(\frac{y}{2}\right)^5 \left(15\,e^4 + 96\,e^3 - 48\,e^2 - 32\,e + 24\right)}{12\,(e-1)^3\,\left(e^2 + 2\,e + 1\right)} \tag{372}$$

$$h_{7_2} = \frac{7 \tan\left(\frac{y}{2}\right)^3 \left(15\, e^4 - 96\, e^3 - 48\, e^2 + 32\, e + 24\right)}{12\, (e-1)^2 \left(e^3 + 3\, e^2 + 3\, e + 1\right)} \tag{373}$$

$$h_{7_3} = \frac{\tan\left(\frac{y}{2}\right) \left(-27\, e^4 + 32\, e^3 + 48\, e^2 + 32\, e + 8\right)}{(4\, e - 4) \left(e^4 + 4\, e^3 + 6\, e^2 + 4\, e + 1\right)} \tag{374}$$

$$h_{7_4} = \frac{\tan\left(\frac{y}{2}\right)^7 \left(27\, e^4 + 32\, e^3 - 48\, e^2 + 32\, e - 8\right)}{4\, (e-1)^4 \, (e+1)} \tag{375}$$

$$h_{7_5} = \tan\left(\frac{y}{2}\right)^8 \left(e^4 + 4\, e^3 + 6\, e^2 + 4\, e + 1\right) - 4\, e \tag{376}$$

$$h_{7_6} = \tan\left(\frac{y}{2}\right)^2 \left(4\, e^4 - 8\, e^3 + 8\, e - 4\right) \tag{377}$$

$$h_{7_7} = \tan\left(\frac{y}{2}\right)^6 \left(-4\, e^4 - 8\, e^3 + 8\, e + 4\right) \tag{378}$$

$$h_{7_8} = \tan\left(\frac{y}{2}\right)^4 \left(6\, e^4 - 12\, e^2 + 6\right) + 6\, e^2 - 4\, e^3 + e^4 + 1 \tag{379}$$

$$h_{7_9} = \tan\left(\frac{y}{2}\right) (2\, e + 2) \left(e^4 + 4\, e^3 + 6\, e^2 + 4\, e + 1\right) \tag{380}$$

$$h_{7_{10}} = 2 \sqrt{e-1}\, (e+1)^{9/2} \tag{381}$$

where $y = \pi - \epsilon$, with ϵ being an arbitrary positive number that is extremely close to zero.

Parameter g_8:

$$g_8 = -\frac{g_{8_1} - \frac{g_{8_3} + g_{8_4} + g_{8_5} + g_{8_6} + g_{8_7} + g_{8_8}}{(e\, \cos(y)+1)^4 \, (e^2-1)^4}}{192\, e^5} \tag{382}$$

where,

$$g_{8_1} = \frac{\operatorname{atanh}\left(\frac{\tan\left(\frac{y}{2}\right)(e-1)}{\sqrt{e^2-1}}\right) g_{8_2}}{\left(e^2-1\right)^{9/2}} \tag{383}$$

$$g_{8_2} = \left(15120\, e^8 - 40320\, e^6 + 48384\, e^4 - 27648\, e^2 + 6144\right) \tag{384}$$

$$\begin{aligned} g_{8_3} = {} & 3072\, y + 8448\, e^3 \sin(y) - 3840\, e^5 \sin(y) - 8016\, e^7 \sin(y) \\ & + 9120\, e^9 \sin(y) - 1170\, e^{11} \sin(y) - 5376\, e^2 \sin(2\, y) \\ & - 3328\, e^3 \sin(3\, y) \end{aligned} \tag{385}$$

$$\begin{aligned} g_{8_4} = {} & 19072\, e^4 \sin(2\, y) - 800\, e^4 \sin(4\, y) + 12736\, e^5 \sin(3\, y) \\ & - 23056\, e^6 \sin(2\, y) + 3080\, e^6 \sin(4\, y) \\ & - 17808\, e^7 \sin(3\, y) \end{aligned} \tag{386}$$

$$\begin{aligned} g_{8_5} = {} & 8640\, e^8 \sin(2\, y) - 4350\, e^8 \sin(4\, y) + 10280\, e^9 \sin(3\, y) \\ & + 2830\, e^{10} \sin(2\, y) \end{aligned} \tag{387}$$

$$\begin{aligned} g_{8_6} = {} & 2575\, e^{10} \sin(4\, y) - 1250\, e^{11} \sin(3\, y) - 640\, e^{12} \sin(2\, y) \\ & - 400\, e^{12} \sin(4\, y) - 3072\, e^2\, y - 17280\, e^4\, y + 38400\, e^6\, y \\ & - 26880\, e^8\, y + 4608\, e^{10}\, y \end{aligned} \tag{388}$$

$$
\begin{aligned}
g_{8_7} = {} & 1152\, e^{12}\, y - 3072\, e\, \sin(y) + 3072\, e^3\, y\, \cos(3\, y) \\
& + 384\, e^4\, y\, \cos(4\, y) - 12288\, e^5\, y\, \cos(3\, y) \\
& - 1536\, e^6\, y\, \cos(4\, y) + 18432\, e^7\, y\, \cos(3\, y)
\end{aligned}
\tag{389}
$$

$$
\begin{aligned}
g_{8_8} = {} & 2304\, e^8\, y\, \cos(4\, y) - 12288\, e^9\, y\, \cos(3\, y) - 1536\, e^{10}\, y \\
& \cos(4\, y) + 3072\, e^{11}\, y\, \cos(3\, y) + 384\, e^{12}\, y\, \cos(4\, y) \\
& + 3072\, e\, y\, \cos(y)\, \left(e^2 - 1\right)^4\, \left(3\, e^2 + 4\right) \\
& + 1536\, e^2\, y\, \cos(2\, y)\, \left(e^2 - 1\right)^4\, \left(e^2 + 6\right)
\end{aligned}
\tag{390}
$$

where $y = \pi - \epsilon$, with ϵ being an arbitrary positive number that is extremely close to zero.

Parameter h_8:

$$
h_8 = \frac{h_{8_1} + \frac{h_{8_3} + h_{8_4} + h_{8_5} + h_{8_6}}{(e\, \cos(y) - 1)^4\, (e^2 - 1)^4}}{192\, e^5}
\tag{391}
$$

where,

$$
h_{8_1} = \frac{\operatorname{atanh}\left(\frac{\tan\left(\frac{y}{2}\right)(e+1)}{\sqrt{e^2-1}}\right) h_{8_2}}{\left(e^2 - 1\right)^{9/2}}
\tag{392}
$$

$$
h_{8_2} = \left(15120\, e^8 - 40320\, e^6 + 48384\, e^4 - 27648\, e^2 + 6144\right)
\tag{393}
$$

$$
\begin{aligned}
h_{8_3} = {} & 3072\,y - 8448\,e^3\,\sin(y) + 3840\,e^5\,\sin(y) + 8016\,e^7\,\sin(y) \\
& - 9120\,e^9\,\sin(y) + 1170\,e^{11}\,\sin(y) - 5376\,e^2\,\sin(2\,y) \\
& + 3328\,e^3\,\sin(3\,y) + 19072\,e^4\,\sin(2\,y) - 800\,e^4\,\sin(4\,y) \\
& - 12736\,e^5\,\sin(3\,y) - 23056\,e^6\,\sin(2\,y)
\end{aligned}
\tag{394}
$$

$$
\begin{aligned}
h_{8_4} = {} & 3080\,e^6\,\sin(4\,y) + 17808\,e^7\,\sin(3\,y) + 8640\,e^8\,\sin(2\,y) \\
& - 4350\,e^8\,\sin(4\,y) - 10280\,e^9\,\sin(3\,y) + 2830\,e^{10} \\
& \sin(2\,y) + 2575\,e^{10}\,\sin(4\,y) + 1250\,e^{11}\,\sin(3\,y) \\
& - 640\,e^{12}\,\sin(2\,y) - 400\,e^{12}\,\sin(4\,y) - 3072\,e^2\,y \\
& - 17280\,e^4\,y + 38400\,e^6\,y - 26880\,e^8\,y + 4608\,e^{10}\,y \\
& + 1152\,e^{12}\,y + 3072\,e\,\sin(y) - 3072\,e^3\,y\,\cos(3\,y)
\end{aligned}
\tag{395}
$$

$$
\begin{aligned}
h_{8_5} = {} & 384\,e^4\,y\,\cos(4\,y) + 12288\,e^5\,y\,\cos(3\,y) - 1536\,e^6\,y \\
& \cos(4\,y) - 18432\,e^7\,y\,\cos(3\,y) + 2304\,e^8\,y\,\cos(4\,y)
\end{aligned}
\tag{396}
$$

$$
\begin{aligned}
h_{8_6} = {} & 12288\,e^9\,y\,\cos(3\,y) - 1536\,e^{10}\,y\,\cos(4\,y) - 3072\,e^{11}\,y \\
& \cos(3\,y) + 384\,e^{12}\,y\,\cos(4\,y) - 3072\,e\,y\,\cos(y) \\
& \left(e^2-1\right)^4\,\left(3\,e^2+4\right) + 1536\,e^2\,y\,\cos(2\,y)\,\left(e^2-1\right)^4 \\
& \left(e^2+6\right)
\end{aligned}
\tag{397}
$$

where $y = \pi - \epsilon$, with ϵ being an arbitrary positive number that is extremely close to zero.

Parameter $\tilde{\mathcal{P}}_9$:

$$\tilde{\mathcal{P}}_9 = -423.3e^9 + 30.979e^8 - 117.56e^7 + .3223e^6 - 24.755e^5 + .00043348e^4 - 7.2094 \times 10^{-6}e^3 + 6.2929 \times^{-8} e^2 - 2.3158 \times 10^{-10}e + 1.972 \times 10^{-13} \tag{398}$$

Parameter g_9:

$$g_9 = \frac{g_{9_1}}{g_{9_2}} - \frac{g_{9_3} - g_{9_4} - g_{9_5} + g_{9_6}}{g_{9_7} + g_{9_8} - g_{9_9} + g_{9_{10}}} \tag{399}$$

where,

$$g_{9_1} = \operatorname{atanh}\left(\frac{\tan\left(\frac{y}{2}\right)\ (2\,e-2)\ (e^4 - 4\,e^3 + 6\,e^2 - 4\,e + 1)}{2\,(e-1)^{9/2}\,\sqrt{e+1}}\right) \left(3\,e^4 + 24\,e^2 + 8\right) \tag{400}$$

$$g_{9_2} = 4\,(e-1)^{9/2}\,(e+1)^{9/2} \tag{401}$$

$$g_{9_3} = \frac{\tan\left(\frac{y}{2}\right)^5\ (-9\,e^4 + 160\,e^3 + 72\,e^2 + 288\,e)}{12\,(e+1)^3\ (e^2 - 2\,e + 1)} \tag{402}$$

$$g_{9_4} = \frac{\tan\left(\frac{y}{2}\right)^3\ (9\,e^4 + 160\,e^3 - 72\,e^2 + 288\,e)}{12\,(e+1)^2\ (e^3 - 3\,e^2 + 3\,e - 1)} \tag{403}$$

$$g_{9_5} = \frac{\tan\left(\frac{y}{2}\right)^7\ (5\,e^4 + 32\,e^3 + 24\,e^2 + 32\,e)}{(4\,e-4)\ (e+1)^4} \tag{404}$$

$$g_{9_6} = \frac{\tan\left(\frac{y}{2}\right)\ (-5\,e^4 + 32\,e^3 - 24\,e^2 + 32\,e)}{(4\,e+4)\ (e^4 - 4\,e^3 + 6\,e^2 - 4\,e + 1)} \tag{405}$$

$$g_{9_7} = 4\,e + \tan\left(\frac{y}{2}\right)^8\ \left(e^4 - 4\,e^3 + 6\,e^2 - 4\,e + 1\right) \tag{406}$$

$$g_{9_8} = \tan\left(\frac{y}{2}\right)^2 \left(-4\,e^4 - 8\,e^3 + 8\,e + 4\right) \tag{407}$$

$$g_{9_9} = \tan\left(\frac{y}{2}\right)^6 \left(4\,e^4 - 8\,e^3 + 8\,e - 4\right) \tag{408}$$

$$g_{9_{10}} = \tan\left(\frac{y}{2}\right)^4 \left(6\,e^4 - 12\,e^2 + 6\right) + 6\,e^2 + 4\,e^3 + e^4 + 1 \tag{409}$$

where $y = \pi - \epsilon$, with ϵ being an arbitrary positive number that is extremely close to zero.

Parameter h_9:

$$h_9 = -\frac{h_{9_1} - h_{9_2} + h_{9_3} - h_{9_4}}{h_{9_5} - h_{9_6} + h_{9_7} + h_{9_8}} - \frac{\operatorname{atanh}\left(\frac{h_{9_9}}{h_{9_{10}}}\right)\,\left(3\,e^4 + 24\,e^2 + 8\right)}{4\,(e-1)^{9/2}\,(e+1)^{9/2}} \tag{410}$$

where,

$$h_{9_1} = \frac{\tan\left(\frac{y}{2}\right)^5\,\left(9\,e^4 + 160\,e^3 - 72\,e^2 + 288\,e\right)}{12\,(e-1)^3\,\left(e^2 + 2\,e + 1\right)} \tag{411}$$

$$h_{9_2} = \frac{\tan\left(\frac{y}{2}\right)^3\,\left(-9\,e^4 + 160\,e^3 + 72\,e^2 + 288\,e\right)}{12\,(e-1)^2\,\left(e^3 + 3\,e^2 + 3\,e + 1\right)} \tag{412}$$

$$h_{9_3} = \frac{\tan\left(\frac{y}{2}\right)\,\left(5\,e^4 + 32\,e^3 + 24\,e^2 + 32\,e\right)}{(4\,e-4)\,\left(e^4 + 4\,e^3 + 6\,e^2 + 4\,e + 1\right)} \tag{413}$$

$$h_{9_4} = \frac{\tan\left(\frac{y}{2}\right)^7\,\left(-5\,e^4 + 32\,e^3 - 24\,e^2 + 32\,e\right)}{4\,(e-1)^4\,(e+1)} \tag{414}$$

$$h_{9_5} = \tan\left(\frac{y}{2}\right)^8 \left(e^4 + 4\,e^3 + 6\,e^2 + 4\,e + 1\right) - 4\,e \tag{415}$$

$$h_{9_6} = \tan\left(\frac{y}{2}\right)^2 \left(4\,e^4 - 8\,e^3 + 8\,e - 4\right) \tag{416}$$

$$h_{9_7} = \tan\left(\frac{y}{2}\right)^6 \left(-4\,e^4 - 8\,e^3 + 8\,e + 4\right) \tag{417}$$

$$h_{9_8} = \tan\left(\frac{y}{2}\right)^4 \left(6\,e^4 - 12\,e^2 + 6\right) + 6\,e^2 - 4\,e^3 + e^4 + 1 \tag{418}$$

$$h_{9_9} = \tan\left(\frac{y}{2}\right) (2\,e + 2) \left(e^4 + 4\,e^3 + 6\,e^2 + 4\,e + 1\right) \tag{419}$$

$$h_{9_{10}} = 2\sqrt{e-1}\,(e+1)^{9/2} \tag{420}$$

where $y = \pi - \epsilon$, with ϵ being an arbitrary positive number that is extremely close to zero.

B LORENTZ FORCE PERTURBATION COEFFICIENTS

$$C_{80} = 2B_0(\frac{q}{m})\left(\frac{\omega_e a \sin i \sin\theta_m \cos^2\frac{i}{2}}{\mu(e^2-1)}\right)\left[\frac{1}{\left(\frac{\omega_e}{n}-2\right)} + \frac{e}{4\left(\frac{\omega_e}{n}-1\right)} + \frac{3e}{4\left(\frac{\omega_e}{n}-3\right)}\right] \tag{421}$$

$$C_{81} = -2B_0(\frac{q}{m})\frac{\omega_e a \sin i \sin\theta_m \sin^2\frac{i}{2}}{\mu(e^2-1)}\left[\frac{1}{\left(\frac{\omega_e}{n}+2\right)} + \frac{e}{4\left(\frac{\omega_e}{n}+1\right)} + \frac{3e}{4\left(\frac{\omega_e}{n}+3\right)}\right] \tag{422}$$

$$C_{82} = 2B_0(\frac{q}{m})\frac{\sin i \sin\theta_m}{na^2(1-e^2)}\left[\frac{e\omega_e}{2n}\left(\frac{\frac{2\omega_e}{n}-\cos i}{\frac{\omega_e^2 a^3}{\mu}-1}\right) + \frac{e^3}{(1-e^2)^{\frac{3}{2}}}\left(\frac{\left(3-\frac{\omega_e^2 a^3}{\mu}\right)}{\left(1-\frac{\omega_e^2 a^3}{\mu}\right)\left(9-\frac{\omega_e^2 a^3}{\mu}\right)}\right)+1\right] \tag{423}$$

$$\begin{aligned} D_{110} = {} & B_0(\frac{q}{m})\frac{\omega_e \sin i \sin\theta_m \sin^2\frac{i}{2}}{4\mu}\left[-\frac{1}{\frac{\omega_e}{n}+1} + \frac{1}{\frac{\omega_e}{n}+3} + \frac{e^2}{2\left(\frac{\omega_e}{n}-1\right)} + \frac{e^3}{4\left(\frac{\omega_e}{n}-2\right)}\right] \\ & + B_0(\frac{q}{m})\frac{\sin i \sin\theta_m}{4a^3 n}\left[\frac{e}{(1-e^2)^{3/2}} + \frac{\omega_e}{n}\right]\left[\frac{e^2}{4\left(\frac{\omega_e}{n}+5\right)} + \frac{e^3}{8\left(\frac{\omega_e}{n}+6\right)} - \frac{\frac{e}{2}-e^3}{\frac{\omega_e}{n}+4} - \frac{\frac{e^F 2}{4}-2}{\frac{\omega_e}{n}+3}\right] + \\ & \frac{B_0 q \sin i \sin\theta_m\left(\frac{7e^3}{8}+\frac{e}{2}\right)}{2m\left(\frac{\omega_e}{n}+2\right)}\left[\frac{\omega_e}{\mu}\left(1-\frac{\cos i}{2}\right) + \frac{e}{2a^3 n(1-e^2)^{3/2}}\right] \\ & - \frac{B_0\omega_e q \sin i \sin\theta_m \sin^2\frac{i}{2}\left(\frac{e^2}{4}-2\right)}{2m\mu\left(\frac{\omega_e}{n}+1\right)} - \frac{B_0 q \sin i \sin\theta_m \sin^2\frac{i}{2}\left(\frac{e}{2}-e^3\right)}{2a^3 mn} \end{aligned} \tag{424}$$

$$\begin{aligned} D_{111} = {} & B_0\frac{q}{m}\frac{\sin i \sin\theta_m \cos^2\frac{i}{2}}{\mu}\left[\frac{n\left(-e^3+\frac{e}{2}\right)}{2} + \frac{\omega_e\left(\frac{e^2}{4}-\frac{3}{2}\right)}{2\left(\frac{\omega_e}{n}-1\right)} + \frac{\omega_e\left(\frac{e^2}{4}-\frac{5}{2}\right)}{2\left(\frac{\omega_e}{n}-3\right)}\right. \\ & + \frac{\omega_e\left(-e^3+\frac{e}{2}\right)}{2\left(\frac{\omega_e}{n}-4\right)} - \frac{\omega_e\left(\frac{7e^3}{8}+\frac{e}{2}\right)}{\frac{\omega_e}{n}-2} - \frac{e^2\omega_e}{8\left(\frac{\omega_e}{n}+1\right)} - \frac{e^3\omega_e}{16\left(\frac{\omega_e}{n}+2\right)} - \frac{e^2\omega_e}{8\left(\frac{\omega_e}{n}-5\right)} \\ & \left. - \frac{e^3\omega_e}{16\left(\frac{\omega_e}{n}-6\right)}\right] \end{aligned} \tag{425}$$

$$D_{112} = \frac{B_0 q \sin i \sin\theta_m}{2a^3 mn\left(1-e^2\right)^{\frac{3}{2}}}\left[\frac{e^5}{32\left(\frac{\omega_e}{n}+6\right)} + \frac{e^4}{8\left(\frac{\omega_e}{n}+5\right)} + \frac{e^5}{4\left(\frac{\omega_e}{n}+4\right)} + \frac{3e^4}{8\left(\frac{\omega_e}{n}+3\right)}\right.$$
$$+ \frac{13e^5}{32\left(\frac{\omega_e}{n}+2\right)} + \frac{-1+e^2+\frac{e^4}{4}}{\left(\frac{\omega_e}{n}+1\right)} + \frac{1-e^2-\frac{e^4}{4}}{\left(\frac{\omega_e}{n}-1\right)} - \frac{13e^5}{32\left(\frac{\omega_e}{n}-2\right)} - \frac{3e^4}{8\left(\frac{\omega_e}{n}-3\right)} - \frac{e^5}{4\left(\frac{\omega_e}{n}-4\right)}$$
$$\left. - \frac{e^4}{8\left(\frac{\omega_e}{n}-5\right)} - \frac{e^5}{32\left(\frac{\omega_e}{n}-6\right)}\right] + \frac{B_0 q \sin i \sin\theta_m}{2a^3 mn}\left(\frac{\omega_e}{n}\right)\left[\frac{e^3}{8\left(\frac{\omega_e}{n}+4\right)} + \frac{e^2}{4\left(\frac{\omega_e}{n}+3\right)}\right.$$
$$- \frac{\frac{e}{2}-e^3}{\left(\frac{\omega_e}{n}+2\right)} + \frac{\cos i}{2\left(\frac{\omega_e}{n}+1\right)} - \frac{\frac{e^2}{4}-2}{\left(\frac{\omega_e}{n}+1\right)} - \frac{\frac{e^2}{4}-2}{\left(\frac{\omega_e}{n}-1\right)} - \frac{\cos i}{2\left(\frac{\omega_e}{n}-1\right)} - \frac{\frac{e}{2}-e^3}{\left(\frac{\omega_e}{n}-2\right)}$$
$$\left. + \frac{e^2}{4\left(\frac{\omega_e}{n}-3\right)} + \frac{e^3}{8\left(\frac{\omega_e}{n}-4\right)}\right] + \frac{\left(B_0 q \sin i \sin\theta_m\left(\frac{7e^3}{8}+\frac{e}{2}\right)\right)}{\left(a^3 mn\right)} \quad (426)$$

$$D_{105_4} = -\frac{B_0 \omega_e q \cos\theta_m \sin^2 i\sqrt{1-e^2}\left(-e^3+\frac{e}{2}\right)}{amn} \quad (427)$$

$$J_1 = \frac{B_0 q \sin\theta_m}{a^3 mn(1-e^2)^{\frac{3}{2}}}\left[-\frac{3e^4\sin^2\frac{i}{2}}{32\left(\frac{\omega_e}{n}+6\right)} - \frac{e^3\sin^2\frac{i}{2}}{8\left(\frac{\omega_e}{n}+5\right)} - \frac{3e^4\sin^2\frac{i}{2}}{8\left(\frac{\omega_e}{n}+4\right)} - \frac{e\sin^2\frac{i}{2}\left(\frac{3e^2}{4}+\frac{3}{2}\right)}{2\left(\frac{\omega_e}{n}+3\right)}\right.$$
$$- \frac{\sin^2\frac{i}{2}\left(\frac{9e^4}{16}+1\right)}{\frac{\omega_e}{n}+2} + \frac{e}{4\left(\frac{\omega_e}{n}+1\right)}\left(\cos i\left(\frac{3}{2}-\frac{e^2}{2}\right) - \frac{3e^2}{4} - \frac{3}{2}\right) - \frac{e^3\sin^2\frac{i}{2}}{8\left(\frac{\omega_e}{n}-1\right)} - \frac{3e^4\sin^2\frac{i}{2}}{32\left(\frac{\omega_e}{n}-2\right)}$$
$$\left. - \frac{3e^4\sin^2\frac{i}{2}n}{8\omega_e}\right] + \frac{B_0 q \sin\theta_m \cos i \sin^2\frac{i}{2}\omega_e}{a^3 mn^2}\left[\frac{e^2}{4\left(\frac{\omega_e}{n}+4\right)} - \frac{e}{2\left(\frac{\omega_e}{n}+3\right)} + \frac{\frac{e^2}{2}+1}{\frac{\omega_e}{n}+2}\right.$$
$$\left. - \frac{e}{2\left(\frac{\omega_e}{n}+1\right)} + \frac{e^2 n}{4\omega_e}\right] \quad (428)$$

$$J_2 = \frac{B_0 q \sin\theta_m \cos^2\frac{i}{2}}{a^3 mn(1-e^2)^{\frac{3}{2}}}\left[\frac{3e^4}{32\left(\frac{\omega_e}{n}-6\right)} + \frac{e^3}{8\left(\frac{\omega_e}{n}-5\right)} + \frac{3e^4}{8\left(\frac{\omega_e}{n}-4\right)} + \frac{3e\left(\frac{e^2}{2}+1\right)}{4\left(\frac{\omega_e}{n}-3\right)}\right.$$
$$+ \frac{\frac{9e^4}{16}+1}{\frac{\omega_e}{n}-2} + \frac{e}{4\cos^2\frac{i}{2}\left(\frac{\omega_e}{n}-1\right)}\left(\cos i\left(-\frac{e^2}{2}+\frac{3}{2}\right) + \frac{3e^2}{4} + \frac{3}{2}\right) + \frac{e^3}{8\left(\frac{\omega_e}{n}+1\right)} + \frac{3e^4}{32\left(\frac{\omega_e}{n}+2\right)}$$
$$\left. + \frac{3e^4 n}{8\omega_e}\right] + \frac{B_0 q \sin\theta_m \cos i \cos^2\frac{i}{2}\omega_e}{a^3 mn^2}\left[-\frac{e^2}{4\left(\frac{\omega_e}{n}-4\right)} + \frac{e}{2\left(\frac{\omega_e}{n}-3\right)} - \frac{\frac{e^2}{2}+1}{\frac{\omega_e}{n}-2}\right.$$
$$\left. + \frac{e}{2\left(\frac{\omega_e}{n}-1\right)} - \frac{e^2 n}{4\omega_e}\right] \quad (429)$$

$$J_3 = \frac{B_0 q \sin\theta_m}{a^3 mn(1-e^2)^{\frac{3}{2}}}\Bigg[-\frac{3e^4}{32\left(\frac{\omega_e}{n}-4\right)} - \frac{e^3}{8\left(\frac{\omega_e}{n}-3\right)} - \frac{3e^4}{8\left(\frac{\omega_e}{n}-2\right)} - \frac{3e\left(1+\frac{e^2}{2}\right)}{4\left(\frac{\omega_e}{n}-1\right)}$$
$$- \frac{3e\left(1+\frac{e^2}{2}\right)}{4\left(\frac{\omega_e}{n}+1\right)} - \frac{3e^4}{8\left(\frac{\omega_e}{n}+2\right)} - \frac{e^3}{8\left(\frac{\omega_e}{n}+3\right)} - \frac{3e^4}{32\left(\frac{\omega_e}{n}+4\right)} - \frac{\left(\frac{9e^4}{16}+1\right)n}{\omega_e}\Bigg] + \frac{B_0 q \sin\theta_m \cos i\omega_e}{a^3 mn^2}$$
$$\left[\frac{e^2}{4\left(\frac{\omega_e}{n}-2\right)} - \frac{e}{2\left(\frac{\omega_e}{n}-1\right)} - \frac{e}{2\left(\frac{\omega_e}{n}+1\right)} + \frac{e^2}{4\left(\frac{\omega_e}{n}+2\right)} + \frac{\left(\frac{e^2}{2}+1\right)n}{\omega_e}\right] \quad (430)$$

$$H_4 = -\frac{B_0 eq\cos i\sin\omega\sin\theta_m}{2a^3 mn(1-e^2)^{\frac{3}{2}}}\left[\frac{3e^3}{8\left(\frac{\omega_e}{n}+2\right)} + \frac{1}{\left(\frac{\omega_e}{n}+1\right)} + \frac{e^3}{8\left(\frac{\omega_e}{n}-2\right)} + \frac{e^3}{8\left(\frac{\omega_e}{n}+4\right)}\right]$$
$$- \frac{3B_0 e^4 q\cos i\sin\omega\sin\theta_m}{16a^3 m\omega_e(1-e^2)^{\frac{3}{2}}} \quad (431)$$

$$H_5 = -\frac{B_0 eq\cos i\sin\omega\sin\theta_m}{2a^3 mn(1-e^2)^{\frac{3}{2}}}\left[\frac{3e^3}{8\left(\frac{\omega_e}{n}-2\right)} + \frac{1}{\left(\frac{\omega_e}{n}-1\right)} + \frac{e^3}{8\left(\frac{\omega_e}{n}+2\right)} + \frac{e^3}{8\left(\frac{\omega_e}{n}-4\right)}\right]$$
$$- \frac{3B_0 e^4 q\cos i\sin\omega\sin\theta_m}{16a^3 m\omega_e(1-e^2)^{\frac{3}{2}}} \quad (432)$$

$$E_{202} = \frac{B_0 eq\cos\omega\sin\theta_m}{2a^3 mn(1-e^2)^{\frac{3}{2}}}\left[\frac{3e^3}{8\left(\frac{\omega_e}{n}+2\right)} + \frac{1}{\left(\frac{\omega_e}{n}+1\right)} + \frac{e^3}{8\left(\frac{\omega_e}{n}-2\right)} + \frac{e^3}{8\left(\frac{\omega_e}{n}+4\right)}\right]$$
$$+ \frac{3B_0 e^4 q\cos\omega\sin\theta_m}{16a^3 m\omega_e(1-e^2)^{\frac{3}{2}}} \quad (433)$$

$$E_{203} = -\frac{B_0 eq\cos\omega\sin\theta_m}{2a^3 mn(1-e^2)^{\frac{3}{2}}}\left[\frac{3e^3}{8\left(\frac{\omega_e}{n}-2\right)} + \frac{1}{\left(\frac{\omega_e}{n}-1\right)} + \frac{e^3}{8\left(\frac{\omega_e}{n}+2\right)} + \frac{e^3}{8\left(\frac{\omega_e}{n}-4\right)}\right]$$
$$- \frac{3B_0 e^4 q\cos\omega\sin\theta_m}{16a^3 m\omega_e(1-e^2)^{\frac{3}{2}}} \quad (434)$$

$$I_{12} = \frac{3B_0e^4q\cos\theta_m\sin i}{8am(e^2-1)} + \frac{B_0e^2\omega_eq\sin 2i\cos\theta_m\sqrt{1-e^2}}{4amn} \tag{435}$$

$$N_1 = \frac{B_0q\sin\theta_m\sin^2\frac{i}{2}}{a^3mn\sin i(1-e^2)^{\frac{3}{2}}}\left[\frac{3e^4}{32(\frac{\omega_e}{n}+6)} + \frac{e^3}{8(\frac{\omega_e}{n}+5)} + \frac{3e^4}{8(\frac{\omega_e}{n}+4)} + \frac{3e(\frac{e^2}{2}+1)}{4(\frac{\omega_e}{n}+3)}\right.$$
$$\left. + \frac{1+\frac{9e^4}{16}}{(\frac{\omega_e}{n}+2)} + \frac{3e(1+\frac{e^2}{2})}{4(\frac{\omega_e}{n}+1)} + \frac{e^3}{8(\frac{\omega_e}{n}-1)} + \frac{3e^4}{32(\frac{\omega_e}{n}-2)} + \frac{3e^4n}{8\omega_e}\right] + \frac{B_0q\sin\theta_m\omega_e\cos i\sin^2\frac{i}{2}}{a^3mn^2\sin i}$$
$$\left[-\frac{e^2}{4(\frac{\omega_e}{n}+4)} + \frac{e}{2(\frac{\omega_e}{n}+3)} - \frac{\frac{e^2}{2}+1}{(\frac{\omega_e}{n}+2)} + \frac{e}{2(\frac{\omega_e}{n}+1)} - \frac{e^2n}{4\omega_e}\right] \tag{436}$$

$$N_2 = \frac{B_0q\sin\theta_m\cos^2\frac{i}{2}}{a^3mn\sin i(1-e^2)^{\frac{3}{2}}}\left[-\frac{3e^4}{32(\frac{\omega_e}{n}-6)} - \frac{e^3}{8(\frac{\omega_e}{n}-5)} - \frac{3e^4}{8(\frac{\omega_e}{n}-4)} - \frac{3e(1+\frac{e^2}{2})}{4(\frac{\omega_e}{n}-3)}\right.$$
$$\left. - \frac{\frac{9e^4}{16}+1}{(\frac{\omega_e}{n}-2)} - \frac{3e(1+\frac{e^2}{2})}{4(\frac{\omega_e}{n}-1)} - \frac{e^3}{8(\frac{\omega_e}{n}+1)} - \frac{3e^4}{32(\frac{\omega_e}{n}+2)} - \frac{3e^4n}{8\omega_e}\right] + \frac{B_0q\sin\theta_m\omega_e\cos i\cos^2\frac{i}{2}}{a^3mn^2\sin i}$$
$$\left[\frac{e^2}{4(\frac{\omega_e}{n}-4)} - \frac{e}{2(\frac{\omega_e}{n}-3)} + \frac{1+\frac{e^2}{2}}{(\frac{\omega_e}{n}-2)} - \frac{e}{2(\frac{\omega_e}{n}-1)} + \frac{e^2n}{4\omega_e}\right] \tag{437}$$

$$N_3 = \frac{B_0q\sin\theta_m\cos i}{a^3mn\sin i(1-e^2)^{\frac{3}{2}}}\left[\frac{3e^4}{8(\frac{\omega_e}{n}+2)} + \frac{3e(1+\frac{e^2}{2})}{4(\frac{\omega_e}{n}+1)} + \frac{3e(1+\frac{e^2}{2})}{4(\frac{\omega_e}{n}-1)} + \frac{3e^4}{8(\frac{\omega_e}{n}-2)}\right.$$
$$\left. + \frac{e^3}{8(\frac{\omega_e}{n}-3)} + \frac{3e^4}{32(\frac{\omega_e}{n}-4)} + \frac{e^3}{8(\frac{\omega_e}{n}+3)} + \frac{3e^4}{32(\frac{\omega_e}{n}+4)} + \frac{(\frac{9e^4}{16}+1)n}{\omega_e}\right] + \frac{B_0q\sin\theta_m\omega_e\cos^2 i}{a^3mn^2\sin i}$$
$$\left[-\frac{e^2}{4(\frac{\omega_e}{n}+2)} + \frac{e}{2(\frac{\omega_e}{n}+1)} + \frac{e}{2(\frac{\omega_e}{n}-1)} - \frac{e^2}{4(\frac{\omega_e}{n}-2)} - \frac{(\frac{e^2}{2}+1)n}{\omega_e}\right] \tag{438}$$

$$L_{177} = -\frac{B_0eq\cos\omega\sin\theta_m}{2a^3mn\sin i(1-e^2)^{\frac{3}{2}}}\left[\frac{3e^3n}{8\omega_e} + \frac{3e^3}{8(\frac{\omega_e}{n}+2)} + \frac{1}{(\frac{\omega_e}{n}+1)} + \frac{e^3}{8(\frac{\omega_e}{n}-2)}\right.$$
$$\left. + \frac{e^3}{8(\frac{\omega_e}{n}+4)}\right] \tag{439}$$

$$L_{178} = \frac{B_0 eq \cos\omega \sin\theta_m}{2a^3 mn \sin i (1-e^2)^{\frac{3}{2}}} \left[\frac{3e^3 n}{8\omega_e} + \frac{3e^3}{8(\frac{\omega_e}{n} - 2)} + \frac{1}{(\frac{\omega_e}{n} - 1)} + \frac{e^3}{8(\frac{\omega_e}{n} + 2)} + \frac{e^3}{8(\frac{\omega_e}{n} - 4)} \right] \quad (440)$$

$$J_{180} = -\frac{B_0 eq \cos i \sin\omega \sin\theta_m}{2a^3 mn \sin i (1-e^2)^{\frac{3}{2}}} \left[\frac{3e^3 n}{8\omega_e} + \frac{3e^3}{8(\frac{\omega_e}{n} + 2)} + \frac{1}{(\frac{\omega_e}{n} + 1)} + \frac{e^3}{8(\frac{\omega_e}{n} - 2)} + \frac{e^3}{8(\frac{\omega_e}{n} + 4)} \right] \quad (441)$$

$$J_{181} = -\frac{B_0 eq \cos i \sin\omega \sin\theta_m}{2a^3 mn \sin i (1-e^2)^{\frac{3}{2}}} \left[\frac{3e^3 n}{8\omega_e} + \frac{3e^3}{8(\frac{\omega_e}{n} - 2)} + \frac{1}{(\frac{\omega_e}{n} - 1)} + \frac{e^3}{8(\frac{\omega_e}{n} + 2)} + \frac{e^3}{8(\frac{\omega_e}{n} - 4)} \right] \quad (442)$$

$$\frac{K_6 \pi}{na^2\sqrt{1-e^2}} \left[K_{11} + K_{13} \sin\omega \right] = -\frac{(\frac{e^2}{2} + 1)\pi B_0 q \cos\theta_m}{na^3 m (1-e^2)^{\frac{3}{2}}} \left[2 + \frac{3e^2}{4} - \frac{\omega_e \sin 2i (1-e^2)^{\frac{3}{2}}}{n \sin i} + \frac{e^2 \sin^2\omega}{2} \right] \quad (443)$$

$$\frac{2\pi K_9}{na^2\sqrt{1-e^2}} \left[\frac{K_{12}}{2} + K_2 \sin\omega + K_{14} \sin^2\omega \right] = \frac{\pi e^2 B_0 q \cos\theta_m}{2na^3 m (1-e^2)^{\frac{3}{2}}} \left[\frac{5}{2} + 3\sin^2\omega \right] \quad (444)$$

$$\frac{\pi K_{10}}{na^2\sqrt{1-e^2}} \left[K_{15} - K_{11} \cos 2\omega + K_{13} \sin\omega \right] = -\frac{\pi e^2 B_0 q \cos\theta_m}{4na^3 m (1-e^2)^{\frac{3}{2}}} \left[\frac{3e^2}{4} - 2\cos 2\omega \right.$$

$$- \frac{3e^2\cos 2\omega}{4} + \frac{\omega_e \sin 2i(1-e^2)^{\frac{3}{2}}\cos 2\omega}{n\sin i} + \frac{e^2\sin^2\omega}{2}\Bigg] \quad (445)$$

$$Q_{142} = -\frac{B_0 q\sin\theta_m\cos i\sin^2\frac{i}{2}}{a^3 mn\sin i(1-e^2)^{\frac{3}{2}}}\Bigg[\frac{3e^4}{32(\frac{\omega_e}{n}+6)} + \frac{e^3}{8(\frac{\omega_e}{n}+5)} + \frac{3e^4}{8(\frac{\omega_e}{n}+4)} + \frac{3e(\frac{e^2}{2}+1)}{4(\frac{\omega_e}{n}+3)}$$
$$+ \frac{1+\frac{9e^4}{16}}{(\frac{\omega_e}{n}+2)} + \frac{3e(1+\frac{e^2}{2})}{4(\frac{\omega_e}{n}+1)} + \frac{e^3}{8(\frac{\omega_e}{n}-1)} + \frac{3e^4}{32(\frac{\omega_e}{n}-2)} + \frac{3e^4 n}{8\omega_e}\Bigg] - \frac{B_0 q\sin\theta_m\omega_e\cos^2 i\sin^2\frac{i}{2}}{a^3 mn^2\sin i}$$
$$\Bigg[-\frac{e^2}{4(\frac{\omega_e}{n}+4)} + \frac{e}{2(\frac{\omega_e}{n}+3)} - \frac{\frac{e^2}{2}+1}{(\frac{\omega_e}{n}+2)} + \frac{e}{2(\frac{\omega_e}{n}+1)} - \frac{e^2 n}{4\omega_e}\Bigg] + \frac{B_0\omega_e q\sin i\sin\theta_m\sin^2\frac{i}{2}}{4a^3 mn^2}$$
$$\Bigg[-\frac{e}{2(\frac{\omega_e}{n}+5)} + \frac{(3+\frac{e^2}{2})}{e(\frac{\omega_e}{n}+1)} + \frac{1}{(\frac{\omega_e}{n}+4)} - \frac{5+\frac{e^2}{2}}{e(\frac{\omega_e}{n}+3)} + \frac{e}{2(\frac{\omega_e}{n}-1)}\Bigg]$$
$$- \frac{B_0 q\sin i\sin\theta_m\sin^2\frac{i}{2}}{4a^3 mn} \quad (446)$$

$$Q_{143} = -\frac{B_0 q\sin\theta_m\cos^2\frac{i}{2}\cos i}{a^3 mn\sin i(1-e^2)^{\frac{3}{2}}}\Bigg[-\frac{3e^4}{32(\frac{\omega_e}{n}-6)} - \frac{e^3}{8(\frac{\omega_e}{n}-5)} - \frac{3e^4}{8(\frac{\omega_e}{n}-4)}$$
$$- \frac{3e(1+\frac{e^2}{2})}{4(\frac{\omega_e}{n}-3)} - \frac{\frac{9e^4}{16}+1}{(\frac{\omega_e}{n}-2)} - \frac{3e(1+\frac{e^2}{2})}{4(\frac{\omega_e}{n}-1)} - \frac{e^3}{8(\frac{\omega_e}{n}+1)} - \frac{3e^4}{32(\frac{\omega_e}{n}+2)} - \frac{3e^4 n}{8\omega_e}\Bigg] -$$
$$\frac{B_0 q\sin\theta_m\omega_e\cos^2 i\cos^2\frac{i}{2}}{a^3 mn^2\sin i}\Bigg[\frac{e^2}{4(\frac{\omega_e}{n}-4)} - \frac{e}{2(\frac{\omega_e}{n}-3)} + \frac{1+\frac{e^2}{2}}{(\frac{\omega_e}{n}-2)} - \frac{e}{2(\frac{\omega_e}{n}-1)} + \frac{e^2 n}{4\omega_e}\Bigg]$$
$$+ \frac{B_0\omega_e q\sin i\sin\theta_m\cos^2\frac{i}{2}}{4a^3 mn^2}\Bigg[\frac{e}{2(\frac{\omega_e}{n}-5)} - \frac{1}{(\frac{\omega_e}{n}-4)} + \frac{(5+\frac{e^2}{2})}{e(\frac{\omega_e}{n}-3)} - \frac{(3+\frac{e^2}{2})}{e(\frac{\omega_e}{n}-1)}$$
$$- \frac{e}{2(\frac{\omega_e}{n}+1)}\Bigg] + \frac{B_0 q\sin i\sin\theta_m\cos^2\frac{i}{2}}{4a^3 mn} \quad (447)$$

$$Q_{144} = -\frac{B_0 q\sin\theta_m\cos^2 i}{a^3 mn\sin i(1-e^2)^{\frac{3}{2}}}\Bigg[\frac{3e^4}{8(\frac{\omega_e}{n}+2)} + \frac{3e(1+\frac{e^2}{2})}{4(\frac{\omega_e}{n}+1)} + \frac{3e(1+\frac{e^2}{2})}{4(\frac{\omega_e}{n}-1)} + \frac{3e^4}{8(\frac{\omega_e}{n}-2)}$$
$$+ \frac{e^3}{8(\frac{\omega_e}{n}-3)} + \frac{3e^4}{32(\frac{\omega_e}{n}-4)} + \frac{e^3}{8(\frac{\omega_e}{n}+3)} + \frac{3e^4}{32(\frac{\omega_e}{n}+4)} + \frac{(\frac{9e^4}{16}+1)n}{\omega_e}\Bigg]$$

$$- \frac{B_0 q \sin\theta_m \omega_e \cos^3 i}{a^3 m n^2 \sin i}\left[- \frac{e^2}{4(\frac{\omega_e}{n}+2)} + \frac{e}{2(\frac{\omega_e}{n}+1)} + \frac{e}{2(\frac{\omega_e}{n}-1)} - \frac{e^2}{4(\frac{\omega_e}{n}-2)} - \frac{(\frac{e^2}{2}+1)n}{\omega_e}\right]$$
$$+ \frac{B_0 q \sin i \sin\theta_m}{a^3 m n (1-e^2)^{\frac{3}{2}}}\left[- \frac{e^3}{32(\frac{\omega_e}{n}-5)} - \frac{e^3}{32(\frac{\omega_e}{n}-3)} + \frac{(\frac{e^3}{8}+e+\frac{1}{e})}{2(\frac{\omega_e}{n}-1)} + \frac{(\frac{e^3}{8}+e+\frac{1}{e})}{2(\frac{\omega_e}{n}+1)}\right.$$
$$\left. - \frac{e^3}{32(\frac{\omega_e}{n}+3)} - \frac{e^3}{32(\frac{\omega_e}{n}+5)} + \frac{2n}{\omega_e}\right] + \frac{B_0 \omega_e q \sin i \sin\theta_m}{2a^3 m n^2}\left[\frac{e}{4(\frac{\omega_e}{n}-3)} - \right.$$
$$\left. \frac{1}{2(\frac{\omega_e}{n}-2)} + \frac{(\frac{e^2}{4}+2-\frac{\cos i}{2})}{e(\frac{\omega_e}{n}-1)} - \frac{(2+\frac{e^2}{4}+\frac{\cos i}{2})}{e(\frac{\omega_e}{n}+1)} + \frac{1}{2(\frac{\omega_e}{n}+2)} - \frac{e}{4(\frac{\omega_e}{n}+3)}\right] \quad (448)$$

$$Q_{145} = \frac{B_0 e q \cos\omega \sin\theta_m \cos i}{2a^3 m n \sin i (1-e^2)^{\frac{3}{2}}}\left[\frac{3e^3 n}{8\omega_e} + \frac{3e^3}{8(\frac{\omega_e}{n}+2)} + \frac{1}{(\frac{\omega_e}{n}+1)} + \frac{e^3}{8(\frac{\omega_e}{n}-2)}\right.$$
$$\left. + \frac{e^3}{8(\frac{\omega_e}{n}+4)}\right] \quad (449)$$

$$Q_{146} = -\frac{B_0 e q \cos\omega \sin\theta_m \cos i}{2a^3 m n \sin i (1-e^2)^{\frac{3}{2}}}\left[\frac{3e^3 n}{8\omega_e} + \frac{3e^3}{8(\frac{\omega_e}{n}-2)} + \frac{1}{(\frac{\omega_e}{n}-1)} + \frac{e^3}{8(\frac{\omega_e}{n}+2)}\right.$$
$$\left. + \frac{e^3}{8(\frac{\omega_e}{n}-4)}\right] \quad (450)$$

$$Q_{147} = \frac{B_0 e q \cos^2 i \sin\omega \sin\theta_m}{2a^3 m n \sin i (1-e^2)^{\frac{3}{2}}}\left[\frac{3e^3 n}{8\omega_e} + \frac{3e^3}{8(\frac{\omega_e}{n}+2)} + \frac{1}{(\frac{\omega_e}{n}+1)} + \frac{e^3}{8(\frac{\omega_e}{n}-2)}\right.$$
$$\left. + \frac{e^3}{8(\frac{\omega_e}{n}+4)}\right] \quad (451)$$

$$Q_{148} = \frac{B_0 e q \cos^2 i \sin\omega \sin\theta_m}{2a^3 m n \sin i (1-e^2)^{\frac{3}{2}}}\left[\frac{3e^3 n}{8\omega_e} + \frac{3e^3}{8(\frac{\omega_e}{n}-2)} + \frac{1}{(\frac{\omega_e}{n}-1)} + \frac{e^3}{8(\frac{\omega_e}{n}+2)}\right.$$
$$\left. + \frac{e^3}{8(\frac{\omega_e}{n}-4)}\right] \quad (452)$$

$$\frac{Q_{149}\pi}{na^2\sqrt{1-e^2}}(K_{11}+K_{13}\sin\omega)=\frac{(\frac{e^2}{2}+1)\pi B_0 q\cos\theta_m\cos i}{na^3m(1-e^2)^{\frac{3}{2}}}\Bigg[2+\frac{3e^2}{4}-\frac{\omega_e\sin 2i(1-e^2)^{\frac{3}{2}}}{n\sin i}+\frac{e^2\sin^2\omega}{2}\Bigg] \quad (453)$$

$$\frac{2\pi Q_{150}}{na^2\sqrt{1-e^2}}\Bigg[\frac{K_{12}}{2}+K_2\sin\omega+K_{14}\sin^2\omega\Bigg]=-\frac{\pi e^2 B_0 q\cos\theta_m\cos i}{2na^3m(1-e^2)^{\frac{3}{2}}}\Bigg[\frac{5}{2}+3\sin^2\omega\Bigg] \quad (454)$$

$$\frac{\pi Q_{151}}{na^2\sqrt{1-e^2}}\Bigg[K_{15}-K_{11}\cos 2\omega+K_{13}\sin\omega\Bigg]=\frac{\pi e^2 B_0 q\cos\theta_m\cos i}{4na^3m(1-e^2)^{\frac{3}{2}}}\Bigg[\frac{3e^2}{4}-2\cos 2\omega-\frac{3e^2\cos 2\omega}{4}+\frac{\omega_e\sin 2i(1-e^2)^{\frac{3}{2}}\cos 2\omega}{n\sin i}+\frac{e^2\sin^2\omega}{2}\Bigg] \quad (455)$$

$$\frac{\pi}{na^2\sqrt{1-e^2}}\Bigg[Q_{43}+Q_{131}Q_{133}+\frac{Q_{131}Q_{134}e}{2}+Q_{132}Q_{134}\cos 2\omega\Bigg]=\frac{\pi B_0 q\cos\theta_m}{na^3m(1-e^2)^{\frac{3}{2}}}\Bigg[4\cos i-\frac{\omega_e}{2n}\cos 2\omega\sin^2 i(1-e^2)^{\frac{3}{2}}\Bigg] \quad (456)$$

where, a, e, i, ω represent semi-major axis, eccentricity, inclination, and argument of perigee, respectively. B_0 represents magnetic dipole moment of Earth, q represents charge of the space object, m represents mass of the space object, n represents orbital mean motion, ω_e represents Earth's rotation rate, μ represents standard gravitational parameter of Earth, and θ_m represents angle between dipole north pole and geographic north pole.

C ANALYTIC EXPRESSIONS FOR THE ENTRIES OF SECOND HYBRID MOMENT OF A PARTIALLY WRAPPED NORMAL DISTRIBUTION

$$\boldsymbol{m}_2(1,1) = \frac{a}{2}[1 - \exp(-C_{11})\cos 2\mu_1] \tag{457}$$

where $a = 1 - exp(-C_{11})$.

$$\boldsymbol{m}_2(1,2) = -\frac{a}{2}exp(-C_{11})\sin 2\mu_1 \tag{458}$$

$$\begin{aligned}\boldsymbol{m}_2(1,3) = \frac{1}{2}exp(-\frac{1}{2}(C_{11} + 2C_{12} + C_{22}))\cos(\mu_1 + \mu_2) \\ + \frac{1}{2}exp(-\frac{1}{2}(C_{11} - 2C_{12} + C_{22}))\cos(\mu_1 - \mu_2) \\ - \cos\mu_1 exp(-C_{11}/2)\cos\mu_2 exp(-C_{22}/2)\end{aligned} \tag{459}$$

$$\begin{aligned}\boldsymbol{m}_2(1,4) &= \frac{1}{2}exp(-\frac{1}{2}(C_{11} + 2C_{12} + C_{22}))\sin(\mu_1 + \mu_2) \\ &\quad -\frac{1}{2}exp(-\frac{1}{2}(C_{11} - 2C_{12} + C_{22}))\sin(\mu_1 - \mu_2) \\ &\quad - \cos\mu_1 exp(-C_{11}/2)\sin\mu_2 exp(-C_{22}/2)\end{aligned} \tag{460}$$

$$\begin{aligned}\boldsymbol{m}_2(1,5) = \frac{1}{2}exp(-\frac{1}{2}(C_{11} + 2C_{13} + C_{33}))\cos(\mu_1 + \mu_3) \\ + \frac{1}{2}exp(-\frac{1}{2}(C_{11} - 2C_{13} + C_{33}))\cos(\mu_1 - \mu_3) \\ - \cos\mu_1 exp(-C_{11}/2)\cos\mu_3 exp(-C_{33}/2)\end{aligned} \tag{461}$$

$$\boldsymbol{m}_2(1,6) = \frac{1}{2}exp(-\frac{1}{2}(C_{11} + 2C_{13} + C_{33}))\sin(\mu_1 + \mu_3)$$

$$- \frac{1}{2}exp(-\frac{1}{2}(C_{11} - 2C_{13} + C_{33}))\sin(\mu_1 - \mu_3)$$
$$- \cos\mu_1 exp(-C_{11}/2)\sin\mu_3 exp(-C_{33}/2) \quad (462)$$

$$\boldsymbol{m}_2(1,7) = -exp\Big(-\frac{C_{11}}{2}\Big)C_{14}\sin\mu_1 \quad (463)$$

$$\boldsymbol{m}_2(1,8) = -exp\Big(-\frac{C_{11}}{2}\Big)C_{15}\sin\mu_1 \quad (464)$$

$$\boldsymbol{m}_2(1,9) = -exp\Big(-\frac{C_{11}}{2}\Big)C_{16}\sin\mu_1 \quad (465)$$

$$\boldsymbol{m}_2(2,2) = \frac{a}{2}\Big(1 + exp(-C_{11})\cos(2\mu_1)\Big) \quad (466)$$

$$\begin{aligned}\boldsymbol{m}_2(2,3) &= \frac{1}{2}exp(-\frac{1}{2}(C_{11} + 2C_{12} + C_{22}))\sin(\mu_1 + \mu_2) \\ &\quad -\frac{1}{2}exp(-\frac{1}{2}(C_{11} - 2C_{12} + C_{22}))\sin(\mu_2 - \mu_1) \\ &\quad - \cos\mu_2 exp(-C_{22}/2)\sin\mu_1 exp(-C_{11}/2) \quad (467)\end{aligned}$$

$$\begin{aligned}\boldsymbol{m}_2(2,4) &= \frac{1}{2}exp(-\frac{1}{2}(C_{11} - 2C_{12} + C_{22}))\cos(\mu_1 - \mu_2) \\ &\quad -\frac{1}{2}exp(-\frac{1}{2}(C_{11} + 2C_{12} + C_{22}))\cos(\mu_1 + \mu_2) \\ &\quad - \sin\mu_1 exp(-C_{11}/2)\sin\mu_2 exp(-C_{22}/2) \quad (468)\end{aligned}$$

$$\begin{aligned}\boldsymbol{m}_2(2,5) &= \frac{1}{2}exp(-\frac{1}{2}(C_{33}+2C_{13}+C_{11}))\sin(\mu_1+\mu_3) \\ &\quad -\frac{1}{2}exp(-\frac{1}{2}(C_{33}-2C_{13}+C_{11}))\sin(\mu_3-\mu_1) \\ &\quad -\cos\mu_3 exp(-C_{33}/2)\sin\mu_1 exp(-C_{11}/2) \end{aligned} \tag{469}$$

$$\begin{aligned}\boldsymbol{m}_2(2,6) &= \frac{1}{2}exp(-\frac{1}{2}(C_{11}-2C_{13}+C_{33}))\cos(\mu_1-\mu_3) \\ &\quad -\frac{1}{2}exp(-\frac{1}{2}(C_{11}+2C_{13}+C_{33}))\cos(\mu_1+\mu_3) \\ &\quad -\sin\mu_1 exp(-C_{11}/2)\sin\mu_3 exp(-C_{33}/2) \end{aligned} \tag{470}$$

$$\boldsymbol{m}_2(2,7) = exp(-C_{11}/2)C_{14}\cos\mu_1 \tag{471}$$

$$\boldsymbol{m}_2(2,8) = exp(-C_{11}/2)C_{15}\cos\mu_1 \tag{472}$$

$$\boldsymbol{m}_2(2,9) = exp(-C_{11}/2)C_{16}\cos\mu_1 \tag{473}$$

$$\boldsymbol{m}_2(3,3) = \frac{b}{2}[1-\exp(-c_{22})\cos 2\mu_2] \tag{474}$$

where $b = 1 - exp(-C_{22})$.

$$\boldsymbol{m}_2(3,4) = -\frac{b}{2}exp(-C_{22})\sin 2\mu_2 \tag{475}$$

$$\boldsymbol{m}_2(3,5) = \frac{1}{2}exp(-\frac{1}{2}(C_{22}+2C_{23}+C_{33}))\cos(\mu_2+\mu_3) + \frac{1}{2}exp(-\frac{1}{2}(C_{22}-2C_{23}+C_{33}))\cos(\mu_2-\mu_3) - \cos\mu_2 exp(-C_{22}/2)\cos\mu_3 exp(-C_{33}/2) \quad (476)$$

$$\begin{aligned}\boldsymbol{m}_2(3,6) &= \frac{1}{2}exp(-\frac{1}{2}(C_{22}+2C_{23}+C_{33}))\sin(\mu_2+\mu_3) \\ &\quad -\frac{1}{2}exp(-\frac{1}{2}(C_{22}-2C_{23}+C_{33}))\sin(\mu_2-\mu_3) \\ &\quad -\cos\mu_2 exp(-C_{22}/2)\sin\mu_3 exp(-C_{33}/2) \quad (477)\end{aligned}$$

$$\boldsymbol{m}_2(3,7) = -exp\Big(-\frac{C_{22}}{2}\Big)C_{24}\sin\mu_2 \quad (478)$$

$$\boldsymbol{m}_2(3,8) = -exp\Big(-\frac{C_{22}}{2}\Big)C_{25}\sin\mu_2 \quad (479)$$

$$\boldsymbol{m}_2(3,9) = -exp\Big(-\frac{C_{22}}{2}\Big)C_{26}\sin\mu_2 \quad (480)$$

$$\boldsymbol{m}_2(4,4) = \frac{b}{2}\Big(1+exp(-C_{22})\cos(2\mu_2)\Big) \quad (481)$$

$$\begin{aligned}\boldsymbol{m}_2(4,5) &= \frac{1}{2}exp(-\frac{1}{2}(C_{33}+2C_{23}+C_{22}))\sin(\mu_3+\mu_2) \\ &\quad -\frac{1}{2}exp(-\frac{1}{2}(C_{33}-2C_{23}+C_{22}))\sin(\mu_3-\mu_2) \\ &\quad -\cos\mu_3 exp(-C_{33}/2)\sin\mu_2 exp(-C_{22}/2) \quad (482)\end{aligned}$$

$$\begin{aligned}\boldsymbol{m}_2(4,6) &= \frac{1}{2}exp(-\frac{1}{2}(C_{22}-2C_{23}+C_{33}))\cos(\mu_2-\mu_3)\\ &\quad -\frac{1}{2}exp(-\frac{1}{2}(C_{22}+2C_{23}+C_{33}))\cos(\mu_2+\mu_3)\\ &\quad -\sin\mu_2 exp(-C_{22}/2)\sin\mu_3 exp(-C_{33}/2)\end{aligned} \tag{483}$$

$$\boldsymbol{m}_2(4,7) = exp(-C_{22}/2)C_{24}\cos\mu_2 \tag{484}$$

$$\boldsymbol{m}_2(4,8) = exp(-C_{22}/2)C_{25}\cos\mu_2 \tag{485}$$

$$\boldsymbol{m}_2(4,9) = exp(-C_{22}/2)C_{26}\cos\mu_2 \tag{486}$$

$$\boldsymbol{m}_2(5,5) = \frac{c}{2}[1-\exp(-C_{33})\cos 2\mu_3] \tag{487}$$

where $c = 1 - exp(-C_{33})$.

$$\boldsymbol{m}_2(5,6) = -\frac{c}{2}exp(-C_{33})\sin 2\mu_3 \tag{488}$$

$$\boldsymbol{m}_2(5,7) = -exp\bigg(-\frac{C_{33}}{2}\bigg)C_{34}\sin\mu_3 \tag{489}$$

$$\boldsymbol{m}_2(5,8) = -exp\bigg(-\frac{C_{33}}{2}\bigg)C_{35}\sin\mu_3 \tag{490}$$

$$\boldsymbol{m}_2(5,9) = -exp\Big(-\frac{C_{33}}{2}\Big)C_{36}\sin\mu_3 \tag{491}$$

$$\boldsymbol{m}_2(6,6) = \frac{c}{2}\Big(1+exp(-C_{33})\cos(2\mu_3)\Big) \tag{492}$$

$$\boldsymbol{m}_2(6,7) = exp(-C_{33}/2)C_{34}\cos\mu_3 \tag{493}$$

$$\boldsymbol{m}_2(6,8) = exp(-C_{33}/2)C_{35}\cos\mu_3 \tag{494}$$

$$\boldsymbol{m}_2(6,9) = exp(-C_{33}/2)C_{36}\cos\mu_3 \tag{495}$$

$$\boldsymbol{m}_2(7,7) = C_{44} \tag{496}$$

$$\boldsymbol{m}_2(7,8) = C_{45} \tag{497}$$

$$\boldsymbol{m}_2(7,9) = C_{46} \tag{498}$$

$$\boldsymbol{m}_2(8,8) = C_{55} \tag{499}$$

$$\boldsymbol{m}_2(8,9) = C_{56} \tag{500}$$

$$\boldsymbol{m}_2(9,9) = C_{66} \tag{501}$$